LEABHARLANN CHOLÁISTE NA TRÍONÓIDE, BAILE ÁTHA CLIATH | TRINITY COLLEGE LIBRARY DUBLIN
Ollscoil Átha Cliath | The University of Dublin

Terms and Conditions of Use of Digitised Theses from Trinity College Library Dublin

Copyright statement

All material supplied by Trinity College Library is protected by copyright (under the Copyright and Related Rights Act, 2000 as amended) and other relevant Intellectual Property Rights. By accessing and using a Digitised Thesis from Trinity College Library you acknowledge that all Intellectual Property Rights in any Works supplied are the sole and exclusive property of the copyright and/or other IPR holder. Specific copyright holders may not be explicitly identified. Use of materials from other sources within a thesis should not be construed as a claim over them.

A non-exclusive, non-transferable licence is hereby granted to those using or reproducing, in whole or in part, the material for valid purposes, providing the copyright owners are acknowledged using the normal conventions. Where specific permission to use material is required, this is identified and such permission must be sought from the copyright holder or agency cited.

Liability statement

By using a Digitised Thesis, I accept that Trinity College Dublin bears no legal responsibility for the accuracy, legality or comprehensiveness of materials contained within the thesis, and that Trinity College Dublin accepts no liability for indirect, consequential, or incidental, damages or losses arising from use of the thesis for whatever reason. Information located in a thesis may be subject to specific use constraints, details of which may not be explicitly described. It is the responsibility of potential and actual users to be aware of such constraints and to abide by them. By making use of material from a digitised thesis, you accept these copyright and disclaimer provisions. Where it is brought to the attention of Trinity College Library that there may be a breach of copyright or other restraint, it is the policy to withdraw or take down access to a thesis while the issue is being resolved.

Access Agreement

By using a Digitised Thesis from Trinity College Library you are bound by the following Terms & Conditions. Please read them carefully.

I have read and I understand the following statement: All material supplied via a Digitised Thesis from Trinity College Library is protected by copyright and other intellectual property rights, and duplication or sale of all or part of any of a thesis is not permitted, except that material may be duplicated by you for your research use or for educational purposes in electronic or print form providing the copyright owners are acknowledged using the normal conventions. You must obtain permission for any other use. Electronic or print copies may not be offered, whether for sale or otherwise to anyone. This copy has been supplied on the understanding that it is copyright material and that no quotation from the thesis may be published without proper acknowledgement.

FINITE ELEMENT SIMULATION OF A METAL FORMING PROCESS & DIE DESIGN

By

Gavin Edward Quinlan

SUBMITTED IN FULFILLMENT OF THE
REQUIREMENTS FOR THE DEGREE OF
DOCTOR OF PHILOSOPHY
AT
UNIVERSITY OF DUBLIN, TRINITY COLLEGE
DUBLIN, IRELAND
MARCH 2000

© Copyright by Gavin Edward Quinlan, 2000

TRINITY COLLEGE
10 JUL 2000
LIBRARY DUBLIN
THESIS
5790

Declaration

Date: **March 2000**

Author: **Gavin Edward Quinlan**

Title: **Finite Element Simulation of a Metal Forming Process & Die Design**

Department: **Mechanical & Manufacturing Engineering**

Degree: **Ph.D.** Year: **2000**

Permission is herewith granted to University of Dublin, Trinity College to circulate and to have copied for non-commercial purposes, at its discretion, the above title upon the request of individuals or institutions.

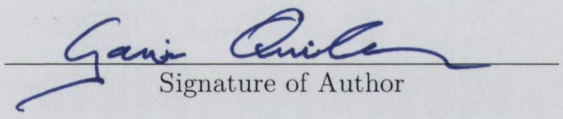

Signature of Author

THE AUTHOR RESERVES OTHER PUBLICATION RIGHTS, AND NEITHER THE THESIS NOR EXTENSIVE EXTRACTS FROM IT MAY BE PRINTED OR OTHERWISE REPRODUCED WITHOUT THE AUTHOR'S WRITTEN PERMISSION.

THE AUTHOR ATTESTS THAT PERMISSION HAS BEEN OBTAINED FOR THE USE OF ANY COPYRIGHTED MATERIAL APPEARING IN THIS THESIS (OTHER THAN BRIEF EXCERPTS REQUIRING ONLY PROPER ACKNOWLEDGEMENT IN SCHOLARLY WRITING) AND THAT ALL SUCH USE IS CLEARLY ACKNOWLEDGED.

To my Parents, Barbara, & Newcastle United

Table of Contents

List of Figures

Acknowledgements

I would like to thank my supervisor Prof. John Monaghan for all his help and guidance through my time as a postgraduate student. I would also like to thank him for the time he devoted to reading this thesis and for helping me to become a better engineer. Without his guidance this thesis would never have come into existence.

I would also like to thank Jim Ryall, Paul Real, Mike Meere, and the other staff at Hi-Life Tools, Shannon for their technical guidance and advice on the realities of thread rolling, and their input to the Measure 1 project.

A special mention must go to Ron Hukari, Steve Buzolits, Len Croissette and the rest of the staff at SPS Technologies, Jenkintown, U.S.A. Their help during the experimental stage of this research was invaluable. Ron was a mine of information at the write-up stage.

I would like to thank the Materials Ireland staff, Michael, Ray, Liam, Toman, and Fiona for the help and support they gave me over my years of research and to the Materials Ireland organisation for their financial support.

I would like to thank all the department's postgraduates for helping keep me sane through my research. A special thanks must go to Conor and Gabriel, two friends who have helped me so much.

I would like to thank John Coyne for creating those social diversions which kept my brain from exploding and for always being there.

A strange but special thanks goes to Newcastle United Football Club, who have given me hours of joy (and sadness) over the years of my research. Let's hope that me finishing this write-up is a sign of the things to come.

Huge thanks must go to my family and especially my parents without whose support I could never have got so far. Mum and Dad, thanks a million.

Last but by no means least, my biggest thanks go to Barbara, who changed my world the day I met her. Without her I would not be writing this today.

Gavin Quinlan
Dublin, Ireland
29 March, 2000

Summary

Thread Rolling (also known as roll threading) is a cold forming process for producing threads or other helical or annular forms on a fastener. This is achieved by rolling the surface profile of hardened steel dies onto the surface of a cylindrical or conical blank. Dies for Thread Rolling may be either flat or cylindrical. In contrast to thread cutting and thread grinding, thread rolling does not remove any metal from the workpiece. However this feature does not mean that threads are formed perfectly. Since the early days of thread rolling defects have been accepted as part and parcel of the thread rolling process.

The objective of this study was to design a new Thread Rolling Die, which would significantly lower the occurrence of the aforementioned fastener defects, particularly internal ones. This design process was undertaken using a combination of advanced finite element techniques and experimental testing. Modifications to the "thread form" of the thread rolling die were considered the most appropriate means by which to alter the design of the standard thread rolling die.

Numerous different thread rolling die designs were simulated and analysed using finite element analysis and an optimum die design was predicted. The optimum thread rolling die design was then produced by a thread rolling die manufacturer. A series of experimental trials using these new thread rolling die designs were carried out in the U.S.A. The occurrence of defects in the fasteners produced using the new die designs was checked. Tensile and fatigue tests of the new fasteners were also performed to ensure that the new thread rolling die designs had no detrimental effects on the mechanical properties of the fasteners. The results from these experimental trials confirmed the finite element predictions.

Nomenclature

A	Cross-sectional area
A_0	Initial cross-sectional area
A_{jN}	Area contribution of the jth element to node N
B	Strain Rate Matrix
C	Constant
C	Volumetric Strain Rate vector
D	Diameter
D_0	Initial Diameter
E	Young's Modulus
F	Effective Strain Rate Coefficient Matrix
$\mathrm{F}(\sigma_{ij})$	Function of stresses
F_i	Traction
G	Shear Modulus
H	Height
H_0	Initial Height
$\mathrm{H}(\bar{\epsilon})$	Work Hardening Function
ΔH	Increment of height
J_1	Linear invariant of stress tensor
J_2	Quadratic invariant of stress tensor
J_3	Cubic invariant of stress tensor
J_1'	Linear invariant of deviatoric stress tensor
J_2'	Quadratic invariant of deviatoric stress tensor
J_3'	Cubic invariant of deviatoric stress tensor
J	Jacobian of coordinate transformation
K	Penalty Constant
K	Stiffness Matrix
N	Shape function matrix
P	Load

$\mathbf{P}$	Effective Strain rate matrix
S	Surface
S_C	Surface of Tool-workpiece contact
S_D	Surface of discontinuity
S_F	Surface where traction is prescribed
T	Thickness
W_P	Total plastic work per unit volume
$\dot{W}_P$	Plastic work-rate per unit volume
X_α	Element of strain-rate matrix $\mathbf{B}$
Y	Yield Stress in uniaxial tension
Y_α	Element of strain-rate matrix $\mathbf{B}$
e	Engineering Strain
f_s	Frictional Stress
$\mathbf{f}$	Nodal point force vector
$f(\sigma_{ij})$	Yield Function
$g(\sigma_{ij})$	Scalar function of stress invariants
$h(\sigma_{ij})$	Scalar function of stress invariants
k	Shear yield stress
m	Friction factor (Chapter 3)
m	Strain rate sensitivity exponent (Chapter 4)
n	Strain-hardening exponent
$\mathbf{n}$	Unit normal to the surface
q_α	Shape functions
t	Time
δt	Time increment
u_i	Velocity component
u_0	Initial velocity
u_s	Relative sliding velocity
$\mathbf{v}$	Velocity vector at nodal point
$\mathbf{v}_0$	Initial velocity vector at nodal point
α	Flow localisation Parameter (Chapter 2)
α	Deceleration coefficient (Appendix B)
$\delta_{\alpha\beta}$	Kronecker delta
γ'	Work Hardening Rate
$\overline{\epsilon}$	Effective Strain
$\dot{\epsilon}_{ij}$	Strain Rate

$d\epsilon_{ij}$	Infinitesimal Strain
$\dot{\epsilon}_{ij}{}^{p}$	Plastic Strain Rate
$\dot{\epsilon}_{ij}{}^{e}$	Elastic Strain Rate
$\dot{\bar{\epsilon}}$	Effective Strain Rate
η	Local coordinate
θ	Angle
λ	Lagrangian Mulitiplier
μ	Coefficient of friction
ν	Poisson's Ratio
ξ	Local coordinate
π	Functional
$\delta\pi$	Variation of functional π
$\delta\pi_D$	Term due to deformation energy rate in $\delta\pi$
$\delta\pi_P$	Penalty Term in $\delta\pi$
$\delta\pi_{S_F}$	Term due to traction in $\delta\pi$
σ_{ij}	Cauchy Stress
$\sigma_{ij}{}'$	Deviatoric Stress
$\overline{\sigma}$	Effective, Flow Stress
σ_m	Mean Stress

Introduction

Thread Rolling (also known as roll threading) is a cold forming process for producing threads or other helical or annular forms on a fastener. This is achieved by rolling the surface profile of hardened steel dies onto the surface of a cylindrical or conical blank. Dies for Thread Rolling may be either flat or cylindrical (Figure 1(a) and 1(b) respectively). Flat Dies operate by a traversing motion. Cylindrical dies use a number of different ways to form the threaded fastener.

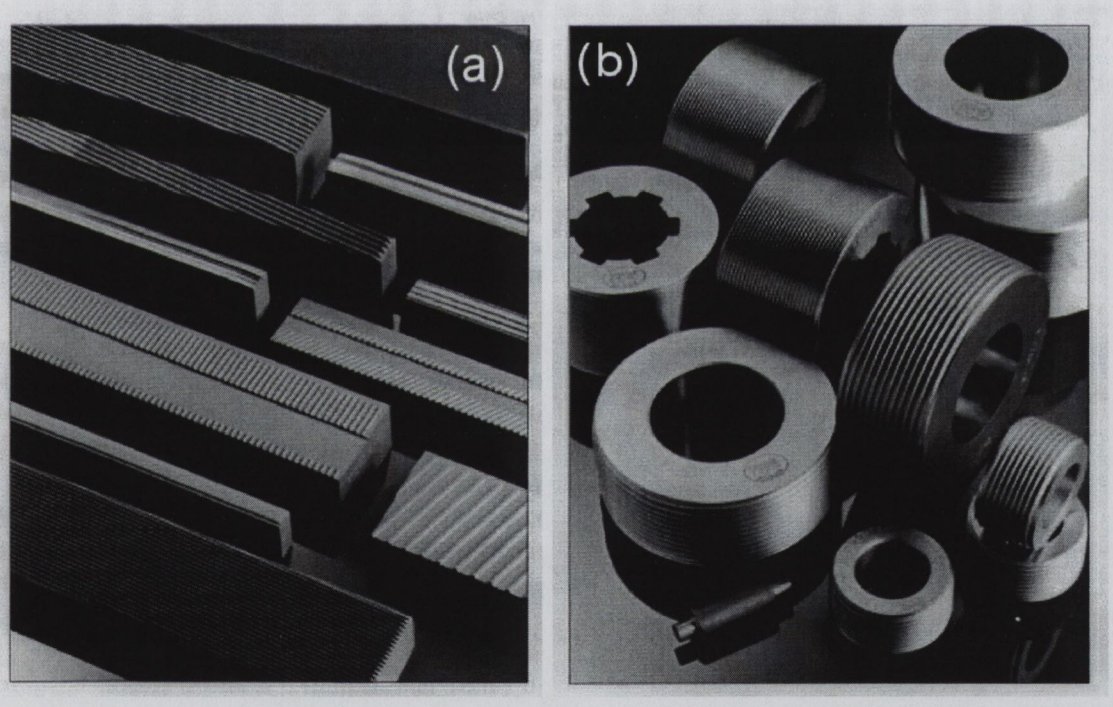

Figure 1: A Selection of Flat (a) & Cylindrical (b) Thread Rolling Dies

In contrast to thread cutting and thread grinding, thread rolling does not remove any metal from the blank (workpiece). This feature of thread rolling is one of the most important, as the worked metal is significantly stronger and harder than that of the original blank. Thus, fasteners with rolled threads are harder and stronger than those

with cut threads. However this feature does not mean that the threads are formed perfectly. Since the early days of thread rolling, surface discontinuities, laps, and other internal defects, see Figure 2, have been accepted as part and parcel of the thread rolling process.

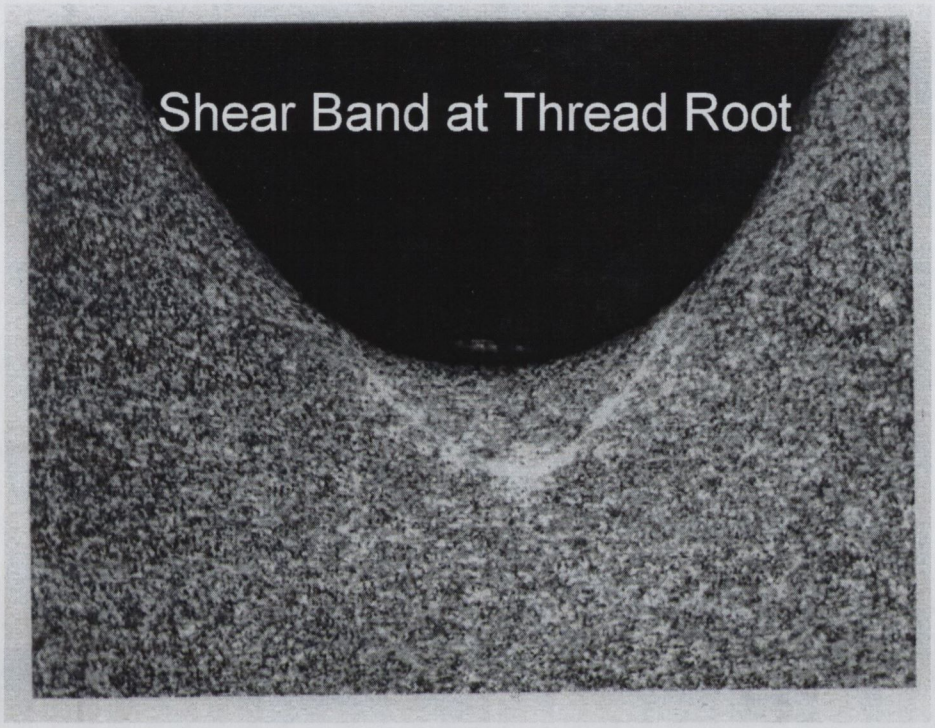

Figure 2: Rolled Thread Defect

For a considerable time it was actually regarded as impossible to eliminate laps when rolling at very high production rates, so industry specifications were written so that some defects were acceptable depending on their location. Though all fastener materials are susceptible to the formation of rolling defects, certain materials e.g. Titanium 6Al-4V, and stainless steel are more prone compared to other materials. The elimination of these defects is of particular importance to the aerospace industry where the fasteners have super critical quality requirements.

Thesis Objective

The objective of this study was to design a Thread Rolling Die which would significantly lower the occurrence of the aforementioned fastener defects, particularly internal ones. This is of particular importance in the automotive and aerospace industries of today. On one hand higher production speeds are demanded, while on the other hand still meeting ever increasing quality demands placed on them by regulatory bodies due to safety concerns for passengers. Acceptance criteria for fasteners manufactured by these industries now approach a 'zero' defect concept. This concept is very difficult to achieve with current thread rolling technology. A new innovative design approach was required to develop this "black art" and give the process a more scientific basis. This design process was undertaken using a combination of advanced finite element techniques and experimental testing and was used to develop a thread rolling die which would meet and exceed all the production and quality requirements placed upon it.

In 1997, Hi-Life Tools, Shannon in conjunction with Materials Ireland, T.C.D. initiated a research project under the Enterprise Ireland Measure 1 scheme to re-design their entire product line. The project was completed in October 1999 and was deemed by Shannon Development to be an exemplary model of how a Measure 1 project should be undertaken and succeed. Thread rolling dies represent the largest percentage turnover of Hi-Life Tool's entire product line and consequently thread rolling die re-design represented a significant portion of the Measure 1 research programme. The author had a significant amount of responsibility for this portion of the research programme. The final design, which originated as part of this work will be outlined in later chapters and is under consideration for patent approval.

In Chapter One the reader will be introduced to the terminology of thread rolling dies and fasteners which is used extensively throughout the rest of the thesis. Chapter two explains the defects which may occur during the thread rolling process in greater detail. In Chapter three a review of plasticity theory and the finite element techniques pertinent to thread rolling problems is presented. Chapter Four outlines the work programme undertaken by the author in the simulation of the thread rolling process,

the design of the new thread rolling dies, and the experimental methods used to verify the success of the new designs. Chapters Five and Six present the finite element results and experimental results respectively and will demonstrate how finite element analysis can be used to enhance the design process and result in a new novel design for thread rolling dies which are now being patented.

Chapter 1

Thread Rolling

This chapter introduces the reader to the area of Thread Rolling. The special terminology involved with threaded fasteners and thread rolling dies will be explained. The actual tools and processes used to create these threads will then be described.

Defects that may arise from this manufacturing process and their effects on the fasteners will be discussed. Finally some of the materials used in the manufacture of fasteners will be mentioned and the term *Rollability* will be explained.

1.1 Introduction

Thread rolling is a simple cold forging process confined almost entirely to external threads. It is referred to as a cold forging process because most rolling is performed on cold blanks. However, rolling of threads on heated blanks has been beneficial in some applications. Today, thread rolling is accepted by many industries as the preferred method of producing uniform, smooth, precise threads of superior physical properties.

Hardened steel dies are used to roll threads. The threaded faces of these dies are pressed against the periphery of a plain cylindrical blank and re-form the surface of the blank into threads as the blank rolls on the die faces (Figure 1.1). The working faces of the dies have a thread form which is the reverse of the thread to be produced. In penetrating the surface of the blank, the dies displace the material to form the roots of the thread and force the displaced material radially outward to form the crests of the thread. The blank has a diameter part way between the major and minor diameter of the thread. A comparison of a cut and rolled threads is shown below in Figures

1.2 and 1.3 respectively. Unlike other threading processes, no material is removed and consequently no chips are produced.

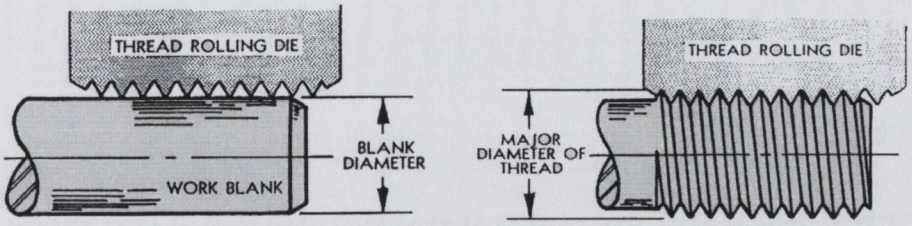

Figure 1.1: Blank and Rolled Fastener

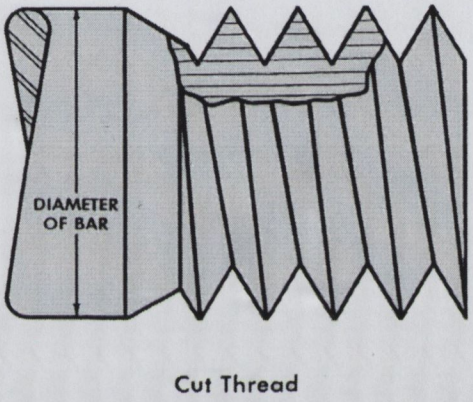

Figure 1.2: Cut Threads

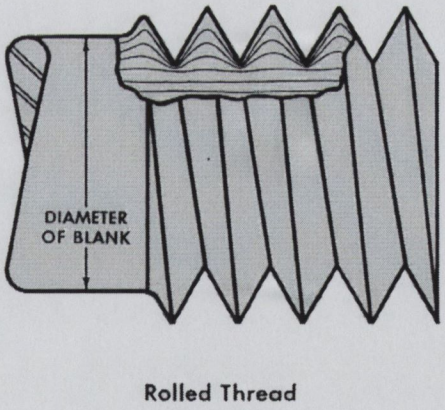

Figure 1.3: Rolled Threads

1.2 Fundamentals

This section explains the terminology that will arise throughout the remainder of this thesis. It will be important for the reader to be able to understand these "buzzwords" so that some of the later descriptions can be fully appreciated [1]. Figure 1.4 shows a schematic of a fastener highlighting all of the different items of interest. Figure 1.5 shows a diagram of the side profile of a flat thread rolling die highlighting the different sections of it.

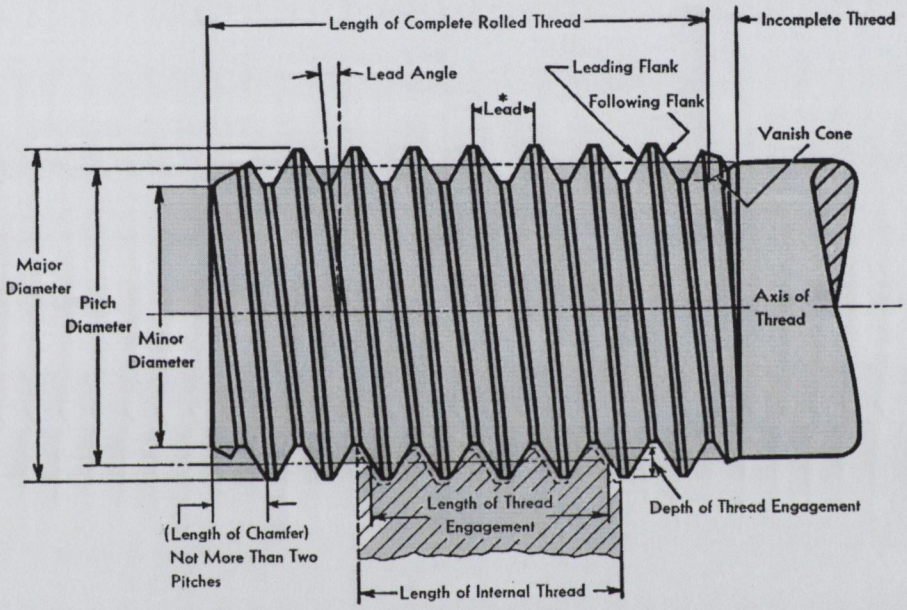

Figure 1.4: Schematic of a Thread Rolled Fastener

Screw Thread: is a helical ridge on the outside surface of a cylinder.

Major Diameter: is the largest diameter or the outside diameter of the threads.

Minor Diameter: is the smallest diameter or the diameter measured at the roots of the threads.

Root: is the bottom surface of the thread which is at the minor diameter of the fastener.

Crest: is the top of the thread which is at the major diameter of the fastener.

Flank of Thread: is the side of the thread which connects the root with the crest.

Thread Angle or Included Angle: is the angle between the two flanks.

Axis: is the centre line which runs lengthwise through the piece

Height or Depth of Thread: is the distance between the crest and root of the thread when measured perpendicular to the axis.

Pitch: is the distance from the a point on a screw thread to the same point on the next thread.

Pitch Line: is a line which passes through the threads at a point where the width between the threads is equal to the width of the thread.

Pitch Diameter: is the distance between the two pitch lines on opposite sides of the fastener

Thickness of Thread: is the width of a thread along a pitch line.

Helix Angle: is the angle formed by a line at 90 Degrees from the axis of the fastener and a line running along the crest of a thread. It is also known as the lead angle.

Lead: is the distance that a screw thread advances in one turn. On a single thread screw, the "lead" and "pitch" are the same. On a double thread screw, the "lead" is twice the 'pitch'.

Complete Thread: is a thread having a full form at both crest and root.

Incomplete/Imperfect Thread: is that part at the ends of a threaded section where the root and/or crest is not fully formed.

Thread Roll Diameter: The portion of the fastener to be threaded.

Body Diameter: The portion of the fastener not to be threaded.

Thread Roll Angle: The angle between the body and the thread roll diameter.

Point Angle: The angle at the end of the thread roll diameter on the point of the fastener.

Grip Length: The distance from under the head of the fastener to the top of the thread roll angle.

Thread Length: The length from the top of the thread roll angle to the point of the bolt.

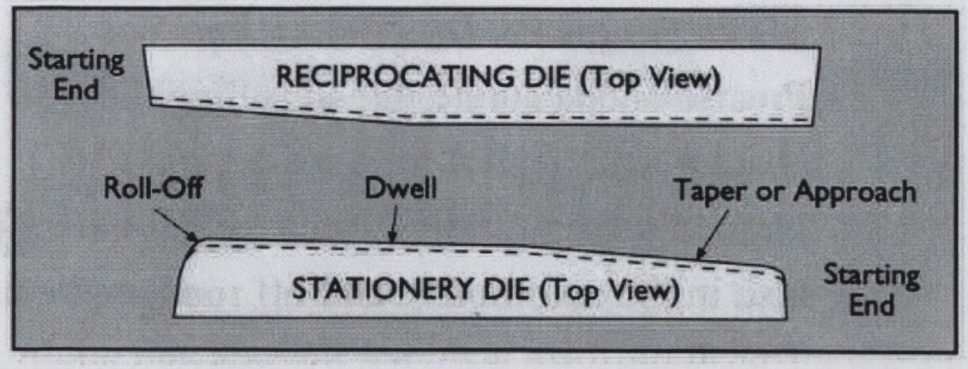

Figure 1.5: Schematic of a Thread Rolling Die

Stationary Die: The smaller of the two flat dies which does not move.

Moving Die: The larger of the two flat dies that moves back and forth.

Die Alignment: The moving and stationary dies must line up with each other, or the threads will be out of alignment.

Start Taper/Ramp section: The Ramp section of a flat thread rolling die is the section in which thread formation takes place. The section is inclined at a specified angle to the horizontal and it dictates the penetration rate.

Dwell section: The Dwell section of a flat thread rolling die ensures that at least the last full revolution of the workpiece occurs after full thread formation. This section is horizontal.

Spindles: Circular dies are mounted on the "spindles".

Cam: The cam controls the in-feed of the circular dies onto the fastener.

1.3 History & Development

Although widespread knowledge of thread rolling is a fairly recent development, the process itself is not new. Records show that it was first demonstrated early in the nineteenth century. US patent office files show that many different people worked on its development, and that most of its fundamentals were known over a hundred years ago. It did not, however, begin to be used in regular production processes until about 1880, and its use from then until the early 1940's was confined almost entirely to the fastener industry.

The slowness of the industry to accept the rolling process is a little hard to explain. It was probably due in part to a reticence within the industry to accept new processes, due to the inferior quality of the early cold forged fasteners, and to the lack of versatility of the production tools and equipment then available.

The first cold forged fasteners were inferior products. They were weak and unreliable because the wrought iron and Bessemer steel, commonly used as raw material, tended to fold and fracture during heading and split during rolling. They varied widely in diameter and roundness because of the difficulties in controlling die sizes. Thread form and lead were also unreliable because accurate thread rolling dies were difficult to obtain, and machines were light and without means for fine adjustment. It became the practice to market these inferior cold forged fasteners under the "Rolled Thread" label to distinguish them from the quality fasteners, then cut from the bar, that were marketed under the "Cut Thread" label. It was natural for the term "Rolled Thread" to be become associated with an inferior and unreliable product. Progress was made, however, in overcoming these early defects. Open hearth steels, including high strength alloys, were soon developed with excellent cold forging properties, so that weak threads and split threads were practically eliminated.

The extruding process, for the production of blanks with full-sized bodies and ends reduced to rolling diameter, was developed during the 20's and widely adopted, making possible the economic production of bolts with uniform diameter and thread. The use of tungsten carbide in wire drawing, heading, and extruding dies, that became prevalent

in the 30's, made it possible for even closer tolerances to be achieved on diameter and the roundness of blanks. Thread rolling machines were made heavier and more reliable, thread rolling dies were developed with accuracy comparable to the accuracy of thread gauges, and operating techniques were steadily improved. Thus, all the defects that characterised the early cold forged fasteners were finally overcome and in addition, it was found that with proper materials, tools, and fabricating techniques, cold working actually strengthened the products so that by the late 30's thread rolling had been accepted throughout the fastener industry as the preferred method of threading its highest quality products.

It is interesting that, as these improvements were being made, no point was found at which the labels could conveniently be changed, and first quality fasteners continued to be referred to as "cut thread", even after manufacturers had adopted the cold forging processes of heading, extruding, and rolling. There can be little doubt, therefore, that this nomenclature which was so firmly imbedded throughout the metal-working industry perpetuated the prejudice against rolled threads in the minds of otherwise well informed purchasers and engineers long after the faults of the early cold forged fasteners had been completely eliminated. It was not until the second world war, that the production of fasteners for the aerospace industry finally and conclusively proved to remaining skeptics the true worth of the rolling process.

The reciprocating flat die thread rolling machine which was the only type commercially available prior to the early 40's, is ideally suited for high speed threading of fasteners up to approximately one inch diameter, but has been used in a limited way for the threading of component parts other than fasteners. To provide greater ease in obtaining accurate threads on precision fasteners and to expand the application of thread rolling to all types of component parts, cylindrical die machines were developed. This type of machine extended the range of thread rolling to a wide variety of formed and threaded parts. This acceptance by the trade has been brought about by the steady improvements in the design of the thread rolling attachments now available.

1.4 Thread Rolling Dies & Processes

As mentioned in the Introduction, dies for thread rolling may be either flat or cylindrical (Fig. 1.6). Flat dies operate by a traversing motion. Methods that use cylindrical dies are classified as radial in-feed, tangential feed, through feed, planetary, and internal. This section will only refer to flat die rolling and radial in-feed rolling. The other types of thread rolling are fully covered in [2].

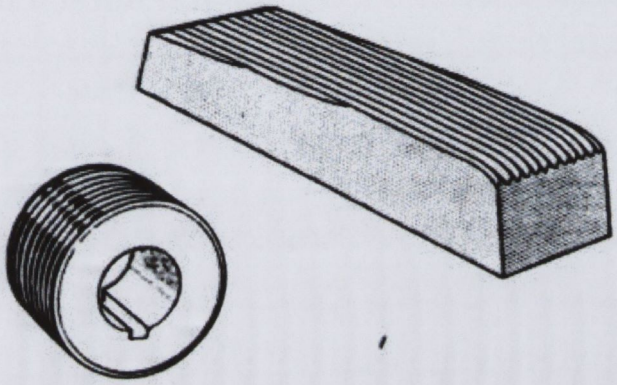

Figure 1.6: A Flat and a Cylindrical Thread Rolling Die

1.4.1 Flat Die Rolling

Flat rolling dies are one of the die types commonly used for rolling threads on commercial fasteners. Figure 1.7 shows the usual configuration of flat thread rolling dies and the unrolled fastener/workpiece.

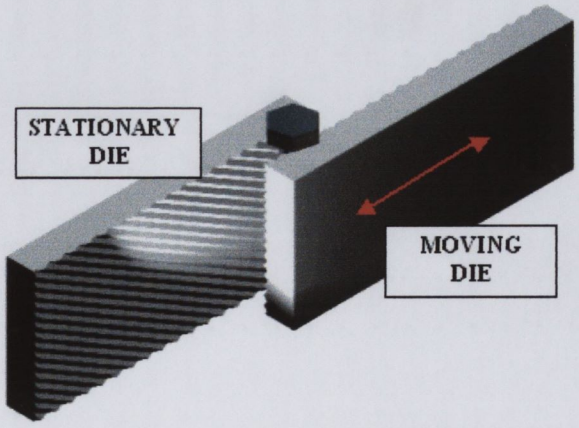

Figure 1.7: Operating Principle of Flat Thread Rolling Dies

Flat Thread Rolling Dies

The dies used in flat rolling consist of a matching pair of rectangular plates, with each of the opposed faces having the reverse image of the form to be produced on the fastener. Dies are made in various widths and are used to roll fasteners of any thread length up to the maximum die capacity. Figure 1.8 shows the different sections of a flat thread rolling die. There are three main sections on the thread rolling die, namely, the *Ramp*

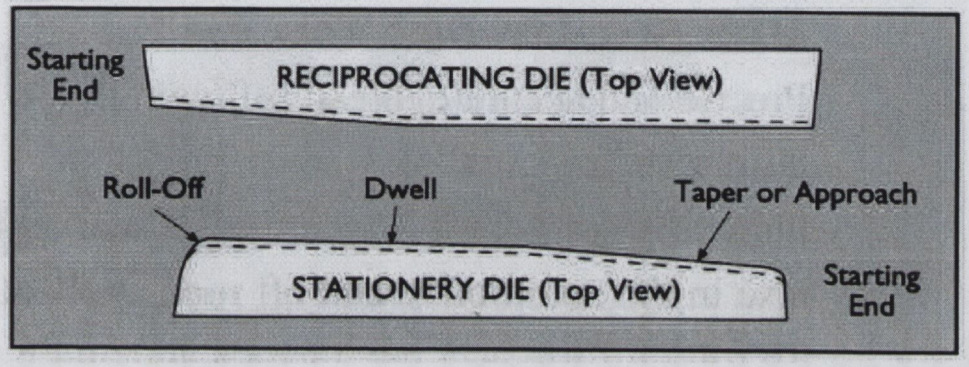

Figure 1.8: Different Sections of a Flat Thread Rolling Die

or taper section, the *Dwell* section, and the *Roll Off* section. Penetration rate (the rate at which the threads are formed) is primarily governed by the length of the ramp section of the die. It is important that the length of the ramp section is long enough to prevent an excessively high penetration rate. This could increase the strain rate to a point that could cause damaging effects in the case of some materials i.e. Titanium. Best manufacturing practice says that complete thread formation should have taken place prior to the last revolution of the workpiece. The last complete revolution of the workpiece should only iron out small surface imperfections and the dwell section of the die performs this function. The helix angle of flat dies can theoretically be between 0 and 45 degrees, but in the case of most standard threads, it is normally less than 5 degrees.

Flat Thread Rolling Process

The workpiece is placed into the space between the two flat rectangular dies and is engaged by the forward motion of the moving die. This causes the workpiece to roll between the threaded faces of the dies where the threads are formed. The distance

between the dies is equal to the minor diameter of the thread to be rolled. Threads are rolled on one workpiece at a time during the forward stroke of the machine. The diameter of the finished thread is controlled by the original workpiece diameter and the distance between the faces of the dwell section of the dies at the end of stroke.

Thread Rolling Machines

There is a large variety of flat die thread rolling machines and these come in a number of sizes, appropriate for the manufacture of particular fastener diameter range and specified die length. As a general rule, the correct machine size accommodates a die length that allows six to eight full revolutions of the workpiece. Most flat die rolling machines have the dies in a side-by-side configuration as shown in Figure 1.8. Most of the newer machines have dies that traverse in a horizontal plane, but have the faces of the die at an angle to the vertical. The feed track for the un-rolled workpieces is also at a angle thereby permitting gravity to feed the workpieces into the dies.

Flat Die Rolling can produce more than one form on the fastener in one operation, such as two entirely different types of threads at opposite ends of a fastener, knurling and a thread, or knurling and an annular groove, on the same part. *Duplex* face dies, Figure 1.9, can be used for rolling straight threads. Such dies have threads on both faces so that they can provide two rolling surfaces.

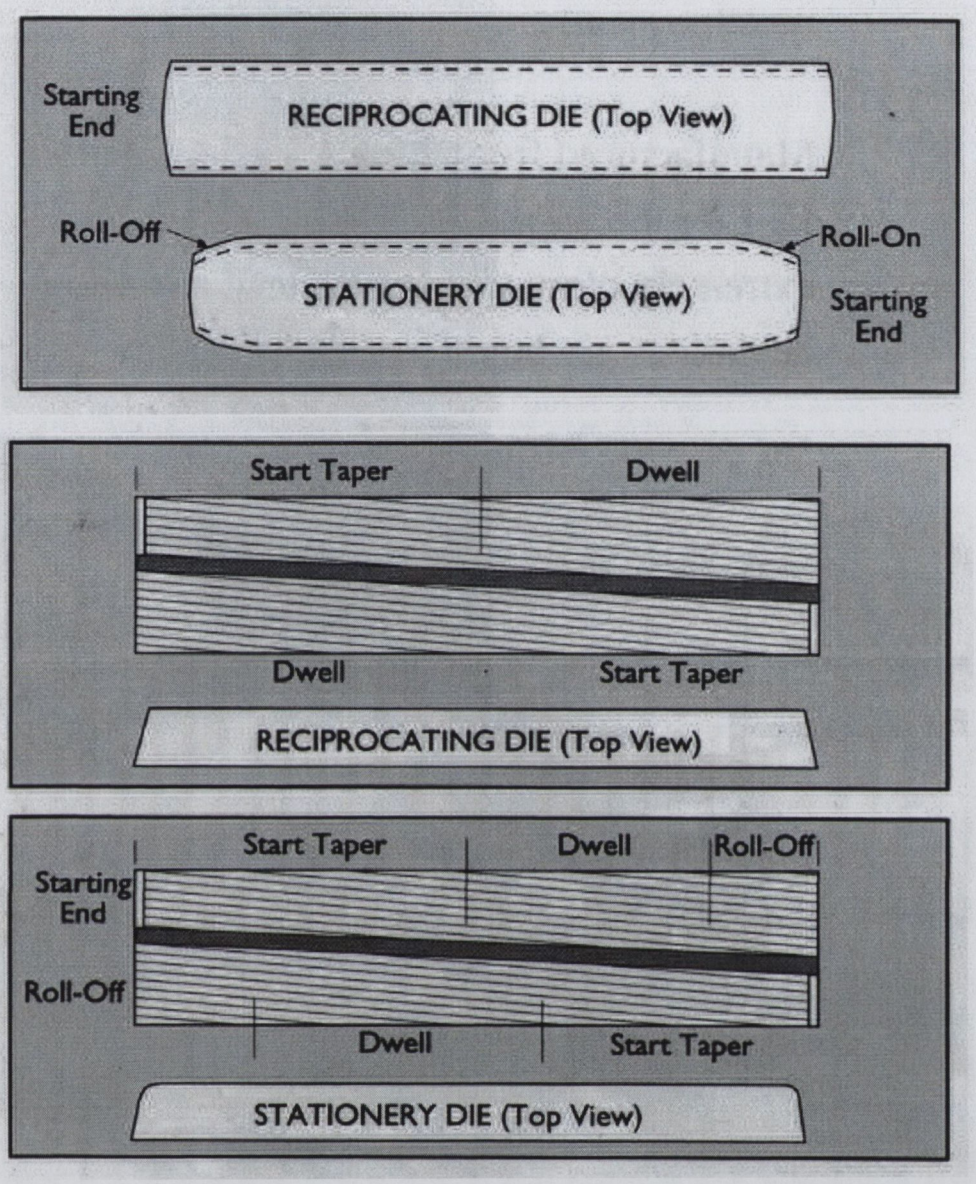

Figure 1.9: Duplex Face and 4 Way Rolling Dies

When the fastener length is less than half the die width, the die can be reversed, top for bottom, so that four rolling faces are available for even better economy. Production Rates vary widely and are usually inversely proportional to the size of the fastener being rolled. Smaller machines are capable of producing parts at a rate of 36,000 to 60,000 per hour. Larger machines, producing fasteners of a diameter range 9.5 to 13mm (3/8 or 1/2 in.), can roll 3,000 to 12,000 pieces per hour. Fasteners of a larger size than those already mentioned are rolled at a much slower rate, ranging from 900 to 3,000 pieces per hour.

1.4.2 Cylindrical Die Rolling

As mentioned earlier cylindrical thread rolling dies are used with a number of different thread rolling techniques, only *in-feed rolling* will be detailed here. Figure 1.10 and figure 1.11 show both of the possible die/workpiece configurations for in-feed rolling. The dies used in cylindrical rolling are usually two to three threads longer than the thread length being rolled. This is to allow for the fact that there is generally some axial movement between the workpiece and the cylindrical dies. Thread rolling occurs by moving the rotating cylindrical dies radially towards the centre of the rotating workpiece.

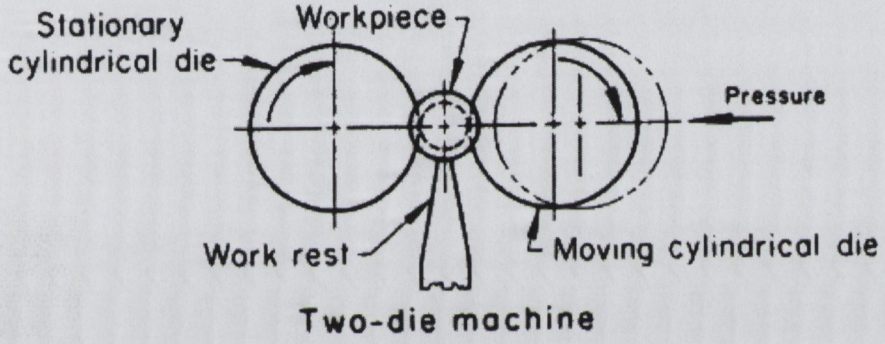

Figure 1.10: Two Die Cylindrical Machine Configuration

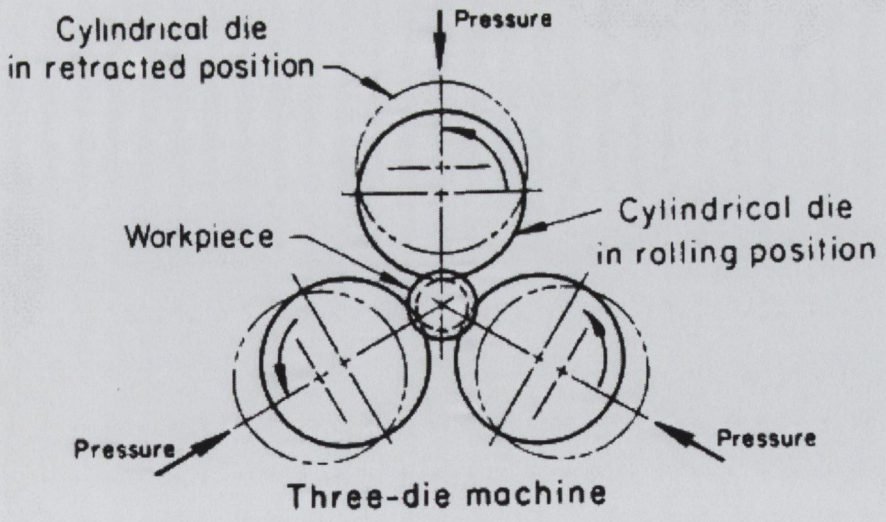

Figure 1.11: Three Die Cylindrical Machine Configuration

Two die machines are usually of the horizontal type, i.e. the workpiece is horizontal during rolling. Rolling Pressure is usually applied hydraulically, but sometimes

mechanically, and typically it is applied from one side only.

On three die cylindrical machines, the workpiece can be orientated either horizontally or vertically. Rolling pressure is applied by all three dies, simultaneously, and the workpiece is held centrally via three point contact i.e. self centering. This self centering design and infinite work revolution capability of a three die set-up results in the production of a high quality thread.

The minimum practical diameter of a workpiece for rolling in two die machines is 1.3mm (0.05in.). The maximum diameter is limited only by the capacity of the available equipment. Two die machines capable of rolling threads 380 mm (15 in.) in diameter and machines that can roll 400 mm (16 in.) are in use. Production rates of up to 60 ppm (parts per minute) can be achieved. Three die machines roll threads from 6.4 to 115 mm (1/4 to 4 1/2 in.) in diameter and up to 125 mm (5 in.) long. The rate of die penetration is adjustable. Production can be hand feed or automatic for rates of up to 100 ppm.

1.4.3 Thread Form

The term Thread Form is used to describe the overall combination of thread angle, crest radius, and root radius on the thread rolling die. Figure 1.12 indicates these variables. The thread form on the thread rolling die is the reverse of the thread,

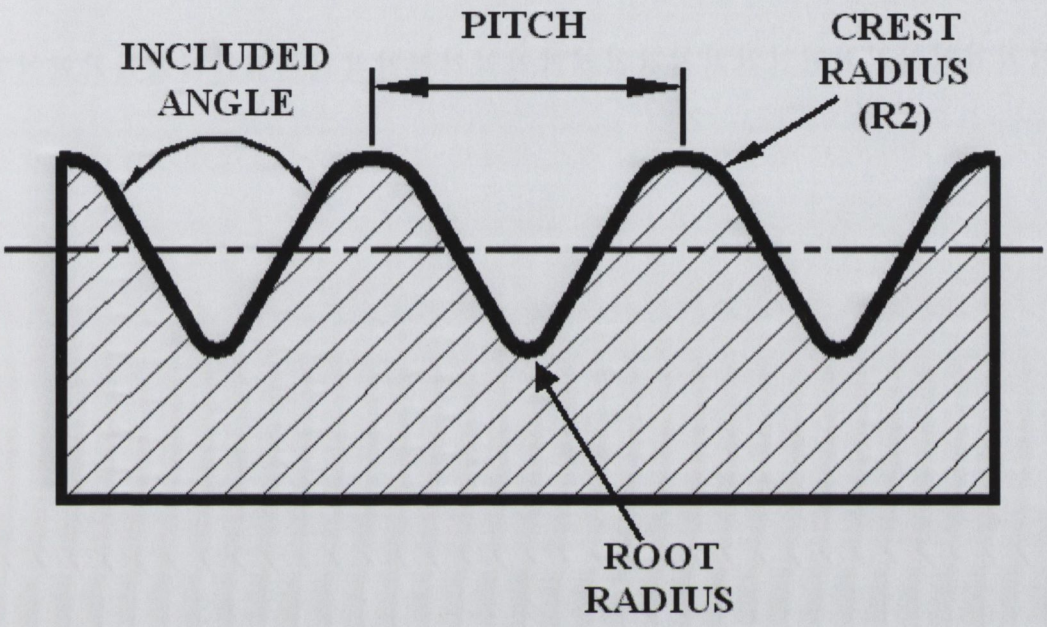

Figure 1.12: Thread Form on Thread Rolling Die

which is produced. There are a number of standard thread forms including Unified and metric. The thread geometry may be for example a fully rounded shape or that of a blunt form i.e. no root radius. The normal included angle of a thread is 60 degrees. Thread forms are standardised by ISO and ANSI committees.

The form of the thread affects the load on the die, surface finish, and thread dimensions. Greater loads are required as the form becomes more blunt. Surface finish is usually independent of the form for 60 degree threads. However, as the thread form becomes more blunt, or if it has sharp root corners, the normal smooth flow pattern of metal being rolled is altered. Restriction of metal flow may cause localised sub-surface shear failures.

1.5 Rollability

Rollability expresses the behaviour of different materials during the thread rolling processes. Rollability may be considered under three distinct headings.

1. The resistance of the material to plastic deformation.

2. The behaviour of the material during displacement.

3. The surface roughness of the rolled material.

1.5.1 Resistance to Plastic Deformation

The resistance of material to plastic deformation is probably the most important element of rollability. This attribute determines the magnitude of the load placed on the dies and the number of pieces the dies will produce before failure. It also determines the power required to roll the material. The total resistance to plastic deformation is influenced by a combination of several material properties. Among these are the yield point, the hardness of the material, and the internal shear resistance developed during plastic deformation and work hardenability.

The yield point may be defined as the stress, in newtons per sq. mm (or pounds per square inch), beyond which a material will undergo permanent or plastic deformation. The yield point is commonly obtained by means of a standard tensile test. The results from a compression test of a cylinder having a height to diameter ratio of one, gives a value for the compressive yield point, which is almost the same as that obtained from a tensile test. However, in the case of localised compression between surfaces where the contact area is relatively small compared to total surface area, the resistance to plastic deformation may reach several times the magnitude of the yield point stress. The resistance to compression may in fact reach values of several times the ultimate tensile strength.

A comparison of the tensile yield points of carbon steel (AISI-C1015) and 18-8 stainless steel (302) shows tensile yield points averaging approximately 310 MN/m^2 (45,000 psi). Yet it takes over twice the power to roll 18-8 as it does the low carbon

steel. Heat treated alloy steel of Rockwell C 40 hardness has a yield strength of approximately 930 MN/m^2 (150,000 psi) and it takes three times as much power to roll this heat-treated steel as it does low carbon steel.

In thread rolling, the fundamental process is one during which dies are progressively forced and rolled into an initially elastic blank. This penetration is resisted by the strength of the material being rolled. The resistance is primarily compressive, although final deformation and movement of the material takes place in the form of a sliding or shearing action within the internal structure of the material.

For some materials there is a reasonably good correlation between tensile yield strength and the resistance to plastic deformation in compression. With these materials, relative resistance to thread formation may be predicted on the basis of the tensile yield point stress. Other groups of materials, particularly the 300 group of stainless steels, which exhibit marked work-hardening properties, cannot be classified according to tensile yield point. In all cases the resistance to further plastic deformation increases as the thread formation progresses.

The internal shear resistance, developed during plastic deformation makes some materials much more difficult to deform than others. It does not appear to be correlated with tensile yield strength, since some materials with high yield strength are easier to move than some with much lower yield strength. The force required to overcome this internal resistance of the material to deform during rolling seems to be related to the amount of axial elongation that occurs during the process. For instance, low carbon steels and other soft materials elongate during rolling, while heat treated alloy steels are much stiffer and sometimes spring back after rolling. This added stiffness of some of the free machining steels accounts for their greater resistance to rolling.

One very important material property which affects the rollability of a material is its work hardening characteristics. As mentioned earlier rolled threads are stronger than cut threads because of this property. While most materials work-harden, some materials so so more than others, because, they offer increased resistance to plastic deformation as they deform. For example 302 stainless (18-8) is one of the more susceptible material types for strain hardening, while 416 stainless (12% Cr) is not.

At present it does not appear likely that a **single** physical property can be determined and used as the final criterion of rollability. There is a vast difference in the manner in which different groups of material behave during the formation of threads.

1.5.2 Behaviour During Displacement

Some materials roll with a fold in the crest of the thread. The fold is of a varying nature and is not always visible to the eye, but can be revealed by etching and magnification. The resulting "seam" normally has little, if any, effect on the strength of the thread. Threads do not generally fail at the crest, either in static loading or fatigue. Loaded threads are most highly stressed at the root, and this is the area that benefits most from thread rolling by the introduction of residual compressive stresses. The strength benefit of rolled threads under both fatigue and static loading has ensured that they are the preferred type for use in the aircraft industry.

Different materials deform differently during rolling. Figure 1.13(a) shows how some materials are affected when the thread rolling die first impinges upon the workpiece. It can be seen that the area affected is large and relatively deep. The areas worked by each die crest overlap causing the section midway between the roots of the thread to move upward faster than the material at the flanks of the threads. Figure 1.13(b) illustrates different stages in the rolling of a thread and explains why material behaving in this manner rolls without a crest fold or seam.

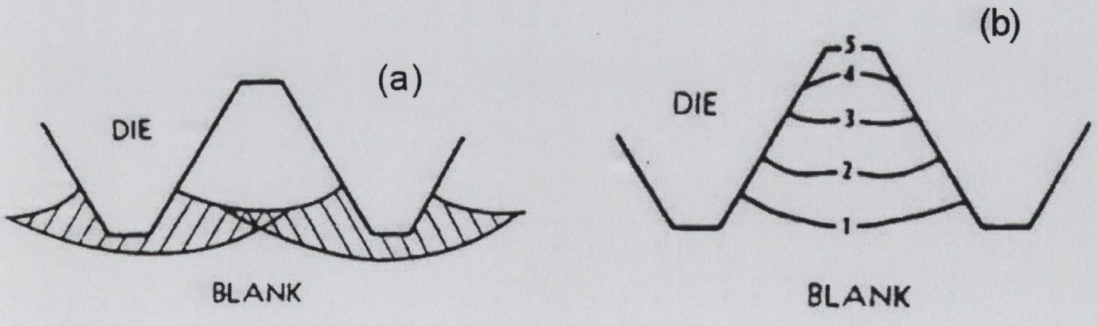

Figure 1.13: Initial Work Pattern (a) & the Stages of Thread Formation (b)

Figure 1.14(a) shows how some other materials are affected when the dies first

penetrate the workpiece. The areas affected are small and confined to the surface layers. The section of the blank between the thread roots has not been affected as previously happened. Figure 1.14(b) illustrates the same stages of thread fill and as before and shows the development of crest fold/seam in the final filled thread. It is possible to roll the material and "pack" the die enough so that the fold in the crest is so tightly squeezed that it is not visible to the eye. However, no amount squeezing will eliminate a fold once it has formed.

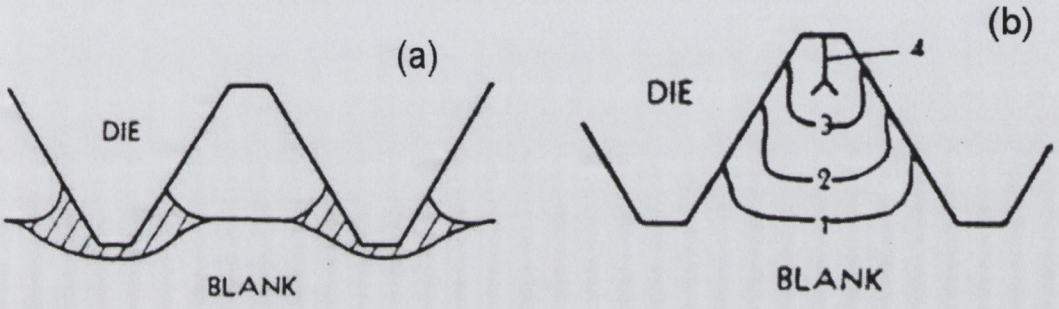

Figure 1.14: Initial Work Pattern II (a) & Stages of Thread Formation (b)

Several factors influence the behaviour of materials in respect of their likelihood to form crest folds. Some of these are physical material properties, and others are factors of the thread rolling process. If the material has a high Young's Modulus or shear strength, it will be more difficult to move the surface layers over the deeper layers. The deeper layers will move too, and as a consequence the area affected by the die penetration will be deeper and more extensive.

As small surface areas are plastically deformed they work-harden and have a higher yield point. By the time the material contacts with the thread rolling die again, the strength of the surface layer may be high enough so that the unworked layer beneath it reaches its yield point before the surface layer does. Thus the area affected extends rapidly with each die contact during each rotation of the fastener.

The width of the crest flat of the die in relation to the thread pitch will obviously influence the area of material affected by each contact as shown in Figures 1.15. In Figure 1.15(a), the narrow crest flat affects a much smaller area of the fastener compared

to the wide crest flat of Figure 1.15(b).

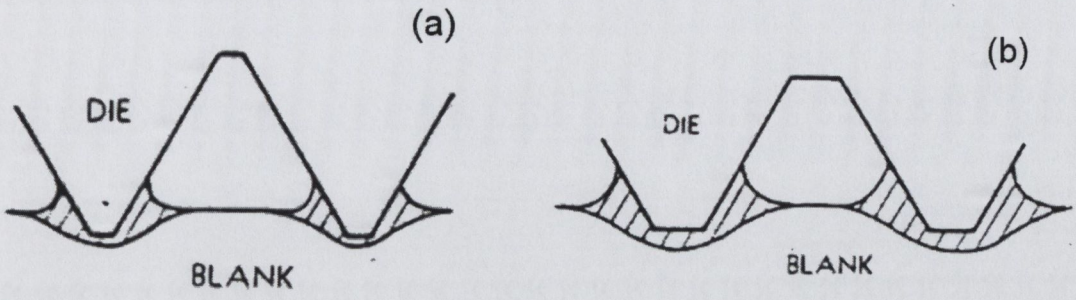

Figure 1.15: Narrow (a) & Wide Crest Flat (b)

Experience has shown that the rate of die penetration per contact affects the extent of the fold. Rates of penetration are considerably higher in flat die rolling compared to cylindrical die rolling, and the extent of the fold produced is somewhat less in flat die rolling. While high penetration rates may be effective in reducing the extent of the fold, the fact remains that as of yet, there is no effective method of rolling some materials without producing a fold in the crest. In addition high penetration rates imply high strain rates and this can lead to difficulties with strain rate sensitive materials, such as titanium.

1.5.3 Surface Finish

Material ductility has an important effect on the thread rolling process. Ductility appears to be closely related to the degree of surface finish obtained, and the most ductile materials roll with the smoothest surfaces. However, this is true for most rolled materials. It is very difficult to machine smooth threads in extremely ductile materials, and so these materials lend themselves to thread rolling. 18-8 stainless, high speed, and high carbon steels are examples of materials that roll to produce a very smooth surface finish. Free machine steels and nonferrous materials are widely used for rolling American Standard and similar threads. Sulphur and manganese are added to steels, and lead to nonferrous materials, for the purpose of making chips more brittle and thereby break as they are removed during machining. However these elements in thread rolled materials are also apt to cause flaking when rolling certain thread forms.

Over-rolling may also result in flakes on the flanks of threads on some materials and should be avoided by correcting workpiece diameters.

Table 1.1 below indicates the rollability indexes for 17 steels and for 6 non-ferrous alloys. The table also indicates the seaming tendency and flaking tendency of these alloys.

Metal	Hardness HB	Rollability Index(a)	Flaking Tendency(b)	Seaming Tendency(c)
Carbon and low alloy steels				
1010	137	1.11	B	C
1018	148	1.08	B	C
1020	156	0.96	B	C
1095	260	0.47	B	B
1095	320	0.42	B	B
1112	198	1.00	C	C
1117	173	1.03	C	C
1144	225	0.78	B	C
4140	205	0.93	B	C
4140	234	0.57	B	C
4140	300	0.42	B	B
4340	235	0.45	B	B
8620	215	0.60	B	C
Stainless steels				
303	174	0.46	C	B
316	150	0.45	B	B
416	221	0.58	C	B
430	225	0.56	C	B
Nonferrous alloys				
Aluminum (2017, 2024)	135	1.40	B	C
Brass				
Cartridge	190	1.55	B	B
Naval	155	1.00	C	B
Phosphor Bronze	130	1.28	C	B
Monel	235	0.93	B	B

Table 1.1: Rollability of Alloys [2]

(a) Index applies to metals rolled at room temperature. The power required to form a thread shape at a given rate in various metals is inversely proportional to the rollability indexes of the metals. (b) B, minor susceptibility; C, strong susceptibility. (c) B, negligible susceptibility; C, moderate susceptibility.

1.5.4 Materials

For the most part, straight carbon steels, structural alloy steels, high speed steels, non-leaded brasses, and copper constitute the majority of the materials used in producing parts for rolled threads and forms. Rolling these materials results in a wide variation in both rolling characteristics and surface finishes.

Carbon Steels

Straight carbon steels, with standard allowable quantities of phosphorous and sulphur, are perhaps ideal materials for rolling. Excellent finishes can be obtained with minimum rolling pressures. Free cutting steels having sulphur in the amounts of 0.08% to 0.33% require about the same amount of rolling power as straight carbon steels for rolling but the finish is not quite the same. The finish is good on standard 60 degree threads but not as good on threads with wide root or crest flats, and steep sidewalls, such as on 29 degree Acme threads.

Stainless Steels

Stainless steels of the 400 series may be heat treated and for the most part do not work harden as much as the 300 series of stainless steels. The rolling of these materials results in an excellent finish. However, considerable pressure is required and a slight to moderate seam may arise.

The 300 series stainless steels work harden rapidly and hence are harder to thread roll then the 400 series. The finishes obtained are excellent but the rolling loads are higher and die life expectancy is lowered to less than that of the 400 series. No fold is produced at the crest.

Nonferrous Metals

Among the nonferrous metals available for thread rolling, copper and many copper based alloys possess excellent cold working properties and are good materials for rolling.

Commercially pure aluminium such as the 2S and 3S series is soft and ductile and can be thread rolled easily. Due to its low strength and poor machining properties

aluminium is often alloyed with other elements to give it greater strength. The 17S and 24S series are the common alloys used for high strength headed parts and are easily thread rolled. Alloying of aluminium and the various hardening processes tend to decrease ductility which in turn affects the rollability.

Titanium

Demands by the aerospace industry for titanium fasteners in super-critical quality areas have presented some new problems, not only in fabricating but also in thread rolling this material. The most common of the alloys used for threaded fasteners are the 4% aluminium, 4% manganese, and the 6% aluminium, 4% vanadium (Ti-6Al-4V) alloys. These alloys have a hardness of between 33 and 38 Rockwell C and work harden very rapidly.

Due to the high work hardening properties of titanium, high penetration rates are required. The best quality fasteners are produced with the minimum number of revolutions and minimum dwell after rolling to full depth. Titanium blanks should have an excellent finish with no blemishes, scratches, or imperfections. Such defects will show up in the rolled threads as laps or folds.

The dies for rolling titanium should have a radius crest thread form and have a high surface finish, the accuracy of all die elements is essential. The thread rolling equipment must provide for accurate machining of the dies and must be able to maintain thread rolling die matching during rolling.

Other Materials

It is possible to roll other materials than those mentioned above, such as Magnesium, Molybdenum, Zirconium etc.

Chapter 2

Thread Rolling Defects

In the thread rolling of materials two main types of defects may occur. These are namely laps and shear bands. In this chapter these two types of defects will be explained in greater detail.

2.1 Introduction

Thread rolling deforms the fastener plastically as it is forced to flow along the contour imposed by the dies. The worked metal in the formed threads is harder and stronger than the workpiece prior to rolling. Thus, fasteners with rolled threads are harder and stronger than those of cut threads, as indicated in Table 2.1.
Data based on 15 pieces of each size and each threading method, made of 4027 steel.

Screw size and pitch	Type of Thread	Tensile Strength(MPa)	Fatigue Life
22.2mm (7/8in.), 9 t.p.i	Rolled	631.2	$71.8x10^3$
	Cut	489.2	$14.3x10^3$
25.4mm (1in.), 8 t.p.i	Rolled	678.1	$51.8x10^3$
	Cut	630.5	$21.3x10^3$
28.6mm (1 1/8in.), 7 t.p.i	Rolled	710.9	$68.5x10^3$
	Cut	629.9	$49.3x10^3$

Table 2.1: Average Mechanical Properties of Hexagonal head capscrews with rolled and cut threads [2]

This attribute of rolled threads does not imply that the fasteners are produced without defects. In fact since the earliest days of thread rolling, surface discontinuities and laps have been accepted in all but the most critical applications as a normal side

effect of the rolling process. Because it was regarded as impossible to eliminate laps when rolling at high production rates industry specifications [3] were written so that some of these defects were acceptable depending on their location (Figures 2.1 and 2.2).

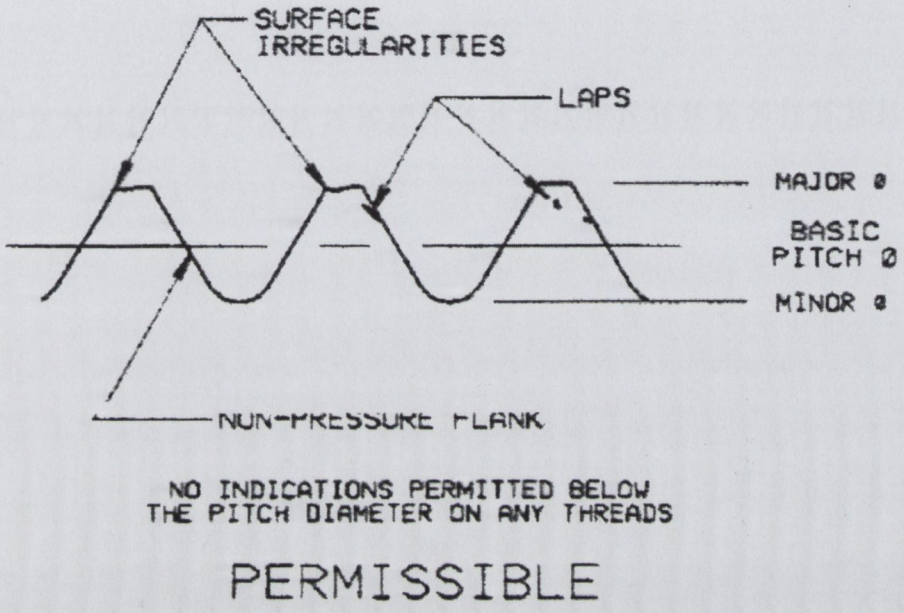

Figure 2.1: Permissible Surface Discontinuities in external threads based on SAE regulations

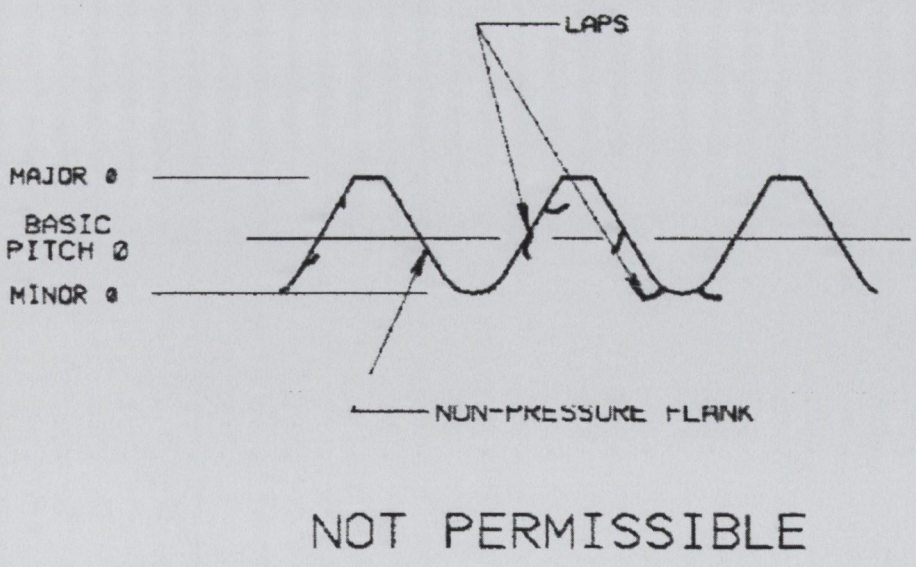

Figure 2.2: Non-Permissible Surface Discontinuities in external threads

2.2 Laps

Conventional flat thread rolling dies do not control blank metal flow, they simply direct it. Varying degrees of material flow are obtained along the length of the die as a result of the ramp section (see section 1.2). Metal flow is initiated on the surface of the fastener blank where there is contact between it and the die. This flow is largely uncontrolled and follows the path of least resistance (where there is no contact) into the voids between the die and workpiece to thus form the threads. Diverted flow occurs along the thread flanks toward the die roots. The material flowing along each flank may ultimately meet, and can in certain circumstances produce a defect referred to as a *lap*, see Figures 2.3 and 2.4.

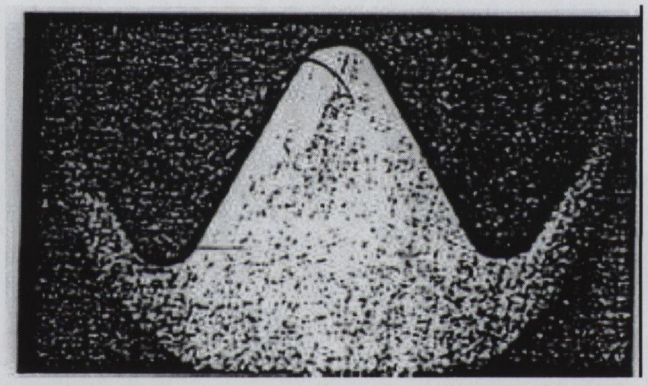

Figure 2.3: Conventional thread showing lap at crest

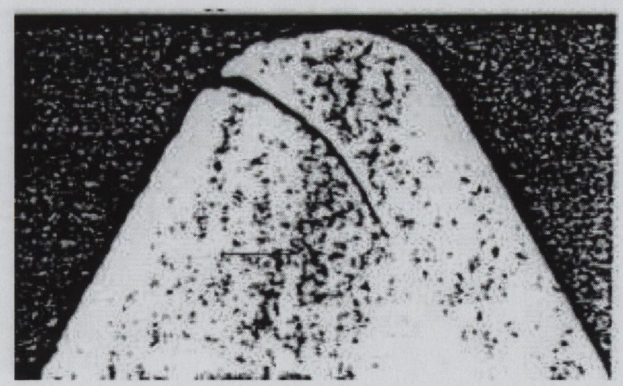

Figure 2.4: Enlarged detail of crest and surface discontinuity

Laps are possible in many locations: at the root, on the pressure and non-pressure side of the thread, above and below the pitch line and at the crest. Laps can be found and sorted using non-destructive methods, such as dye penetrant or magnetic particle

inspection. In order to determine the depth, orientation and location of the laps, metallographic sections have to be prepared. Laps are visible in both the as-polished and the etched condition. Care must be taken not to over-etch or produce to much edge rounding during sample preparation because this can make laps difficult to detect.

2.3 Shear Bands

2.3.1 Introduction

Shear Bands, or regions of localised plastic flow crossing many grains, are not uncommon during the deformation of metals. They may occur under nominally isothermal conditions (tooling and workpiece at the same initial temperature) as well as non-isothermal conditions (tooling and workpiece at different temperatures). Under isothermal conditions, the localisation of plastic flow is a function of the geometry involved in the metalworking operation, the deformation rate, and material properties such as the work hardening or flow softening rate of the material and its strain rate sensitivity.

The occurrence of flow localisation is well known in the deformation processing of ductile metals. Under tensile forms of loading, flow localisation occurs through necking, as for example occurs during a tensile test on round specimens. Flow localisation is important because the occurrence of necking often limits the amount of uniform deformation that can be imposed and hence determines the overall formability of a metal.

In contrast, the formability of metals under compressive loading conditions, or workability as it is more commonly known, is not controlled by necking. In bulk forming operations, defects such as free surface fractures, and central bursts often limit workability. However, another kind of defect, known as a *Shear Band* can also appear. This defect arises from a flow localisation process. The primary attribute in the formation of shear bands is assumed to be a localisation of plastic flow crossing many grains. Shear bands are macroscopic internal features and should not be confused with deformation bands or slip bands which are considered microscopic regions of localised flow. An example of shear bands occurring from the isothermal sidepressing of Ti-6242 Si cylinders are shown below in Figure 2.5.

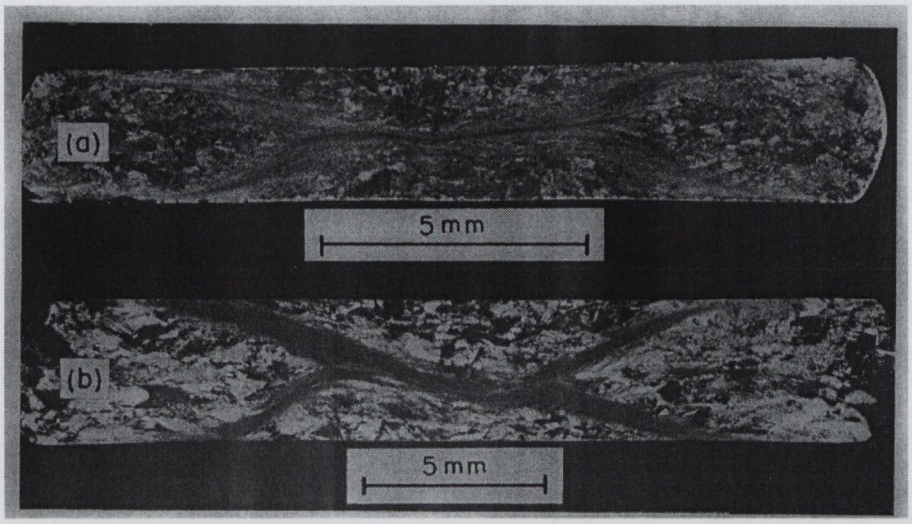

Figure 2.5: Shear Bands in an isothermally sidepressed Ti-6242Si cylinder [4]

The occurrence of Shear Bands has been documented in a variety of bulk forming operations such as rolling, sidepressing of cylinders, cold heading, machining etc [5] and in a number of different materials, aluminium alloys [6], low and medium carbon steels [7], and in titanium [8]. Shear bands have also been noted in hot metalworking operations [4, 9]. In [10] shear bands were shown to initiate along directions coinciding with the slip lines or lines of velocity discontinuity within the deforming material.

In all the metal forming operations researched, the occurrence of shear bands can be attributed to a loss or exhaustion of the strain hardening capacity of the metal being deformed. When shear bands occur as a result of deformation heating, they are often referred to as adiabatic shear bands. A number of simple criteria have been developed to predict the strain at which the flow stress passes through a maximum under these conditions and thus flow localisation occurs [5]. It has been shown in reference [4] that a flow stress maximum is a necessary, but not sufficient condition for shear band occurrence under isothermal deformation conditions. It has also been shown that the workpiece must also undergo a certain degree of flow softening, or a decrease of flow stress with increasing deformation.

2.3.2 Shear Band Occurrence

By far the largest number of observations of shear bands in worked metals has been in processes performed under isothermal conditions. At low strain rates, any deformation heat that develops is dissipated into the tooling and the temperature changes in the workpiece are negligible. At high strain rates, deformation, or adiabatic, heating raises the workpiece temperature but limited heat transfer within the workpiece, or between the tooling and the workpiece can occur because of short deformation times.

The effect of material properties on the tendency to form flow localisations during isothermal forging has been discussed in [11]. In [12], a criterion was developed to predict unstable bulging in uniaxial compression was extended to predict shear band formation. A test to evaluate flow localisation during forging was developed in [13]. Unstable flow in forging is assumed to require a maximum in flow stress σ at some point (or points) in the flow field:

$$d\sigma = 0 = \left(\left. \frac{\partial \sigma}{\partial \epsilon} \right|_{\dot{\epsilon},T} \right) d\epsilon + \left(\left. \frac{\partial \sigma}{\partial \dot{\epsilon}} \right|_{\epsilon,T} \right) d\dot{\epsilon} + \left(\left. \frac{\partial \sigma}{\partial T} \right|_{\epsilon,\dot{\epsilon}} \right) dT \tag{2.1}$$

In this expression, ϵ, $\dot{\epsilon}$, and T denote strain, strain rate, and temperature respectively. Equation 2.1 can be manipulated to yield an expression for the expected rate of flow localisation, $1/\dot{\epsilon}(d\dot{\epsilon}/d\epsilon)$, once instability sets in:

$$\frac{1}{\dot{\epsilon}} \frac{d\dot{\epsilon}}{d\epsilon} = -\frac{\gamma'}{m} = \alpha \tag{2.2}$$

in which,

$$\gamma' = \frac{1}{\sigma} \left. \frac{d\sigma}{d\epsilon} \right|_{\dot{\epsilon}} \tag{2.3}$$

and

$$m = \left. \frac{\partial \ln \sigma}{\partial \ln \dot{\epsilon}} \right|_{\epsilon,T} \tag{2.4}$$

It is seen that the flow localisation tendency (in terms of the fractional change of strain rate with strain) is dependent on the nondimensional work hardening (or softening) rate of the material and its strain rate sensitivity parameter. The former is determined from flow curves measured in constant strain rate compression or tension tests, and the latter from step-strain-rate-change tests run over various strain rate changes. From

equation 2.2, it is obvious that large flow softening rates (i.e., negative work hardening rates), which are often found in hot working, and small strain rate sensitivities favour the localisation of strain.

In [12] it was suggested that materials with α parameters of five or greater were particularly susceptible to *persistent* flow localisations. This hypothesis was supported by observations in [4].

2.3.3 Shear Bands in Thread Rolling

During thread rolling there are two types of shear band which may arise. These are thread root shear bands, characterised by a V-shape and delineating a dead metal zone and the "whisker type" curvilinear shear bands occurring as single or multiple shear bands extending from the thread root area towards the centre of the formed thread. These two types of shear band can be seen in Figures 2.6 and 2.7 respectively.

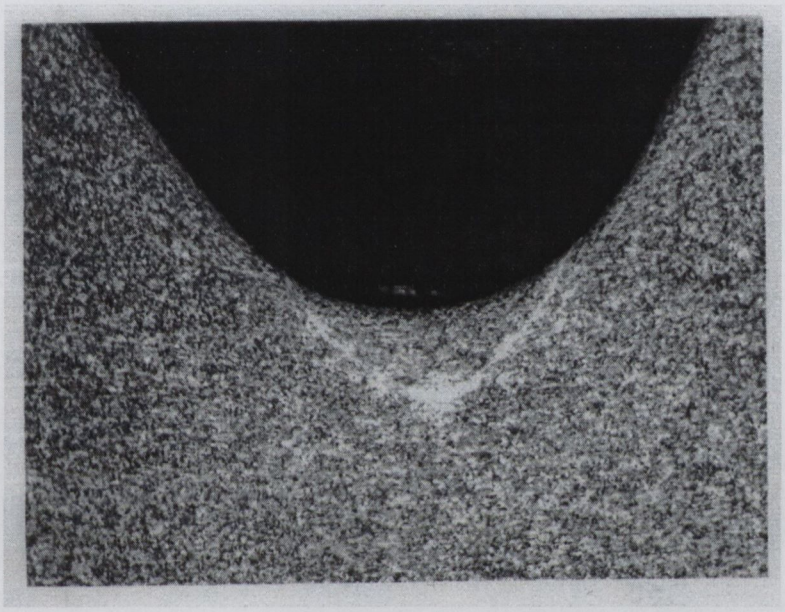

Figure 2.6: V shaped thread root shear band

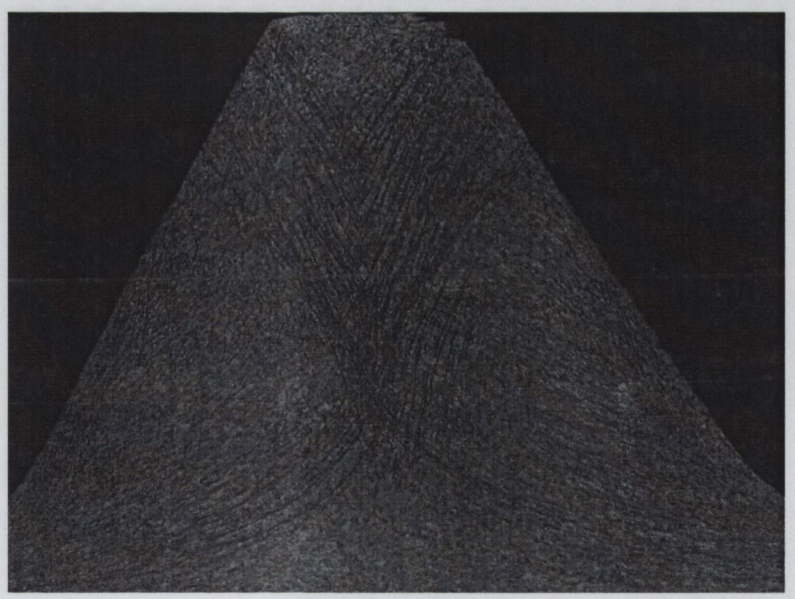

Figure 2.7: Whisker type shear band in formed thread

In characterising these two types of shear bands it has been found that their patterns correspond to the planes of maximum shear stress as illustrated by slip line fields. A review of the maximum shear stress lines for different loading conditions [14] indicated that the penetration of a tool into a slab with a $h/L \approx 4$ (thickness of workpiece/contact width of tool ratio), Figure 2.8, produces a field similar to that observed in the thread root.

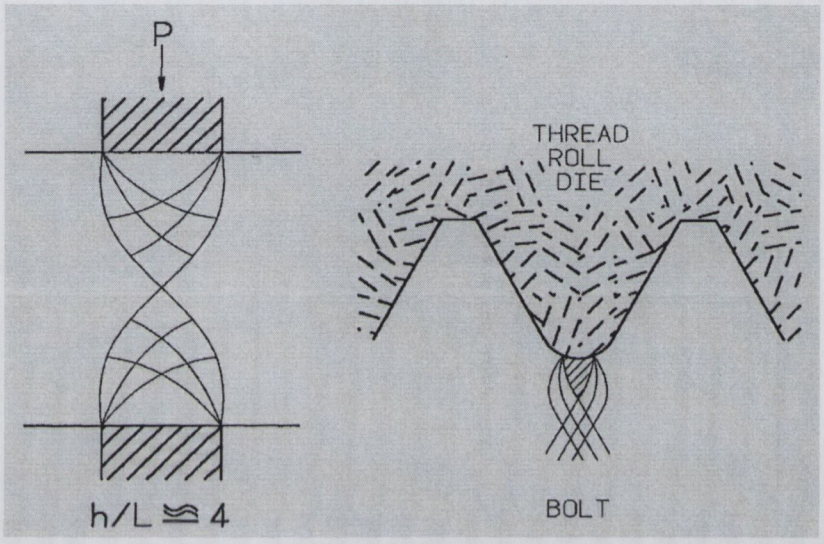

Figure 2.8: Maximum Shear surfaces resulting from the penetration of a tool and the observed deformation lines in a thread root

The "whisker type" shear bands observed in the formed thread follow patterns, Figure 2.9, that are quite similar to the shear stress state proposed for an extrusion process.

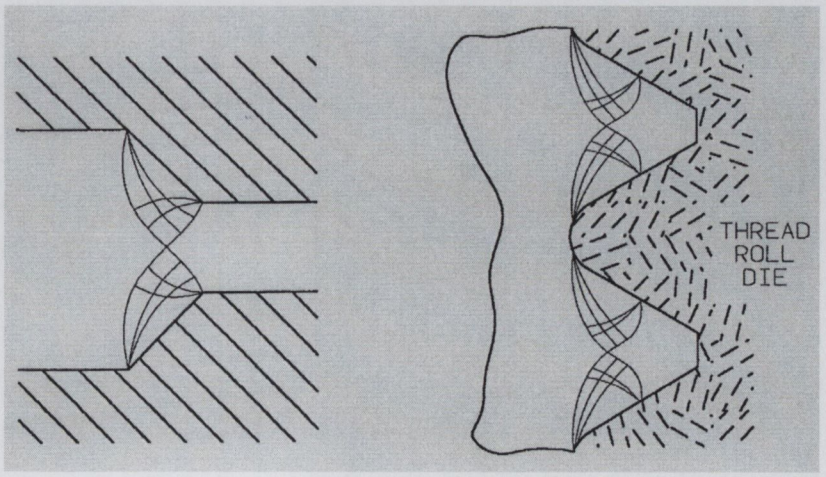

Figure 2.9: Maximum Shear surfaces for an extrusion process and the observed deformation lines in the rolled threads

These whisker type shear band defects in rolled Titanium 6Al-4V can be seen again in Figure 2.10 below.

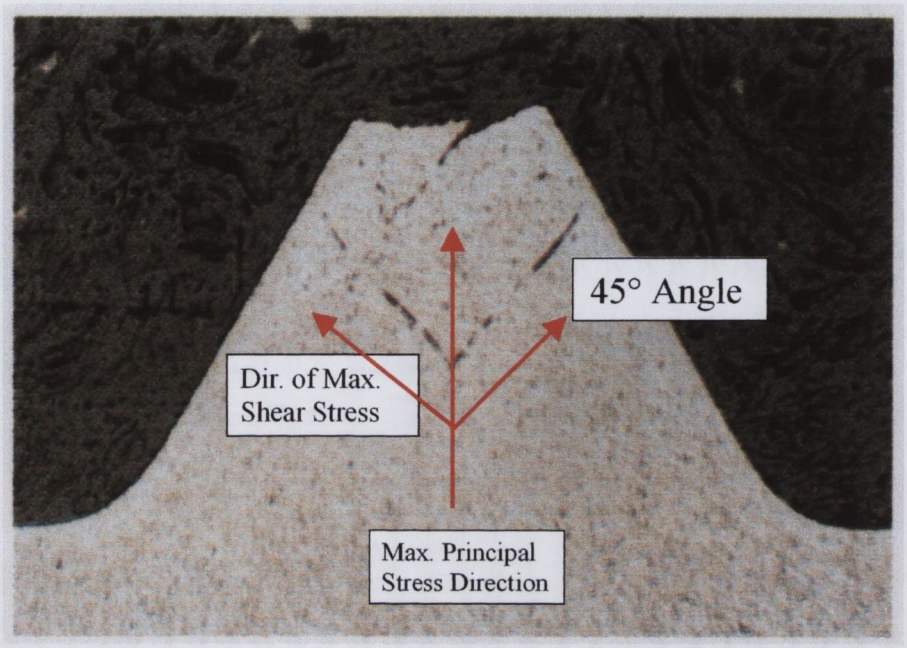

Figure 2.10: Preferentially etched Whisker type Shear Band Defects

These defects match up with the lines of maximum shear stress which act at 45° to the direction of maximum principal stress. These lines are also indicated on the figure. Titanium 6Al-4V having an hexagonally packed metallic structure is very susceptible to the formation of both of these types of shear bands and the defects associated with them. This is because there are fewer slip systems in the material thus making it more susceptible to void formation.

The incidence of shear bands is also believed to be affected by the material properties of the deforming material. Figure 2.11 shows the yield and ultimate tensile strength of solution treated and 1000°F aged Titanium-6Al-4V alloy as a function of tensile test temperature. The yield strength of the material is shown to decrease as temperature increases. Titanium alloys exhibit a low coefficient of thermal conductivity relative to other fastener materials; Titanium-6Al-4V = 6.8 W/mK, MP35N = 11.2 W/mK, and hardened and tempered AISI 4140 = 42.7 W/mK. Consequently when the Titanium-6Al-4V alloy is thread rolled at room temperature the adiabatic heat generated along the shear band is not readily dissipated. This can result in a localised reduction of yield

strength caused by the increased temperature and this can lead to further preferential yielding of the material along the shear band. Increasing the overall temperature of the workpiece reduces the temperature differential between the newly formed shear band and surrounding material, thus promoting uniform deformation of the material in the threads. However, hot forming of threads reduces the overall fatigue strength of the fastener and is not recommended.

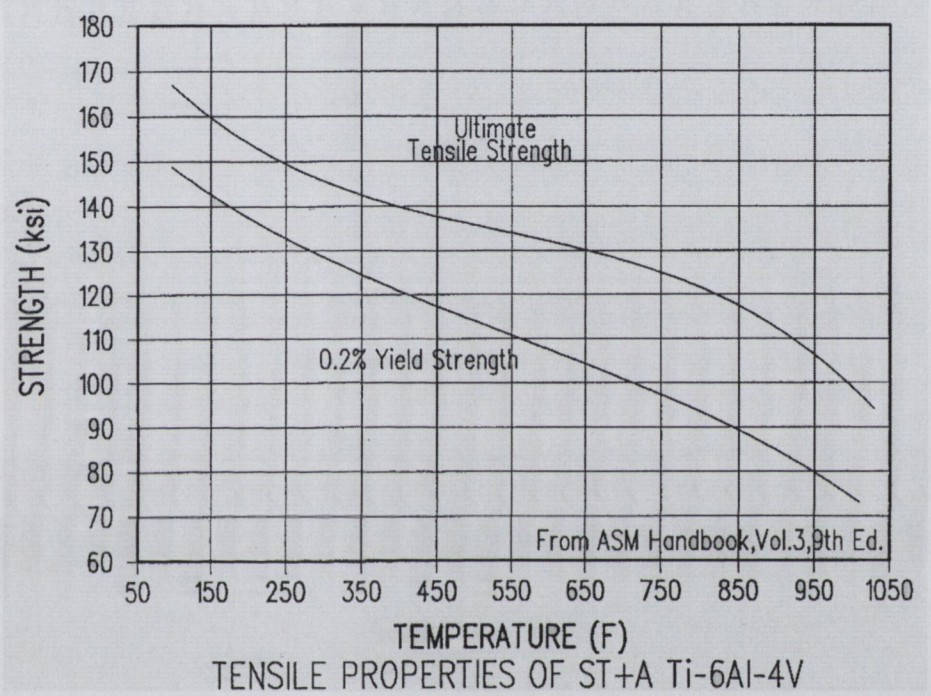

Figure 2.11: Tensile properties of Solution treated and aged Titanium-6Al-4V

2.3.4 Shear Band Visualisation

The metallographic technique used to reveal these shear bands can itself have a pronounced effect on the observed severity of the shear band. The metallographic etchant tends to selectively attack the most severely strained material along the shear band. This localised chemical dissolution can result in chemically induced microvoids and cracks that can be misidentified as thread rolling induced discontinuities. An example of this phenomenon is shown in Figures 2.12 to 2.15 for a single thread root exposed to 2 percent HF etchant for total times of 15, 25, 45, and 90 seconds respectively.

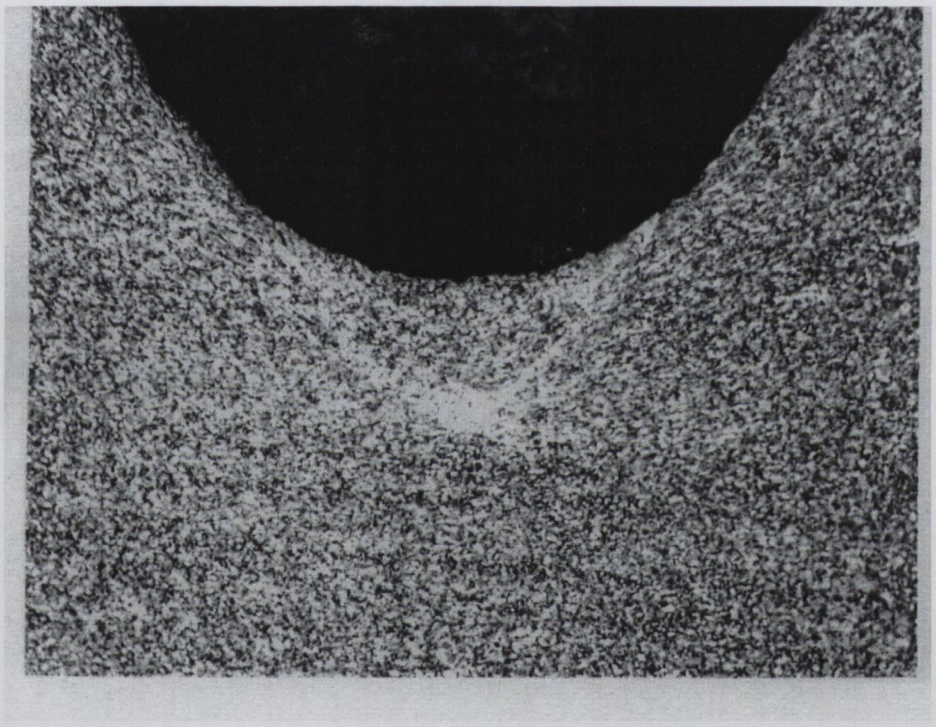

Figure 2.12: Thread root Shear Band after 15 seconds exposure to 2% HF etchant [15]

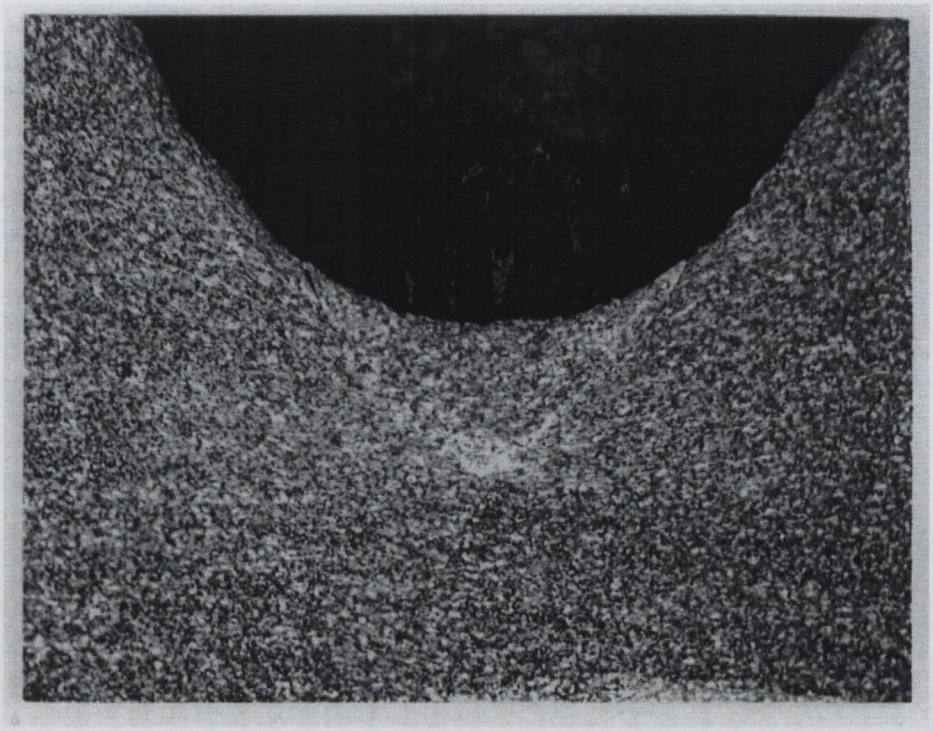

Figure 2.13: Thread root Shear Band after 25 seconds exposure to 2% HF etchant [15]

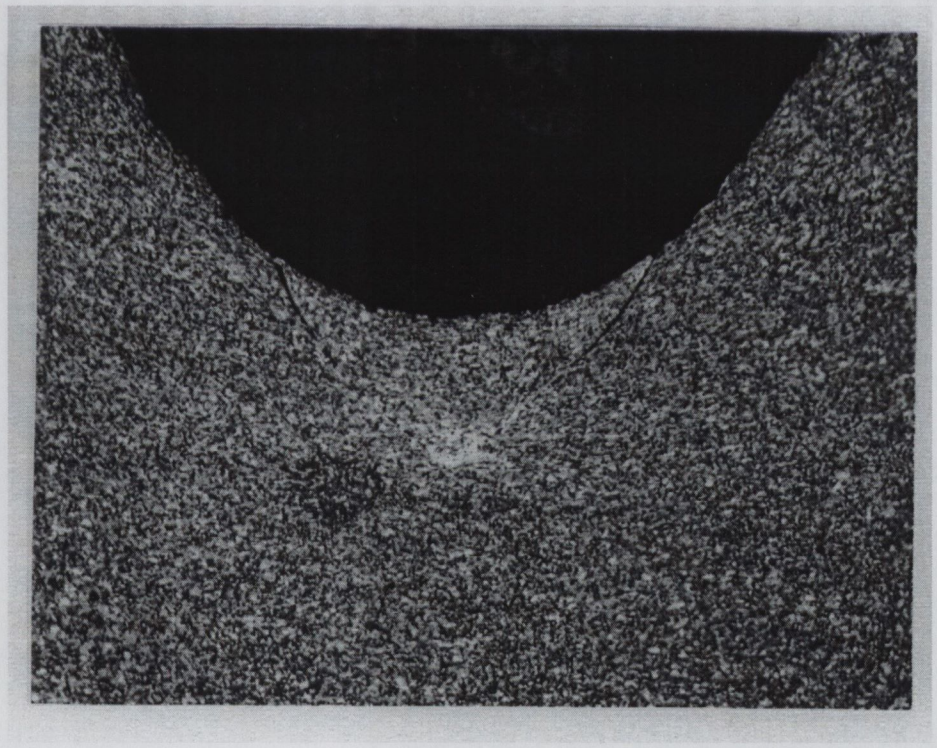

Figure 2.14: Thread root Shear Band after 45 seconds exposure to 2% HF etchant [15]

Figure 2.15: Thread root Shear Band after 90 seconds exposure to 2% HF etchant [15]

A 15 second etching time, Figure 2.12, revealed the thread root shear band as a light shaded V-shaped feature. Increasing the total exposure to 25 seconds, Figure 2.13, resulted in a discernible crack-like feature at the intersection of the thread root and shear band. Additional exposure to the etchant for 45 and 90 seconds, Figure 2.14 and Figure 2.15 respectively, resulted in further material dissolution along the shear band and growth of the crack like feature. The chemical dissolution of the shear band is not just confined to the 2 percent HF acid etchant.

Chapter 3

Metal Forming and the Finite Element Method

In order to be capable of designing a new thread rolling die that will eliminate or significantly reduce the occurrence of internal defects within a fastener, (explained in Chapter 2), the factors that influence the material flow and hence strains in the thread rolling process needed to be examined and quantified. These factors include tool geometry, material properties, forming temperatures, lubrication, etc. Finite element analysis (FEA) was chosen as the most appropriate method to simulate the thread rolling process and the finite element "package" used in this work to simulate the process was DEFORM [16, 17].

This chapter introduces the pertinent plasticity theory and the finite element method used to model metal forming processes. In the analysis of metal forming, plastic strains usually outweigh elastic strains and the idealisation of rigid plastic material behaviour is acceptable. The resulting analysis based on this assumption is known as the *flow formulation* [18, 19]. In other applications, phenomena associated with elasticity cannot be neglected. In the so called *solid formulation* [20], the material is considered to behave as an elasto-plastic solid.

The solid formulations of the finite element method for metal forming problems have been based on the use of the Prandtl Reuss equations for elasto-plastic materials. The formulation is given in a rate form and assumes the infinitesimal theory of deformation applies. In analysing metal forming processes, however, the elasto-plastic finite element method with infinitesimal formulation has severe drawbacks. The large

amount of rotation involved in metal forming rules out infinitesimal analysis, and large deformation analyses also have some difficulties in reproducing observed phenomena, such as foldover during compression of cylinders [21]. Furthermore, the nature of elasto-plastic constitutive equations requires short time steps in nonsteady state analysis, a requirement that is severe when the body goes from elastic to plastic deformations.

A simplified solution to this problem is to neglect the elastic portion of deformation and treat all plastic deformation as a flow problem. In general, this makes infinitesimal analysis feasible and large steps possible. Extensive references on the use of the finite element method in metal forming applications can be found in [22, 23, 24, 25, 26, 27, 28, 29, 30, 31, 32, 33].

The first section of this chapter contains a general overview of the theory of plasticity. Subsequently the finite element method for metal forming will be described along with the specialist techniques, which must be used in order to solve a finite element analysis of a metal forming problem will be presented. Detailed derivation of some of the aspects of plasticity and finite element theory are outlined in Appendix B.

3.1 Plasticity

3.1.1 Introduction

The theory of plasticity describes the mechanics of deformation in plastically deforming solids, and as applied to metals and alloys, it is based on experimental studies of the relationship between stress and strain under simple loading conditions. The theory ignores the Bauschinger effect and is valid only at temperatures for which creep, and thermal phenomena can be neglected. The basic theory of plasticity was described by Hill [34], and also in reference [35]. It is important that some of these aspects are presented in order to properly explain the finite element solutions of metal forming problems.

First, the different measures of stress and strain are introduced. Then the basic laws governing plastic deformation and principles that are the foundations of the analysis are described.

3.1.2 Stress, Strain, and Strain Rate

The basic quantities used to describe the mechanics of deformation when a body deforms from one configuration to another under an external load are the *stress, strain, and strain-rate.* Various measures of these quantities are defined, depending upon how closely these definitions represent actual situations. These measures are introduced using the simple uniaxial tensile test as an example.

Consider the uniaxial tension test of a round specimen whose initial length is l_0 and cross-sectional area is A_0. The specimen is stretched in the axial direction by a force P to the length l and the cross-sectional area A at time t, as shown in Fig. 3.1. The response of the material is recorded as a load-displacement curve, and converted to a stress-strain curve. Deformation is homogeneous until necking begins.

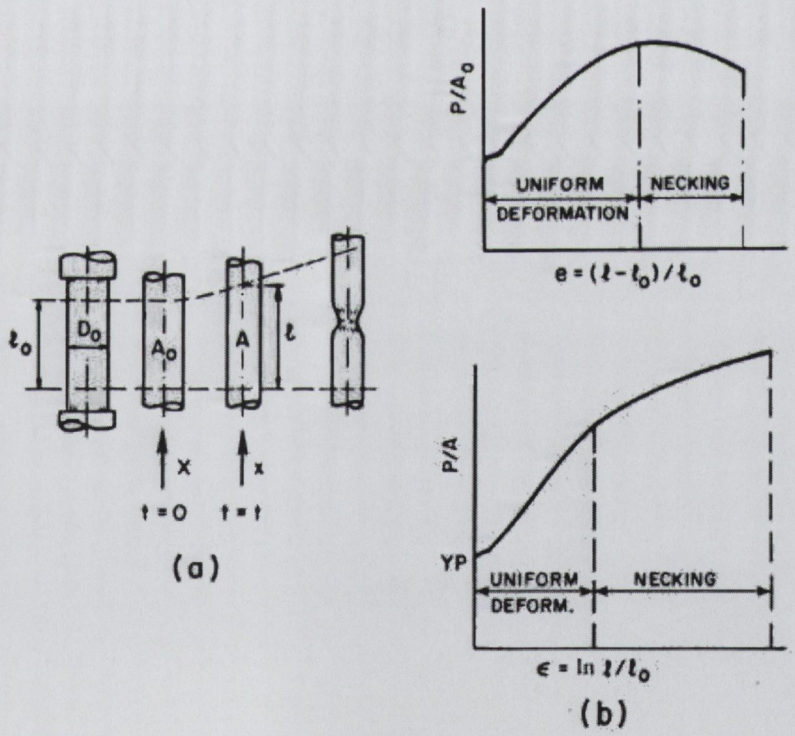

Figure 3.1: Uniaxial Tension (a) Tension Specimen (b) Stress-Strain Curves

In *infinitesimal deformation* theory, the stresses and strain-rates (or infinitesimal

strains) are expressed with respect to a fixed coordinate system in the material configuration at a time under consideration. In uniaxial tension, they are defined by

$$\begin{aligned} \text{stress} \quad \sigma &= \frac{P}{A} \\ \text{strain rate} \quad \dot{\epsilon} &= \frac{\dot{l}}{l} \\ \text{infinitesimal strain} \quad d\epsilon &= \frac{dl}{l} \end{aligned} \tag{3.1}$$

where the dot denotes the time derivative. The stress defined in eq. (3.1) is called the true stress or Cauchy stress. The total amount of deformation is measured by integrating the infinitesimal strain as

$$\epsilon = \int_{l_0}^{l} d\epsilon = \ln\left(\frac{l}{l_0}\right) \tag{3.2}$$

and is called the logarithmic or natural strain.

For the analysis of metal forming processes, flow formulation is based on infinitesimal deformation theory, while solid formulation is based on finite deformation.

The strain rate tensor $[\dot{\epsilon}_{ij}]$, where $i, j = x, y, z$ is symmetric and the tensor components are defined by

$$\begin{aligned} \dot{\epsilon}_x = \frac{\partial u_x}{\partial x},\ \dot{\epsilon}_y = \frac{\partial u_y}{\partial y},\ \dot{\epsilon}_z = \frac{\partial u_z}{\partial z}, \\ \dot{\epsilon}_{xy} &= \frac{1}{2}\left(\frac{\partial u_x}{\partial y} + \frac{\partial u_y}{\partial x}\right) = \frac{\dot{\gamma}_{xy}}{2} \\ \dot{\epsilon}_{yz} &= \frac{1}{2}\left(\frac{\partial u_y}{\partial z} + \frac{\partial u_z}{\partial y}\right) = \frac{\dot{\gamma}_{yz}}{2} \\ \dot{\epsilon}_{zx} &= \frac{1}{2}\left(\frac{\partial u_z}{\partial x} + \frac{\partial u_x}{\partial z}\right) = \frac{\dot{\gamma}_{zx}}{2} \end{aligned} \tag{3.3}$$

where u_i are the velocity components and $\dot{\gamma}_{ij}$ are engineering shear strain-rate components. Using suffix notation, eq. (3.3) can be written as

$$\dot{\epsilon}_{ij} = \frac{1}{2}(u_{i,j} + u_{j,i}) \tag{3.4}$$

where a comma denotes differentiation with respect to the coordinates that follow.

The Cauchy stress tensor $[\sigma_{ij}]$, where $i, j = x, y, z$ is also symmetric and is represented by the nine stress components as

$$[\sigma_{ij}] = \begin{bmatrix} \sigma_{11} & \sigma_{21} & \sigma_{31} \\ \sigma_{12} & \sigma_{22} & \sigma_{32} \\ \sigma_{13} & \sigma_{23} & \sigma_{33} \end{bmatrix} = \begin{bmatrix} \sigma_x & \tau_{yx} & \tau_{zx} \\ \tau_{xy} & \sigma_y & \tau_{zy} \\ \tau_{xz} & \tau_{yz} & \sigma_z \end{bmatrix} \tag{3.5}$$

The stress may also be specified by the three principal stress components, or by the three tensor invariants. The principal stresses $(\sigma_1, \sigma_2, \sigma_3)$ are the roots of the cubic equation

$$\sigma^3 - J_1\sigma^2 - J_2\sigma - J_3 = 0 \tag{3.6}$$

where J_1, J_2, J_3 are quantities independent of the direction of the axes chosen and called the three invariants of the stress tensor σ_{ij}.

$$\begin{aligned} J_1 &= \sigma_1 + \sigma_2 + \sigma_3 = \sigma_x + \sigma_y + \sigma_z \\ J_2 &= -(\sigma_1\sigma_2 + \sigma_2\sigma_3 + \sigma_3\sigma_1) = -(\sigma_x\sigma_y + \sigma_y\sigma_z + \sigma_z\sigma_x) + \tau_{xy}^2 + \tau_{yz}^2 + \tau_{zx}^2 \\ J_3 &= \sigma_1\sigma_2\sigma_3 = \sigma_x\sigma_y\sigma_z + 2\tau_{xy}\tau_{yz}\tau_{zx} - \sigma_x\tau_{xz}^2 - \sigma_y\tau_{zx}^2 - \sigma_z\tau_{xy}^2 \end{aligned} \tag{3.7}$$

The first (linear) and second (quadratic) invariants have particular importance for the theory of plasticity.

3.1.3 The Yield Criteria

A yield criterion is a law that determines the stress level at which plastic deformation begins and can be written in the general form

$$f(\sigma_{ij}) = C(\text{constant}) \tag{3.8}$$

The function of stresses $f(\sigma_{ij})$ is called a yield function and C is a material parameter to be determined experimentally. The suitability of any yield criterion must be verified experimentally. For isotropic materials, plastic yielding can depend only on the magnitude of the three principal stresses and not their directions. This implies that a yield criterion should be a function of the three stress invariants only

$$f(J_1, J_2, J_3) = C \tag{3.9}$$

Experimental observations indicate plastic deformation of metals is essentially independent of hydrostatic pressure. Consequently yielding depends only on the principal components $(\sigma_1', \sigma_2', \sigma_3')$ of the deviatoric stress tensor.

$$\sigma_{ij}{}' = \sigma_{ij} - \delta_{ij}\sigma_m \tag{3.10}$$

where $\sigma_m = \frac{1}{3}(\sigma_1 + \sigma_2 + \sigma_3)$ is the hydrostatic component of the stress and δ_{ij} (=1 for $i = j$ and =0 for $i \neq j$) is the Kronecker delta. The principal components of the deviatoric stress tensor are not independent, since $\sigma'_1 + \sigma'_2 + \sigma'_3$ is identically zero.

The yield criterion can be reduced to the form

$$f(J'_2, J'_3) = C \tag{3.11}$$

where J'_2 and J'_3 are the second and third invariants of the deviatoric stresses, and are equal to

$$\begin{aligned} J'_2 &= -(\sigma'_1\sigma'_2 + \sigma'_2\sigma'_3 + \sigma'_3\sigma'_1) \\ J'_3 &= \sigma'_1\sigma'_2\sigma'_3 \end{aligned}$$

3.1.4 Two Criteria

The two simplest criteria, which have been extensively used for the analysis of metal deformation, are the Tresca criterion and the Von Mises (or Hueber-Mises) criterion.

The Tresca yield criterion (1864)

This states that yielding begins when the maximum shear stress reaches a critical value. It states that yielding begins when

$$\sigma_1 - \sigma_3 = 2k \tag{3.12}$$

with $\sigma_1 \geq \sigma_2 \geq \sigma_3$.

The Von Mises yield criterion (1913)

Von Mises suggested that yielding occurs when J'_2 reaches a critical value, or in other words that the yield function eq. (3.11) does not involve J'_3. The second deviatoric stress invariant, J'_2, can be written explicitly as

$$J'_2 = \frac{1}{2}\sigma_{ij}{}'\sigma_{ij}{}' = \frac{1}{2}(\sigma_1'^2 + \sigma_2'^2 + \sigma_3'^2) = k^2 \tag{3.13}$$

or

$$(\sigma_1 - \sigma_2)^2 + (\sigma_2 - \sigma_3)^2 + (\sigma_3 - \sigma_1)^2 = 6k^2 \tag{3.14}$$

or

$$(\sigma_x - \sigma_y)^2 + (\sigma_y - \sigma_z)^2 + (\sigma_z - \sigma_x)^2 + 6(\tau_{xy}^2 + \tau_{yz}^2 + \tau_{xz}^2) = 6k^2 \qquad (3.15)$$

The constants in eqs. (3.12 to 3.15) may be determined from analyses of some simple stress states, such as uniaxial tension. At yield in simple tension, $\sigma_1 = Y$ and $\sigma_2 = \sigma_3 = 0$. Therefore, eqs. (3.12 to 3.15) may be written as

$$\sigma_1 - \sigma_3 = Y$$

and

$$(\sigma_1 - \sigma_2)^2 + (\sigma_2 - \sigma_3)^2 + (\sigma_3 - \sigma_1)^2 = 2Y^2 \qquad (3.16)$$

respectively. The parameter k in eqs. (3.13 to 3.15) can be identified as the shear yield stress by considering yielding in simple shear and $k = Y/\sqrt{3}$ according to the Tresca criterion.

where k is a parameter regulating the stress scale and dependent on a material property. In the suffix notation used in eq. (3.13), a recurring letter suffix indicates that the sum must be formed of all terms obtainable by assigning to the suffix the values x, y, z (or 1, 2, 3).

It should be noted that the yield criteria defined by eq. (3.16) must depend on the previous process of plastic deformation (*strain hardening*). If it is assumed that hardening occurs if, and only if, plastic work is done, then the assumption that yield criterion is independent of the hydrostatic component implies that there is no volume change during plastic deformation. For most metals Von Mises' law fits the experimental data more closely than Tresca's.

3.1.5 The Prandtl Reuss Equation and the Levy-Mises Equation

These equations form the basis for the finite element formulation described in Appendix B. With the yield function given by $f(\sigma_{ij})=J_2' = \frac{1}{2}\sigma_{ij}'\sigma_{ij}'$, (eq. 3.13), eq. (B.10) becomes, in the rate form,

$$\dot{\epsilon}_{ij}{}^{p} = \sigma_{ij}'\dot{\lambda} \tag{3.17}$$

since

$$\frac{\partial f}{\partial \sigma_{ij}} = \frac{\partial f}{\partial \sigma_{kl}'}\frac{\partial \sigma_{kl}'}{\partial \sigma_{ij}} = \sigma_{ij}'$$

noting that the repeated subscripts k and l indicate summation with respect to these quantities.

Equation (3.17) can be written as

$$\frac{\dot{\epsilon}_x{}^{p}}{\sigma_x'} = \frac{\dot{\epsilon}_y{}^{p}}{\sigma_y'} = \frac{\dot{\epsilon}_z{}^{p}}{\sigma_z'} = \frac{\dot{\gamma}_{xy}{}^{p}}{2\tau_{xy}} = \frac{\dot{\gamma}_{yz}{}^{p}}{2\tau_{yz}} = \frac{\dot{\gamma}_{zx}{}^{p}}{2\tau_{zx}} \tag{3.18}$$

Combining the elastic strain rate components $\dot{\epsilon}_{ij}{}^{e}$ and the plastic strain rate components $\dot{\epsilon}_{ij}{}^{p}$, according to $\dot{\epsilon}_{ij} = \dot{\epsilon}_{ij}{}^{e} + \dot{\epsilon}_{ij}{}^{p}$, we obtain the Prandtl-Reuss equations for elastic plastic solids, as

$$\dot{\epsilon}_{ij} = \sigma_{ij}'\dot{\lambda} + \frac{1}{2G}\dot{\sigma}_{ij}' + \delta_{ij}\frac{(1-2\nu)}{E}\dot{\sigma}_m \tag{3.19}$$

where G, E and ν are the shear modulus, Young's Modulus, and Poisson's ratio, respectively.

For rigid plastic materials, the assumption $\dot{\epsilon}_{ij} \cong \dot{\epsilon}_{ij}{}^{p}$, and the Levy Mises equations are obtained by removing the superscripts p in equation (3.18). They are expressed in terms of the stress components σ_{ij} by three equations of the type

$$\dot{\epsilon}_x = \{\sigma_x - \frac{1}{3}(\sigma_x + \sigma_y + \sigma_z)\}\dot{\lambda} = \{\sigma_x - \frac{1}{2}(\sigma_y + \sigma_z)\}\frac{2}{3}\dot{\lambda} \tag{3.20}$$

and three of the type

$$\dot{\epsilon}_{xy} = \frac{\dot{\gamma}_{xy}}{2} = \tau_{xy}\dot{\lambda} \tag{3.21}$$

From this point forward, the plastic strain rate and infinitesimal plastic strain are indicated without the subscript p, unless otherwise specified. These Levy-Mises equations

are required to determine the effective strain rate which in turn is used to determine the effective strain rate matrix used in the finite element method described in section B.2.4. Without this matrix a solution to the finite element stiffness equation could not be determined.

3.2 Finite Element Method

3.2.1 Introduction

Most modern metal forming simulation codes are based on the finite element method (FEM) which is essentially a mathematical procedure based on the "divide and conquer" principle. The finite element method is a mathematical procedure where individual objects (dies and workpiece) are divided into a series of smaller geometric entities referred to as elements. Each element is subdivided into points in space called nodes. The number of nodes needed to describe an element is determined by the choice of element which is used. The nodes and elements are assigned material properties and boundary conditions which are used to describe friction and the other characteristics of the forming process. All this information comprises a mathematical description of the forming process. After the information has been converted into a series of mathematical equations and solved by a computer, the solution is represented graphically to depict the behaviour of the forming process. Because material properties such as work hardening change non-linearly, a series of time steps is used to approximate the process behaviour at given points in time.

All finite element simulations consist of a three step sequence which consists of pre-processing, simulation, and post processing:

- Pre-processing allows interactive data input by the user to assign material properties, workpiece, and die geometry, forming machine characteristics, friction, and simulation controls.

- One aspect that can not be overemphasised is that the accuracy of the simulation model is significantly affected by the accuracy of the input data, especially the material properties.

- The post-processor is used to display the simulation results in various graphic forms. Some of the useful features include contour plots of stress, strain, and velocity vectors which allow the direction of metal flow to be ascertained.

The first time that the concept of a finite element procedure was suggested for use was back in 1943. At that time Courant [36] approximated a warping function linearly in each element of an assemblage of triangular elements used to model the St. Venant torsion problem and proceeded to solve the problem using the principle of minimum potential energy. The term "finite element" was first introduced by Clough [37] in the study of plane elasticity problems. Extensive references on the use of the finite element method in metal forming simulations can be found in the following references [22, 23, 24, 25, 26, 27, 28, 29, 30, 31, 32, 33].

The finite element models used to model the thread rolling process investigated in this thesis were rigid plastic plane strain models. This means that the elastic portion of the stress strain curve was ignored. These particular facets of the finite element method are described in full in Appendix B. Two areas of the finite element method, which are of particular importance to the models in this thesis are friction and contact and rezoning. These are described in the following two sections.

3.2.2 Friction & Contact

Friction conditions at the die-material interface greatly influence metal flow during thread rolling, formation of surface and internal defects, stresses acting on the dies, and load and energy requirements. Numerous studies of the modelling of friction in metal forming processes have been prepared [38, 39, 40, 41, 42, 43]. There are three basic types of lubrication condition that govern the frictional conditions in metal forming [44], [45].

1. Under dry conditions, no lubricant is present at the interface and only the oxide layers present on the die and workpiece materials act as a "separating" layer. In this case friction is high, and such a situation is desirable in only a few selected forming operations, such as hot rolling of plates and slabs and nonlubricated extrusion of aluminium alloys.

2. "Hydrodynamic" conditions exist when a thick layer of lubricant is present between the dies and the workpiece. In this case the friction conditions are governed by the viscosity of the lubricant and by the relative velocity between the die and the workpiece. The viscosities of most lubricants decrease rapidly with increasing temperature. Consequently, in most practical high-speed forming operations, such as strip rolling and wire drawing, the hydrodynamic conditions exist only within a certain regime of velocities, where the interface temperatures are relatively low [45].

3. "Boundary" lubrication is the most widely encountered situation in metal forming. Increases in temperature at the interface and the relatively high forming pressures do not usually allow the presence of a hydrodynamic lubrication region. Boundary lubrication, however, does not lend itself to reliable analysis. Consequently, most of the knowledge on metal forming lubrication is empirical.

In most forming applications, the lubricity of a lubricant is the single most important factor, since it directly determines the interface friction. In order to evaluate

the performance of different lubricants, it is necessary to express the interface friction quantitatively. The friction shear stress, f_s, is most commonly expressed as

$$f_s = \mu p \tag{3.22}$$

p being a compressive normal stress to the interface, or as

$$f_s = mk \tag{3.23}$$

where k being the shear strength of the deforming material, where $0 \leq m \leq 1$.

It has been recommended [16] that eq. (3.23) better represents the friction condition in bulk forming processes while eq. (3.22) is more commonly used to represent friction in sheet metal forming. A reason for this is that the compressive normal stress at the interface in sheet metal forming is much smaller in magnitude, in comparison to a bulk forming process. For various forming conditions, the values of m vary as follows:

- m = 0.05-0.15 in cold forming of steels, aluminium alloys, and copper, using conventional phosphate soap lubricants or oils.
- m = 0.2-0.4 in hot forming of steels, aluminium alloys, and copper with graphite based lubricants.
- m = 0.1-0.3 in hot forming of titanium and high temperature alloys with glass lubricants
- m = 0.7-1.0 when no lubricant is used, e.g. in hot rolling of plates or slabs and in nonlubricated extrusion of aluminium alloys.

In determining the friction factor m for hot forming, in addition to lubrication effects, the effects of die chilling or heat transfer from the hot material to colder dies must be included. Consequently, a good test for determining the lubricity must be able to include these variables. Lubricity, as defined by the friction factor m, is most commonly measured by using the ring test. In the ring test, a flat ring-shaped specimen is compressed to a known reduction. The change in internal and external diameters of the forged ring is very much dependent on the friction at the die-workpiece interface.

The change in the internal diameter represents a simple method for evaluating interface friction [44], [45].

This test highlights the fact that there exists a neutral point (or region) along the die-workpiece interface where the velocity of the deforming material relative to the die becomes zero. This phenomenon is not unique to the ring compression test and appears in a number of rolling and forging operations. The location of this point depends on the magnitude of the frictional stress. In order to deal with these situations, a velocity dependent frictional stress is used as an approximation to the condition of constant frictional stress. At the interface, the velocity boundary condition is given in the direction normal to the interface by the die velocity, and the traction boundary condition is expressed by

$$f_s = -mk\frac{u_s}{|u_s|} \cong -mk\left\{\frac{2}{\pi}\tan^{-1}\left[\frac{u_s}{u_0}\right]\right\} \tag{3.24}$$

where f_s is the frictional stress, u_s is the sliding velocity of a material relative to the die velocity (relative sliding velocity), and u_0 is a small positive number compared to u_s. This approximate expression for a constant frictional stress has been used for the smooth transition of the frictional stress near the neutral point [46].

Contact Modelling

The contact conditions can be mathematically described as follows

$$[\boldsymbol{v}] \cdot \mathbf{n} = 0, \qquad [\mathbf{t}] = 0 \tag{3.25}$$

where $\boldsymbol{v}$ and $\mathbf{t}$ are the velocity and traction vectors, respectively, $\mathbf{n}$ is a unit normal to the contact surface, and [ ] indicates the discontinuity amount across the contact boundary. Moreover, the traction in the tangential direction should satisfy the frictional law. The interface conditions given in eq. (3.25) can be written in variational form as

$$\int_S K_i \Delta v_n \delta \Delta v_n dS + \int_S t_s \delta \Delta v_s dS = 0 \tag{3.26}$$

where Δv_n is a penetrating velocity in the normal direction, Δv_s a sliding velocity in the tangential direction, and t_s a traction representing frictional stress. K_i is a large positive constant to penalise the penetration.

Due to the discretization of the boundary and kinematic constraints imposed on the finite element, eq. (3.26) cannot be used directly for finite element simulation. In finite element analysis the contact condition has to be imposed in an average sense. A typical contact configuration is shown in Fig. 3.2.

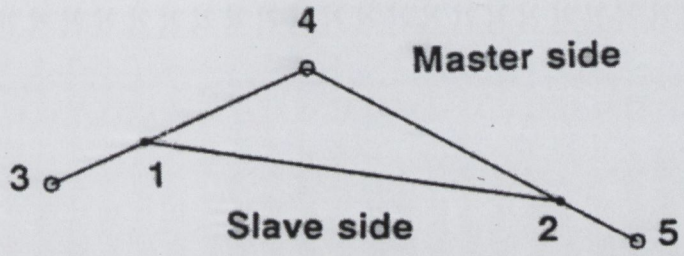

Figure 3.2: Typical contact configuration in finite element analysis

The kinematics of the contact condition in finite element analysis is defined by simple geometric relations. For example, the penetrating velocity at node 1 is defined by the relative motion between node 1 and line segment 34 in the normal direction to line segment 34. The penetrating velocity at node 4 is defined by the relative distance change rate between node 4 and slave side 12 in direction normal to side 12. When the master sides 34 and 45 are not colinear, then the penetrating velocity at node 4 should be adjusted in such a way that pure sliding by slave side 12 should give zero penetrating velocity at node 4. The penetrating velocity at node 2 is determined in a similar fashion to node 1.

By using the penetrating and sliding velocities at nodes 1, 4, and 2, the expression given in eq. (3.25) can be evaluated assuming penetrating and sliding velocities are linearly distributed between nodes. The integration of the interface condition is carried out over the slave elements.

3.2.3 Rezoning

In most metal forming processes, deformation is normally very large, which in turn will generate large values of effective strain and strain energy within elements. Also the relative motion between the tool surface and the deforming workpiece material can also be large. This situation of large deformations and displacements can cause a number of problems during a finite element analysis, namely:

- Difficulties in incorporating the die boundary shape into the finite element mesh when there is increasing relative displacement between tool and workpiece
- Difficulty in accommodating the considerable change of deformation mode within one mesh
- Mesh degradation: formation of unacceptable element shapes leading to negative Jacobians due to large local deformation

In order to overcome these difficulties, it is necessary to periodically redefine the mesh during the simulation process. This rezoning consists of two parts. One is the generation of a new mesh for the workpiece and the other is the transfer of pertinent information from the old to the new mesh through interpolation [47, 48, 49]. The first stage is easily achieved through the use of the finite element software's in-built mesh generator. The variables that depend on deformation history, such as effective strain and temperature, must be interpolated on to the new mesh. These two variables are dealt with differently.

Temperatures are given at the nodal points, when using the finite element method and thus the temperature distribution in the workpiece is expressed by using the finite element shape functions. Interpolation in this case is easily achieved by simply evaluating the temperatures at the new node locations.

In the case of effective strains an extra step is required. In the DEFORM finite element analysis package the effective strains are given at the reduced integration point of each element. Therefore, before interpolation it is necessary to calculate the effective

strains at the nodal points. Thus, effective strain distributions can be expressed in the same manner as the temperatures above.

For a linear rectangular element, one value of effective strain is given at the centre of each element. A method of area weighted averaging is used in DEFORM to calculate the nodal values of the effective strain. This method is extremely convenient and sufficiently accurate for rezoning in metal-forming simulations.

In this area-weighted averaging method, the nodal value is calculated on the basis of the average of the adjacent element values weighted by the associated size. Consider a node N surrounded by adjacent elements as shown in Figure 3.3.

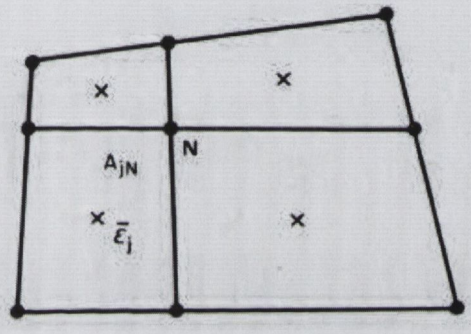

Figure 3.3: Node N surrounded by adjacent elements for area-weighted average.

The nodal value of the effective strain at node N can be determined by the following equation

$$\bar{\epsilon}_N = \frac{\sum_j \bar{\epsilon}_j A_{jN}}{\sum_j A_{jN}} \tag{3.27}$$

$\bar{\epsilon}_N$ is the effective strain value at node N and $\bar{\epsilon}_j$ is the effective strain value at the centre of element j that surrounds node N. A_{jN} is the area contribution of the j th element to node N and is defined by

$$A_{jN} = \int_{A_j} q_N(x, y) dA \tag{3.28}$$

Where q_N is the element shape function of element j at node N. The summation of equation 3.27 is performed over all the elements that surround node N. Once these effective strains have been calculated at all the nodes, the strain distribution over each element can be described by

$$\bar{\epsilon}(x, y) = \sum_\alpha q_\alpha \bar{\epsilon}_\alpha \tag{3.29}$$

Where q_α is the element shape function. The interpolation from the old to the new mesh is achieved by evaluating the effective strain values at the integration point locations of the new mesh. This method provides very accurate interpolation results for internal nodes when the trend of the field variable is well defined by the values of the surrounding elements but can present difficulties at the boundary nodes where they do not have a sufficient number of surrounding elements. For practical purposes, the method provides sufficient accuracy for metal-forming simulations. Figures 3.4 & 3.5 show how this rezoning procedure affected a standard thread rolling die model.

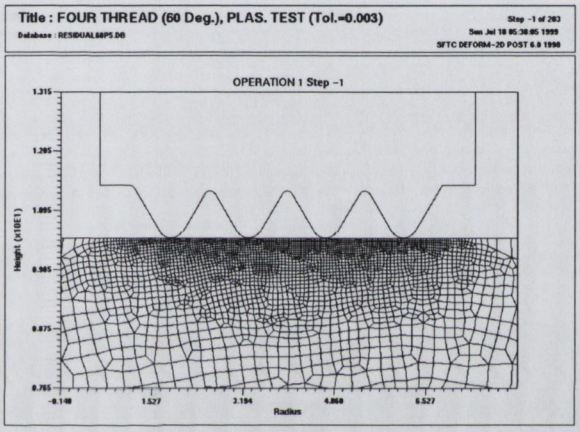

Figure 3.4: Undeformed Mesh

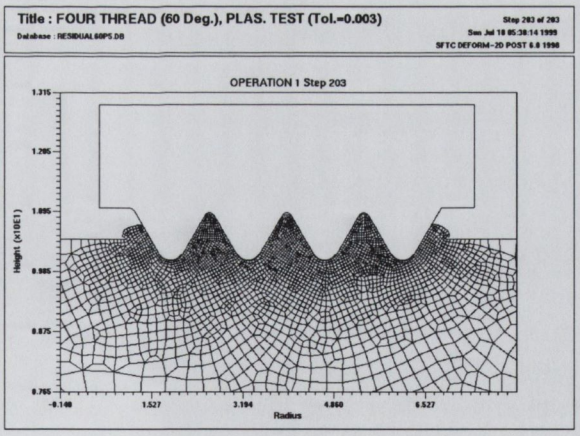

Figure 3.5: Deformed Mesh

Figure 3.4 shows the starting mesh of one of the thread rolling finite element analyses and Figure 3.5 shows a mesh further into the deformation process after a few remeshing operations have occurred.

Chapter 4

Work Programme

This chapter will outline the work programme undertaken in the design and development of the new flat thread rolling dies. The finite element models developed to model the thread rolling process will be detailed. The experimental programme used to determine the effectiveness of the new thread rolling dies designs on Titanium 6Al-4V fasteners will also be explained. In this chapter references will be made to the different parts of the thread rolling die and fastener, described earlier in Section 1.2.

4.1 Finite Element Models

4.1.1 Introduction

An extensive literature search for previous research papers on the application of finite element modelling to thread rolling, proved to be to no avail, hence the modelling of the thread rolling process had to be developed from basics. This implied building finite element models, that accurately reflected the actual thread rolling process and in particular features of it such as, thread fill (the amount the thread form fills during the rolling process). As in any finite element analysis, determination of the boundary conditions was of critical importance. The correct boundary conditions for the forming process had to be determined as these have a huge effect on the ability of the modelling process to reflect reality.

The focus of the modelling was to investigate the influence of the overall thread form of the thread rolling die on the stress and strain at the thread root. The thread form is composed of the included angle, crest radius (R2), and root radius, see Figure 4.1.

This focus was to vary features of the thread form geometry in order to determine an optimum design for the thread form, which minimised strain levels within the fastener, and therefore reduced the incidence of internal defects. The results obtained using these models will be detailed in Chapter 5.

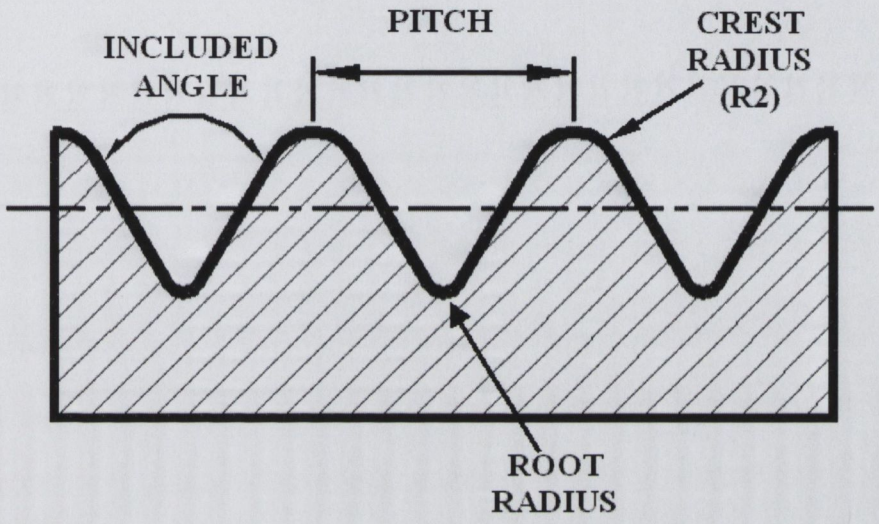

Figure 4.1: Thread Form of a Thread Rolling Die

4.1.2 Basic Assumptions

While thread rolling does involve three dimensional (3D) deformation, due to the influence of the helix or lead angle on a thread rolling die, it was decided that a two dimensional (2D) approach was a reasonable approximation of the thread rolling process. This is because the workpiece is axisymmetric and the applied load is one of *line contact*, see Figure 4.2, i.e. at any point during the rolling process, the thread rolling die only contacts the workpiece or blank along a line.

Obviously one limitation of this 2D modelling approach, is that the influence of the helix or lead angle (see section 1.2) on the thread rolling die cannot be accounted for. This limitation should not significantly influence the results as the value of the helix angle is small on the thread rolling dies modelled, i.e. 3-4 degrees.

The friction factor (m) used in all analyses was 0.1. This value is low but is in the recommended levels outlined in section 3.2.2. The use of this low value may also be argued for on the basis that the full impact of friction cannot be captured by a 2D

analysis and so only a component of the 3D frictional vector is included in our analyses, which is lower than the full friction.

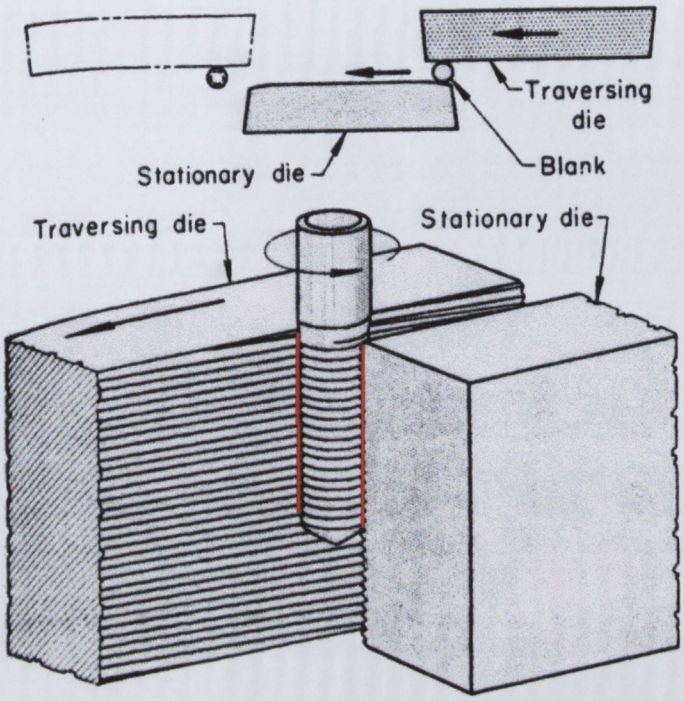

Figure 4.2: Thread Rolling, Line Contact $\Longrightarrow$ Two Dimensional Problem

Another facet of the thread rolling process that cannot be included in a 2D model is that of blank rotation. However, one major advantage of using 2D models, is that the modelling process becomes simpler and solution times are reduced. A 3D problem can be one to one and half orders of magnitude more demanding than a comparable 2D problem [50]. Furthermore 2D models provide a very good indication of trends that arise due to variations in the forming parameters. Another advantage of the 2D modelling approach is that, in general, more detail can be gleaned from a set of 2D results compared to an over-complicated 3D model.

Because the behaviour of the blank (workpiece) was of primary interest, the thread rolling die was modelled as a rigid object in most of the finite element analyses performed. This assumes that the thread rolling die does not undergo any deformation or deflection during rolling. Due to the negligible effects of elastic deformation and thermal effects, the blank was modelled as a rigid plastic material (see section 3.2.1) that only included the effect of plastic deformation. All the analyses were performed

using a Plane Strain formulation. The fastener (blank) was modelled in plane strain because metal flow was assumed to occur in the radial and longitudinal directions with negligible spread in the hoop direction.

4.1.3 Initial Models

The initial finite element analyses modelled ten threads of a *standard*, 15.875mm (0.625in.) - 18 threads per inch (t.p.i), thread rolling die. The standard thread rolling die for this size of fastener has the following thread form, 60 degree included angle and a crest radius (R2) of 0.24384mm (0.0096in.), see Figure 4.3.

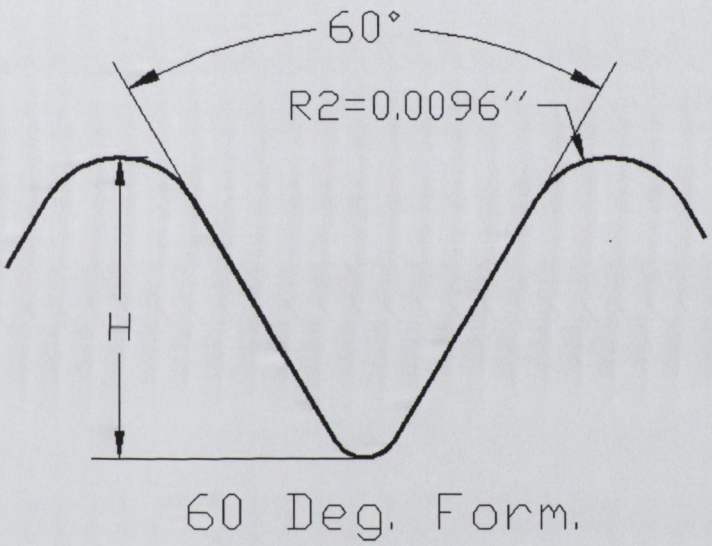

Figure 4.3: "Standard" Thread Form

Figure 4.4 shows one of these finite element models with a more detailed description of the thread rolling die/workpiece contact area shown in Figure 4.5. In these figures the thread rolling die is represented by a rigid surface (black line) and the workpiece (blank/fastener) is the meshed area. Since deformation is symmetric about the centre line of the workpiece, appropriate boundary conditions were applied at the centre line and only one half of the workpiece was modelled. The boundaries of the fastener, which were not completely modelled i.e. the full geometry was not included, were unfixed and free to move. These boundary conditions were a "first guess" of what occurs during actual thread rolling.

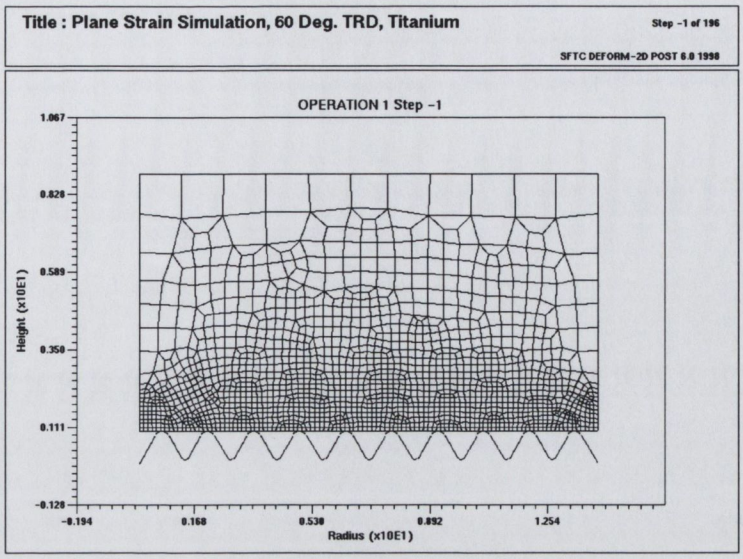

Figure 4.4: Initial Finite Element Model

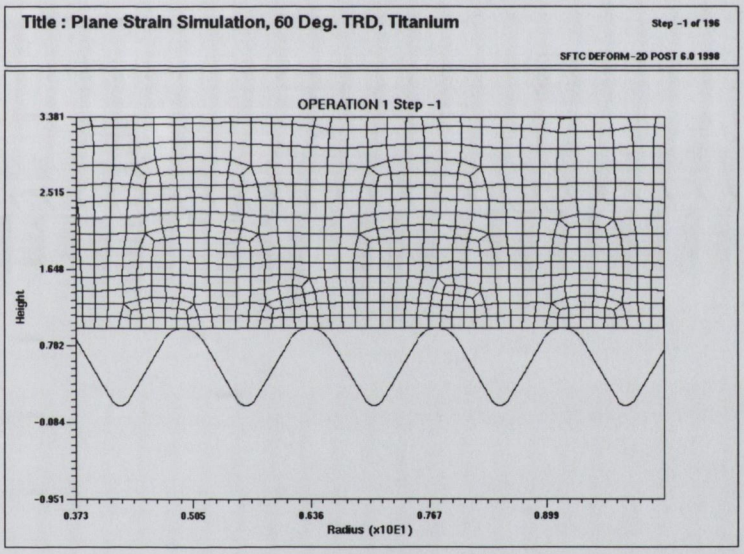

Figure 4.5: Close up of Thread Rolling Die/Workpiece Interface

The workpiece (fastener) mesh shown in Figure 4.4 has 1500+ elements, concentrated in the upper surface of the blank next to the thread rolling die (Figure 4.5). The elements of the mesh must be concentrated in this manner so that at later stages in the forming process, the "thread fill" feature of a thread rolling process is properly captured. If the elements in this region of the fastener are too large they will not be able to fill the thread form properly and the finite element software will stop the analysis and prevent any further deformation.

This mesh concentration also served another purpose, because the results of greatest

interest are from material at the thread root, the concentration of elements in this region ensures greater accuracy. The results from these models indicated that some fine tuning of the boundary conditions was required. This was evident from the level of thread fill achieved within the thread forms. This fine tuning was dealt with in a subsequent set of finite element models.

Initially two materials were used in the finite element analyses, namely, Titanium 6Al-4V and SPS 0.9 alloy. These two materials were used to determine the effect, if any, the fastener material was having on the thread rolling process. After the initial models had been completed and analysed, it was established that the type of fastener material was not a dominant factor, consequently only the Titanium 6Al-4V material was used in the later models. The stress strain curve for Titanium 6AL-4V was described using the following law [44] for strain rate sensitive materials.

$$\overline{\sigma} = C(\dot{\overline{\epsilon}})^m \tag{4.1}$$

This law accounts for both a change in strain rate and strain during deformation. The values for C and m at various strains can be seen in the table below. These values hold for a strain rate ($\dot{\overline{\epsilon}}$) range of 0.25 to 16.0.

Strain	C	m
0.1	1400.74	0.017
0.2	1444.83	0.015
0.3	1419.34	0.015

Table 4.1: C and m values for Titanium 6Al-4V, Room Temperature

The SPS 0.9 Alloy stress strain curve is presented in Figure 4.6.

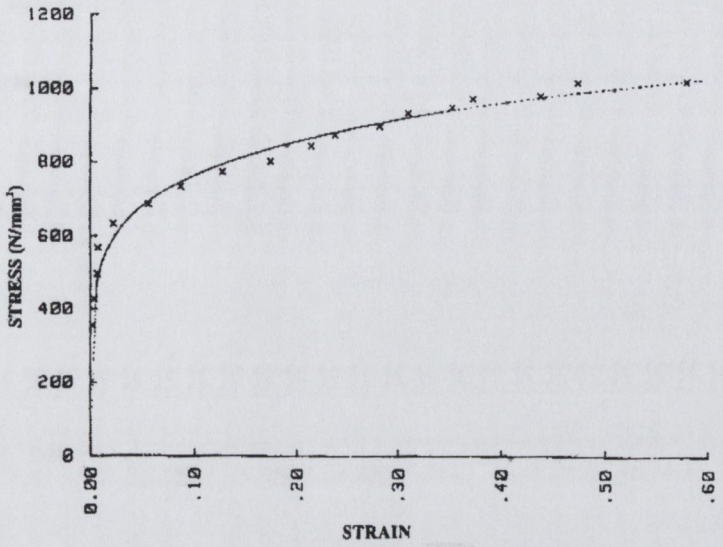

Figure 4.6: Stress Strain Curve for SPS 0.9 Alloy

4.1.4 Boundary Conditions

As mentioned the fastener modelled had the following specifications, 15.875mm (0.625in.) blank diameter, and 18 threads per inch (t.p.i.), the completed thread height (H) is equal to 0.88mm (0.0346in.), from root to crest. Figure 4.7 shows the standard 60 degree included angle with crest radius (R2)=0.2438mm (0.0096in.) thread form of the thread rolling die.

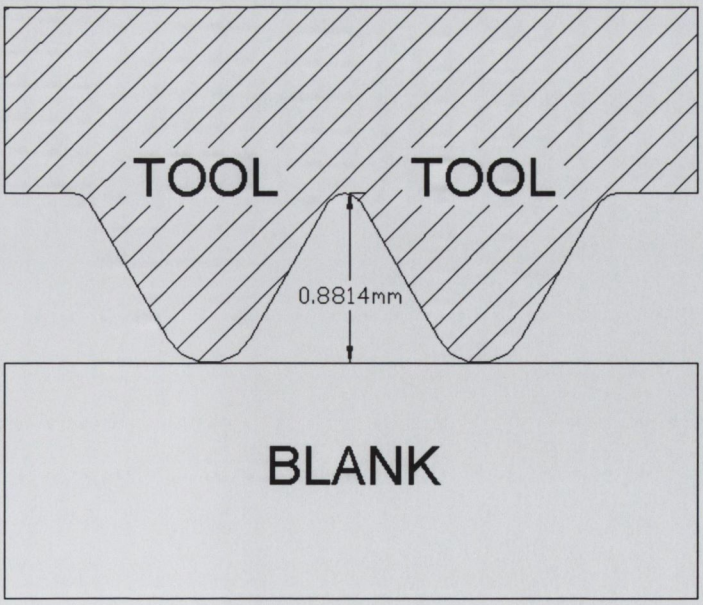

Figure 4.7: Maximum Thread Height

Following an analysis of the results from the initial set of models, it became obvious that proper thread fill was not being achieved using the first guess boundary conditions. The reason for incomplete thread fill was because in the initial models the fastener material was free to move axially at the "head" and "point" ends of the fastener i.e. incorrect boundary conditions were prescribed. These results necessitated the creation of a new set of models having more appropriate boundary conditions. In these models the complete fastener geometry was included i.e. the full length of fastener, the point geometry, details of the radius run-out (RRO) on the thread rolling die were all included, see Figure 4.8.

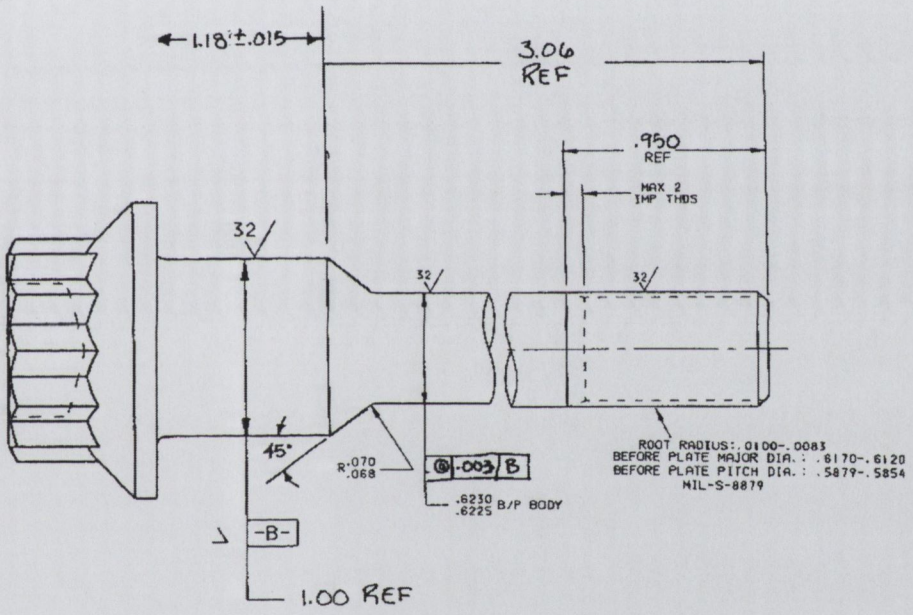

Figure 4.8: Schematic of Fastener Geometry

Models having two different sets of end-fixing boundary conditions were used for this section of the work programme. One model had the head or shank end (left hand side) of the fastener fixed to prevent any axial flow in the x-direction, the other model had no such end constraints. The mesh of the fastener in these two models contained 1500+ elements. The model used is shown in Figure 4.9.

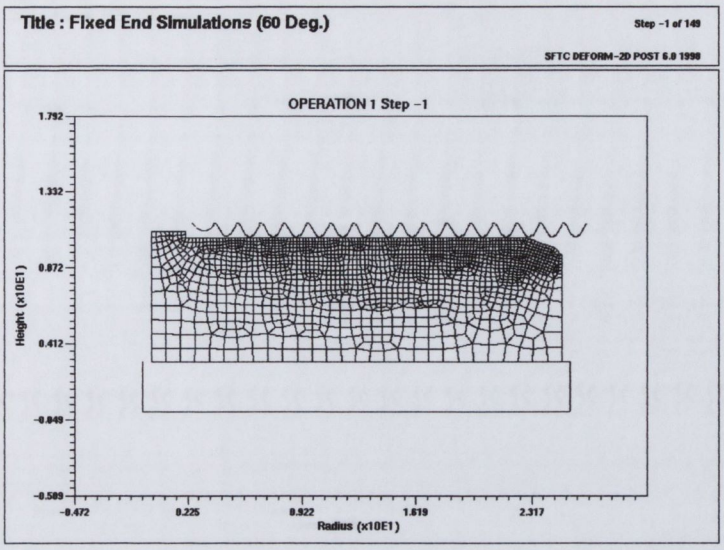

Figure 4.9: Finite Element Model for Boundary Condition analysis

The results from the model with the fixed shank end gave better thread fill results and also showed a biased metal flow in the direction of the point of the fastener. This last feature has been observed in actual thread rolling. Figure 4.10 and Figure 4.11 show velocity vector plots for the two different boundary condition models. The boundary conditions were further developed in the next section.

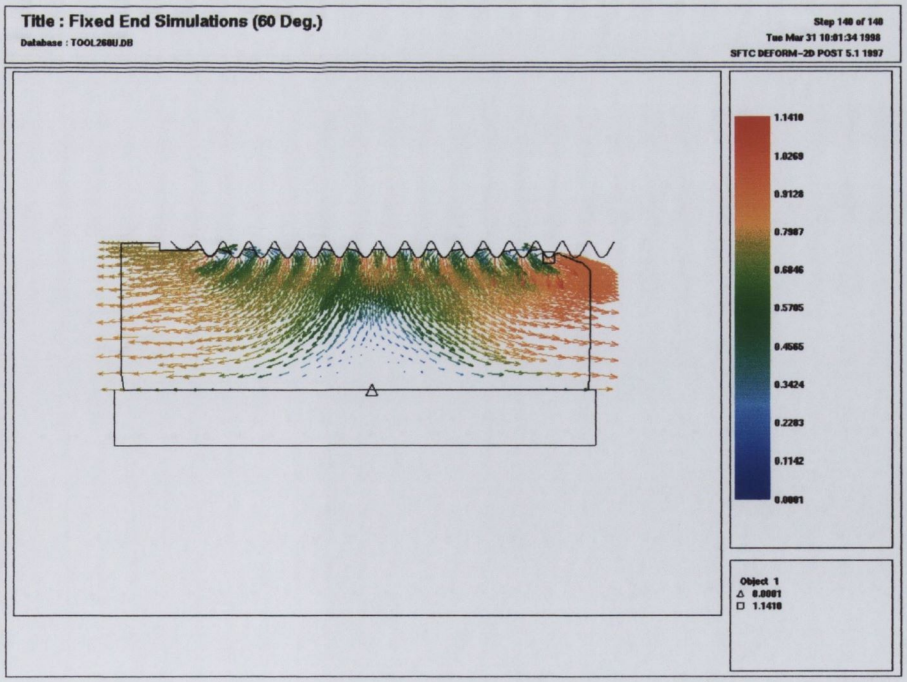

Figure 4.10: Velocity Vector Plot for Unfixed Shank End

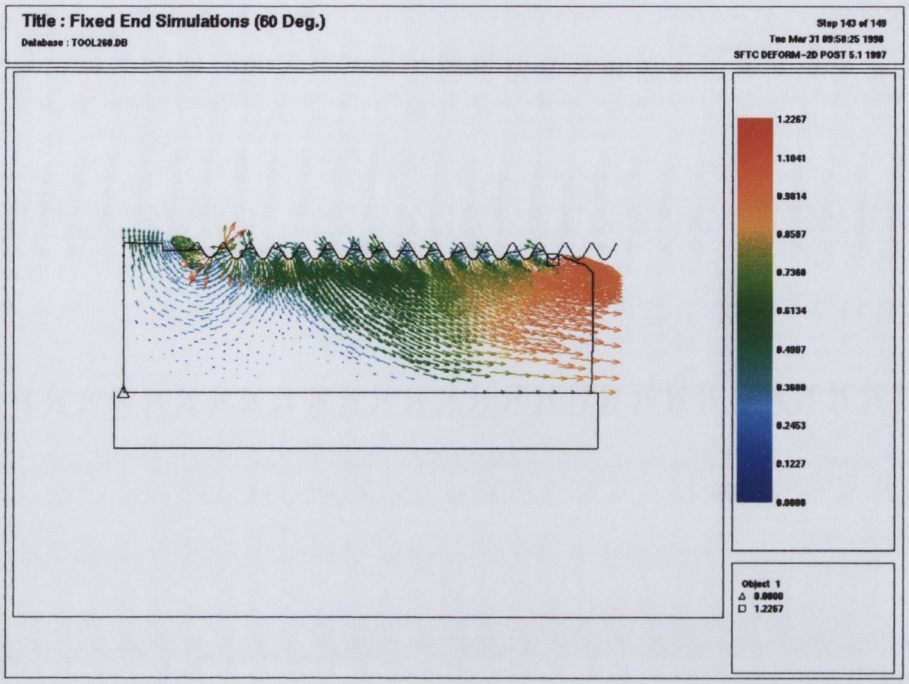

Figure 4.11: Velocity Vector Plot for Fixed Shank End

4.1.5 Included Angle Designs

The third set of models constructed and analysed were known as the "Included Angle Design" models. These new designs involved a two stage thread rolling process with initial deformation performed using a 120 degree or 90 degree included angle thread form and final thread formation performed using the standard 60 degree included angle form. This two stage design became known as a *progressive thread rolling die.* The geometry of the new 120 degree and 90 degree included angle thread forms can be seen are shown in Figure 4.12. The crest radius in all these designs was maintained at the standard R2 value of 0.24384mm (0.0096in.).

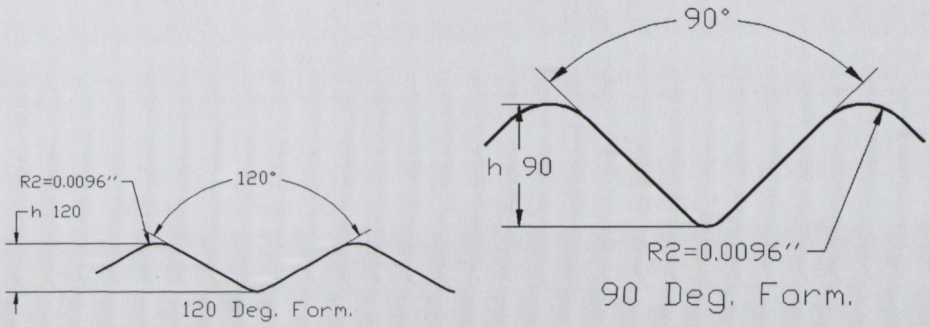

Figure 4.12: 120 Degree and 90 Degree Included Angle Designs

The initial models for this section of the thesis were constructed and analysed based on the boundary condition models of the last section. The similarities between these models and those of the previous section are evident. These initial included angle models still contained the full thread rolling die and fastener geometry. This allowed for comparison of the results between the new included angle designs and the standard 60 degree included angle results. They were used to simulate the initial thread formation i.e. up to the point where transfer to the standard 60 degree form would have taken place. A 120 degree included angle design finite element model is presented in Figure 4.13.

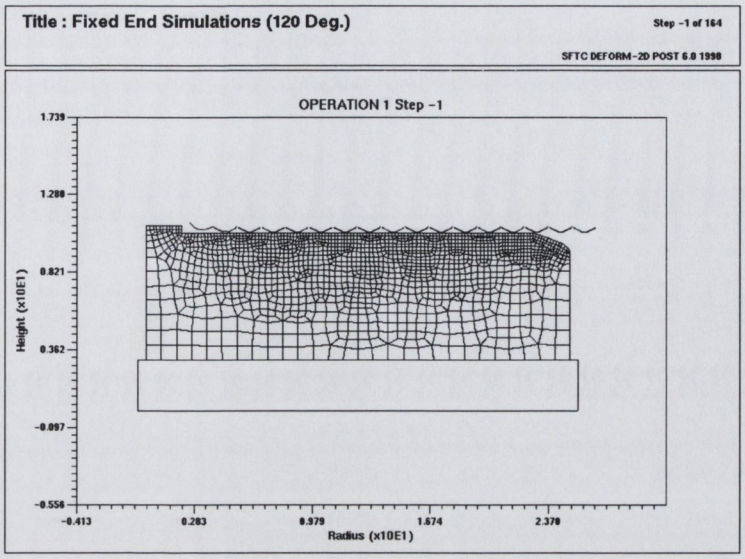

Figure 4.13: 120 Degree Included Angle Design Model

At this point it was decided to simplify the models. This decision was taken because while all the features of the thread rolling die were included the models did not provide sufficient detail at the area of interest (the thread root). By modelling the complete fastener it was found that there were too many variables interacting and it was difficult to isolate the effects that varying the included angle of the thread form was having on the stress and strain distributions, particularly at the thread root. As a result models were then constructed, which consisted of only four threads of a flat thread rolling die, i.e. three actual threads being formed on the fastener blank. These models provided better results for the area of interest, and highlighted in greater detail the influence that altering the included angle had on the material flow and the resulting stress and strain distributions within the formed thread. A representative model from this set of analyses is presented in Figure 4.14 below.

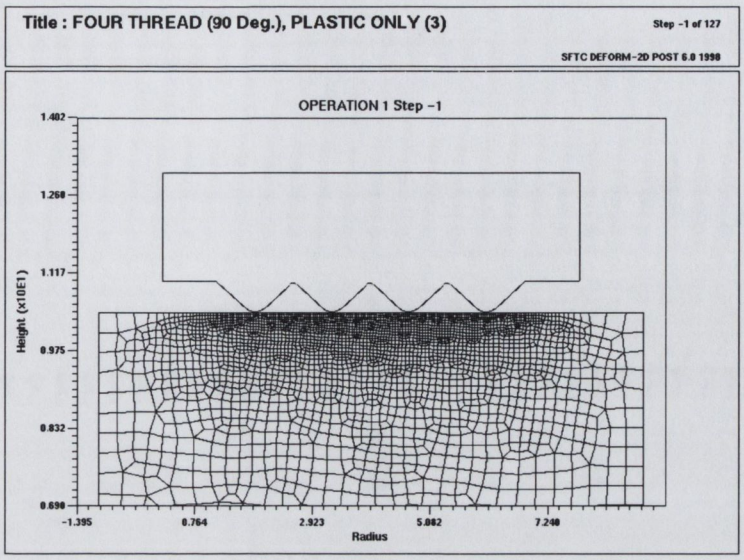

Figure 4.14: 90 Degree Included Angle Design, Four Thread Model

These models had 3000+ elements and were constrained on their left and right hand side in both the x and y directions to prevent axial flow. These boundary conditions, while not true for the whole of the fastener, were considered to provide a reasonable approximation of the material behaviour in the centre of the thread rolling die.

The final shape (form) that the formed thread must have, regardless of the starting form, is an included angle of 60 degrees. This implies that to achieve complete thread formation using a 120 degree included angle design, that at some point the material will have to be transferred to a section of the thread rolling die having the required standard 60 degree included angle thread form. Given the geometry of a larger included angle there is a maximum amount of thread formation (height) that can occur with this larger included angle. Table 4.2 below shows the maximum thread height attainable with a 120 degree and a 90 degree included angle design before transfer to a standard 60 degree included angle die section becomes necessary.

Included Angle	Max. Height (mm)	Max. Height (in.)
120 Degrees	0.356mm	0.0140in.
90 Degrees	0.564mm	0.0222in.
60 Degrees	0.881mm	0.0347in.

Table 4.2: Maximum Thread Height attainable with Larger Flank Angle

The "Four Thread" models discussed above included this "transfer" portion of the

forming process. The inclusion of an initial, transition, and final 60 degree form ensured that the complete thread formation process could be simulated using the new included angle die designs. This approach enabled a comparison of the stress/strain distributions and material flow of the new die designs compared to those obtained using a standard 60 degree form. Results for thread fill from these models indicated that the boundary conditions chosen, reflected the material behaviour in an actual thread rolling process very well i.e. proper thread fill was achieved.

4.1.6 Crest Radius Designs

The fourth set of models constructed and analysed were known as the "Crest Radius Design" models. These new thread rolling die designs were based on modifications to the radius on the crest of the standard 60 degree thread form, see Figure 4.15. This radius is commonly referred to as R2 and as mentioned previously, the standard value for R2 on a 15.875mm (0.625in.) diameter, 18 threads per inch fastener is 0.24384mm (0.0096in.) Figure 4.15 indicates the range of new R2 designs investigated. Each new R2 design reflects a certain % height of the standard thread form (Table 4.3). These particular models basically represent a truncated form of the standard 60 degree form. This truncation is brought about by increasing the size of the R2 or crest radius. For these models the included angle was maintained constant at 60 degrees in each case.

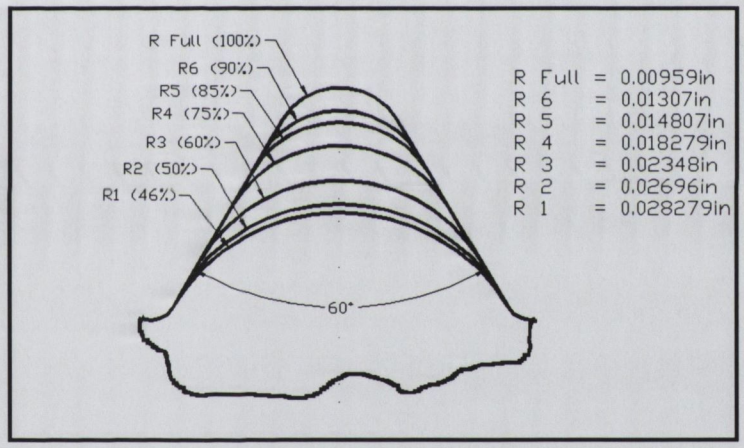

Figure 4.15: Different R2 models used in finite element models

The first set of modified R2 models involved simulations using just a single thread with a modified crest radius (R2) deforming the fastener surface (see Figure 4.16). These models had 3000+ elements in the mesh. Complete thread formation was not simulated as the aim of these models was to see the effect that varying the crest radius had on the strain, strain rate, and stress distribution within the fastener material.

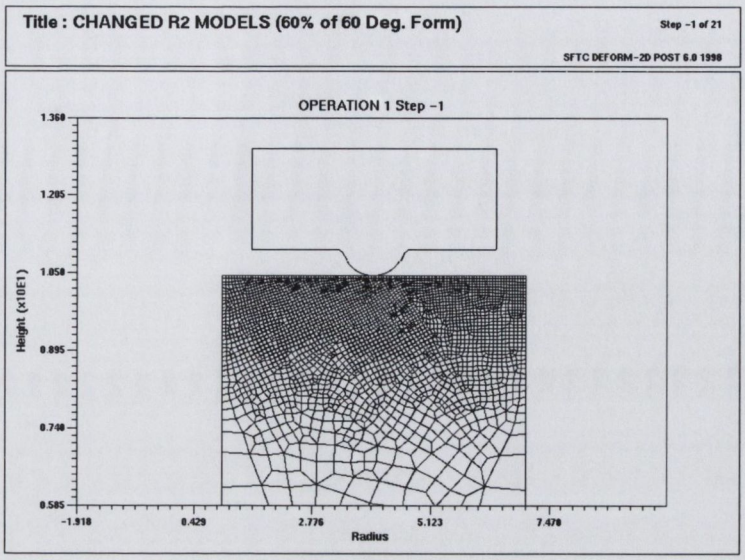

Figure 4.16: Single Thread R2 model

The next set of models were created in the same manner as the "four thread" included angle models, described earlier, so as to allow for direct comparison between the two sets of results. As can be seen from Figure 4.17 they showed four threads, with modified crest radii (R2), of a thread rolling die deforming the fastener surface.

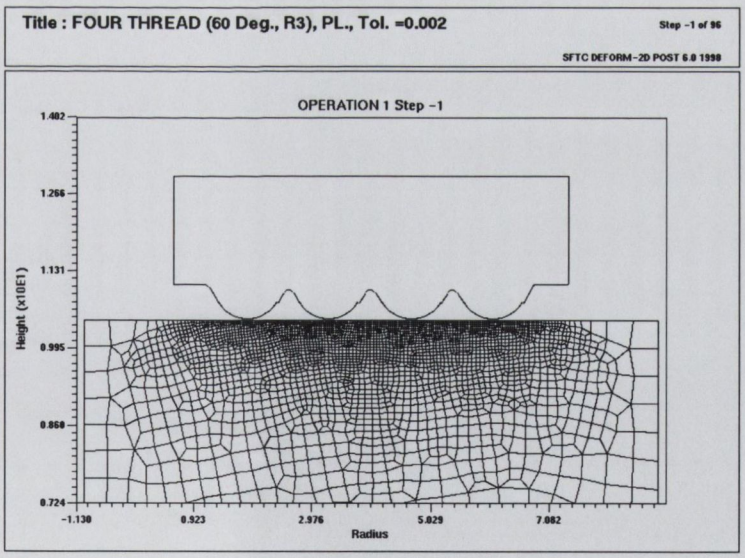

Figure 4.17: Four Thread Modified R2 model

As in the case of the included angle designs there is a maximum to the amount of thread formation (height) that can occur with a die having a given (R2) crest radius. The table below (Table 4.3) shows the maximum thread height attainable with the different modified crest radii designs.

Crest Radius (R2)	% Height of Standard 60	Max. Height(mm)	Max. Height(in.)
0.2438mm(0.0096in.)	100%	0.881mm	0.0347in.
0.3327mm(0.0131in.)	90%	0.793mm	0.0312in.
0.3759mm(0.0148in.)	85%	0.749mm	0.0295in.
0.4648mm(0.0183in.)	75%	0.661mm	0.0260in.
0.5969mm(0.0235in.)	60%	0.529mm	0.0208in.
0.7188mm(0.0283in.)	46%	0.441mm	0.0174in.

Table 4.3: Maximum Thread Height attainable with Larger Crest Radius (R2)

As with the included angle designs these modified crest radii analyses simulated the complete thread formation process, including the transfer from the modified crest radius thread form section of the thread rolling die to the final standard 60 degree with R2 = 0.24384mm (0.0096in.) section.

4.1.7 Combination Designs

The final set of models were constructed to simulate the combination of the optimum included angle design with the optimum crest radius (R2) design together on a single thread rolling die. Analysis of results from the previous two sets of designs had indicated that this design might prove to be very beneficial in terms of the reduction of internal defects. As in the previous two sets of simulations, the transfer from the modified thread form design used at the start of the process to the standard 60 degree thread form for final thread formation was included.

4.2 Experimental Tests

4.2.1 Introduction

After the final designs for the thread rolling dies had been agreed upon, a programme of experimental tests had to be developed to assess how successful the new designs, developed in this thesis, were in reducing the occurrence of internal defects within Titanium 6Al-4V fasteners. In February 1999, this experimental programme was undertaken by the author at SPS Technologies, Jenkintown, Philadelphia, U.S.A.

These tests involved rolling Titanium 6Al-4V fasteners on a standard thread rolling machine using the new thread rolling die designs, sectioning the resultant fasteners, and preparing samples for microscopic analysis from these sections. "Defect counts" were obtained from this microscopic analysis for comparative purposes. Mechanical tests were also undertaken on the rolled fasteners to ensure that the mechanical properties i.e. tensile & fatigue, were not affected detrimentally compared to that of a fastener produced using a standard 60 degree thread form flat die and the current best manufacturing method.

4.2.2 Thread Rolling

When an aerospace fastener is being thread rolled, the thread rolling machine must be set-up to ensure that the very strict specifications of the product are met, i.e. pitch diameter, major diameter etc. This set-up procedure is conducted by performing pre-production runs using test studs, see Figure 4.18.

Figure 4.18: Titanium 6Al4V Test Studs

The studs are manufactured from the same material as the actual fastener product. The studs are then rolled through the thread rolling machine and the relevant dimensions measured. When inspection of the rolled studs indicate that the required dimensions are within tolerance, and therefore the machine set-up is as required the actual product rolling can commence.

Initially threads were rolled on Titanium 6Al-4V, 15.875mm (0.625in.) blank diameter studs, 18 threads per inch, i.e. the same diameter as the fasteners under investigation. Rolling was performed on a 60 Waterbury thread rolling machine at room temperature and at the standard rolling rate of 40 strokes per minute. The machine speed was maintained constant during rolling. From these rolled studs defect counts were made (see section 4.2.3). The results from this analysis are presented in a later chapter.

Threads were then rolled on the actual Titanium aerospace fastener blanks using the new thread rolling die designs. These threaded fasteners were then divided into three groups for further testing. The first group was used for defect count analysis, the second group was used for tensile testing, and the third group for fatigue testing. The purpose of the last two groups of tests was to confirm that the new thread rolling die designs did not effect the mechanical properties of the fasteners compared to fasteners

manufactured using standard flat dies.

4.2.3 Defect Counts

To be able to assess the effect of the new thread rolling die designs in reducing the occurrence of internal defects, a method had to be derived for counting and comparing these internal defects. Firstly the samples had to be prepared for the purpose of these defect counts, and in the case of both the studs and the rolled fasteners, the samples for inspection were prepared in the same manner. Firstly, the threaded region was sectioned two ways to produce four 90 degree quarters, see Figure 4.19. These were then polished to minimise scratches with the final sanding performed with FEPA P#4000 paper and the final polishing with an SiO_2 suspension.

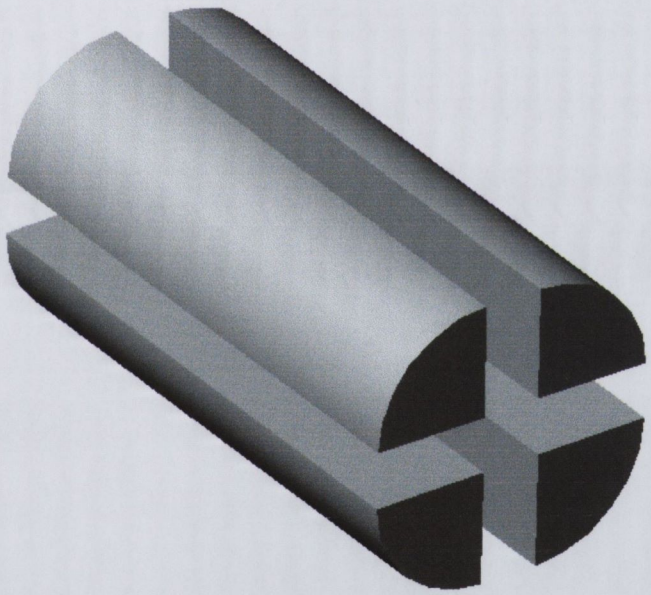

Figure 4.19: How the test studs were sectioned

To highlight the internal defects the specimens were then etched with Kroll's etch (15 ml HF, 35 ml HNO3, 950 ml H_2O) and the mounted thread sections were then examined at 200X magnification using a Vanox microscope. Counts were made of defects in the thread root region, in material below the pitch diameter but not in the thread root, and in the material above the pitch diameter. Defects were not counted if there was only one and its length was less than 0.0005in. (0.0127mm). If the above

condition existed it was too hard to tell if what the microscope was showing was actually an internal defect. If more than one existed (usually in a row following a shear band) they were counted as one regardless of length.

A sheet was used to record and classify these defects, a copy of this sheet can be seen in Table 4.4.

TABLE FOR RATING INTERNAL DEFECT SEVERITY

Micro Identification:

	DEFECT SEVERITY			
	No Defects	1 Defect	2 to 3 Defects	>3 Defects
ROOT				
BELOW P.D.				
ABOVE P.D.				

Table 4.4: Table used for Defect Count and Classification

Directions for use:

1. Identify the micro being examined at the top of the table.

2. Inspect each thread in a given micro at the three locations specified.

3. Rate each location using the four stated categories (No Defects, 1 Defect, 2 to 3 Defects, > 3 Defects), enter a tally stroke.

4. Total number of strokes per row should approximate the number of threads in the micro.

4.2.4 Tensile Tests

The tensile tests were performed on the thread rolled fasteners using National Aerospace Standard NASM1312-8 [51], which is also known as MIL-STD-1312-8. This test is applicable to the tensile testing of all fasteners at room temperature. It is intended to determine the tensile strength of the fastener itself.

The tensile tests were performed on a Tinius Olsen, Super L, hydraulic tensile testing machine. The machine has a load capacity of 120,000 lbs (534 kN) and was calibrated according to ASTM standard E4.

Results for these tests are presented in Chapter 6

4.2.5 Fatigue Tests

The fatigue tests were performed on the thread rolled fasteners using National Aerospace Standard NASM1312-11 [52], which is also known as MIL-STD-1312-11. This test is used for determining tension fatigue life of bolts, screws, and nuts at room temperature.

The machine used for the fatigue tests was an Amsler Vibrophore (electro-resonant), Model HFP1093. The capacity of the machine was 100,000 lbs (445 kN).

Results for these tests are presented in Chapter 6

Chapter 5

Finite Element Results

This chapter will outline the results obtained from the different stages used in the finite element modelling of the thread rolling die design. The different modelling stages have been outlined in the preceding chapter.

5.1 Initial Models

The initial finite element models incorporated ten threads of a standard thread rolling die (15.875mm (0.625in) diameter, 18 threads per inch). Figure 5.1 below shows the starting configuration of the thread rolling die and workpiece in one of these models.

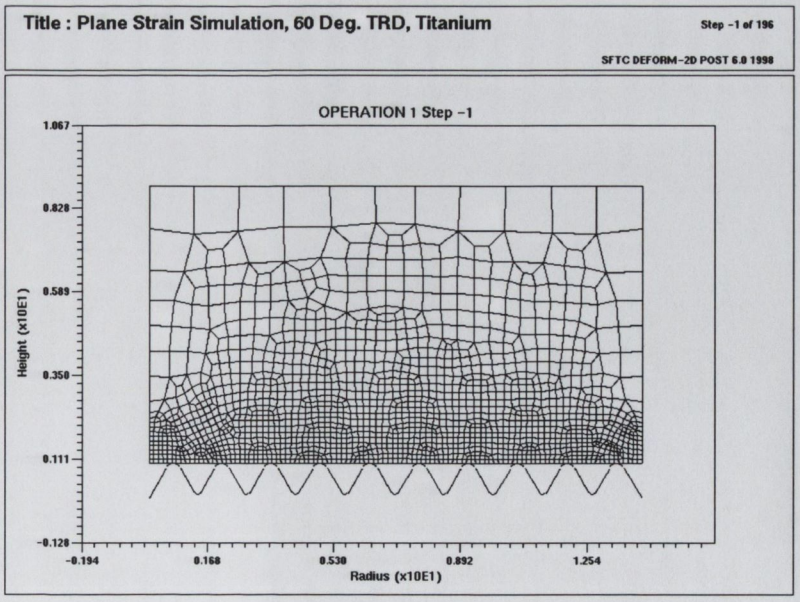

Figure 5.1: Initial Model, Starting Configuration

The following set of figures show some of the results obtained from this set of initial models. The regions of high stress and strain (red contours) are obvious from the figures. Figures 5.1 & 5.1 show the plots for effective stress and strain for the Titanium 6Al-4V model while figures 5.1 & 5.1 show the plots for the SPS 0.9 Alloy model. It is clear from these plots that the same patterns of stress and strain occur in each material. These results suggest that the stress and strain distributions are primarily tool geometry dependent rather than material dependent. Both sets of results indicate regions of "High" stress and strain at the thread root, and "Low" stress and strain in the material flowing to form the thread.

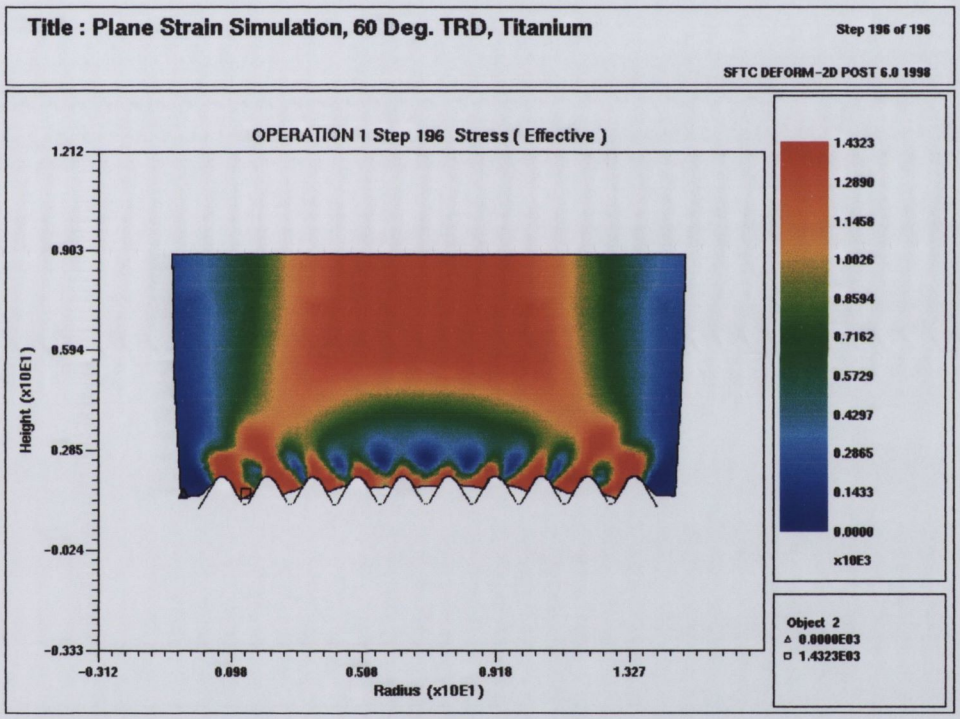

(Maximum 1430 N/mm^2, Minimum 0 N/mm^2)

Figure 5.2: Effective Stress (Titanium 6Al-4V)

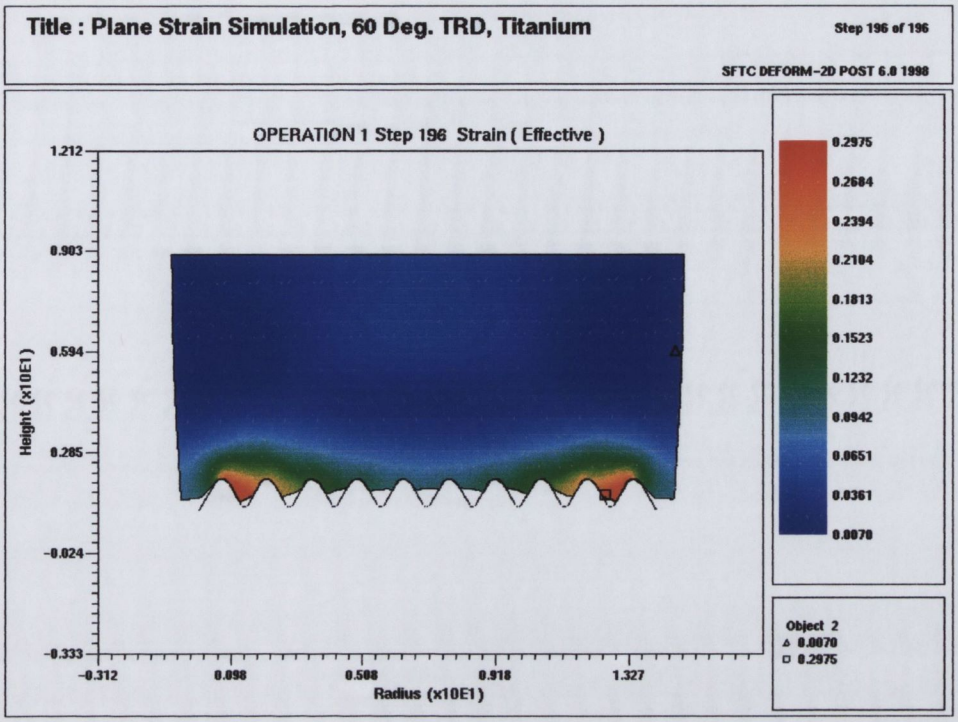

(Maximum: 0.2975, Minimum: 0)

Figure 5.3: Effective Strain (Titanium 6Al-4V)

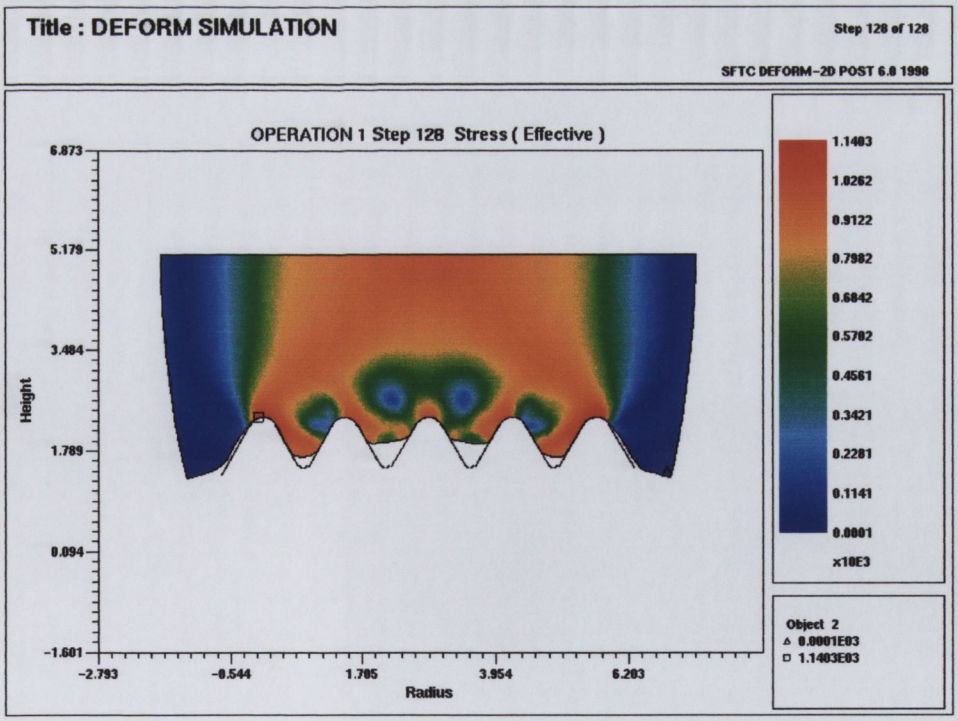

(Maximum: 1140 N/mm^2, Minimum: 0 N/mm^2)

Figure 5.4: Effective Stress (SPS 0.9 Alloy)

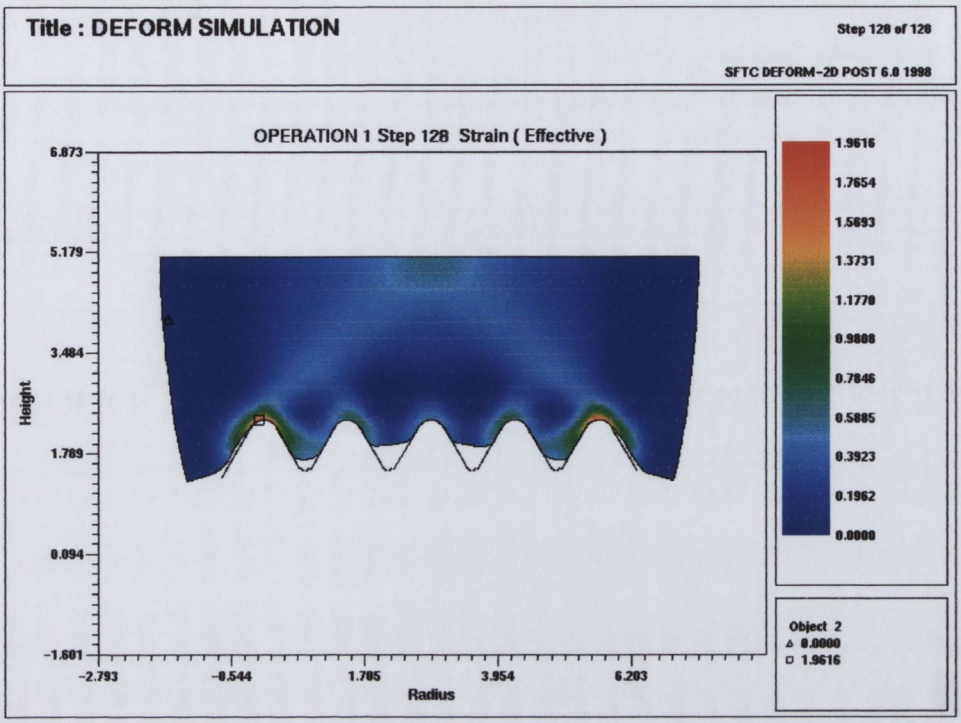

(Maximum: 1.96, Minimum: 0)

Figure 5.5: Effective Strain (SPS 0.9 Alloy)

5.2 Boundary Condition Models

The second set of models analysed included the changes to the boundary conditions outlined in Section 4.1.4. As mentioned previously these changes were included to improve the representation of the material flow in the fastener during thread rolling, i.e. more flow towards the point end rather than the shank of the bolt. Details of the point geometry of the fastener and the radius run-out (RRO) on the thread rolling die were included. The full thread rolling die and fastener geometry were all modelled.

The results from this second set of models, which include the point and RRO geometry and the modified boundary conditions, are shown in Figures 5.6 & 5.7. It can be seen from these two figures that a change in the boundary conditions has a large effect on the material flow. Restraining the shank end from horizontal movement better simulates the material flow during an actual thread forming operation, particularly with Titanium 6Al-4V which has a tendency to elongate during thread rolling.

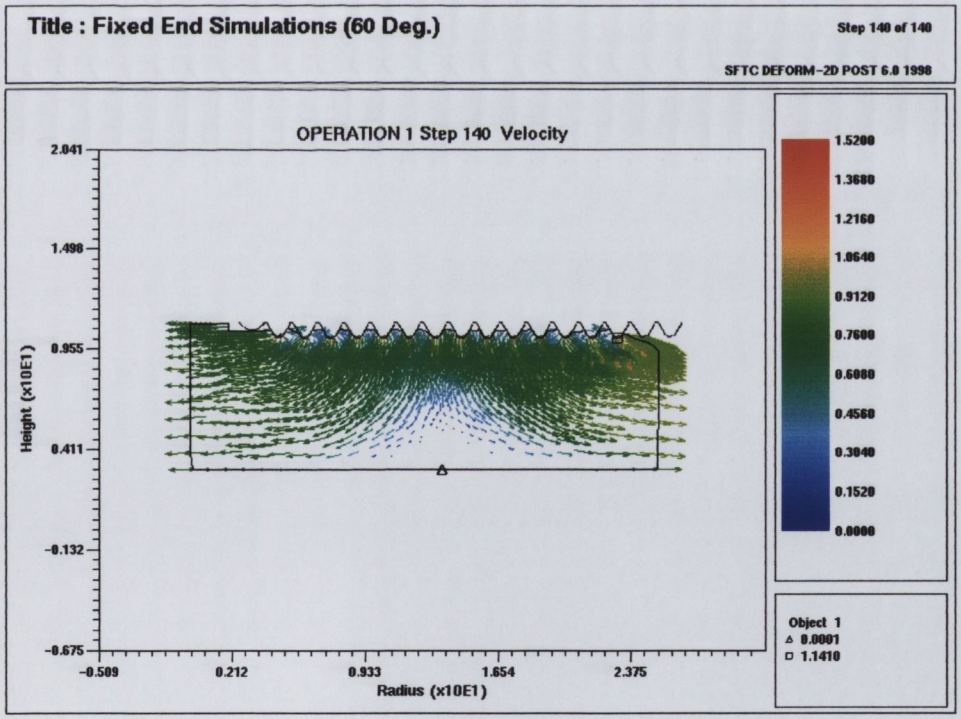

Figure 5.6: Metal Flow in Fastener (Shank End, Unfixed)

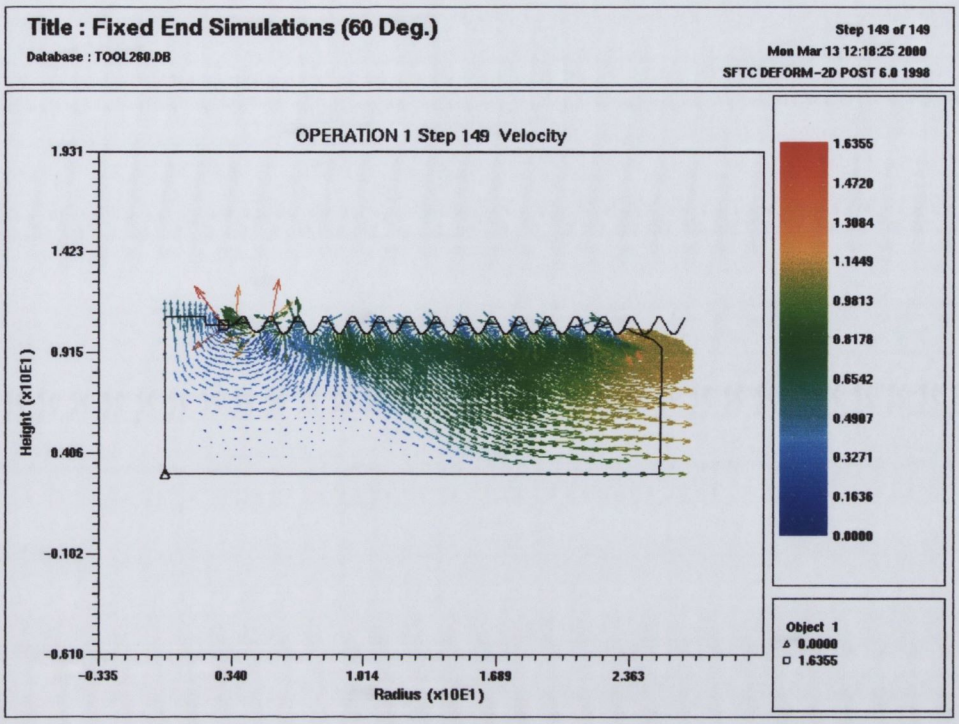

Figure 5.7: Metal Flow in Fastener (Shank End, Fixed)

In this case the material flow is biased towards the point end which is a better representation of what is observed during thread rolling. These results also confirm that the distribution of stress and strain is influenced by tool geometry and boundary conditions and not by the fastener material. It also indicates that the selection of boundary conditions is crucial to the outcome, incorrect selection produces erroneous results.

5.3 Included Angle Designs

The third set of analyses, described previously in section 4.1.5 were performed to investigate the influence of varying the included angle on the stress, strain, and strain rate distributions in the vicinity of the thread root. Finite element models for the new thread rolling die designs of 120 and 90 degree included angles were analysed.

The results from the initial models in this section can be seen in Figures 5.8 & 5.9. These results indicate the distributions of strains and stresses present in these models. Table 5.1 gathers together the results for the different included angle designs. For completeness the table also includes results for the standard 60 degree included angle design. It is clear from these results that the stress, and more importantly the strain, decreases at the thread root as the included angle increases from 60 degrees to 120 degrees.

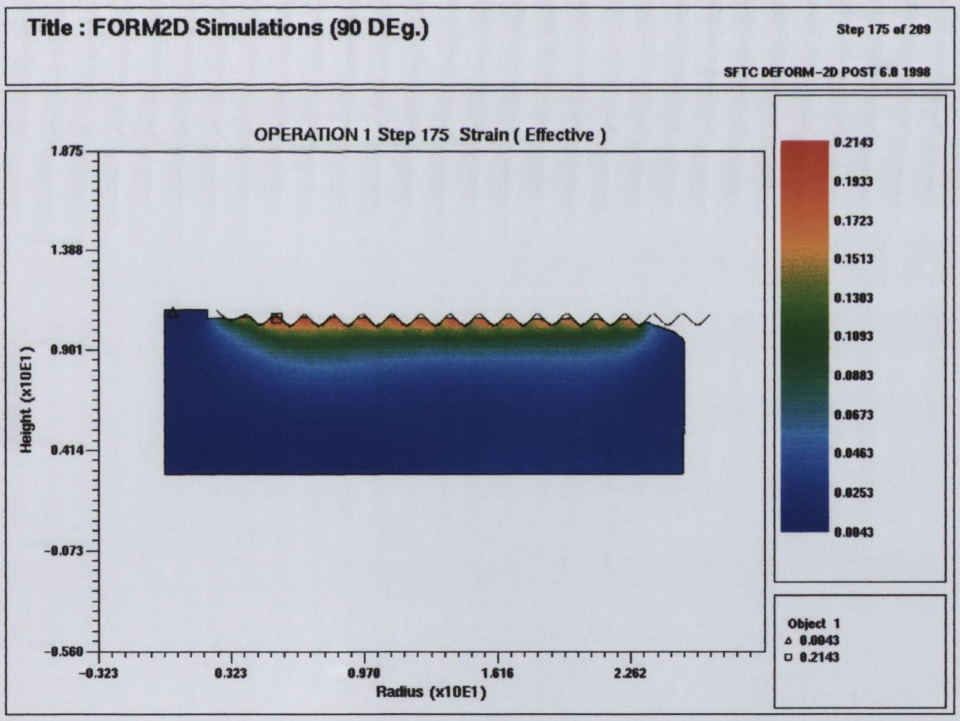

(Maximum: 0.21, Minimum: 0)

Figure 5.8: Effective Strain (Thread Root, 90 Degree Included Angle Design)

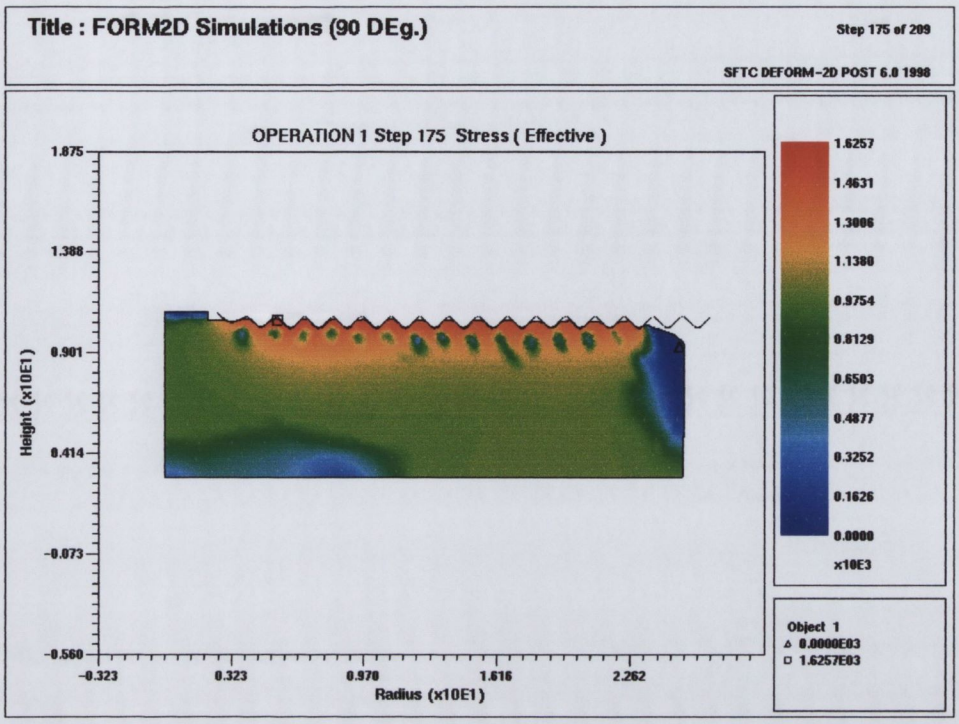

(Maximum: 1625 N/mm^2, Minimum: 0 N/mm^2)

Figure 5.9: Effective Stress (Thread Root, 90 Degree Included Angle Design)

FORM ANGLE	60 Degree	90 Degree	120 Degree
Strain	0.3	0.17	**0.13**
Stress, N/mm^2	1800	1572	**1500**

Table 5.1: Influence of Included Angle, 18 Thread Models

While it is necessary to reduce strains in the forming thread, to ensure that defect occurrence is reduced it is also necessary to ensure that the magnitude of effective stress at the thread root is not decreased significantly. This is due to the fact that cold rolled fasteners rely on residual compressive stresses at the thread root to produce good fatigue properties. It can be seen from Table 5.1 that both these criteria are met.

Four Thread Included Angle Models

After the initial modelling of the new included angle die designs had been completed, it was decided to examine these designs in more detail. The initial models only investigated the results at the fully formed thread position. Since shear bands and internal defects are most probably created at the start of the deformation process, more detail was required from results obtained during this stage of the thread rolling process.

The standard included angle (60 degrees) and the two new included angle designs investigated previously were used again, namely, 90, and 120 degrees. In each of these designs the R2 value remained constant at 0.2438mm (0.0096in.). The stresses, strains, and strain rates generated throughout the thread rolling process are illustrated in the next three sections using a special technique known as "Point Tracking". Figures 5.10 & 5.11 show the Initial and Intermediate positions of the ten tracking points used to investigate the finite element results in greater detail. Thread height is used as the measurement of the progression of thread formation through the deformation process. The tracking points are set-up in a very particular manner. Point 1 is situated directly beneath the apex of the crest radius while point 10 is exactly half way between two thread crest radii.

At this juncture it should be noted that some anomalies in the contour bands can be seen in certain figures. This is a facet of the rezoning procedure (Section 3.2.3), which occurs at stages during the finite element simulations. The rezoned mesh may not have a perfectly symmetric distribution and this will lead to small differences in the stress, strain, etc. distributions shown in the upcoming figures. The reader is asked to refer to the graphs within the relevant sections for actual stress, strain, and strain rate magnitudes at the tracking points.

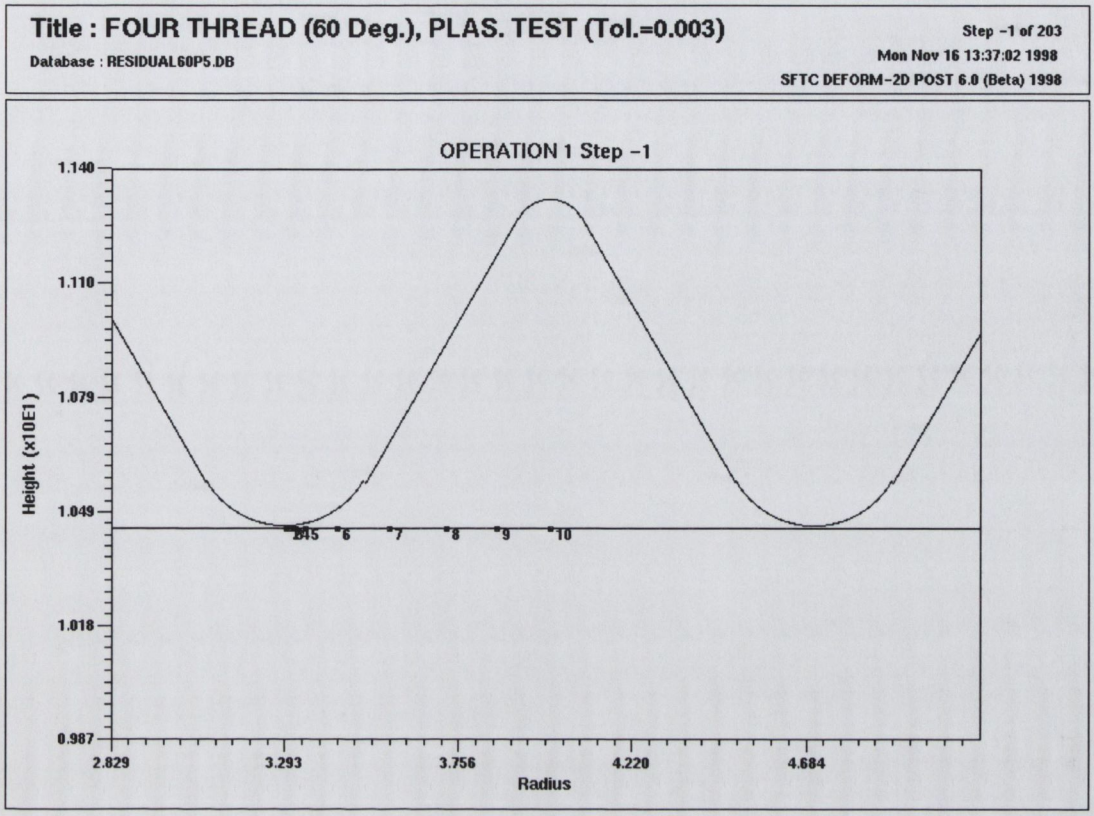

Figure 5.10: Initial Tracking Point Positions

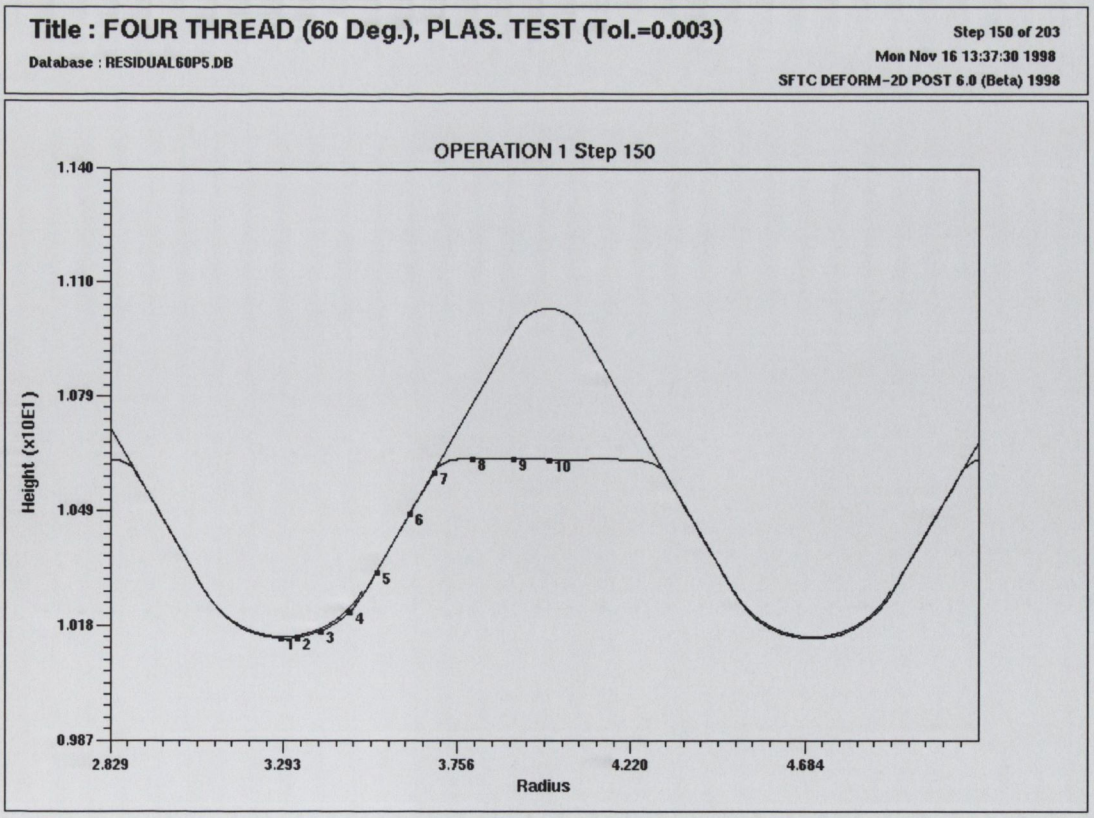

Figure 5.11: Intermediate Tracking Point Positions

5.3.1 Effective Stress Results

This section will describe the effective stress results obtained from the new included angle designs, at three stages in the thread formation process corresponding to thread heights of 0.09mm, 0.44mm, and 0.84mm respectively. In these models a fully formed thread is assumed to have a height of 0.88mm (0.03465in.) from thread root to crest.

Thread Height= 0.09mm

It can be seen from Figure 5.15 that the effective stress is constant between points 1 - 6, at approximately 1525 N/mm^2 for all three included angle designs. In all the models these points are in contact with the flank of the thread form, as can be seen in Figures 5.12, 5.13, and 5.14. A rapid decrease in the magnitude of the stress occurs between points 6 and 7, because this is the point at which contact between the deforming material and the flank of the thread form ends. Point 7 is on the free surface but close to the deformation zone. Points 8 - 10 are on the free surface so the stress is lower and constant, approximately = 1200 N/mm^2, indicating that while the material in this region is not in contact with the flank of the thread form, it is still under stress. This is due to the fact that the deforming material is being squeezed into the diminishing width of the thread form (see section 1.5).

It can be seen from the effective stress curves in Figure 5.15, that there is little or no change in the magnitude of the effective stress between the different included angle designs at this early stage of the thread formation process. The crest radius (R2) of 0.24384mm (0.0096in.) which was applied to all the designs, seems to be the controlling feature at this early stage of thread formation. The depth of deformation is constant in all the designs and equal to 0.679mm.

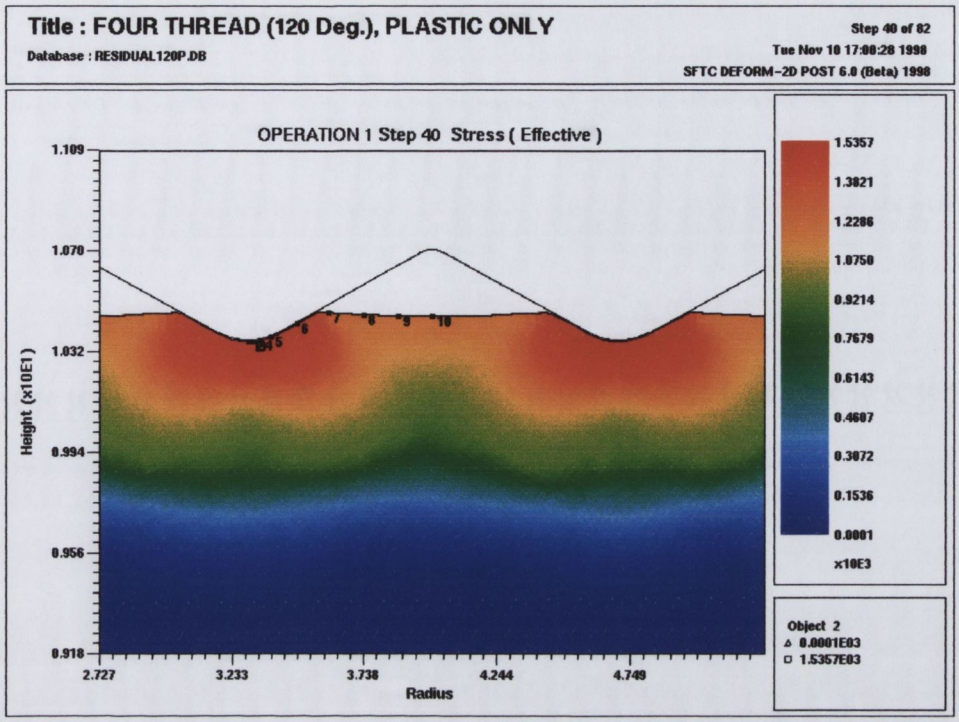

(Maximum: 1536 N/mm^2, Minimum: 0 N/mm^2)

Figure 5.12: Effective Stress at 0.09mm, 120 Degree Included Angle Design

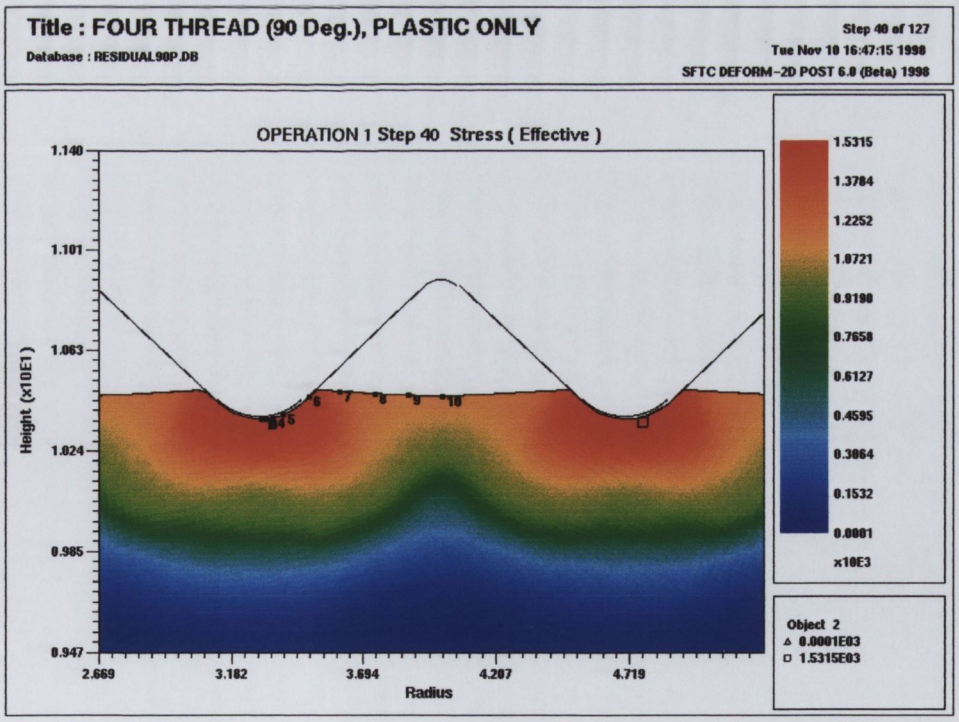

(Maximum: 1532 N/mm^2, Minimum: 0 N/mm^2)

Figure 5.13: Effective Stress at 0.09mm, 90 Degree Included Angle Design

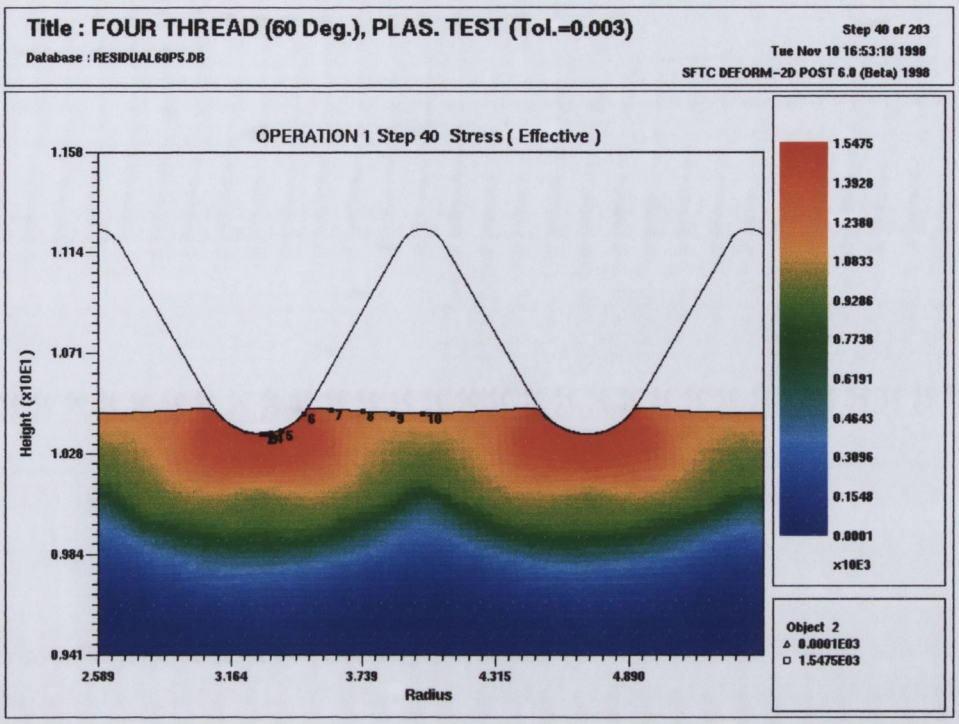

(Maximum: 1547 N/mm^2, Minimum: 0 N/mm^2)

Figure 5.14: Effective Stress at 0.09mm, Standard 60 Degree Included Angle

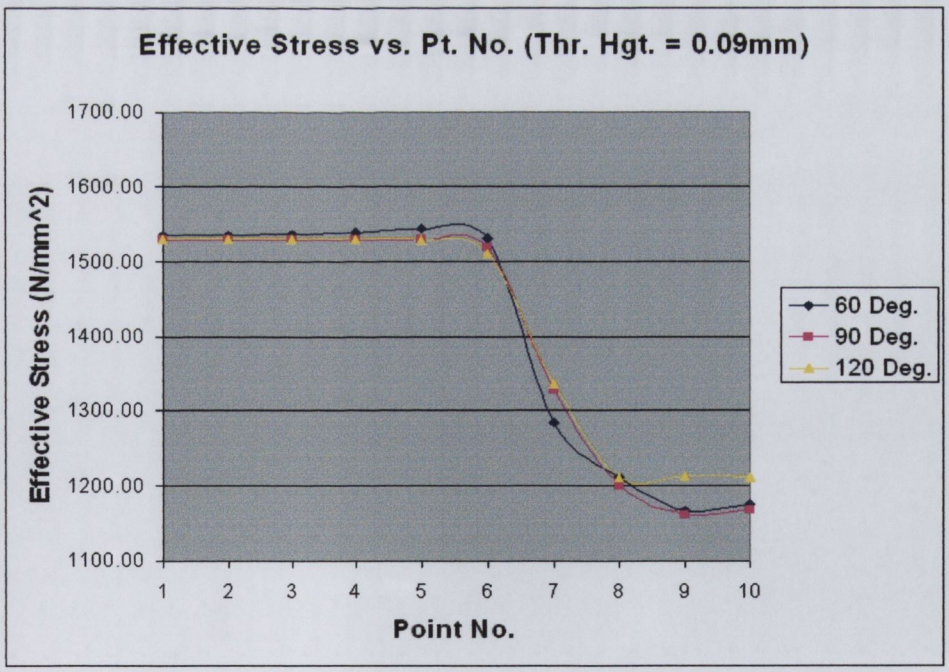

Figure 5.15: Effective Stress vs. Pt. No., Thread Height = 0.09mm

Thread Height = 0.44mm

In the last chapter (section 4.1.5) it was explained that the larger the included angle, the smaller the thread height that can be produced using a given thread form. This feature implies that there is a maximum amount of deformation that can be achieved with the new larger included angle die designs. After this maximum thread height has been achieved deformation must be continued in a smaller included angle section of the thread rolling die to produce further thread height. Since the final thread form has to have a 60 degree included angle, the new designs must have a transition region leading into the standard 60 degree thread form.

Figure 5.16 shows the 120 degree included angle design, and with this die design, only 0.3556mm of thread formation (Completed Thread Height = 0.88mm) can be performed before it must be transferred to the standard 60 degree included angle section of the die to produce the final formed thread height of 0.88mm. This feature can be seen quite clearly in the figure. By 0.44mm thread formation, points 1-6 are in contact with the flank of the thread form, there is then a rapid drop in the effective stress between point 7 and point 8 where the material previously in contact with the flank of the 120 degree thread form is now on the free surface.

In the case of the 90 degree included angle design, Figure 5.17, which has not yet been transferred to a standard 60 degree included angle, full contact occurs up until a point between 8 and 9, while points 9 & 10 are still on the free surface. The magnitude of the stress at all tracking points appears to be constant, between 1500 & 1600 N/mm^2. The deformation of the material at this stage is almost at the point where transfer to the standard 60 degree form must take place.

In the standard 60 degree included angle die design, Figure 5.18, contact between the deforming fastener material and the thread rolling die occurs until just after point 7. It can be seen that for the standard form a drop in effective stress occurs between points 8 and 9 but rises again slightly at point 10, which is on the free surface.

The maximum effective stress occurs at the same point (point 1) in all three included angle designs. This point is at the apex of the crest radius (R2) on a thread form

of the thread rolling die. The deforming material in this region experiences the greatest compression while simultaneously experiencing tensile stresses within the material flowing to form the thread.

One interesting phenomenon of the standard thread rolling process (60 degree included angle) occurs at point 5 where there is a dip on the effective stress curve shown in Figure 5.20. This phenomenon is also very evident in the effective stress plot for this model (Fig. 5.18) where a small region of lower stress (blue/green contour) can be seen in contact with the flank of the thread form at point 5. This phenomenon is caused by the different regions of material flow within the forming thread, as illustrated clearly in the vector plot of Figure 5.19.

As in the previous section there is little significant difference in the effective stress results between the three included angle designs, Figure 5.20. Differences can be seen in the curves after point 7 where the amount of deformed material on the free surface varies between the three designs at this stage of thread formation and this is reflected in differences in the effective stress curves.

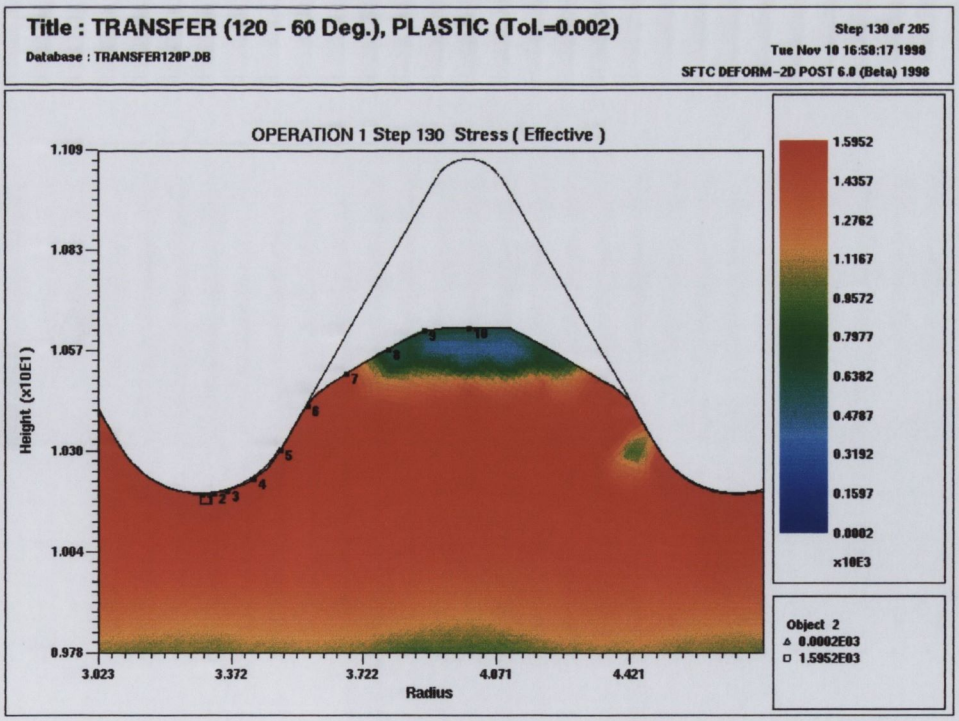

(Maximum: 1595 N/mm^2, Minimum: 0 N/mm^2)

Figure 5.16: Effective Stress at 0.44mm, 120 Degree Included Angle Design

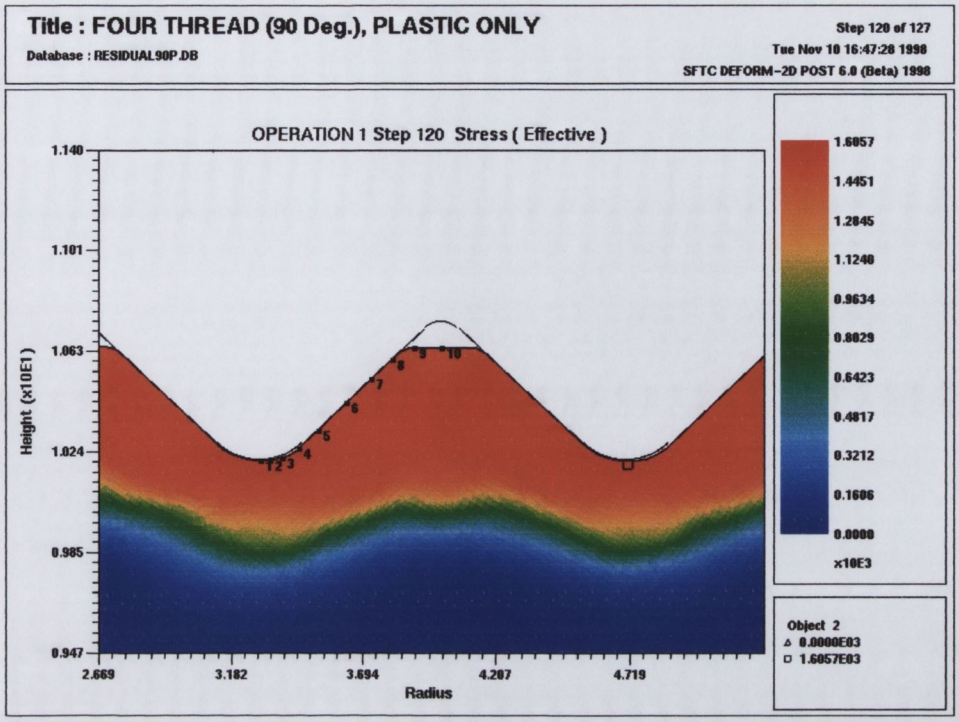

(Maximum: 1606 N/mm^2, Minimum: 0 N/mm^2)

Figure 5.17: Effective Stress at 0.44mm, 90 Degree Included Angle Design

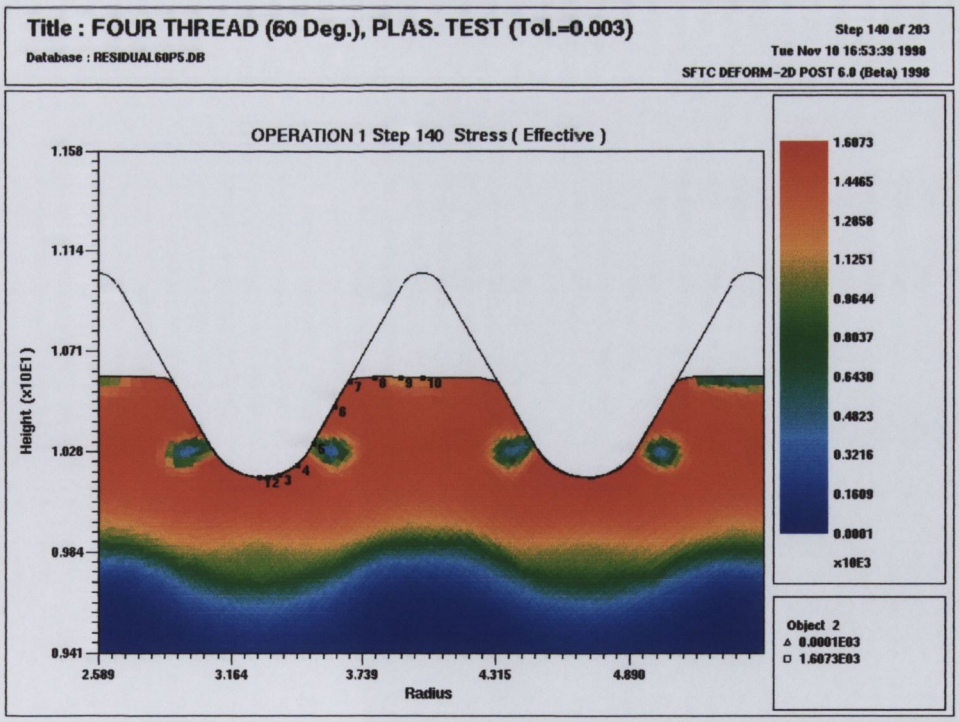

(Maximum: 1607 N/mm^2, Minimum: 0 N/mm^2)

Figure 5.18: Velocity vectors at 0.44mm, Standard 60 Degree Included Angle

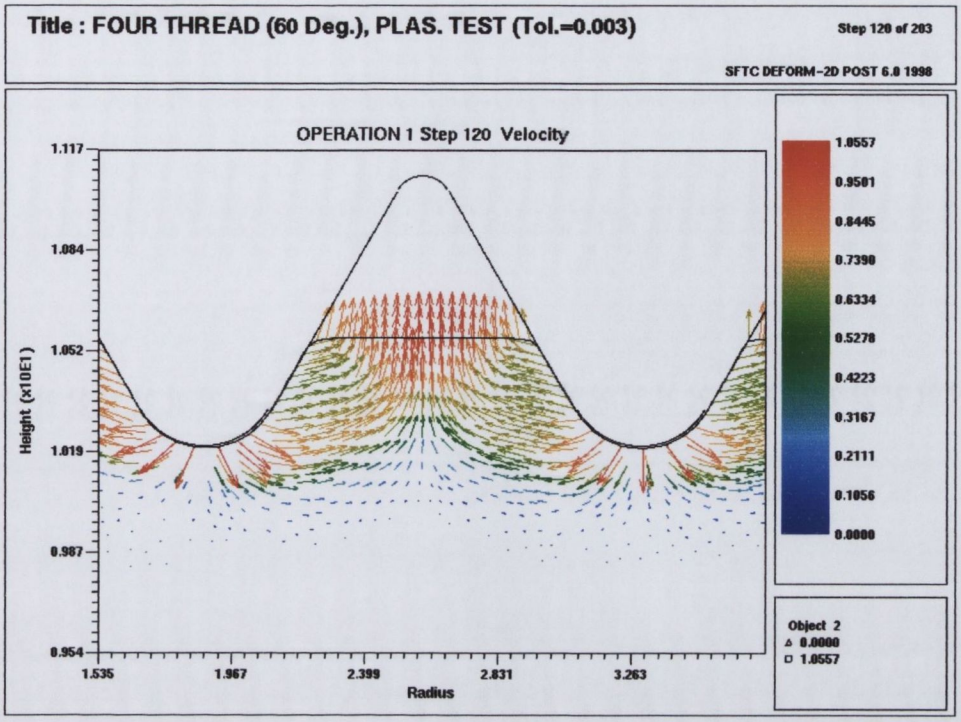

Figure 5.19: Velocity vectors at 0.44mm, Standard 60 Degree Included Angle

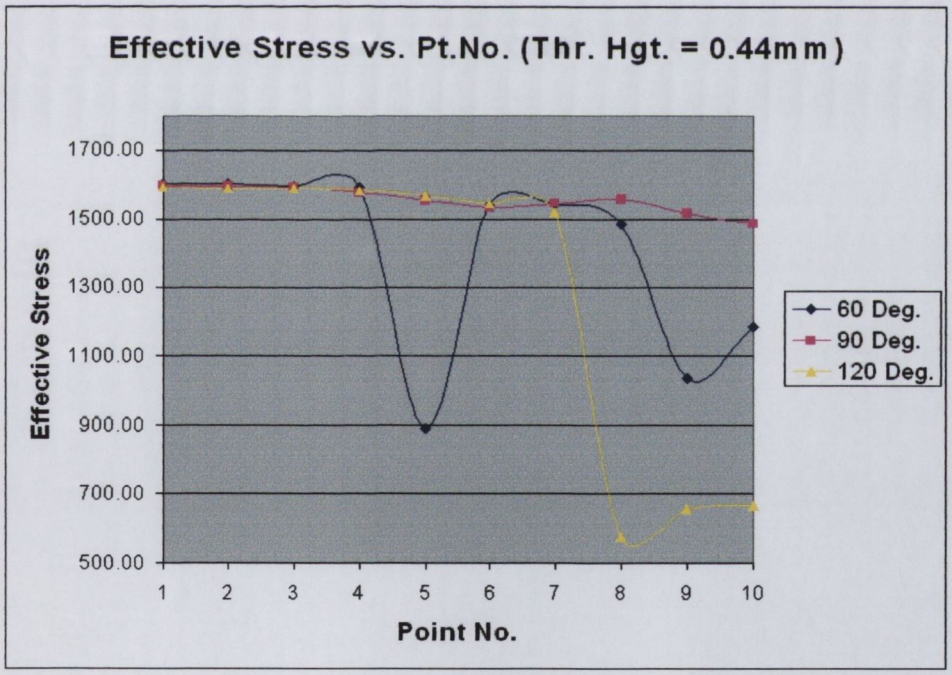

Figure 5.20: Effective Stress vs. Tracking Point No., Thread Height = 0.44mm

Thread Height = 0.84mm

By this stage of thread formation (close to full formation) the deformed material in both the larger included angle die designs (90 & 120 degree) has been transferred to the standard 60 degree thread form (Figures 5.21 and 5.22). The results for the standard 60 degree thread form can be seen in Figure 5.23. As before the maximum effective stress still occurs at point 1 (apex of crest radius (R2)) in all three included angle die designs, though the magnitude does vary slightly (1610 N/mm^2 for 60 degree vs. 1580 N/mm^2 for the 120 & 90 degree designs).

The change in effective stresses over the tracking points (1-10) at this level of thread formation can be seen from the curves in Figure 5.24. The 120 & 90 degree included angle designs both indicate a slightly lower effective stress within the rolled thread but all included angle designs display similar distributions over the tracking points. However, the decrease in the magnitude of the effective stress is small and should not have a significant effect on the fatigue properties of the fastener. All the included angle designs also show a "low" stress region between points 4 to 6 on the flank which are above the root, but below the pitch line of the formed thread and are illustrated as a lighter orange/yellow region in Figures 5.21 and 5.22.

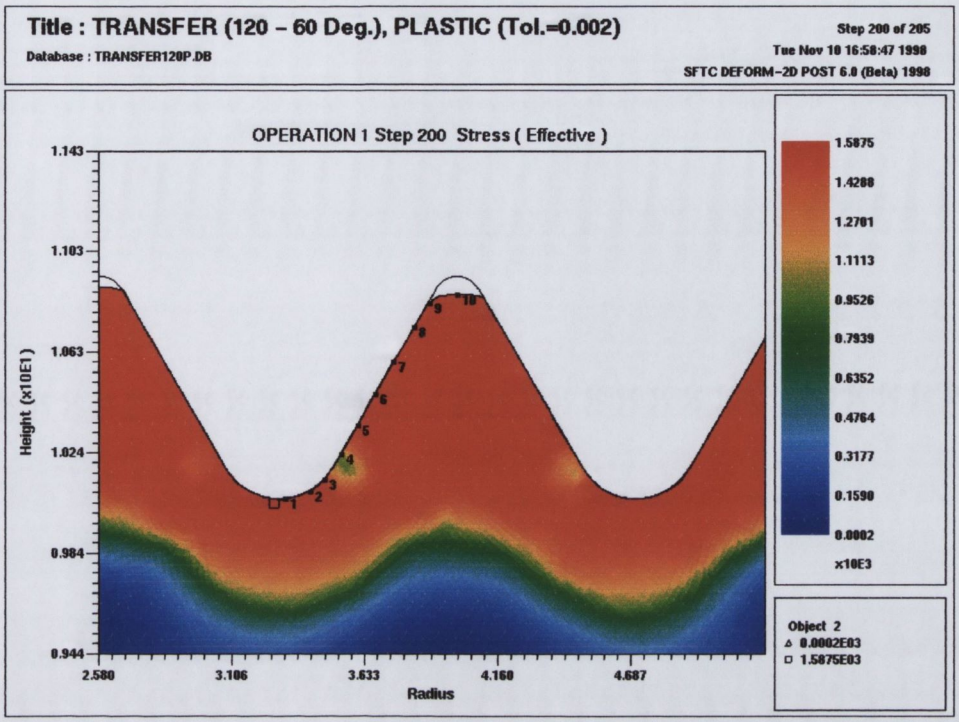

(Maximum: 1587 N/mm^2, Minimum: 0 N/mm^2)

Figure 5.21: Effective Stress at 0.84mm, 120 Degree Included Angle Design

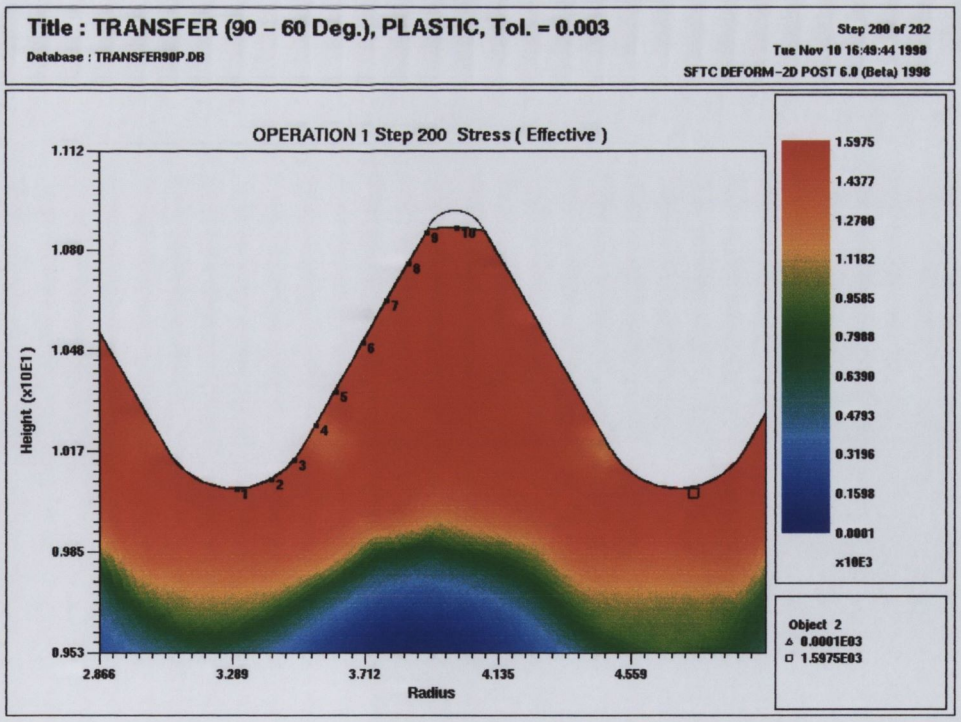

(Maximum: 1597 N/mm^2, Minimum: 0 N/mm^2)

Figure 5.22: Effective Stress at 0.84mm, 90 Degree Included Angle Design

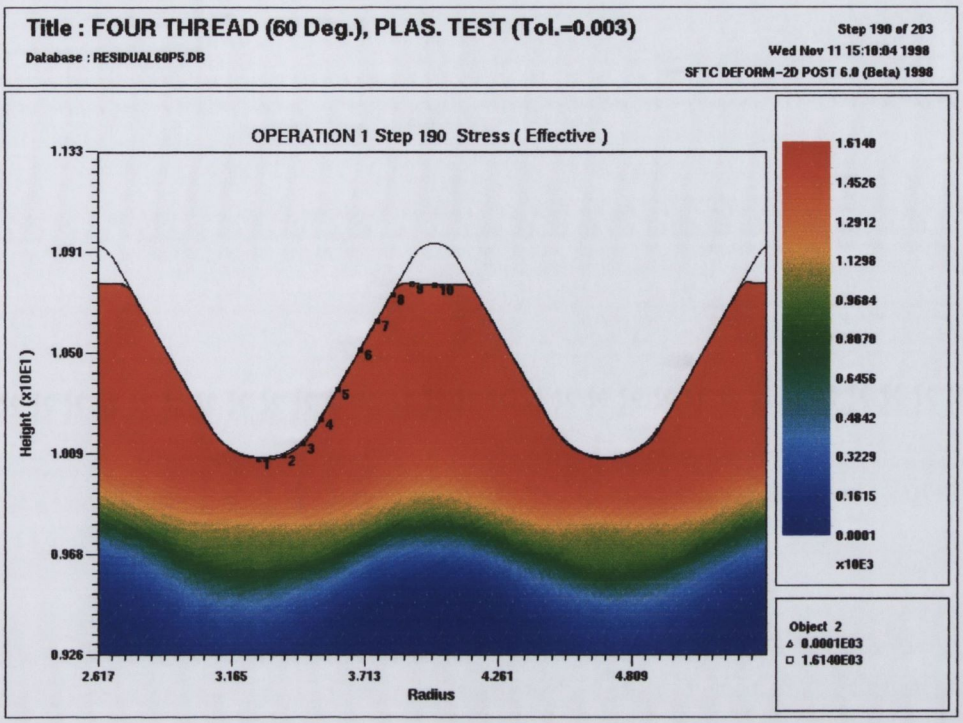

(Maximum: 1614 N/mm^2, Minimum: 0 N/mm^2)

Figure 5.23: Effective Stress at 0.84mm, Standard 60 Degree Included Angle

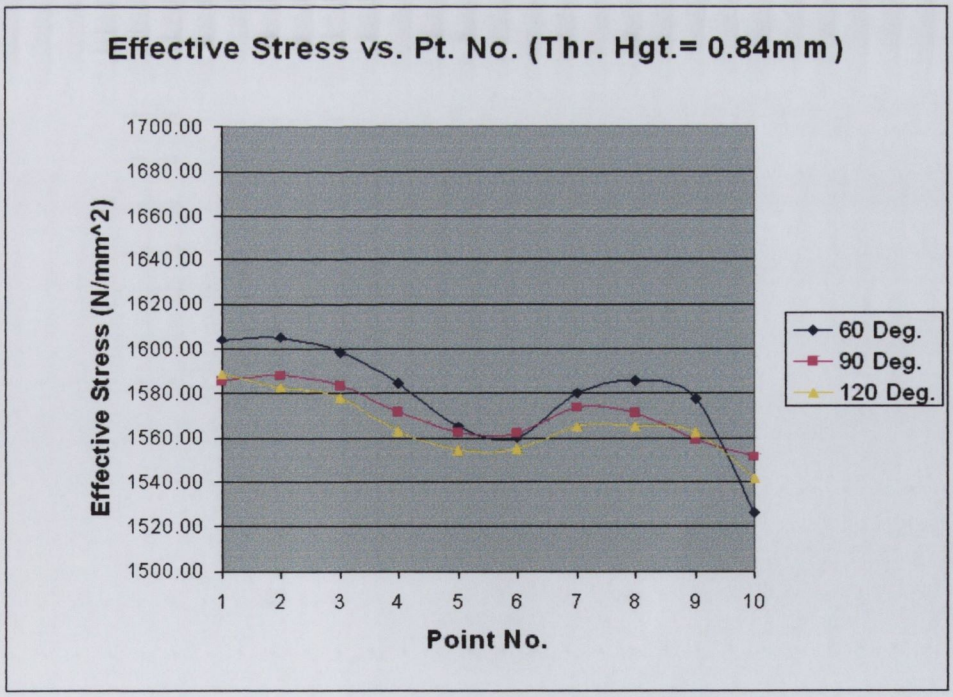

Figure 5.24: Effective Stress vs. Tracking Pt. No., Thread Height = 0.84mm

5.3.2 Effective Strain Results

Thread Height = 0.09mm

While effective stress can influence residual stresses at the thread root it is the effective strain distribution which has the greatest effect on the occurrence of defects.

Figures 5.25 and 5.26 show the effective strains for the 120 & 90 degree included angle designs respectively at this early stage in the deformation process. As in the case of the effective stress results, the maximum effective strain occurs in a very concentrated region at the apex of the crest radius on the thread form. Figure 5.27 shows the effective strain for the standard 60 degree form. All the designs indicate similar effective strain distributions both in magnitude and area of effect. It should be noted that these regions of high strain correspond very closely to the regions where shear banding occurs in Figures 5.28

The graph in Figure 5.29 confirms that all three designs produce very similar magnitudes of effective strains at all the tracking points, with the 120 & 90 degree designs being marginally lower than the 60 degree design. The trends of the effective strain over the tracking points are also very similar for all three die designs. In each case the maximum effective strain is ≈ 0.6 and occurs between points 1-6 dropping between points 6 and 7 to a value less than 0.1 and remains at this value for the remainder of the tracking points. It can be seen from Figure (5.25) that this rapid drop in the magnitude of the effective strain between points 6 and 7 is caused by the fact that the material is no longer in contact with the tool. Points 7-10 show a very low strain $\approx$ 0.1. These results confirm those seen for effective stress at the early thread formation stage. That is that while the included die angle is having a small effect the crest radius (R2) of 0.2438mm (0.0096in.) on each thread form is having the dominant effect.

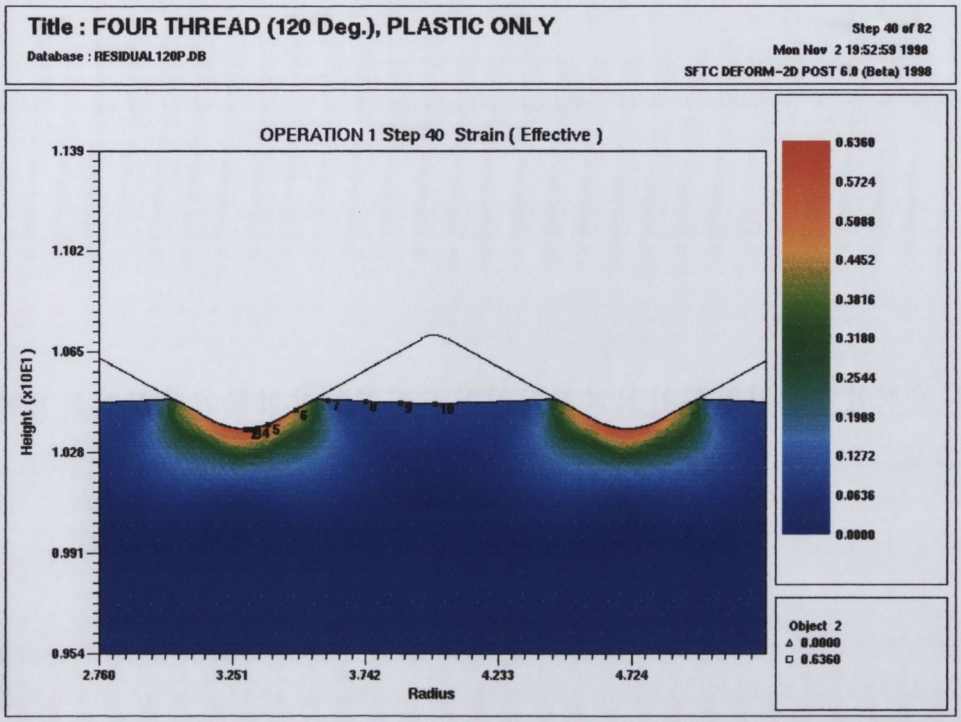

(Maximum: 0.636, Minimum: 0)

Figure 5.25: Effective Strain at 0.09mm, 120 Degree Included Angle Design

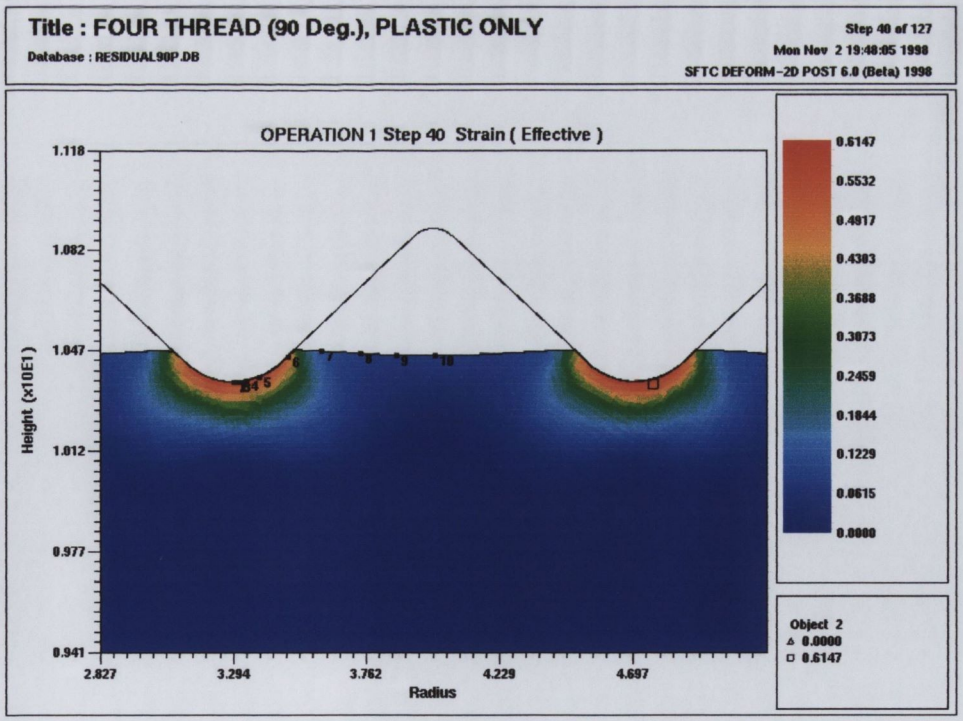

(Maximum: 0.6147, Minimum: 0)

Figure 5.26: Effective Strain at 0.09mm, 90 Degree Included Angle Design

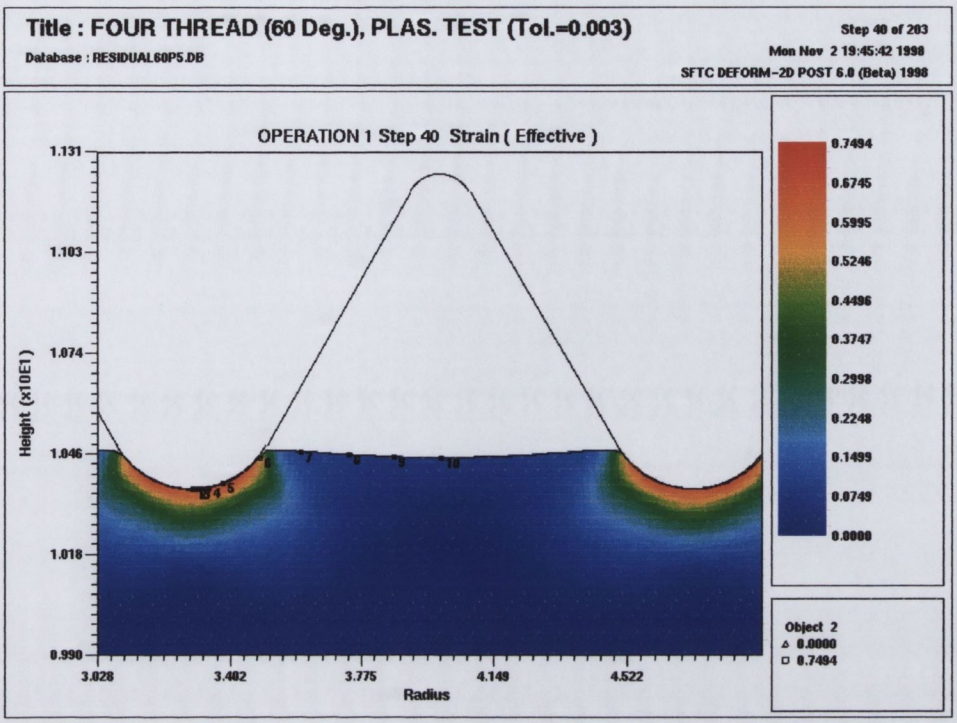

(Maximum: 0.7494, Minimum: 0)

Figure 5.27: Effective Strain at 0.09mm, Standard 60 Degree Included Angle

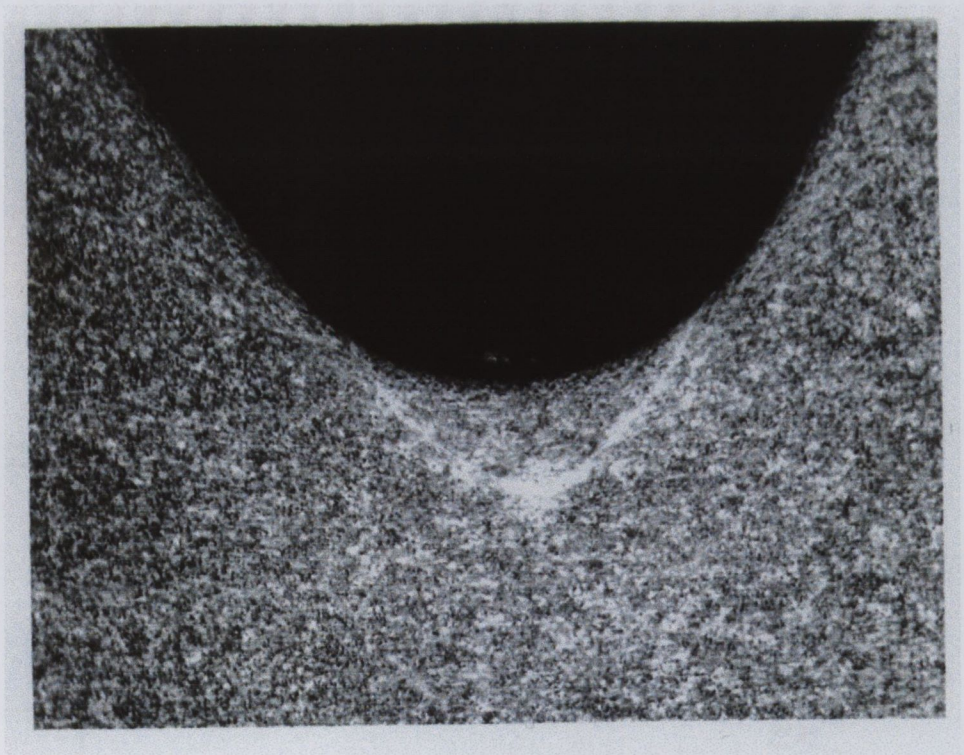

Figure 5.28: Thread Root Shear Band

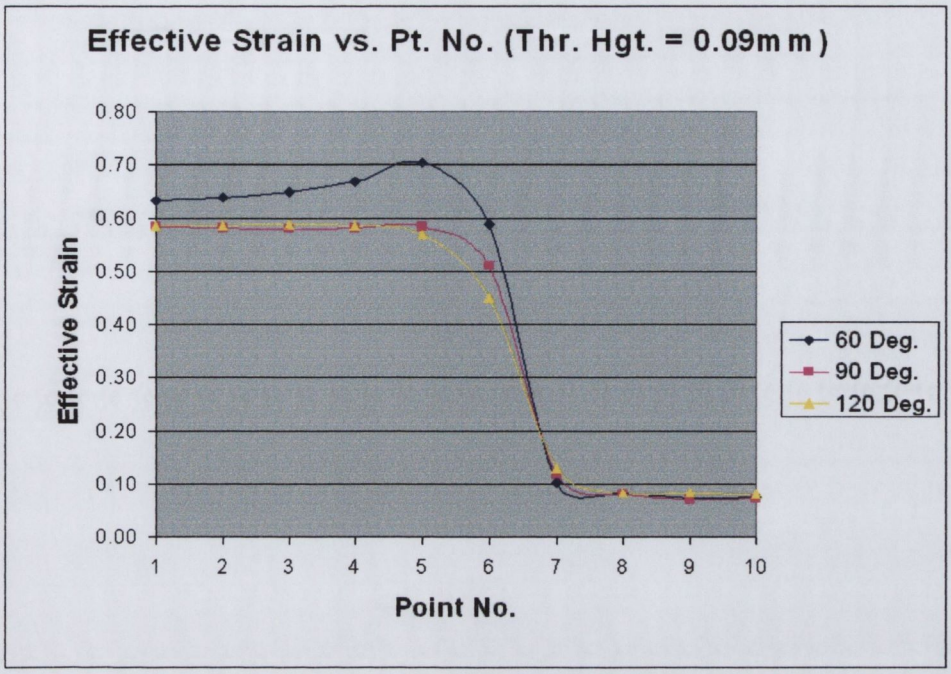

Figure 5.29: Effective Strain vs. Tracking Pt. No., Thread Height = 0.09mm

Thread Height = 0.44mm

Figures 5.30 and 5.31 show the effective strain distributions for the 120 degree & 90 degree included angle die designs respectively for this level of thread formation. The material from the 120 degree included angle die design has passed its transfer point and is shown being deformed by the standard 60 degree form. The effective strain distribution in this design looks very similar to the effective strain distributions shown in the previous section. The strain is at a maximum beneath the apex of the crest radius (point 1), dropping away to a minimum at the top of the forming thread (point 10). The effect of the 120 degree included angle design can be seen on the forming thread at points 7-9 where the material slopes away from the flank of the thread form.

In the case of the 90 degree included angle design, it can be seen from Figure 5.31, that a thread height of 0.44mm has almost fully filled the die cavity. The strain in this case follows a similar trend to that of the 120 degree included angle design as shown in the graph given in Figure 5.33.

The standard 60 degree form, Figure 5.32, also shows a similar trend in effective strain to the previous two designs. Bands of strain are evident extending at 45 degrees from the points where contact between the material and the flank of the thread form finishes and in towards the centre of the forming thread.

The magnitude of the strain of 1.5 has increased significantly from 0.6+ at the earlier thread formation stage of 0.09mm. However it should be noted that all these strain values should only be viewed as qualitative rather than quantitative. The maximum strain occurs over points 1-5, and there is a gradual drop from $\approx$ 1.5 at point 1. It can be seen that the effective strain drops for both the standard 60 degree and the 90 degree included angle die designs to $\approx$ 0.6. The 120 degree included angle design has a continuous drop from 1.5 to $\approx$ 0.4.

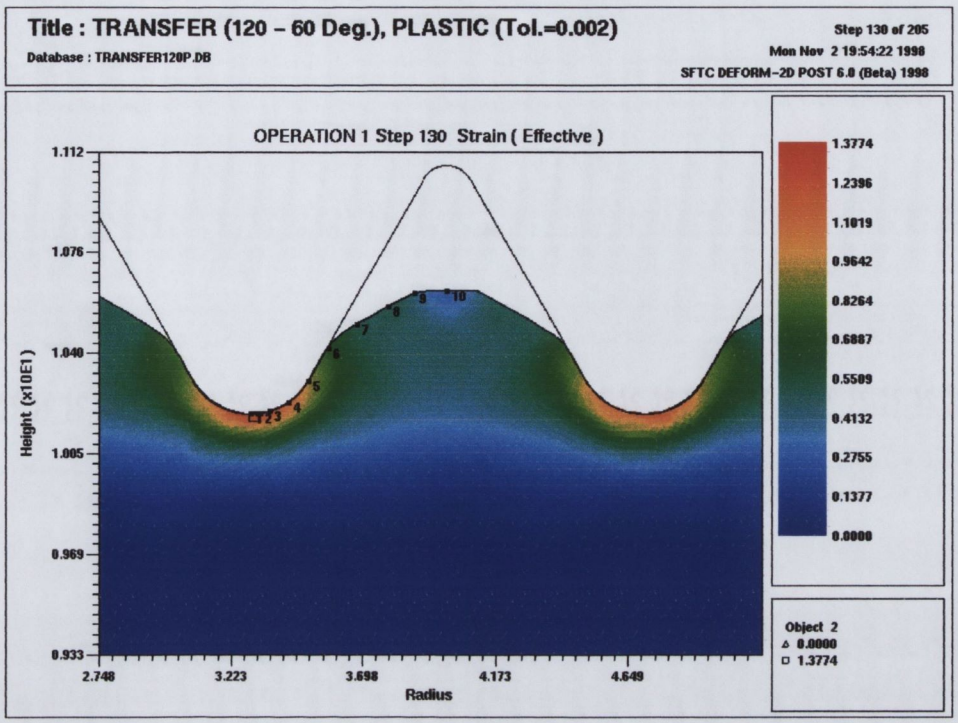

(Maximum: 1.3774, Minimum: 0)

Figure 5.30: Effective Strain at 0.44mm, 120 Degree Included Angle Design

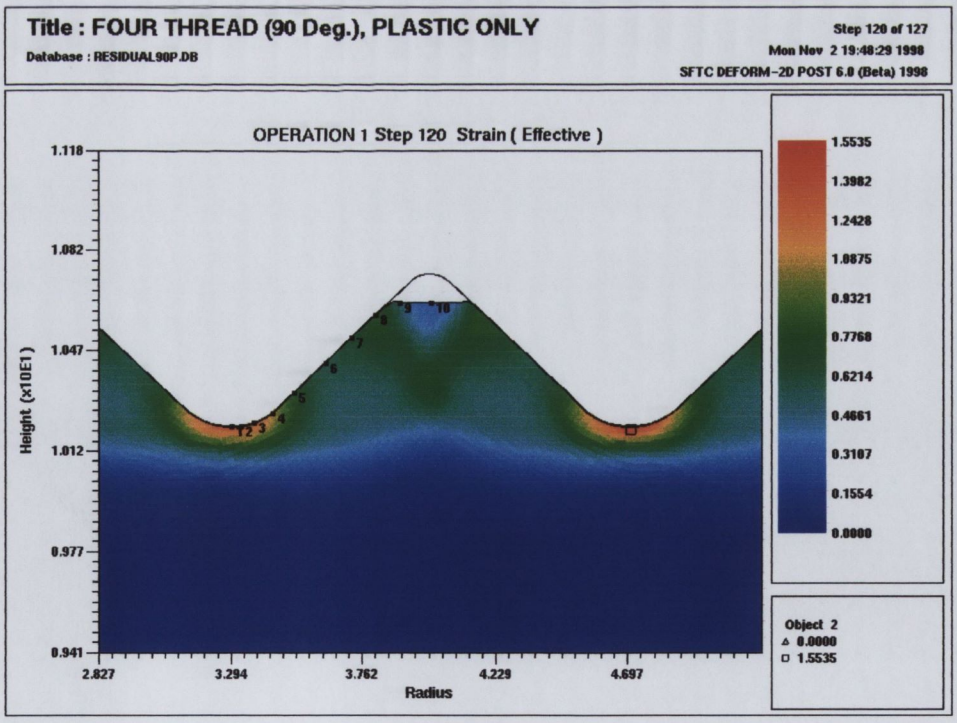

(Maximum: 1.5535, Minimum: 0)

Figure 5.31: Effective Strain at 0.44mm, 90 Degree Included Angle Design

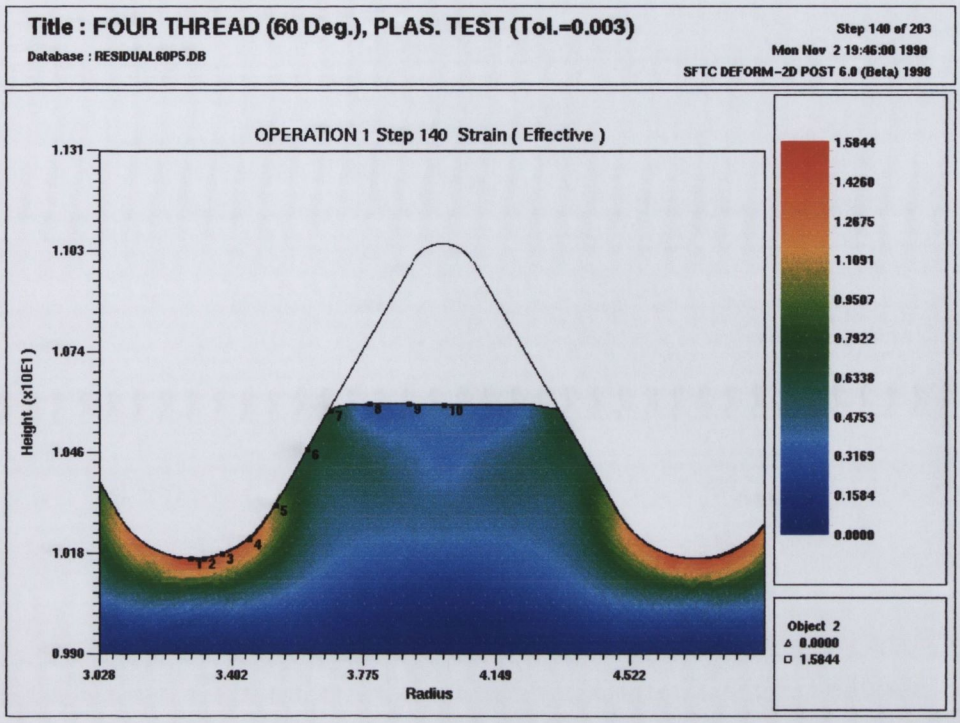

(Maximum: 1.5844, Minimum: 0)

Figure 5.32: Effective Strain at 0.44mm, Standard 60 Degree Included Angle

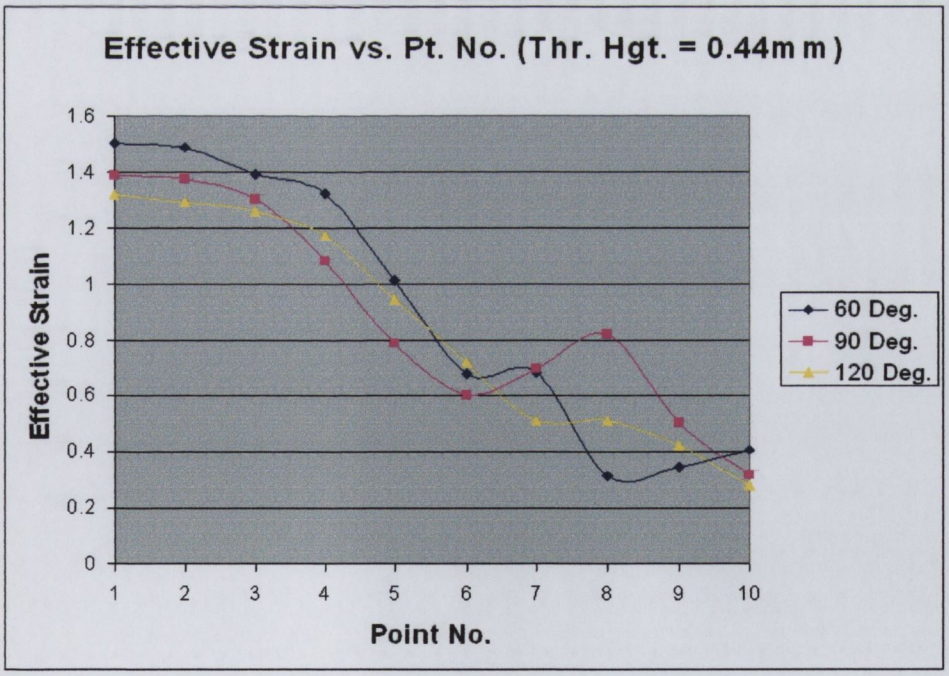

Figure 5.33: Effective Strain vs. Tracking Pt. No., Thread Height = 0.44mm

Thread Height = 0.84mm

Figures 5.34 and 5.35 show the effective strain distributions for the two new included angle die designs at a stage very close to full thread formation. Previous to this level of thread formation the 90 degree included angle design has also been transferred to the standard 60 degree form so as to enable complete thread formation.

In all three models the strain distributions extends 0.238mm into the material. The graph in Figure 5.38 indicated the trend of effective strain over the tracking points at this stage of the thread formation process. It can be seen that the magnitude of the effective strain in both the 120 & 90 degree included angle designs is considerably lower than that of the standard 60 degree form over most the tracking points. There is a drop in the level of effective strain between points 3 and 7 which is evident in the three effective strain curves, Figures 5.38.

Another feature evident from the three effective strain plots for this level of deformation is the chevron pattern that has formed in the upper portion of the formed thread (orange contour band). This area is larger and more pronounced in the 120 degree and 90 degree included angle designs but is of a lower magnitude compared to the standard 60 degree form. These bands are a progression of the strain bands noted in the earlier stage of thread formation. They also reflect the area where the whisker type shear bands develop, shown in Figure 5.37.

In the standard 60 degree thread form a maximum strain value of 1.5 is located at point 1 against a value of 1.25 with 120/90 included angle design. The minimum strain occurs at point 6 which is in the vicinity of the pitch line and is approximately equal to 0.8 for each die design. There is a rise to $\approx$ 1.0 - 1.2 over points 7-9 (above pitch line).

These results indicate that using a larger included angle at the start of a thread rolling process has a definite beneficial effect on reducing the magnitude of the effective strain values within the fastener material at the end of the thread formation process.

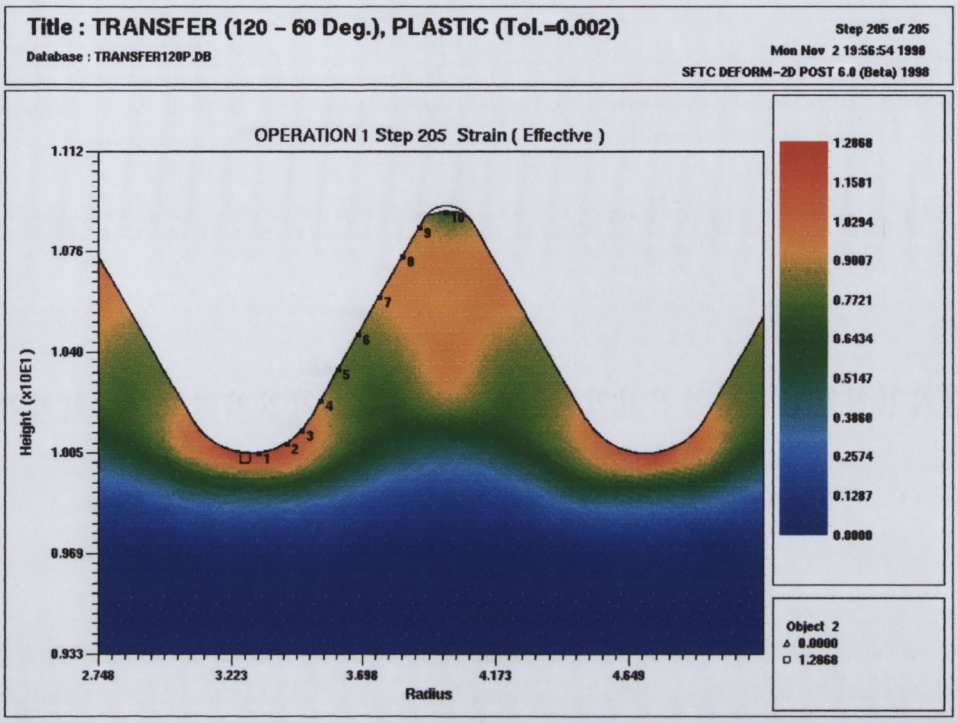

(Maximum: 1.2868, Minimum: 0)

Figure 5.34: Effective Strain at 0.84mm, 120 Degree Included Angle Design

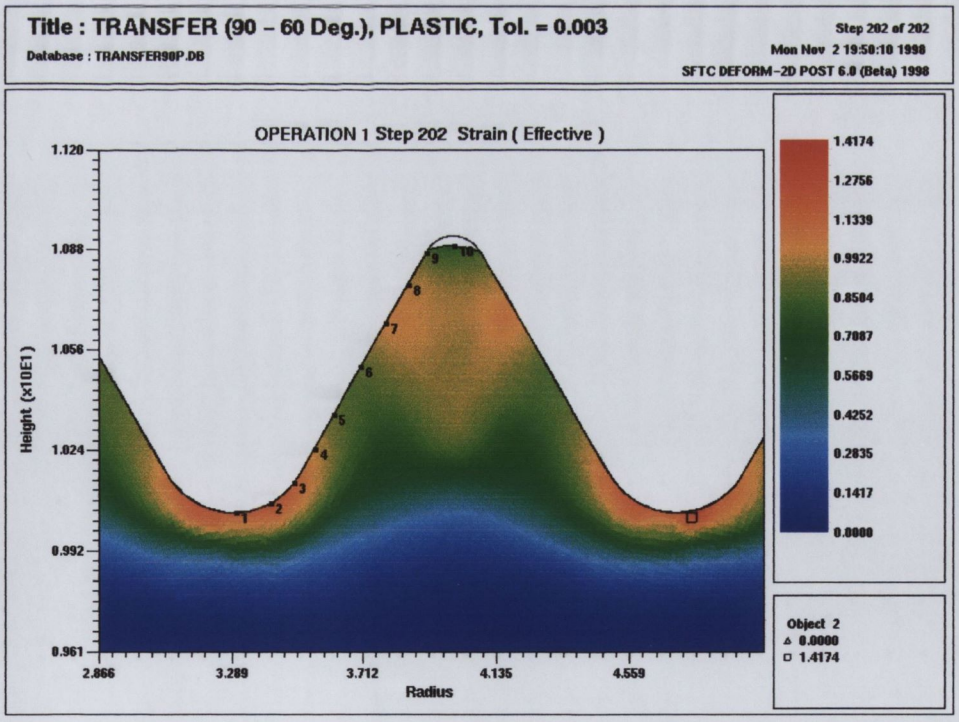

(Maximum: 1.4714, Minimum: 0)

Figure 5.35: Effective Strain at 0.84mm, 90 Degree Included Angle Design

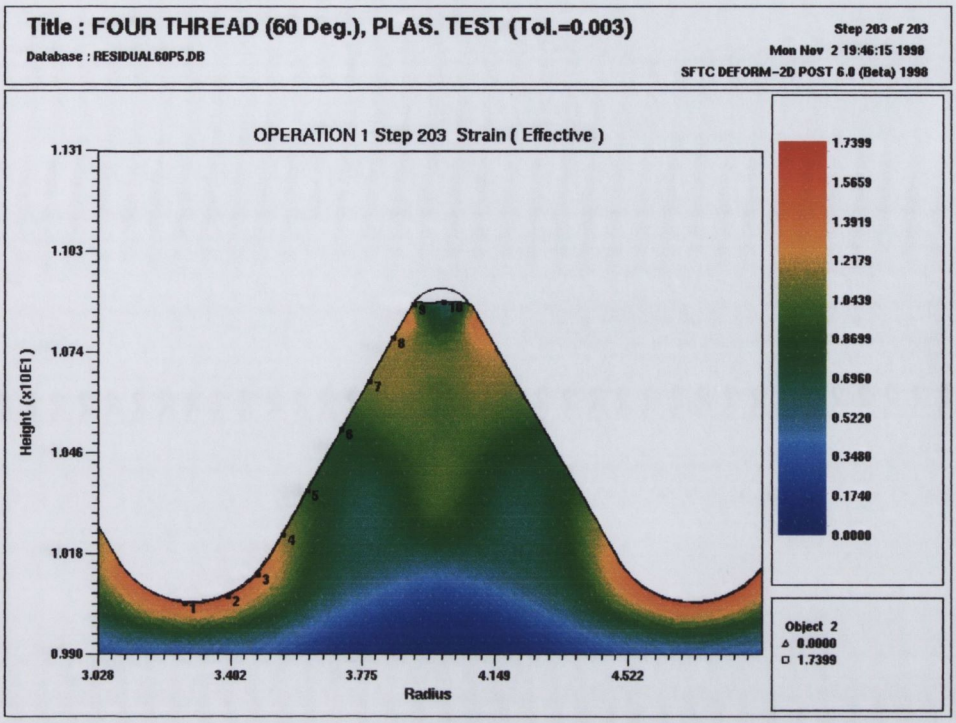

(Maximum: 1.7399, Minimum: 0)

Figure 5.36: Effective Strain at 0.84mm, Standard 60 Degree Included Angle

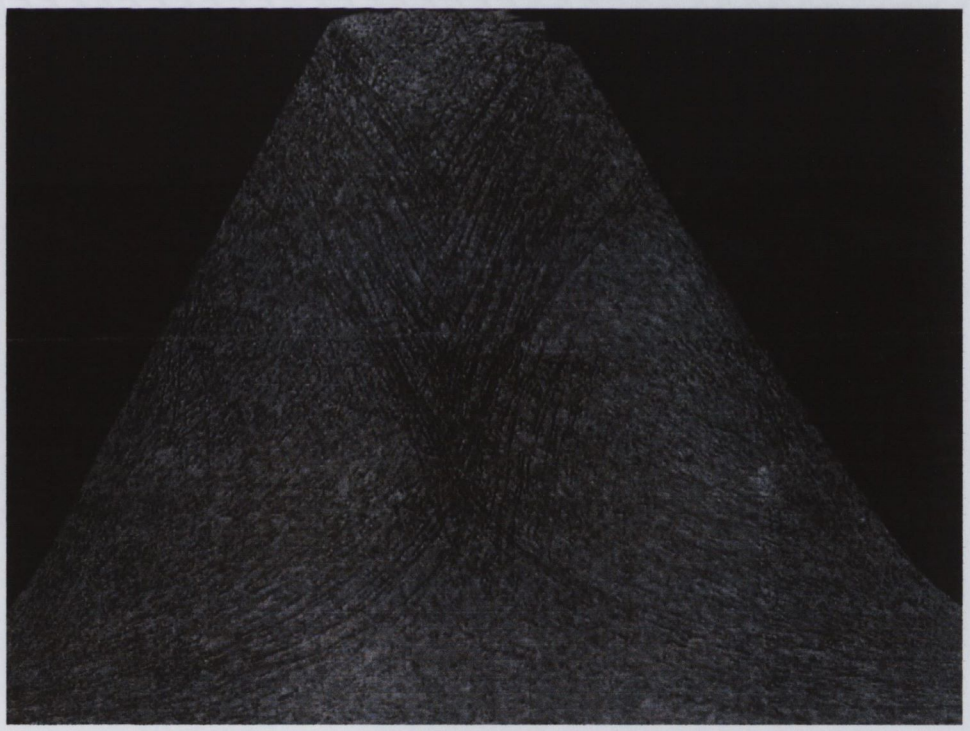

Figure 5.37: "Whisker" Type Shear Bands

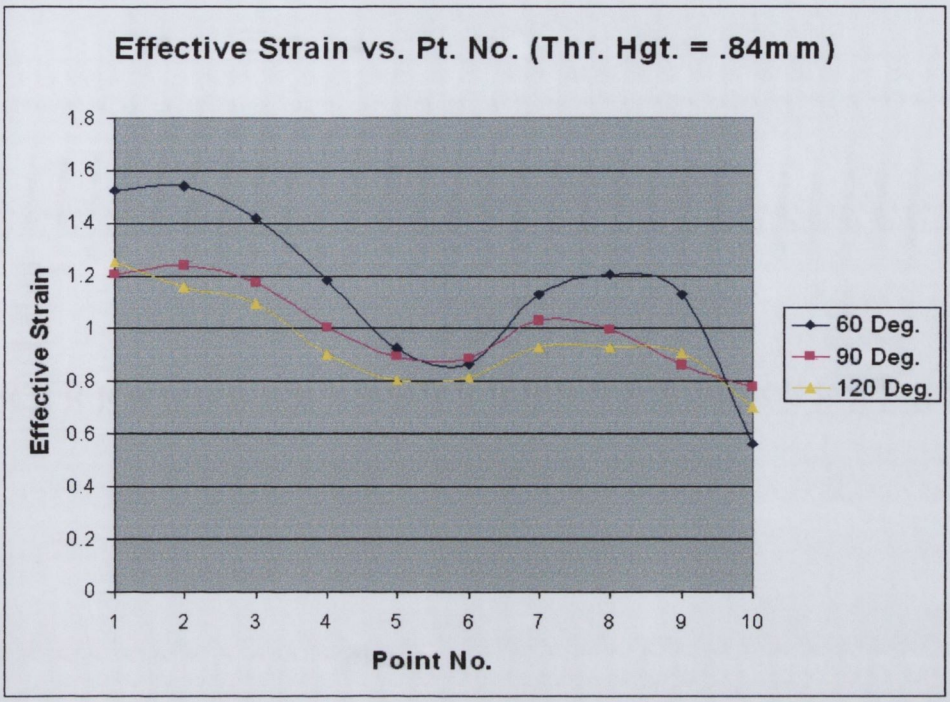

Figure 5.38: Effective Strain vs. Tracking Pt. No., Thread Height = 0.84mm

5.3.3 Effective Strain Rate Results

Strain rate results are presented in this report for a number of reasons. Titanium 6Al-4V is a known to be a strain rate sensitive material and strain rates are related to production rates. The formation of defects could be influenced by strain rate if regions of maximum strain and strain rate were to coincide.

Thread Height=0.09mm

Figure 5.39 shows the effective strain rate at a formed thread height of 0.09mm in the 120 degree included angle die design. Point 1 has a strain rate value of 7 s^{-1} but drops away quickly from point 3 to zero at point 5 but then increases again between points 6 and 7 and back to zero again at points 8-10 on the free surface. These changes in strain rate are visible in the effective strain rate plot shown in Figures 5.39 where there are three distinct areas of strain rate around the deforming crest radius. This is caused by the contact made by the larger included angle and the fastener material.

Figure 5.40 shows the effective strain rate in the 90 degree included angle die design and Figure 5.41 the effective strain rate in the standard 60 degree form. Both these designs show similar effective strain rate distributions. The smaller included angle produces a deeper area of strain rate effect and it is also more concentrated in a region directly beneath the crest radius compared to that for the 120 degree included angle die design. As in the case of the effective stress, and the effective strain, the maximum effective strain rate occurs directly beneath the apex of the crest of the thread rolling die.

From the graph in Figure 5.42 it is obvious that the strain rate values for the 90 and 60 degree included angle designs follow each other very closely. The strain rate does not drop away until a position further along the flank of the die (point 5) and they both show higher strain rates on the free surface (points 7-10) compared to the 120 degree included angle die design. Given that Ti-6Al-4V is a strain rate sensitive material this could have implications for the initiations of shear bands.

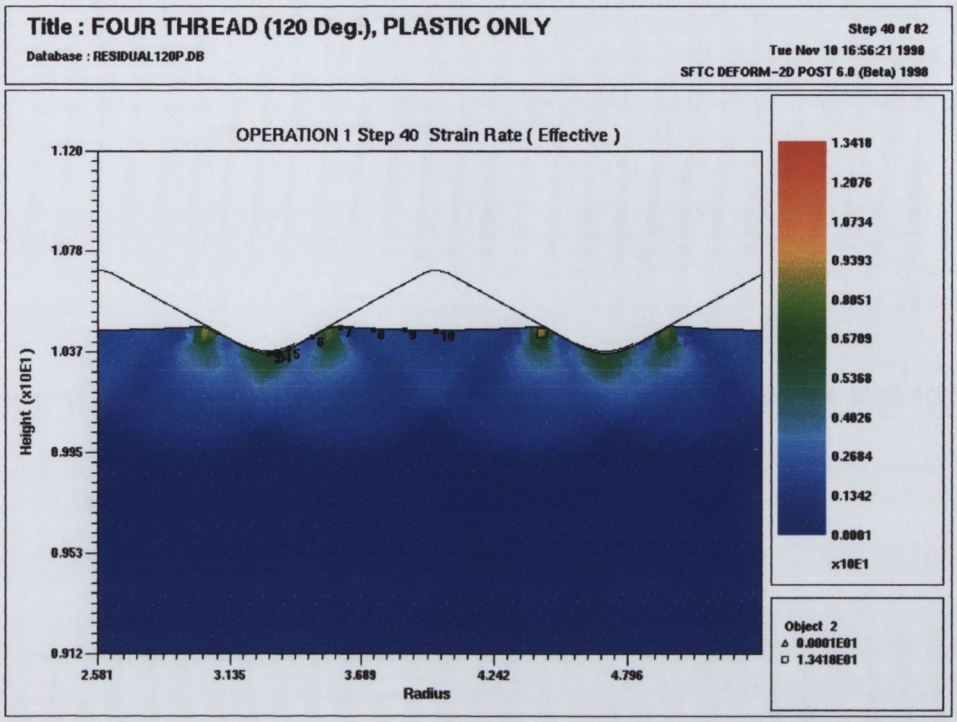

(Maximum: 13.42 s^{-1}, Minimum: 0 s^{-1})

Figure 5.39: Effective Strain Rate at 0.09mm, 120 Degree Included Angle Design

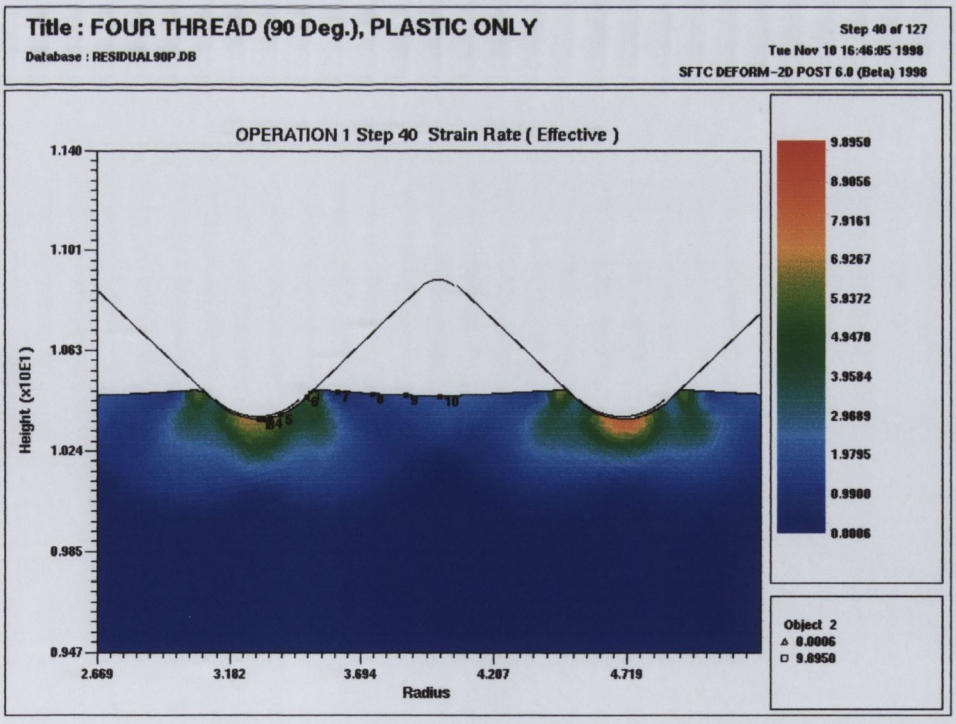

(Maximum: 9.89 s^{-1}, Minimum: 0 s^{-1})

Figure 5.40: Effective Strain Rate at 0.09mm, 90 Degree Included Angle Design

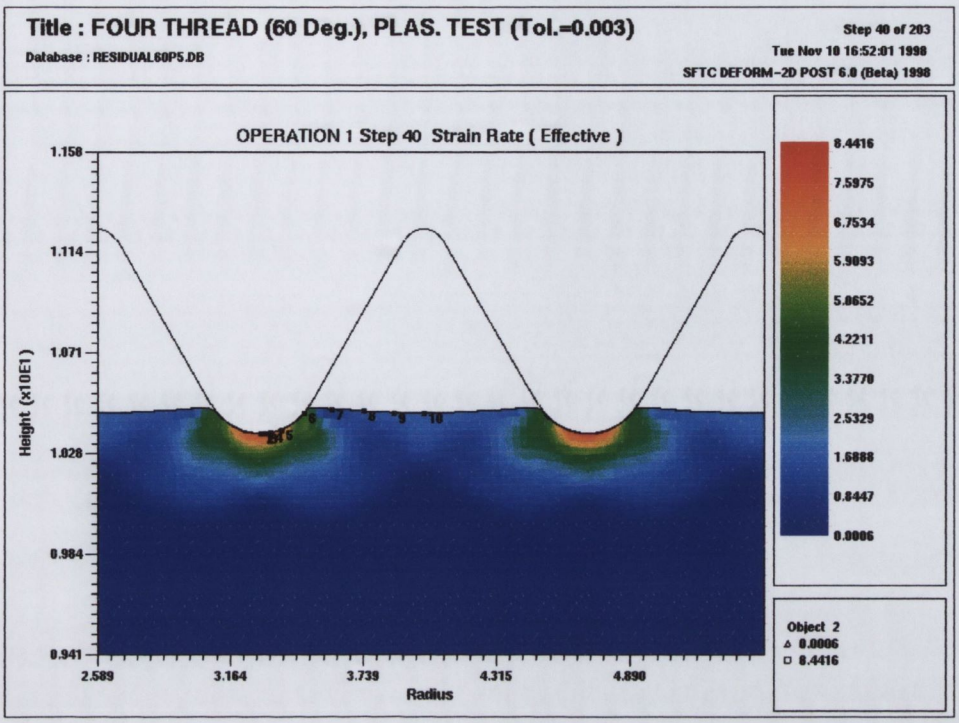

(Maximum: 8.44 s^{-1}, Minimum: 0 s^{-1})

Figure 5.41: Effective Strain Rate at 0.09mm, Standard 60 Degree Included Angle

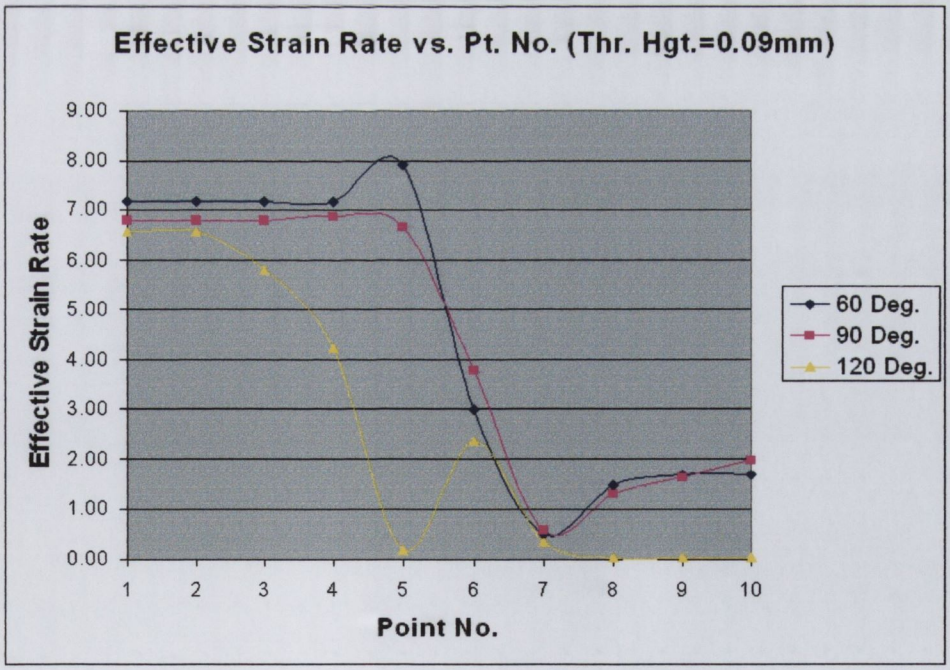

Figure 5.42: Effective Strain Rate vs. Pt. No., Thread Height = 0.09mm

Thread Height = 0.44mm

By this stage of the deformation process the material shown in Figure 5.43 for the 120 degree included angle design has been transferred to the standard 60 degree included angle thread form before this level of thread formation, and distinct banding of the strain rates is visible. They criss-cross each other extending from the last point of contact (between point 6 and 7) on the flank of the thread form to the area of maximum strain rate at the root of the forming thread (around point 1) and form what is called a *chevron* pattern. The points on the free surface experience a very low strain rate.

These patterns clearly illustrate the regions of most intense shear activity and are potential planes of weakness. In each case the maximum strain rate occurs in the fastener material close to the root of the thread which is the area where shear bands formation is the most common. It can also be seen that the strain rate bands appear to follow the regions of maximum shear stress and velocity discontinuity shown previously in Figures 2.8 and 2.9.

In the 90 degree included angle design (Figure 5.44), the banding mentioned above is not as pronounced due to the effect of the included angle. This design has almost reached the maximum formed thread height and material is being trapped or *packed* into the thread form. Strain rates increase dramatically in this region of the forming thread, where points 8-9 experience strain rates greater than 15 s^{-1} and then drop away on the small free surface area (point 10) in between the two bands of high strain rate. These bands again extend from the last contact point on the flank of the thread form to the root of the forming thread. It is possible that such high levels of strain rate in this region could contribute to the formation of internal defects above the pitch line.

In Figure 5.45, the standard 60 degree form, the strain rate distributions are similar to those of the material in the transferred 120 degree included angle die design (Figure 5.43. Again the strain rate bands form at 45 degrees from the usual initiation points. The chevron pattern is very distinct. The maximum strain rate (12 s^{-1}) still occurs at point 1 but the peak in effective strain rate at point 7 (on the 45 degree band) can

also be seen in the graph tracking the effective strain rates at the defined points, see Figure 5.46.

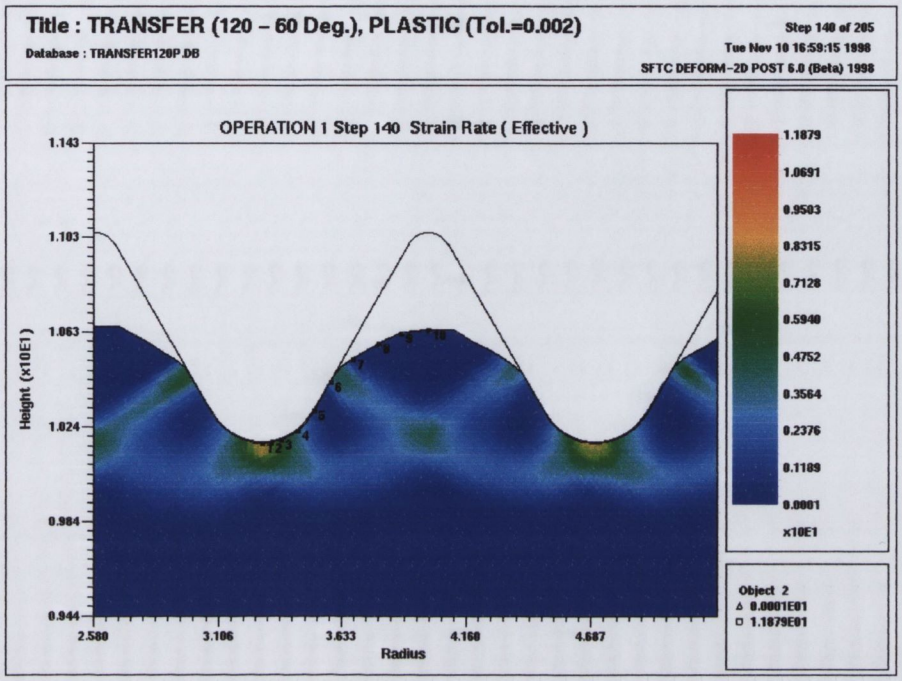

(Maximum: 11.88 s^{-1}, Minimum: 0 s^{-1})

Figure 5.43: Effective Strain Rate at 0.44mm, 120 Degree Included Angle Design

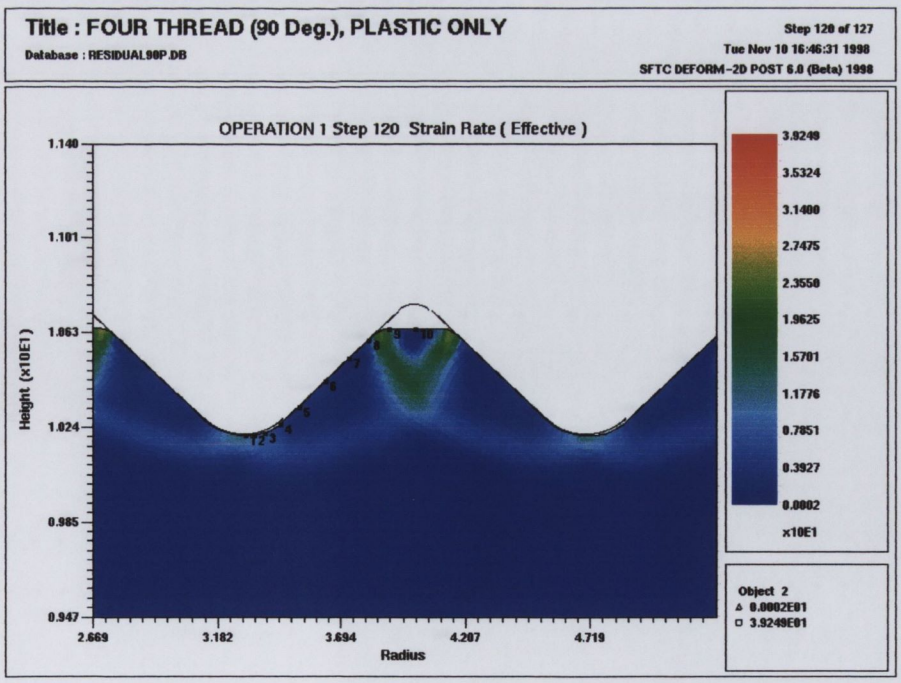

(Maximum: 39.25 s^{-1}, Minimum: 0 s^{-1})

Figure 5.44: Effective Strain Rate at 0.44mm, 90 Degree Included Angle Design

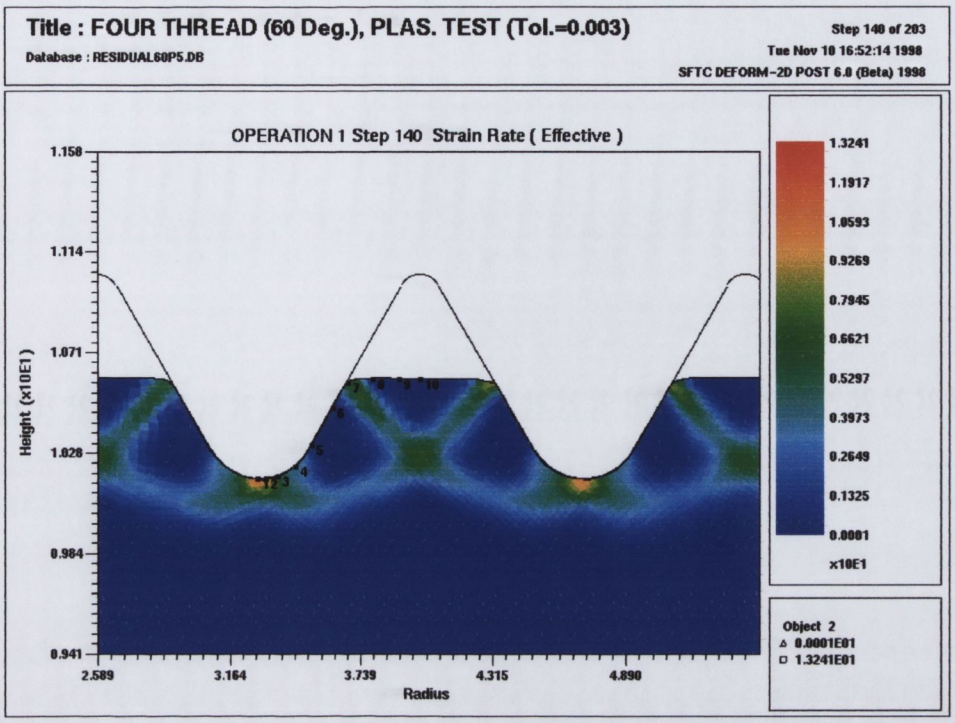

(Maximum: 13.24 s^{-1}, Minimum: 0 s^{-1})

Figure 5.45: Effective Strain Rate at 0.44mm, Standard 60 Degree Included Angle

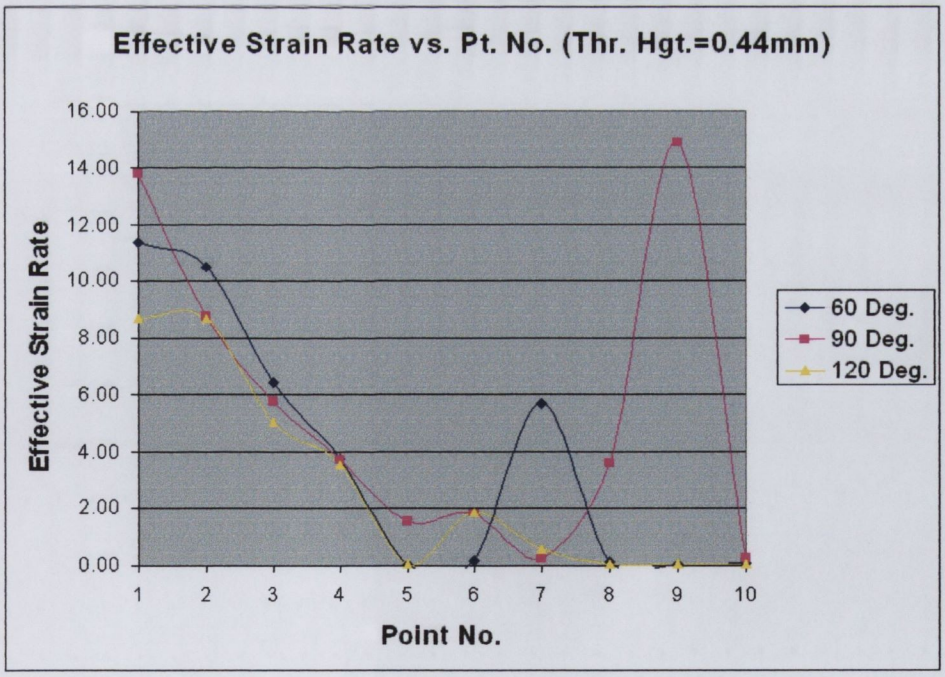

Figure 5.46: Effective Strain Rate vs. Tracking Point No., Thread Height = 0.44mm

Thread Height = 0.84mm

At this stage of the deformation process the plots for each die design shows *packing* of the material taking place at a point where thread formation is almost fully complete. This is evident from the high strain rates seen at points 8-10 in all the effective strain rate plots and in the graph of Figure 5.50. The standard 60 degree thread form indicates the highest strain rate of all three included angle designs (>40 s^{-1}). For the first time, the maximum shifts from the point beneath the crest radius (point 1) to a point at the top of the almost formed thread . This occurs because at this stage of the process it is only the small amount of material being forced into the apex of the thread form cavity that is moving. The effective strain rate curves show how strain rates are now much lower at point 1, and stay relatively constant up until the packing region where they increase dramatically.

In Figure 5.47 (120 degree included angle design), banding of the strain rate along lines of maximum shear stress extending from the thread root to the top of the formed thread is evident (light blue contour). As in previous thread forming stages, the bands cross over each other at the centre of the formed thread just below the pitch line.

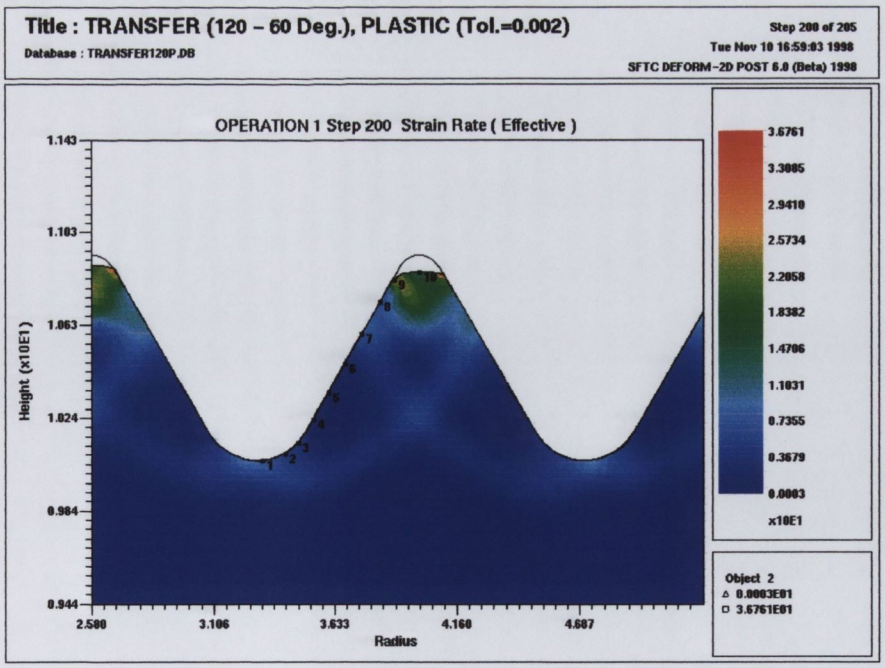

(Maximum: 36.76 s^{-1}, Minimum: 0 s^{-1})

Figure 5.47: Effective Strain Rate at 0.84mm, 120 Degree Included Angle Design

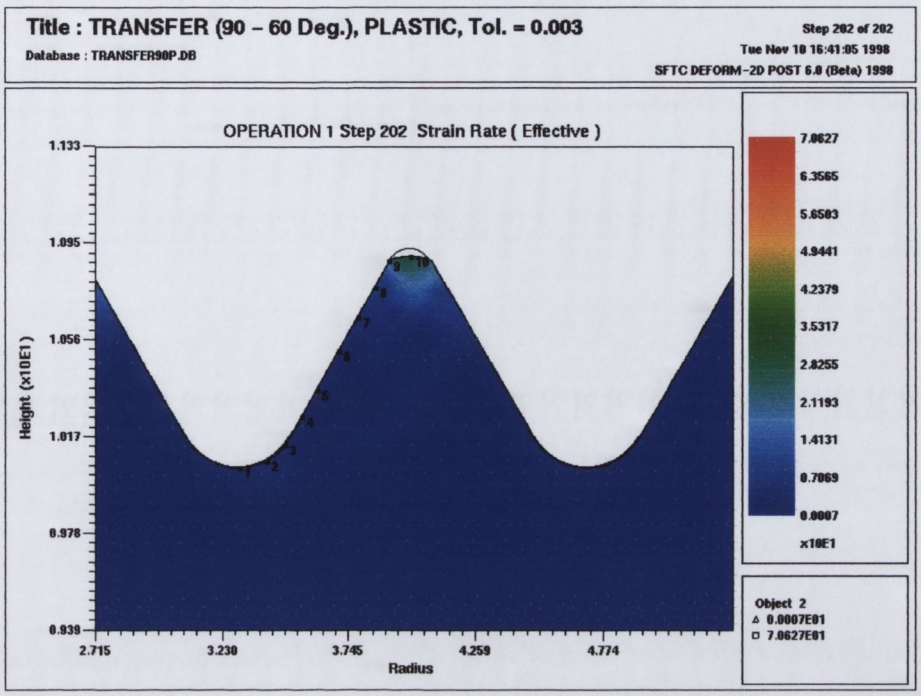

(Maximum: 70.62 s^{-1}, Minimum: 0 s^{-1})

Figure 5.48: Effective Strain Rate at 0.84mm, 90 Degree Included Angle Design

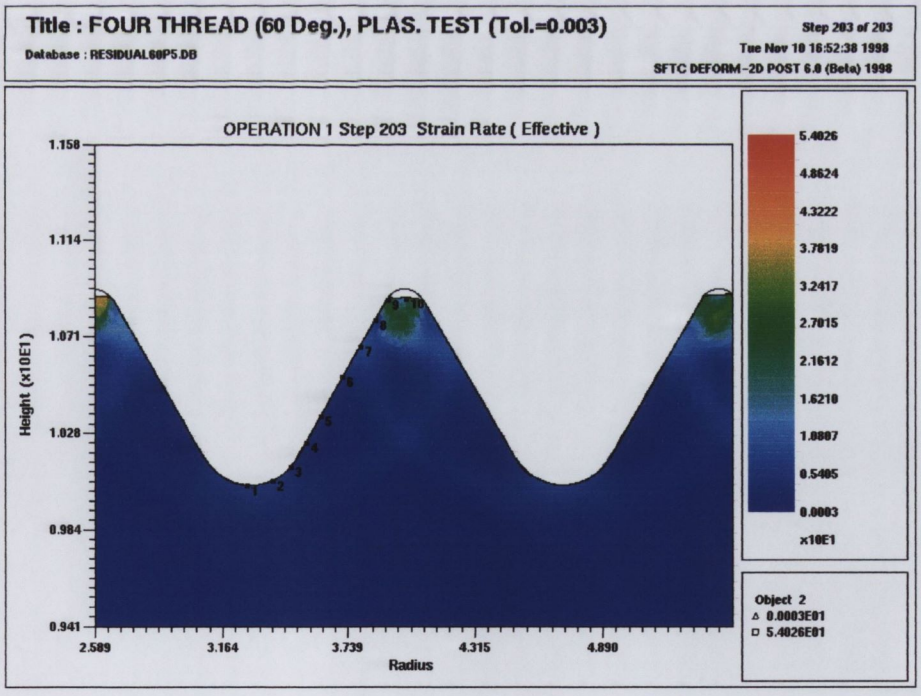

(Maximum: 54.03 s^{-1}, Minimum: 0 s^{-1})

Figure 5.49: Effective Strain Rate at 0.84mm, Standard 60 Degree Included Angle

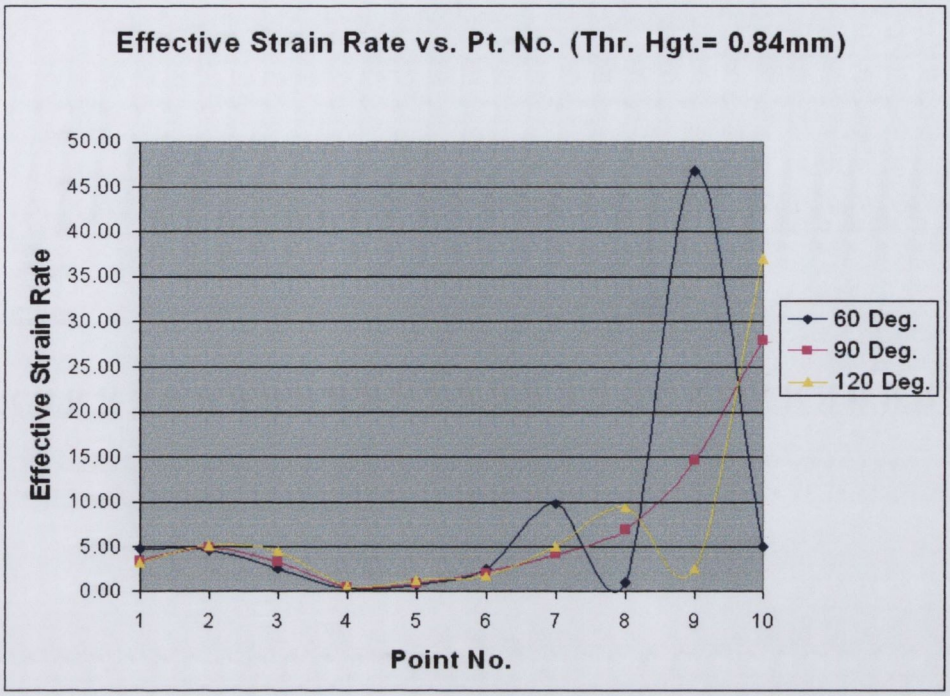

Figure 5.50: Effective Strain Rate vs. Tracking Pt. No., Thread Height = 0.84mm

5.3.4 Summary

Figure 5.51 shows a graph of the maximum effective strain at tracking point 1 (directly beneath the crest radius) against formed thread height for the three die designs. Point 1 is where the maximum strain occurred at all stages of the forming process. The information that can be gleaned from this graph and the other analyses presented previously may be summarised as follows.

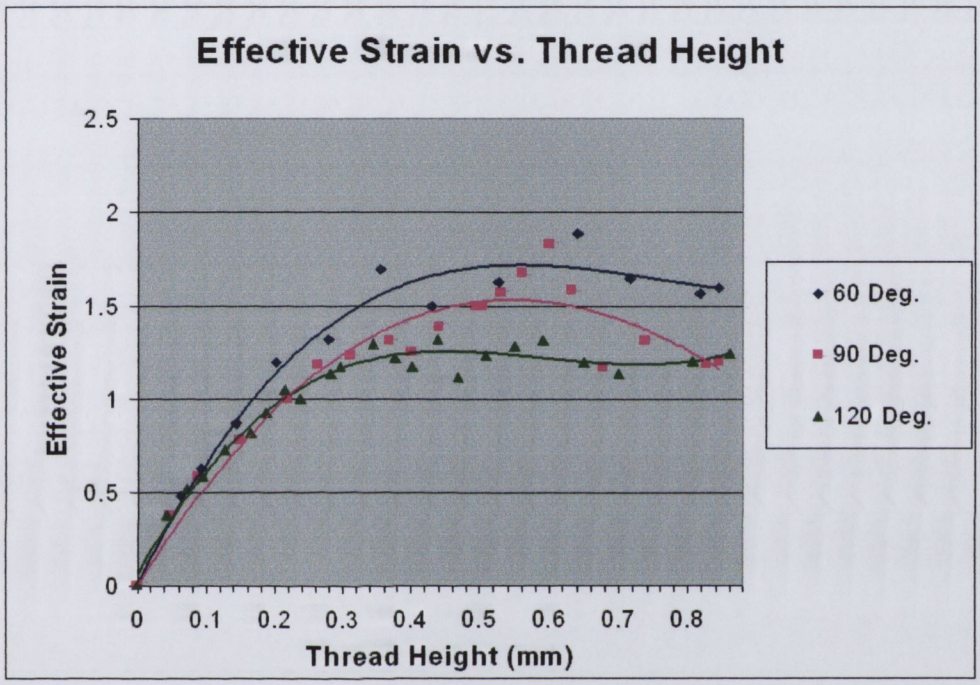

Figure 5.51: Effective Strain vs. Thread Height

- With a constant R2 of 0.2438mm (0.0096in.) no significant difference in the magnitude of the strain was noted during initial deformation for the included angles of 120, 90, and 60 degrees as is evident in Figure 5.51. Differences only become significant above a thread height of $\approx$ 0.2mm (0.008in.).

- The standard 60 degree included angle shows the highest overall strain and strain rate profile over the forming process.

- The new 90 and 120 degree included angle designs (after transfer to the standard 60 degree included angle) both indicate lower final strains and strain rates suggesting that changing the included angle is having some effect, but only towards

the end of the process.

- The 120 degree included angle design is the best overall design from this set of analyses. However since it has been assumed that the majority of internal strain related defects form at the start of thread formation process, then, changing the included angle alone will not improve the situation markedly.

5.4 Crest Radius (R2) Designs

The fourth set of analyses undertaken involved models to investigate the effect that varying the crest radius (R2) on the thread form might have on the material flow and stress/strain distribution. Figure 5.52 indicates the different R2 models constructed. As can be seen the effect of varying the crest radius on a tool is to produce a partially formed thread with a more rounded profile. All the die designs used the standard included angle of 60 degrees.

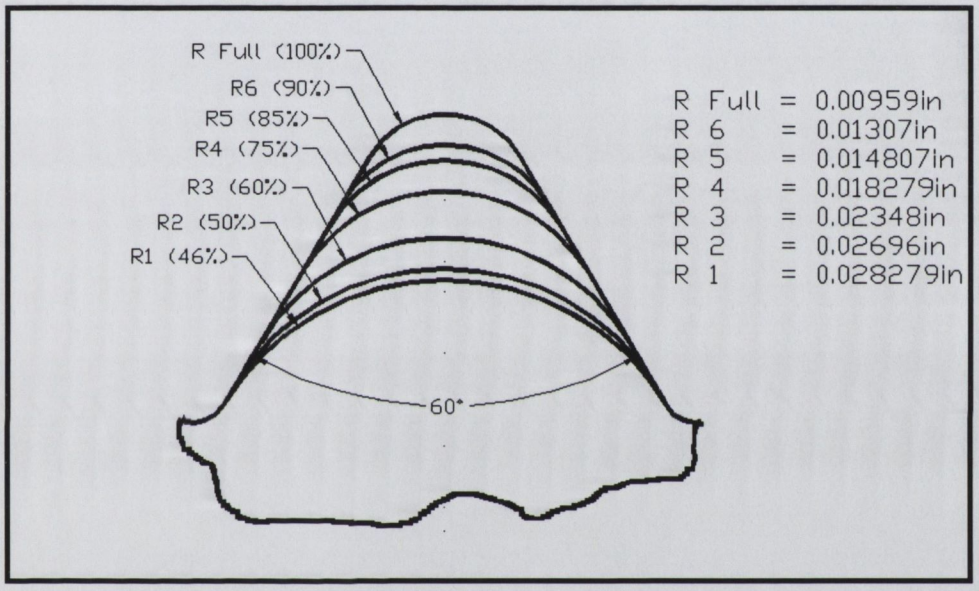

Figure 5.52: Different R2 Models used in finite element analyses

Figure 5.53 shows a representative strain distribution plot for one of the single thread modified crest radius (R2) designs, (R2 = 0.0235in).

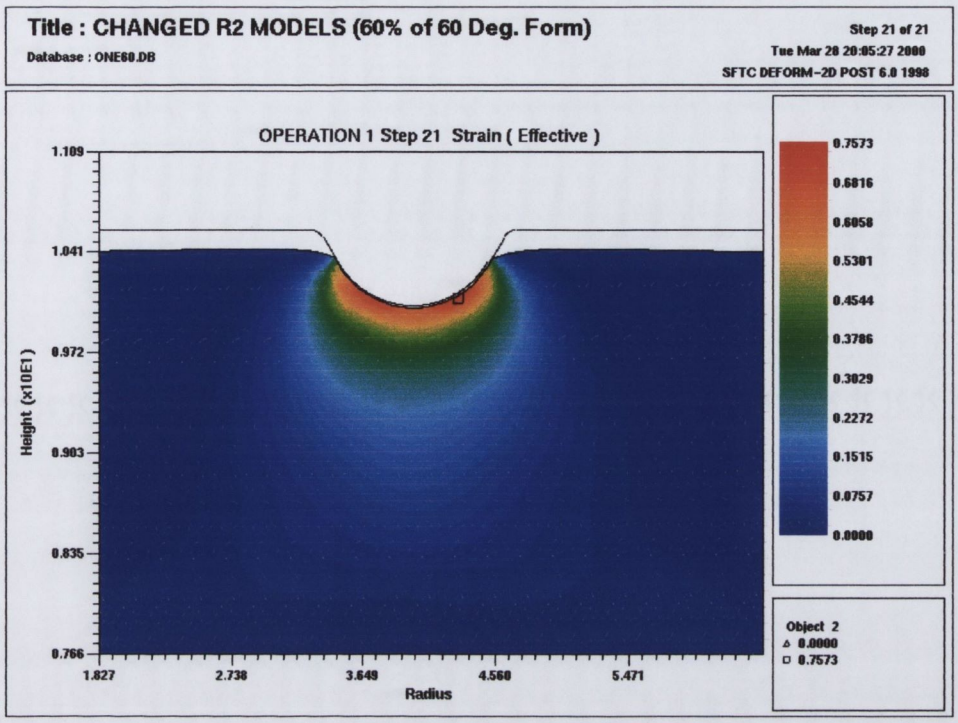

(Maximum: 0.757, Minimum: 0)

Figure 5.53: Effective Strain, Modified Crest Radius (R2)=0.5969mm (0.0235in.)

The maximum strains for the different modified crest radius designs are tabulated in Table 5.2

Crest Radius (R2)	*Strain*
R2=0.2438mm (0.0096in.)	1.44
R2=0.3327mm (0.0131in.)	1.13
R2=0.3759mm (0.0148in.)	1.09
R2=0.4648mm (0.0183in.)	0.86
R2=0.5969mm (0.0235in.)	0.76
R2=0.7188mm (0.0283in.)	0.61

Table 5.2: Influence of Crest Radius (R2), Single Thread Models

It is obvious from Table 5.2 that modifying the crest radius (R2) which initially deforms the fastener has a significant effect on the magnitude of the maximum effective strains. The R2=0.3327mm (0.0131in.) design lowered the strain by approximately

20% compared to the standard crest radius, while the R2=0.5969mm (0.0235in.) design lowered the maximum effective strain beneath the crest radius of the deforming thread form by almost 50% compared to the standard crest radius of 0.2438mm (0.0096in.).

After analysing these results and taking into account the maximum amount of thread formation (see Table 4.3, Section 4.1.6) that each of these new modified crest radius designs could perform, it was decided to investigate these modified crest radius designs further.

Four Thread Crest Radius (R2) Models

In this section (as in the included angle designs) the initial crest radius models were investigated in greater detail. In the following sections two of the modified crest radii (R2) designs will be looked at in particular. These designs are the crest radius (R2) values of 0.3327mm (0.0131in.) and 0.5969mm (0.0235in.) respectively. These two modified crest radius designs are chosen as they show the effect of a small increase in the size of the crest radius (R2) versus a large increase compared to the standard R2=0.2438mm (0.0096in.) design. The point tracking technique was once again used to acquire detailed results from the area of interest. Thread height was used as a measurement of the progression of thread formation throughout the deformation process.

5.4.1 Effective Stress Results

This section will describe the change in effective stress resulting from modifying the crest radius (R2) on a standard 60 degree included angle thread form. As with the included angle die designs results are presented for three stages during the formation of the thread, and these three stages correspond to the formed thread heights of 0.09mm, 0.44mm, and 0.72mm used previously.

Thread Height = 0.09mm

The R2=0.5969mm (0.0235in.) design (Figure 5.54), shows a higher stress at the tracking points on the free surface (points 8-10) than either of the smaller R2 designs (Figures 5.55 and 5.56) . This is due to the fact that the larger radius effects a greater area of the fastener material during initial deformation. However, the magnitude of the stresses at the tracking points beneath the crest radius for R2=0.5969mm (0.0235in.) (points 1-6) is lower. These results imply that while the larger R2 affects a greater area, the average stress magnitude within this region is lower. This design produces the lowest maximum effective stress $\approx$1450 N/mm^2, and this might have implications for the tensile and fatigue strength of the fastener.

Figures 5.55 and 5.56 show the effective stress plots for the R2=0.3327mm (0.0131in.)

and the standard R2=0.2438mm (0.0096in.) design respectively. The stress distributions in these designs are very similar, as are the stress magnitudes involved. This implies that changing the radius by this small amount has little or no effect on the magnitude of the effective stresses at the beginning of the thread formation process. It can also be seen from these plots, that the deformation regions in each case is made of two hemispherical zones that merge, while in the case of the R2=0.5969mm (0.0235in.) design, the deformation zone is much more flat and even. This flatter stress distribution will have the beneficial effect of producing a reasonably constant compressive layer near the surface of the fastener which should improve tensile and fatigue strength and compensate for the slightly lower level of effective stress at the thread root.

The effective stress curves over the tracking points for the three different designs are plotted in Figure 5.57. They are all quite similar and confirm the comments made above. The curve for the R2=0.5969mm (0.0235in.) design does not start to drop away until point 7 because of its greater area of effect. The other two designs initially peak higher (1525 N/mm^2) but start to fall away earlier (point 6) because of their smaller crest radii.

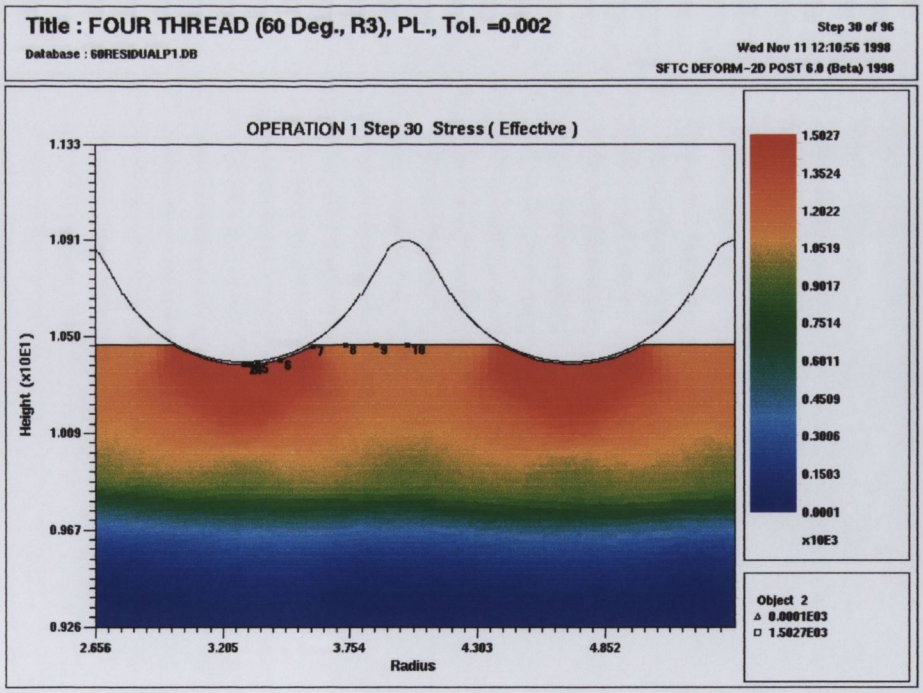

(Maximum: 1503 N/mm^2, Minimum: 0 N/mm^2)

Figure 5.54: Effective Stress at 0.09mm, R2=0.5969mm (0.0235in.) Design

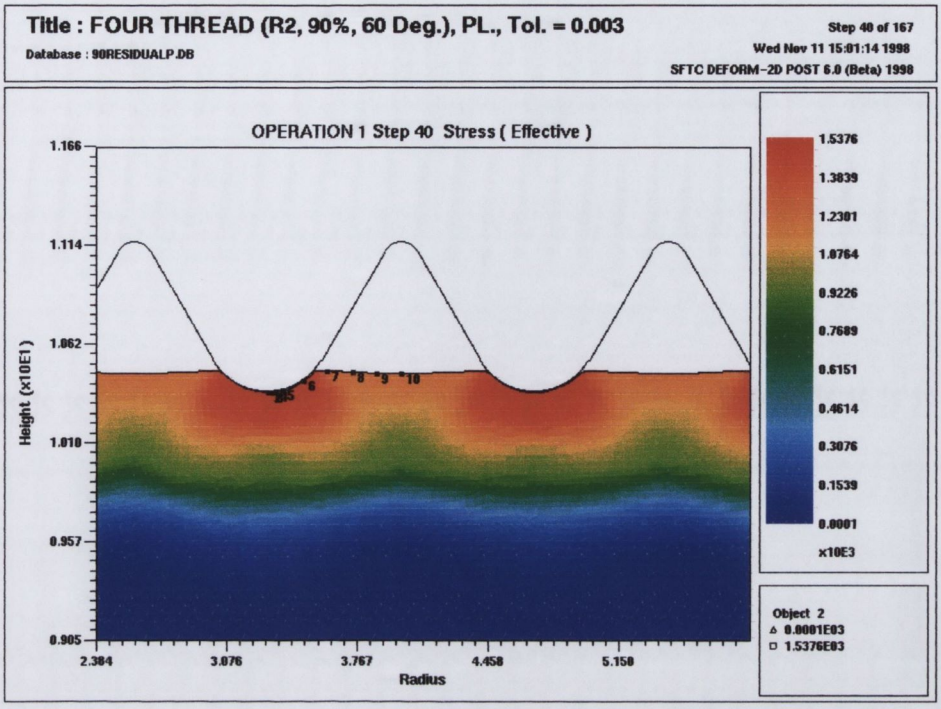

(Maximum: 1538 N/mm^2, Minimum: 0 N/mm^2)

Figure 5.55: Effective Stress at 0.09mm, R2=0.3327mm (0.0131in.) Design

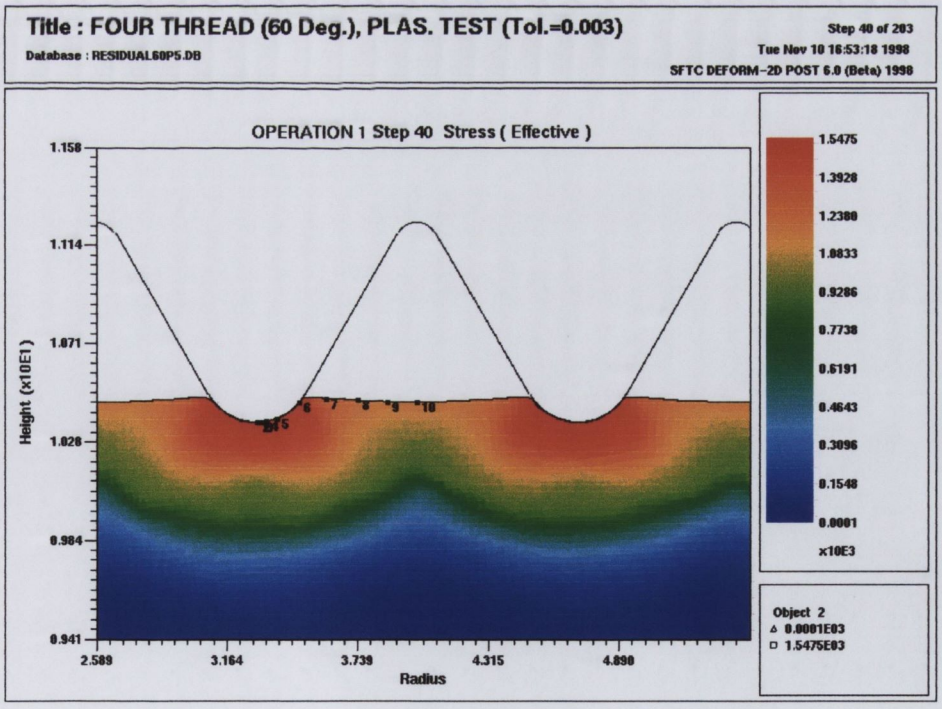

(Maximum: 1547 N/mm^2, Minimum: 0 N/mm^2)

Figure 5.56: Effective Stress at 0.09mm, Standard Crest Radius=0.2438mm (0.0096in.)

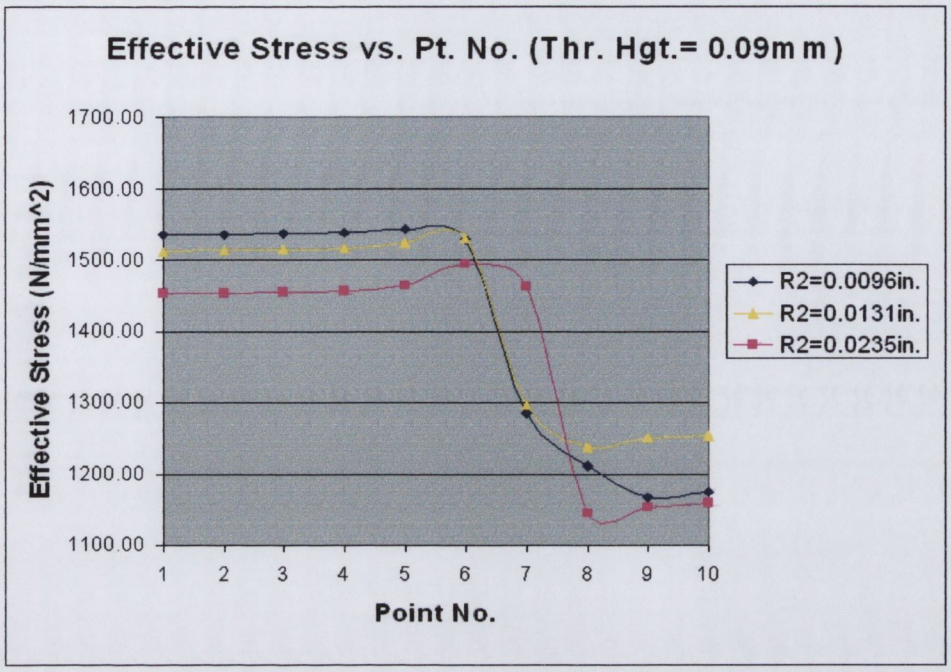

Figure 5.57: Effective Stress vs. Pt. No., Thread Height = 0.09mm

Thread Height = 0.44mm

It can be seen in Figure 5.58, that with the R2=0.0235in design, the maximum thread height that can be formed using this geometry has almost been reached (0.5288mm). The effective stress has a magnitude of $\approx$ 1600 N/mm^2 and all the deformed material within the thread form appears to be at this level of stress. In this effective stress plot the depth to which the stress affects the material is slightly greater directly beneath the two crest radii compared to the material flowing to form the thread.

In both the R2=0.3327mm (0.0131in.) and the standard R2 designs, Figures 5.59 and 5.60, the small regions of low stress on the flank of the thread form mentioned earlier are again visible. These regions are only picked up on the graph of effective stress (Figure 5.61) for the standard R2 design (point 5) because of where the tracking points are situated.

As was the case in the early stages of thread formation (0.09mm) the magnitudes of the stresses in all three modified crest radius die designs are very similar $\approx$ 1600 N/mm^2 except for the low stress region mentioned above which occurs at point 5 on the curve for the standard R2 form. The deformed material in the R2=0.5969mm (0.0235in.) design, Figure 5.58 does not experience a drop off in stress until point 9 because the material is being packed into the top of the thread form.

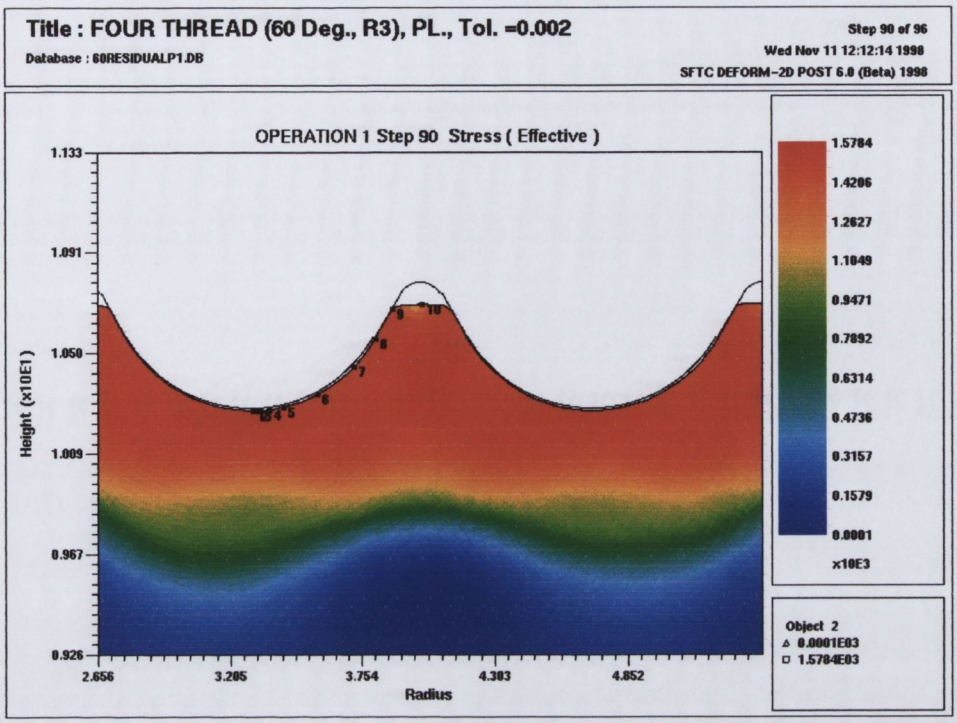

(Maximum: 1578 N/mm^2, Minimum: 0 N/mm^2)

Figure 5.58: Effective Stress at 0.44mm, R2=0.0235in. Design

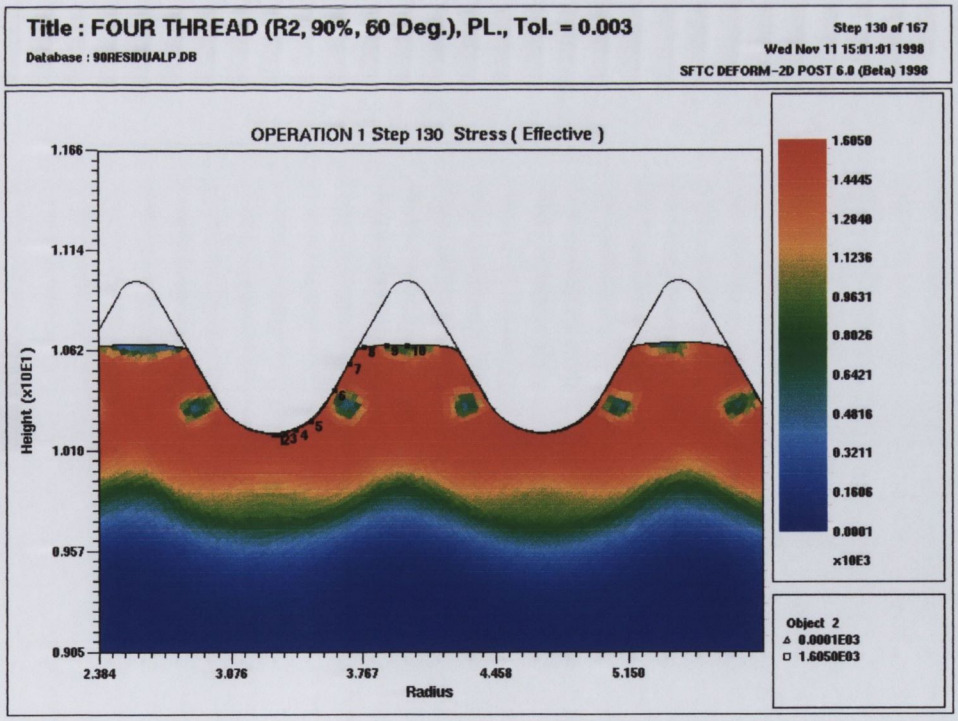

(Maximum: 1605 N/mm^2, Minimum: 0 N/mm^2)

Figure 5.59: Effective Stress at 0.44mm, R2=0.0131in. Design

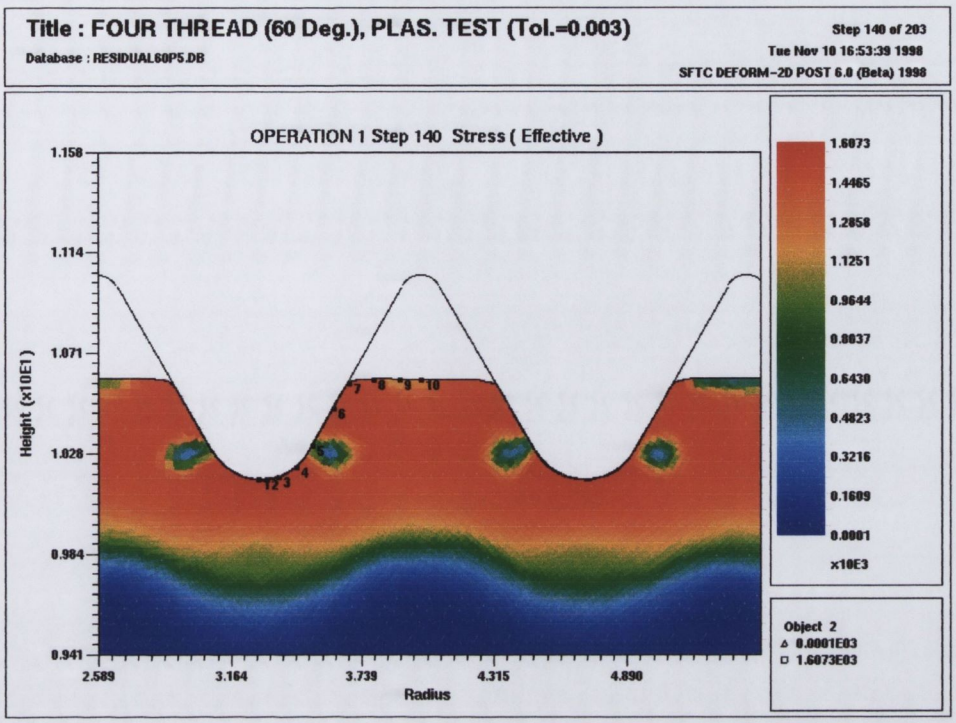

(Maximum: 1607 N/mm^2, Minimum: 0 N/mm^2)

Figure 5.60: Effective Stress at 0.44mm, Standard R2=0.0096in. Design

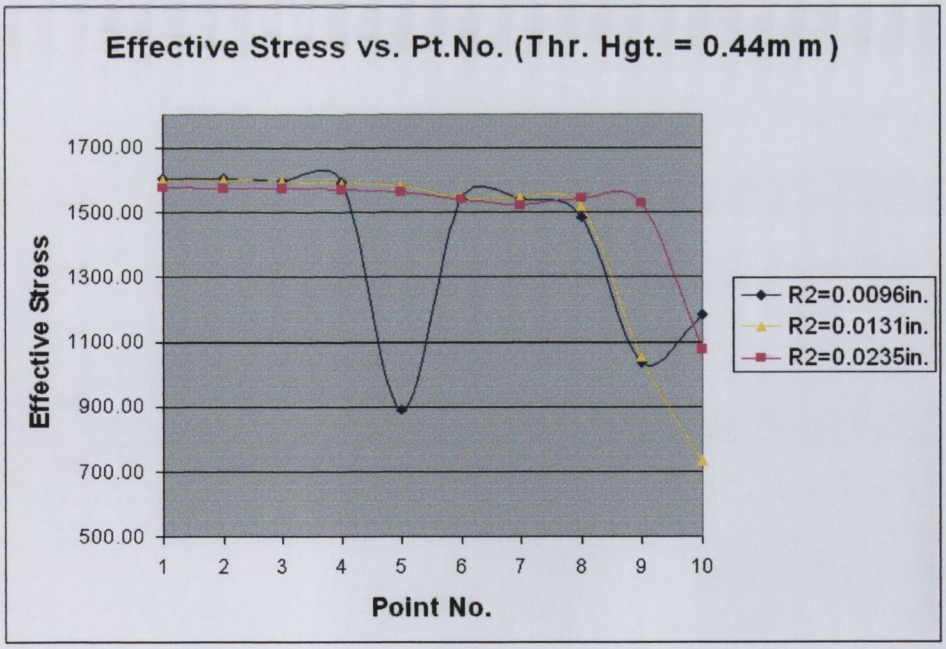

Figure 5.61: Effective Stress vs. Pt. No., Thread Height = 0.44mm

Thread Height = 0.72mm

Figure 5.62 shows the effective stress distributions for the R2=0.5969mm (0.0235in.) die design after the deforming material has been transferred to the standard R2 thread form and further deformed. This transition from one thread form to another can be seen on the upper surface of the deformed thread where the material slopes away from the flank of the thread form. The curvature on the deformed surface is evident from the figure. This curvature means that there is a relatively large area at the top of the forming thread which is initially a free surface that has not yet come into contact with the final thread form thus leaving it lowly stressed. The occurrence of such a transition region raises some concerns regarding the impact it might have on the quality of the finished fastener.

The R2=0.3327mm (0.0131in.) and the standard R2 designs (Figures 5.63 and 5.64) show very similar stress distributions for this level of thread formation. The material in the R2=0.3327mm (0.0131in.) design is almost at the point where it has to be transferred to the standard R2 thread form. The maximum effective stress in both these models occurs at tracking point 1 and has a value of $\approx$ 1600 N/mm^2.

The effective stress in the R2=0.5969mm (0.0235in.) design is distributed more evenly compared to the other two designs, and as mentioned previously this should be better for the fatigue life of the fastener.

The graph in Figure 5.65 shows the effective stresses at the tracked points for all three designs. As expected the R2=0.3327mm (0.0131in.) design and the standard R2 show very similar results as shown by examination of the effective stress plots. The curve for the R2=0.5969mm (0.0235in.) design also confirms the results shown in the effective stress plot. Effective stress is fairly constant until point 6 where contact between deforming material and the flank of the thread form ends and the free surface begins, this is reflected by the sudden drop in the magnitude of the effective stress at point 6.

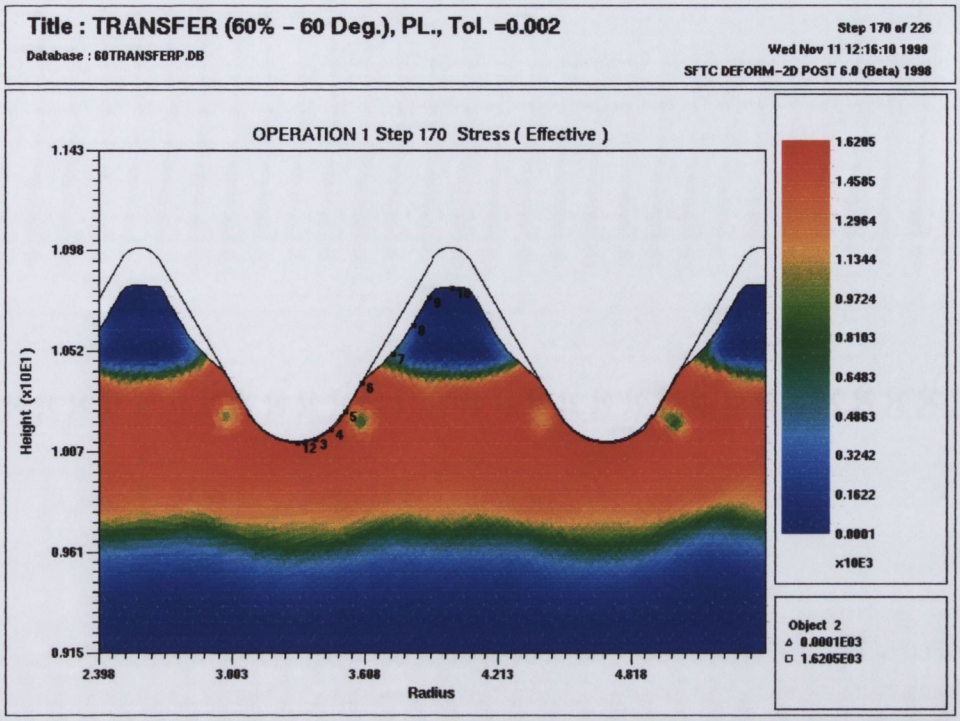

(Maximum: 1620 N/mm^2, Minimum: 0 N/mm^2)

Figure 5.62: Effective Stress at 0.72mm, R2=0.5969mm (0.0235in.) Design

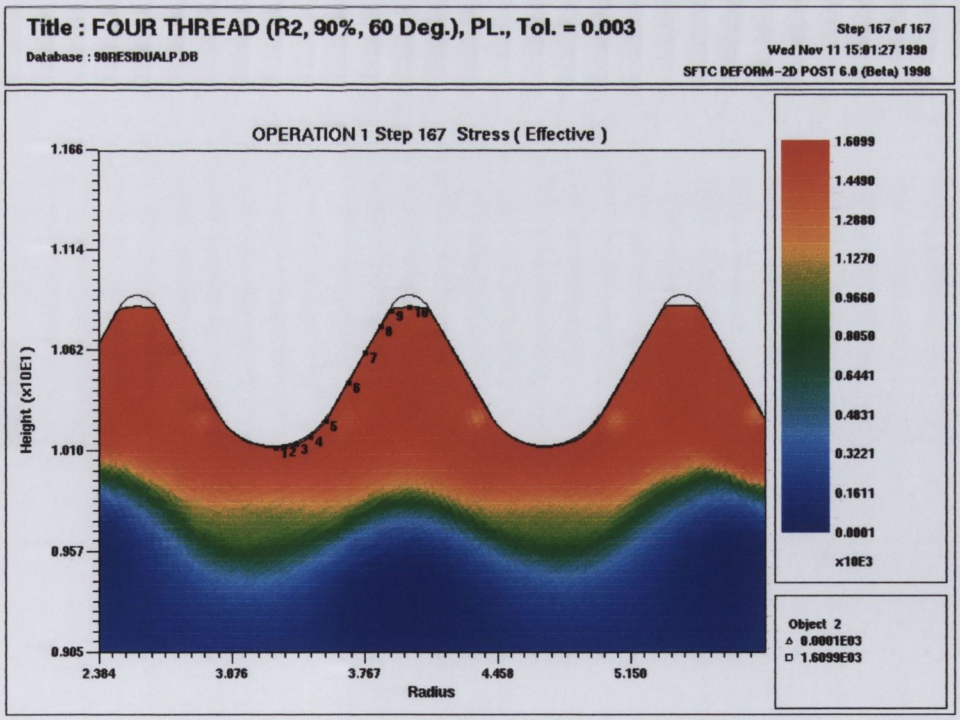

(Maximum: 1610 N/mm^2, Minimum: 0 N/mm^2)

Figure 5.63: Effective Stress at 0.72mm, R2=0.3327mm (0.0131in.) Design

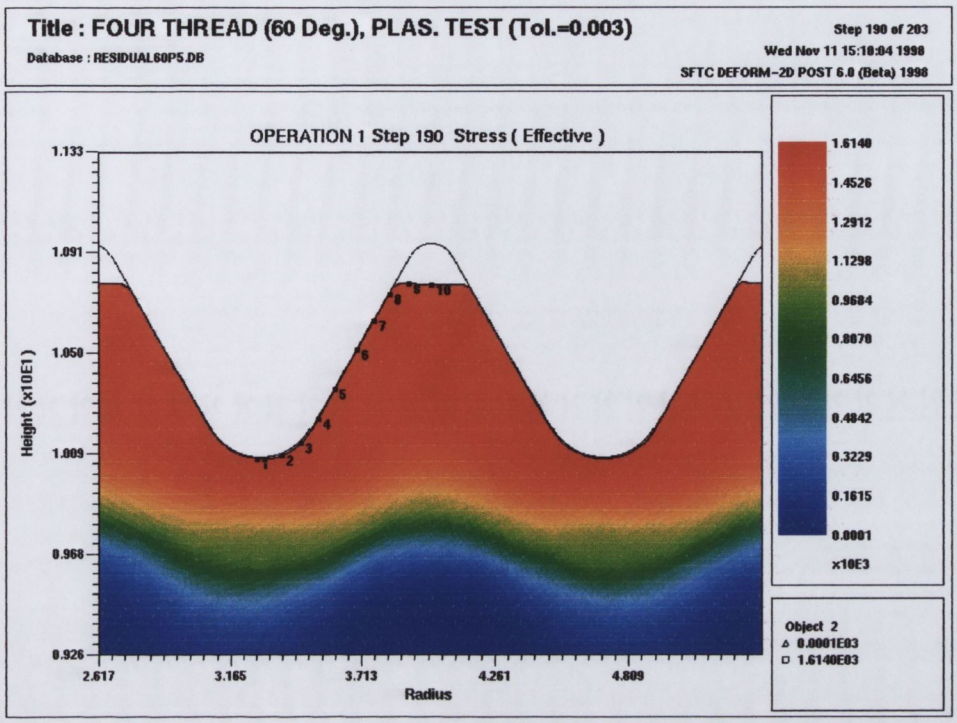

(Maximum: 1614 N/mm^2, Minimum: 0 N/mm^2)

Figure 5.64: Effective Stress at 0.72mm, Standard R2=0.2438mm (0.0096in.) Design

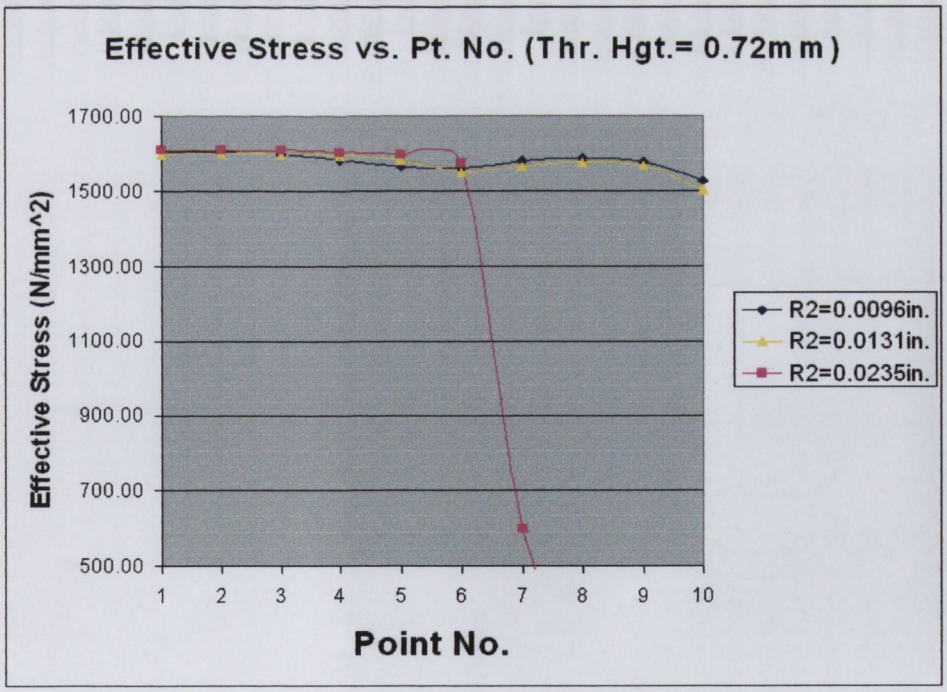

Figure 5.65: Effective Stress vs. Tracking Pt. No., Thread Height = 0.72mm

5.4.2 Effective Strain Results

As mentioned previously when commenting on the included angle die designs the objective of this thesis was to optimise the thread rolling die geometry so as to reduce the overall level of strain at the thread root. Consequently particular emphasis is placed on the factors that reduce the strains at the early stages of the thread formation process at which it is believed internal defects are initiated.

Thread Height = 0.09mm

In Figure 5.66 the effective strain plot of the largest R2 design (R2=0.5969mm (0.0235in.)) at an early stage of thread formation can be seen. The contact that this larger R2 radius makes with the fastener surface seems to produce three distinct strain concentrations, one directly beneath the apex of the crest radius and two either side of the apex. These concentrations are picked up by an increase in the effective strain curve in the graph of Figure 5.69. The maximum effective strain for the R2=0.5969mm (0.0235in.) die design occurs at point 6, which is situated in one of the strain distributions to the side of the crest radius, the effective strain jumps from a value of 0.2 at the thread root to 0.4 at point 6.

The effective strain plots for the R2=0.3327mm (0.0131in.), Figure 5.67, and the standard R2 design (Figure 5.68) show similar strain concentrations beneath the crest radius. The maximum effective strain at this level of thread formation occurs at point 6 and point 5 respectively, again just of to the side of the apex of the crest radius.

While the area of material effected is wider in the case of the R2=0.3327mm (0.0131in.) design, compared to the standard die due to the effect of deforming the fastener surface with a larger crest radius, however the magnitude of the strain in this wider area does not reach the level of that achieved using the standard R2 design. This can be seen clearly from the curves in Figure 5.29 where the R2=0.3327mm (0.0131in.) design starts at a strain of 0.4 while the standard R2 design starts at a strain of 0.6.

The benefit of using a larger crest radius (R2) at the start of thread formation can be clearly seen from Figure 5.69. The trends of the effective strain in all three designs

are similar but the magnitude for the effective strain of the R2=0.5969mm (0.0235in.) design is lower by over 60% between points 1-5 compared to the standard crest radius (R2) design. All points on the free surface experience similar levels of effective strain.

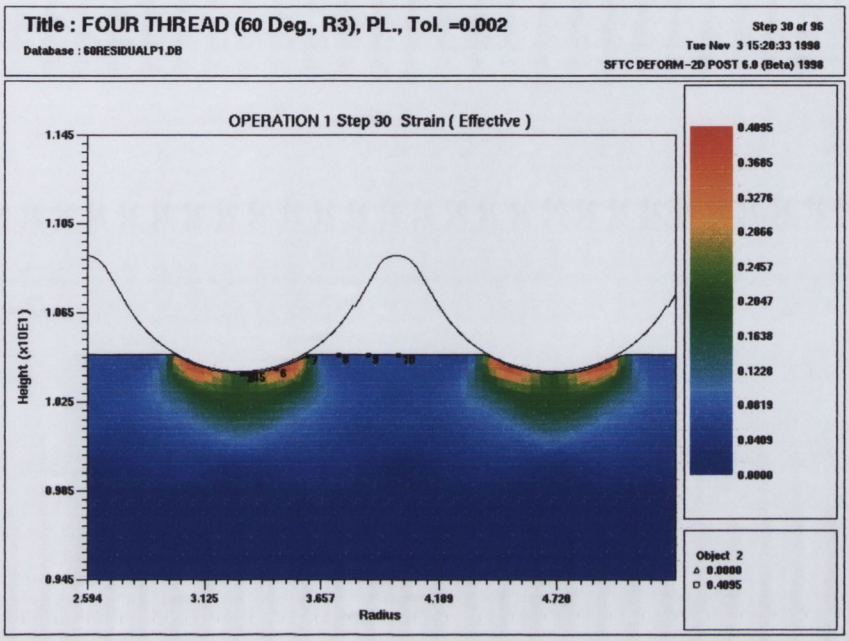

(Maximum: 0.4095, Minimum: 0)

Figure 5.66: Effective Strain at 0.09mm, R2=0.5969mm (0.0235in.) Design

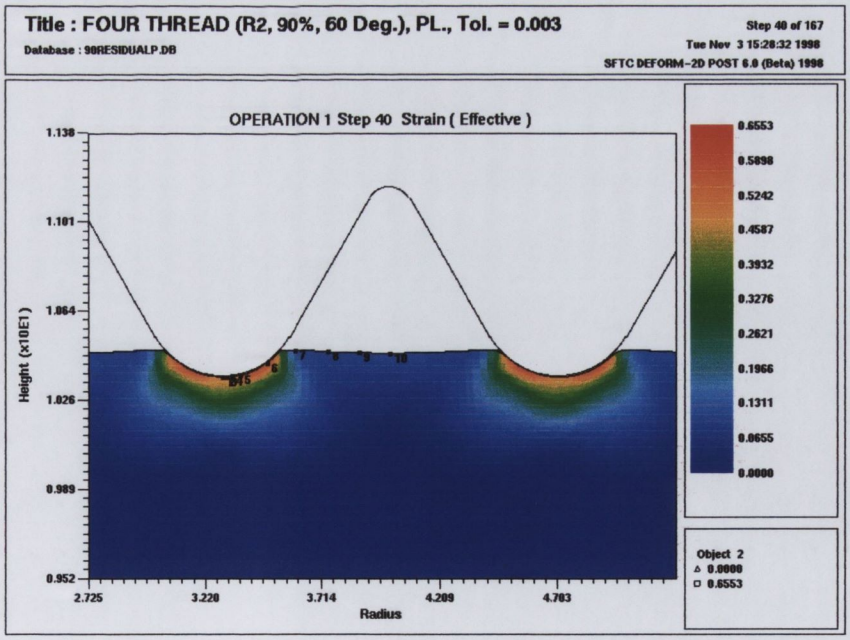

(Maximum: 0.6553, Minimum: 0)

Figure 5.67: Effective Strain at 0.09mm, R2=0.3327mm (0.0131in.) Design

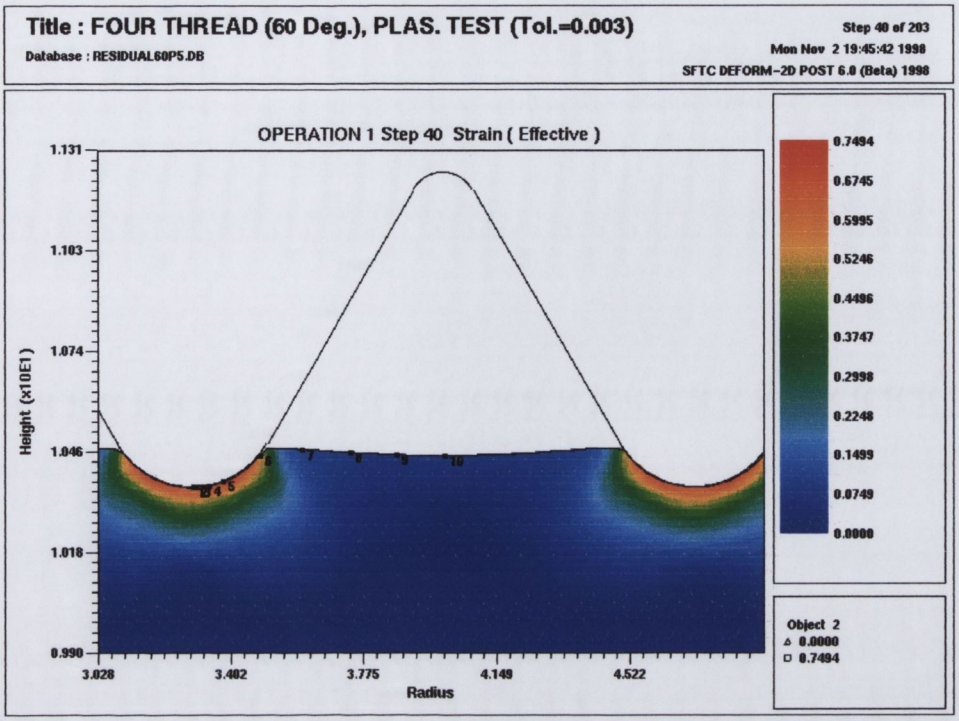

(Maximum: 0.7494, Minimum: 0)

Figure 5.68: Effective Strain at 0.09mm, Standard R2=0.2438mm (0.0096in.)

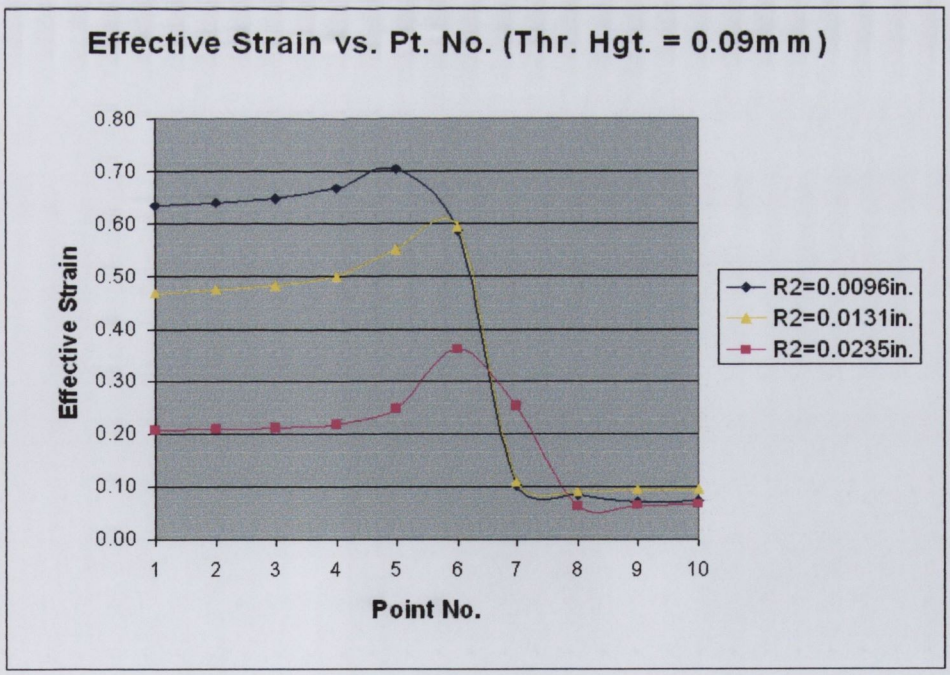

Figure 5.69: Effective Strain vs. Tracking Pt. No., Thread Height = 0.09mm

Thread Height = 0.44mm

Figure 5.70 shows the effective strain for the R2=0.5969mm (0.0235in.) design. At this level of thread formation, the material in this die design is almost at the stage where for any further thread formation to take place it must be transferred to the standard 60 degree form. The regions of intense strain are again situated just below the apex of the crest radius and in the central area of the formed thread (orange contours) where two bands of strain have merged. The maximum effective strain occurs beneath the apex of the crest radius (point 1) but is still of a lower magnitude than either the R2=0.3327mm (0.0131in.) or standard R2 die designs by over 30%.

As in the earlier stage of thread formation, the R2=0.3327mm (0.0131in.) die design and the standard R2 form produce similar effective strain distributions as shown in Figures 5.71 and 5.72 respectively. The tracked effective strain values in Figure 5.73 for these two designs match each other very closely in both magnitude and trend. They both have higher effective strain values than the R2=0.0235in. die design over points 1-5. The peak on the curve of the R2=0.5969mm (0.0235in.) die design at points 8-9 reflects the bands of high strain visible in the effective strain plot, Figure 5.70.

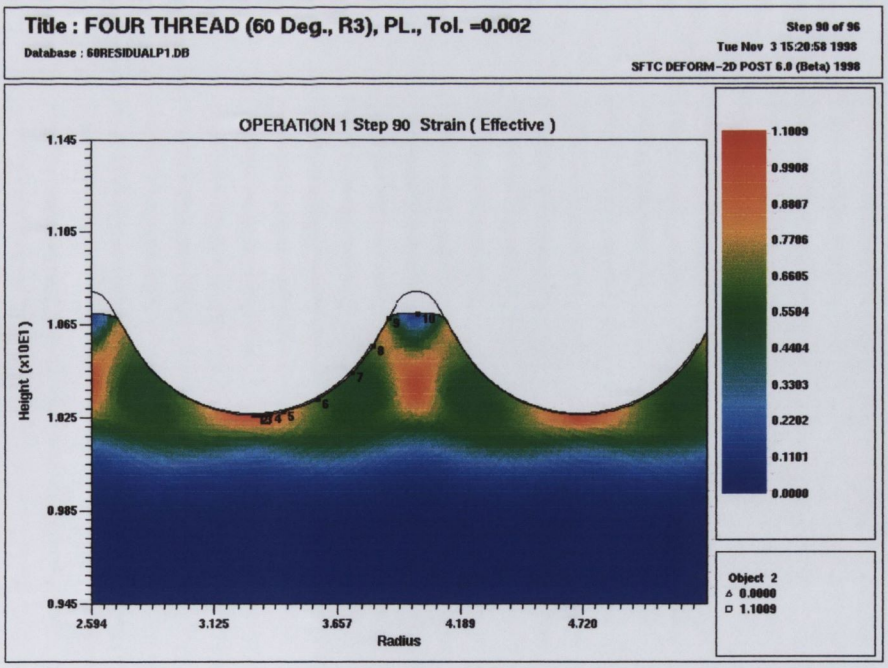

(Maximum: 1.101, Minimum: 0)

Figure 5.70: Effective Strain at 0.44mm, R2=0.5969mm (0.0235in.) Design

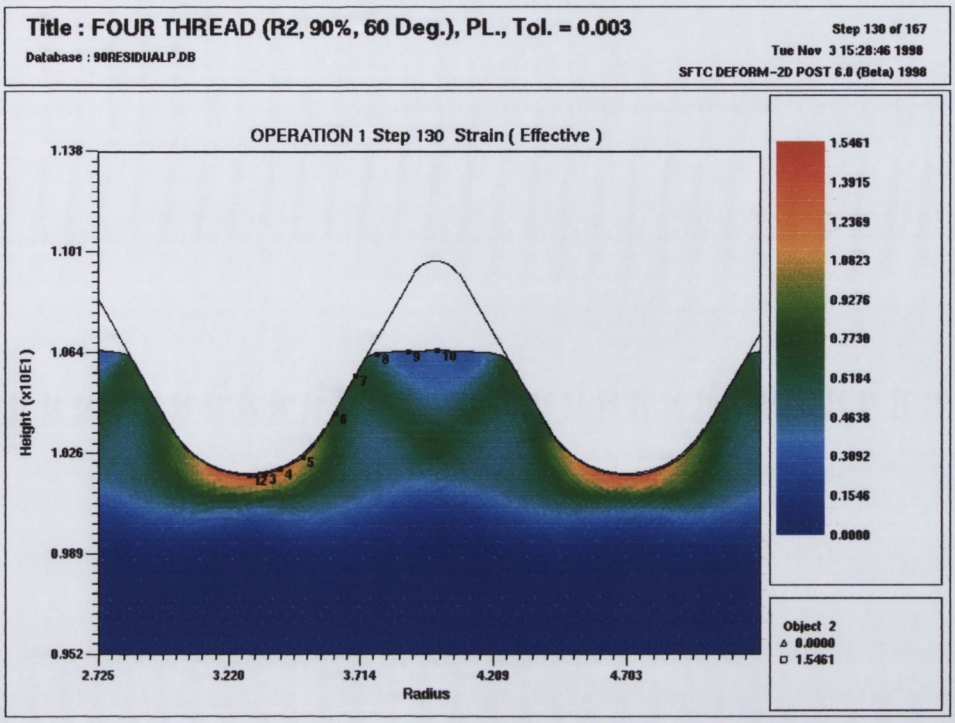

(Maximum: 1.5461, Minimum: 0)

Figure 5.71: Effective Strain at 0.44mm, R2=0.3327mm (0.0131in.) Design

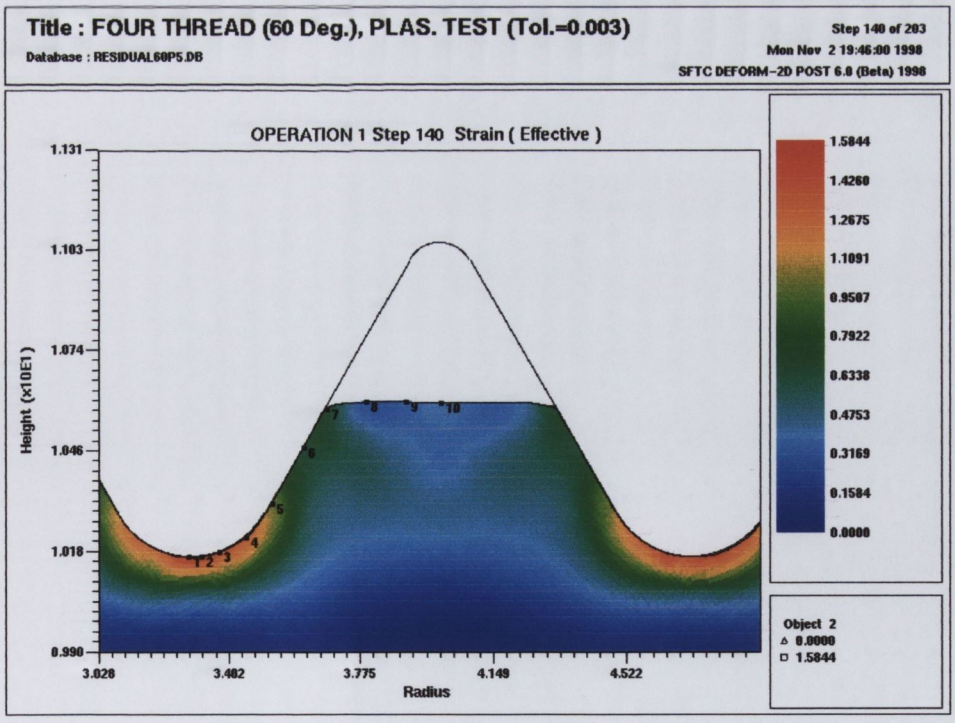

(Maximum: 1.5844, Minimum: 0)

Figure 5.72: Effective Strain at 0.44mm, Standard R2=0.2438mm (0.0096in.)

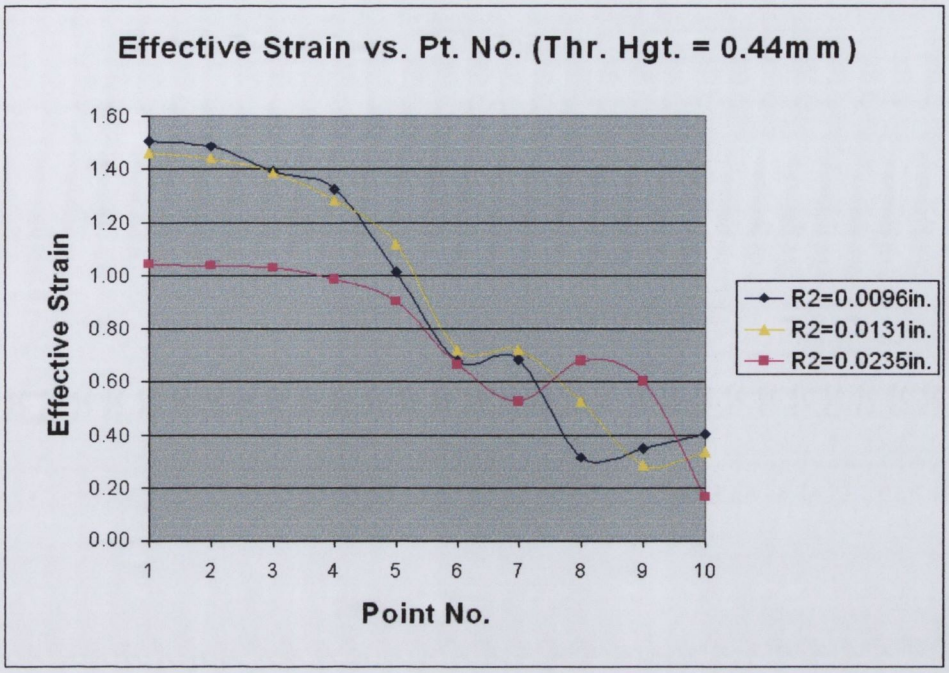

Figure 5.73: Effective Strain vs. Tracking Pt. No., Thread Height = 0.44mm

The results for this level of deformation clearly show the advantages of the larger crest radius (R2) in reducing the magnitude of the maximum strain in the region of the thread root.

Thread Height = 0.72mm

By the stage that a thread height of 0.72mm has been formed, the material in the R2=0.5969mm (0.0235in.) die design has been transferred to a standard 60 degree R2 form (Figure 5.74). The evidence of this transition is again obvious on the upper portion of the formed thread where the deformation caused by the larger R2 crest radius can be clearly seen. The strain plots are similar to those presented earlier in section 5.3.2 for the various included angle designs. The material in the R2=0.5969mm (0.0235in.) die design now sustains a higher level of strain compared to the material in the standard R2 design (Figure 5.76). This is made more obvious be examining the effective strain curves in Figure 5.77. Whereas points 1-3 show similar magnitudes, these higher strains are shown over points 3-6.

As before, the strain for the R2=0.3327mm (0.0131in.) design and the standard R2 design (Figures 5.75 and 5.76) both show a similar trend and magnitude. This plot and the curve in Figure 5.77 shows how at this level of thread formation there is very little difference between the R2=0.3327mm (0.0131in.) design and the standard R2. The central strain bands which were visible at the earlier stage of the R2=0.5969mm (0.0235in.) design are also now evident in the other two designs (orange contours joining in the centre of the forming thread). They extend from the final contact points of the material on the flank of the thread form and join in the centre of the forming thread. They match up exactly with areas where shear bands are known to exist.

The overall result from this set of analyses is that the beneficial effect of the larger crest radius (R2) diminishes at higher levels of thread formation.

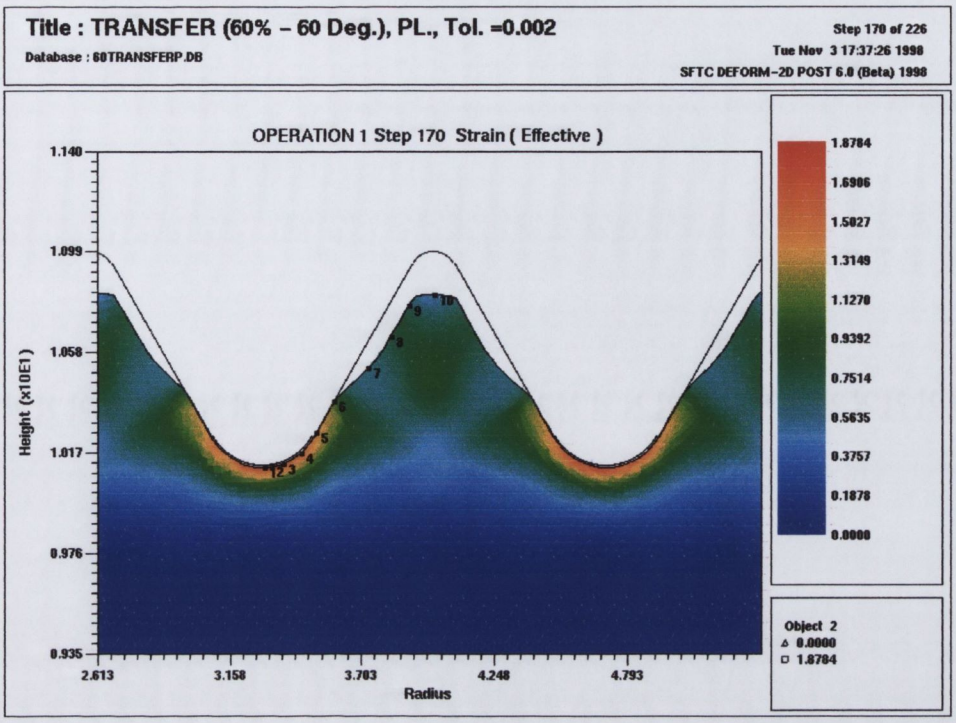

(Maximum: 1.8784, Minimum: 0)

Figure 5.74: Effective Strain at 0.72mm, R2=0.5969mm (0.0235in.) Design

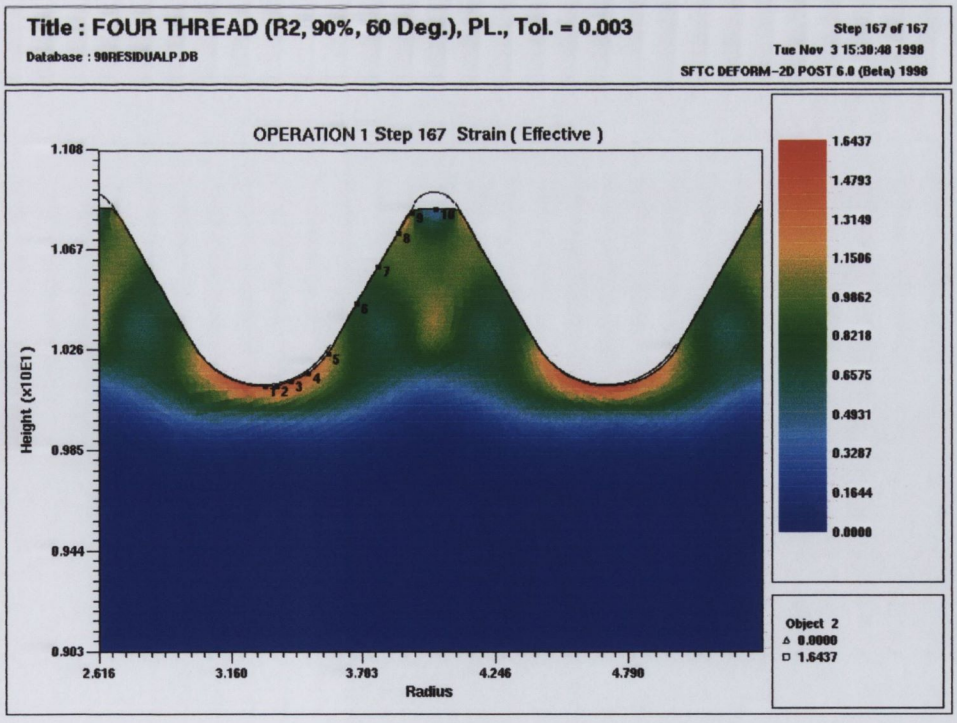

(Maximum: 1.6437, Minimum: 0)

Figure 5.75: Effective Strain at 0.72mm, R2=0.3327mm (0.0131in.) Design

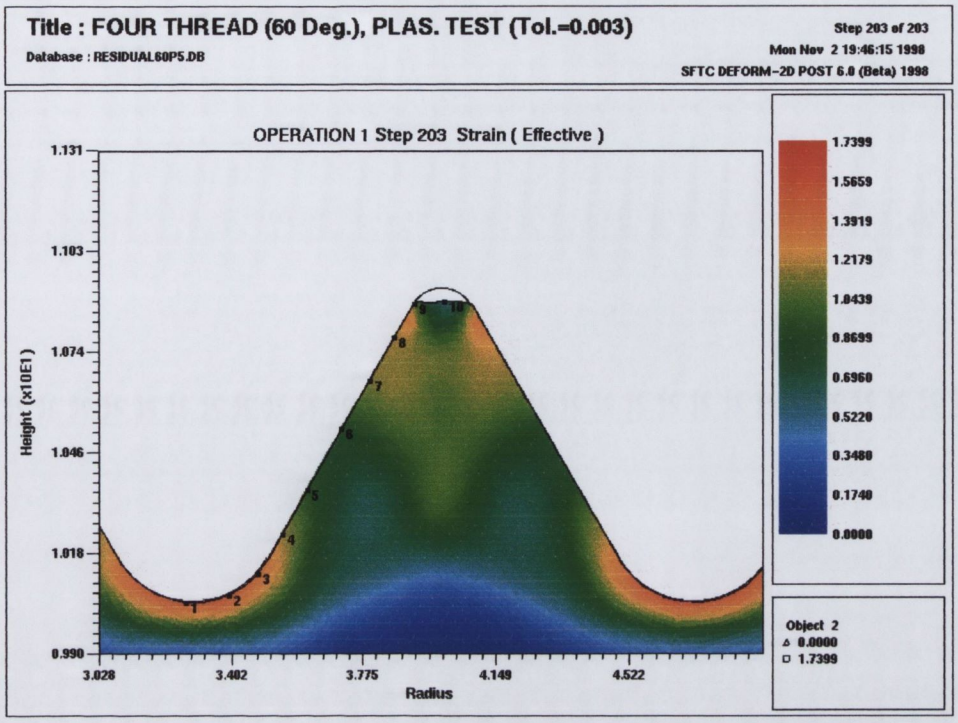

(Maximum: 1.7399, Minimum: 0)

Figure 5.76: Effective Strain at 0.72mm, Standard R2=0.2438mm (0.0096in.)

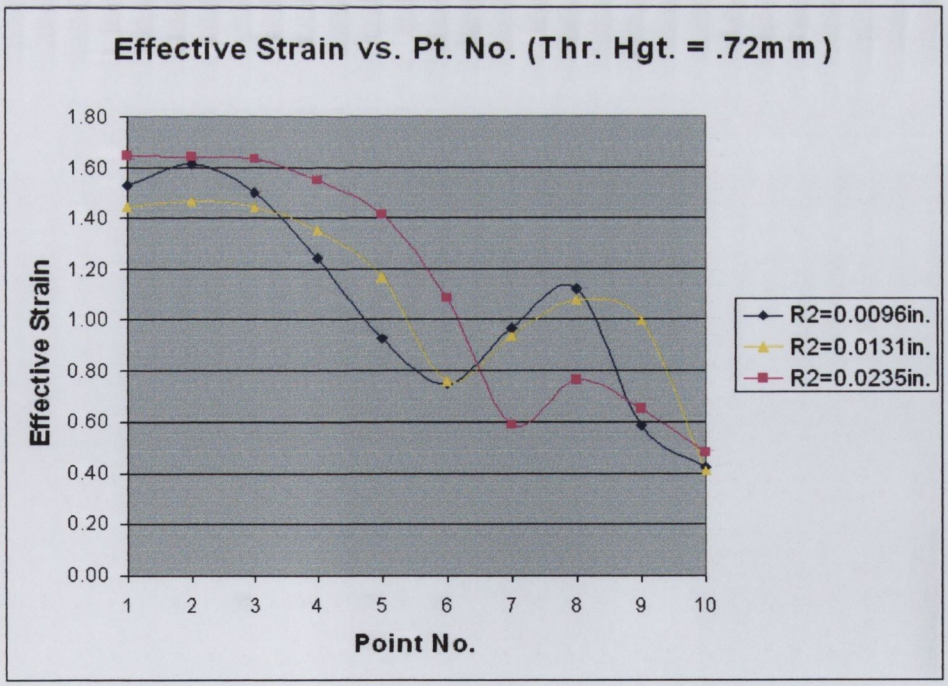

Figure 5.77: Effective Strain vs. Pt. No., Thread Height = 0.72mm

5.4.3 Effective Strain Rate Results

As in the case of the included angle designs, the variations in strain rate for the various modified crest radius (R2) designs is again investigated.

Thread Height=0.09mm

In the R2=0.5969mm (0.0235in.) design, Figure 5.78, the contact this die design makes with the fastener surface creates different areas of strain rate concentration compared to that for the R2=0.3327mm (0.0131in.) and the R2=0.2438mm (0.0096in.) designs, Figures 5.79 and 5.80 respectively. In the latter designs the strain rate is concentrated beneath the crest radius whereas in the former design the strain rates are concentrated at the points where the larger crest radius contact with the surface of the deforming fastener material. The area of strain rate concentration is deeper in both the R2=0.3327mm (0.0131in.) and the standard R2 designs than in the R2=0.5969mm (0.0235in.) design. This is caused by the smaller crest radius creating a smaller contact area but having a higher strain rate.

From the effective strain rate graphs of Figure 5.81, the following comments can be made. The R2=0.3327mm (0.0131in.) and the R2=0.5969mm (0.0235in.) curves follow the same trend but the R2=0.5969mm (0.0235in.) design produces slightly lower strain rates compared to the R2=0.3327mm (0.0131in.) design. The curve of the standard R2 form has a significantly higher strain rate over points 1-5 ($7s^{-1}$ as opposed to $4.5s^{-1}$) but drops away faster. This is due to the fact that the smaller radius makes less contact with the surface but the contact is more concentrated, hence the velocity of the metal flow is increased in the contact region.

Overall, as with the effective strain results, the strain rate produced at the thread root was lowest for the die design having the largest crest radius (R2) and this must be beneficial in terms of the initiation of strain related defects.

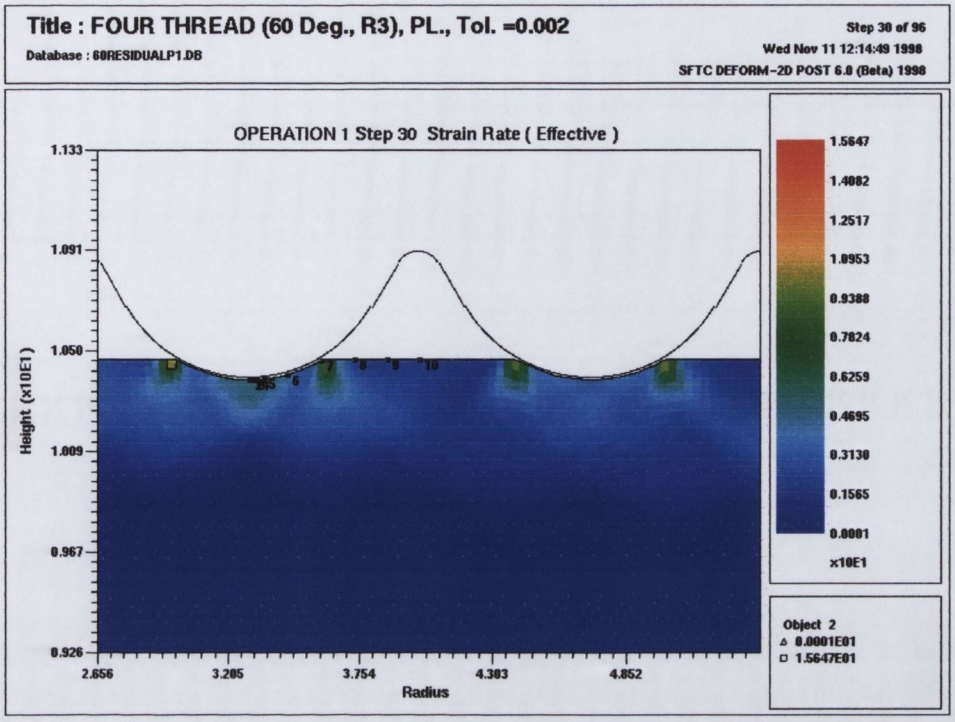

(Maximum: 15.65 s^{-1}, Minimum: 0 s^{-1})

Figure 5.78: Effective Strain Rate at 0.09mm, R2=0.5969mm (0.0235in.) Design

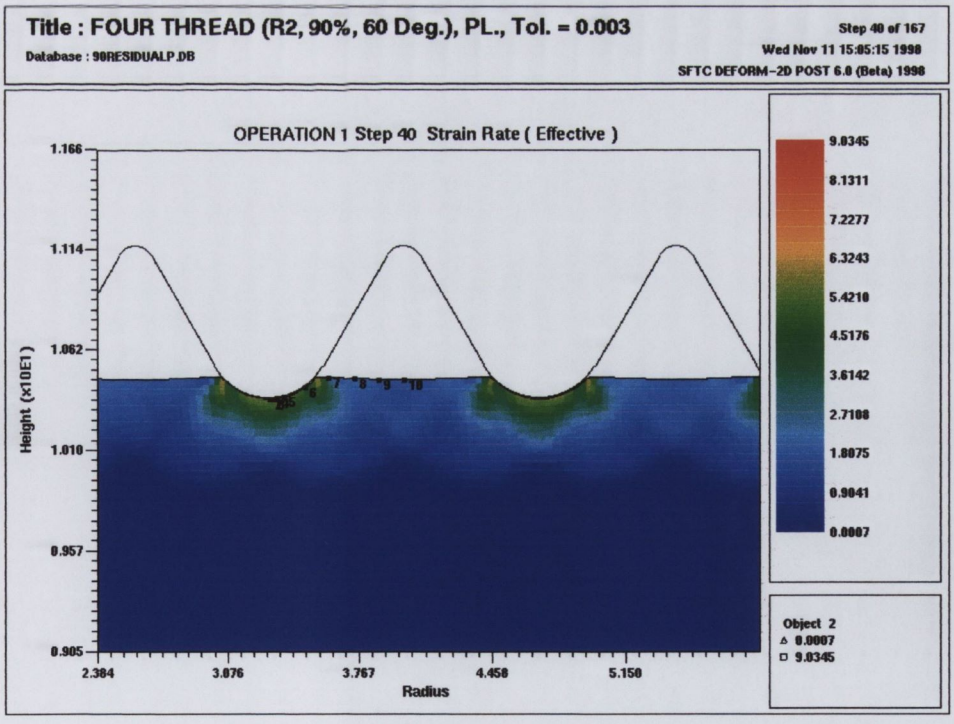

(Maximum: 9.035 s^{-1}, Minimum: 0 s^{-1})

Figure 5.79: Effective Strain Rate at 0.09mm, R2=0.3327mm (0.0131in.) Design

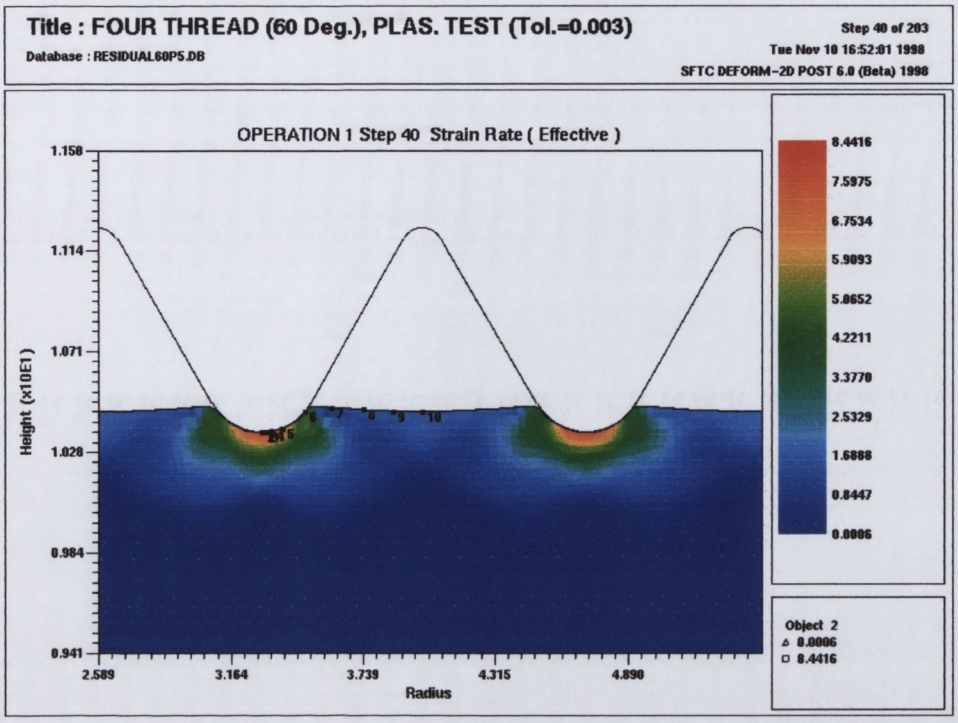

(Maximum: 8.44 s^{-1}, Minimum: 0 s^{-1})

Figure 5.80: Effective Strain Rate at 0.09mm, Standard R2=0.2438mm (0.0096in.)

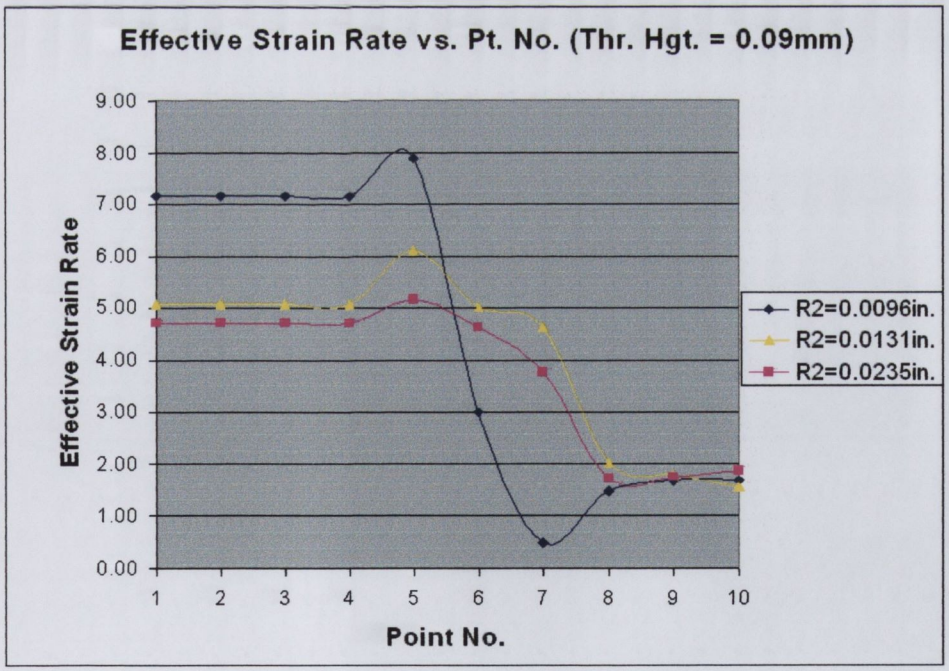

Figure 5.81: Effective Strain Rate vs. Pt. No., Thread Height = 0.09mm

Thread Height = 0.44mm

It can be seen that in the case of the R2=0.5969mm (0.0235in.) die design (Figure 5.82) it has almost formed its maximum possible thread height by this stage of the process. The packing of the deforming material which is occurring at this stage of thread formation is very evident at the top of the formed thread (green contour) where strain rates are concentrated. This concentration is caused by the two strain rate bands which extend from the final contact point of the material on the flank of the thread form. Because this material is packed into the top of the thread form the two bands appear to have merged into one central area.

In Figure 5.83, the R2=0.3327mm (0.0131in.) die design and Figure 5.84, the standard R2 die design, the bands of high strain rate are very noticeable. They again extend from the flank of the thread at an angle of approximately 45 degrees (in the case of the standard R2). As the material is moved further into the die, this angle seems to change slightly, as the final contact point changes. It is closer to 60 degrees in the case of the R2=0.3327mm (0.0131in.) die design. These strain rate bands join with the strain rate concentration areas beneath the apex of the crest radii (evident in Figures 5.83 and 5.84).

Figure 5.85 shows the effective strain rate curves over the tracking points for the three designs at this level of thread formation. The R2=0.0235in. design (as in the previous stage of deformation) shows the lowest strain rate beneath the crest radius (points 1-3) but the magnitude of this strain rate is maintained over points 4-8 and jumps significantly at point 8 due to the packing of the material which was seen in the effective strain plot. The other two designs follow a similar trend with the peak in effective strain rate occurring at the same point in the plots but picked up at different tracking points due to the different geometries.

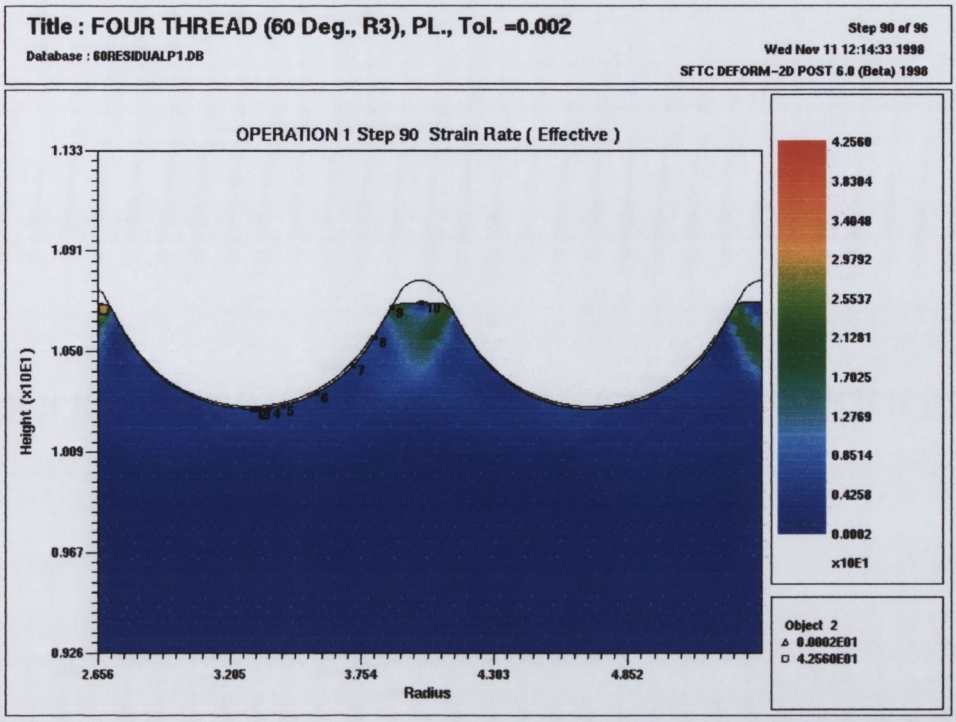

(Maximum: 42.56 s^{-1}, Minimum: 0 s^{-1})

Figure 5.82: Effective Strain Rate at 0.44mm, R2=0.5969mm (0.0235in.) Design

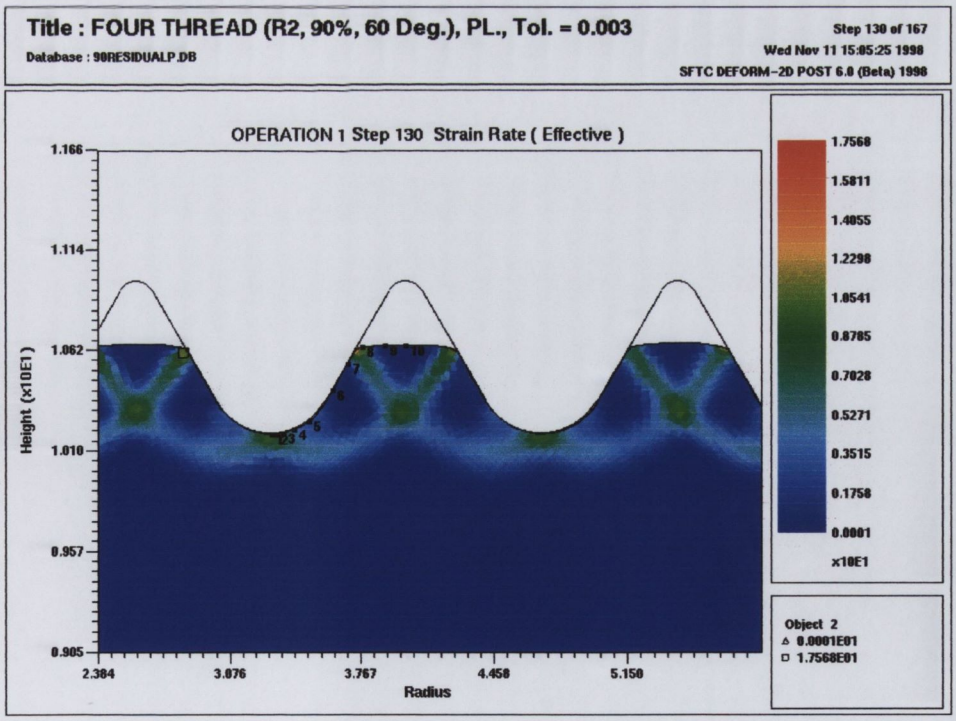

(Maximum: 17.57 s^{-1}, Minimum: 0 s^{-1})

Figure 5.83: Effective Strain Rate at 0.44mm, R2=0.3327mm (0.0131in.) Design

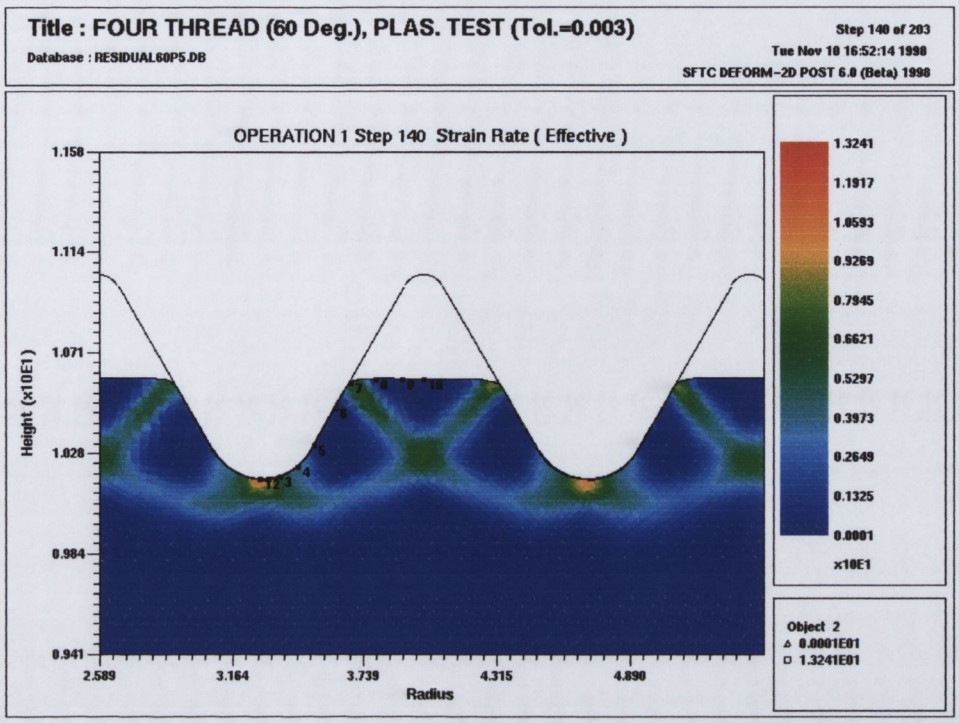

(Maximum: 13.24 s^{-1}, Minimum: 0 s^{-1})

Figure 5.84: Effective Strain Rate at 0.44mm, Standard R2=0.2438mm (0.0096in.)

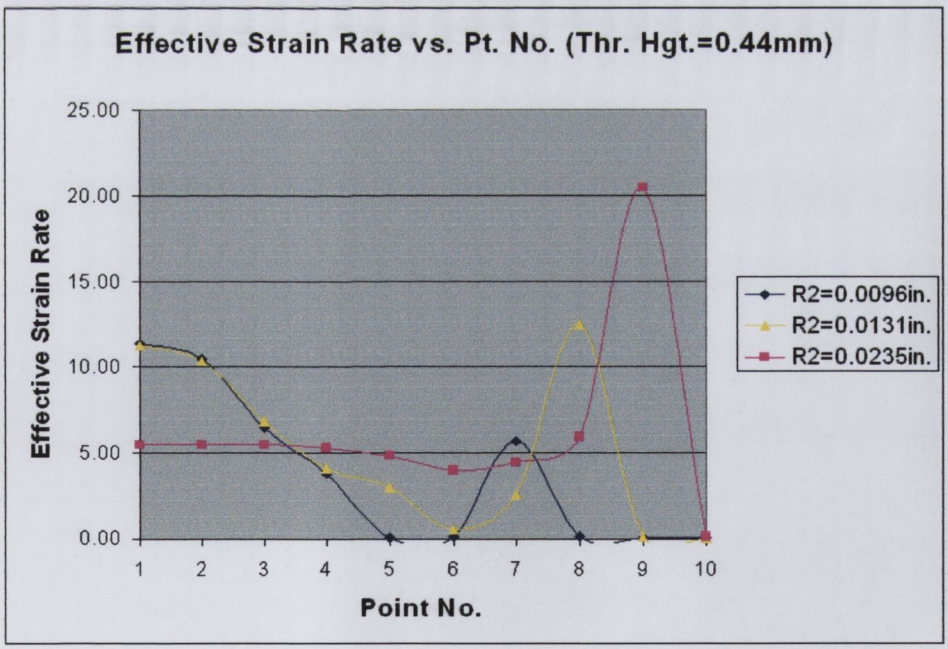

Figure 5.85: Effective Strain Rate vs. Pt. No., Thread Height = 0.44mm

Thread Height = 0.72mm

The deforming material for the R2=0.5969mm (0.0235in.) die design in Figure 5.86 has at this stage been transferred to the standard 60 degree form so that the final thread form may be completed. This transition between thread forms is again evident on the upper part of the partially formed thread. Strain rate banding is also evident as is the merging of these bands with the strain rate concentrations beneath the crest radius.

In the other two designs, the R2=0.3327mm (0.0131in.) die design and the standard R2 die design, Figures 5.87 and 5.88 respectively, packing of the fastener material is taking place at the top of the thread form and so strain rates are concentrated in this area. In the R2=0.3327mm (0.0131in.) die design, the deformed material is almost at the point where it is transferred to the standard R2 thread form so as to complete thread formation. There are still traces of strain rate bands from the flank of the thread form extending to the deformed material at the crest radius.

The curves for effective strain rate in Figure 5.89 again show that at the thread root the larger crest radii (R2) die designs do not perform as well as the standard tooling at this level of thread formation. However, strain rates are dramatically lower over points 7-10 for the large crest radius dies. The material in the standard R2 design and the R2=0.3327mm (0.0131in.) designs experience strain rates greater than 40 s^{-1}. However the R2=0.5969mm (0.0235in.) design shows the highest strain rates over points 1-4 (beneath the crest radius). This is caused by the smaller R2 of the standard thread form deforming the surface previously deformed by the larger R2=0.0235in. design.

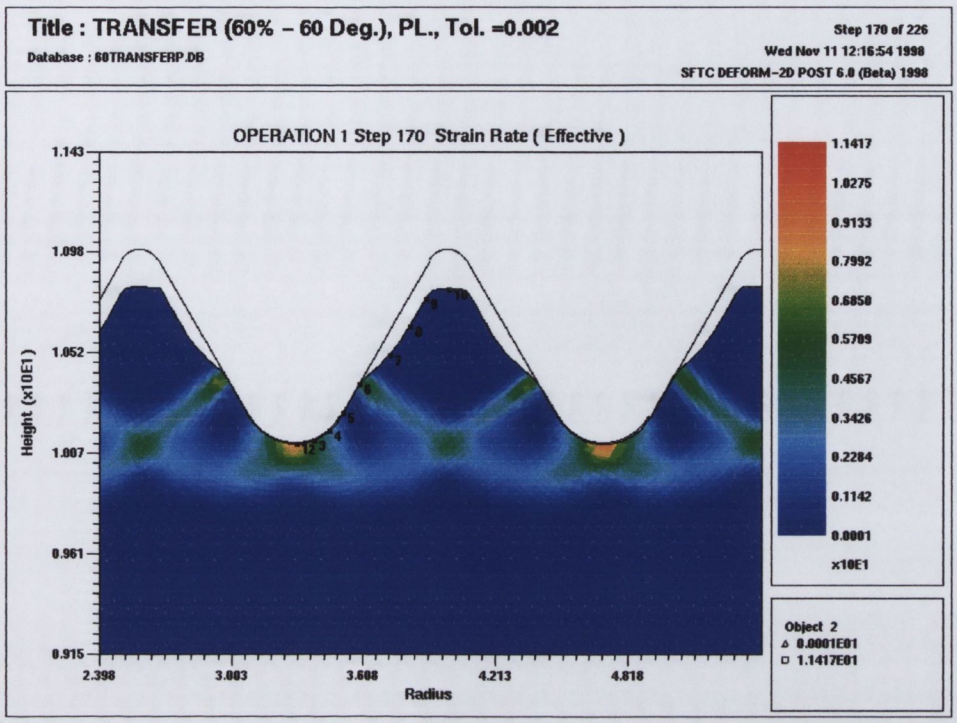

(Maximum: 11.42 s^{-1}, Minimum: 0 s^{-1})

Figure 5.86: Effective Strain Rate at 0.72mm, R2=0.5969mm (0.0235in.) Design

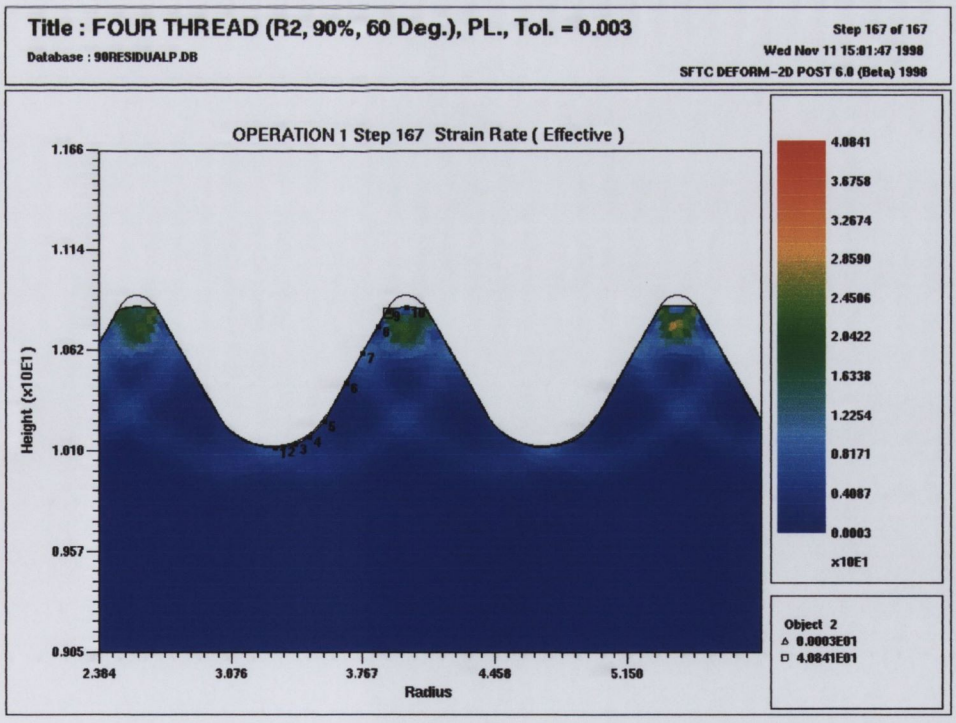

(Maximum: 40.84 s^{-1}, Minimum: 0 s^{-1})

Figure 5.87: Effective Strain Rate at 0.72mm, R2=0.3327mm (0.0131in.) Design

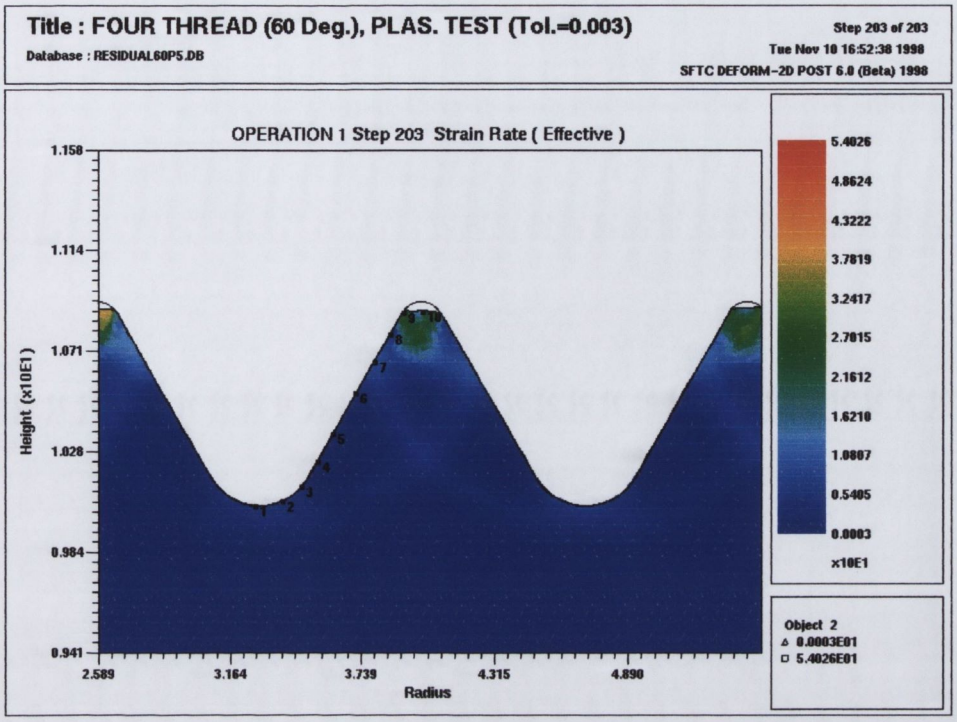

(Maximum: 54.03 s^{-1}, Minimum: 0 s^{-1})

Figure 5.88: Effective Strain Rate at 0.72mm, Standard R2=0.2438mm (0.0096in.)

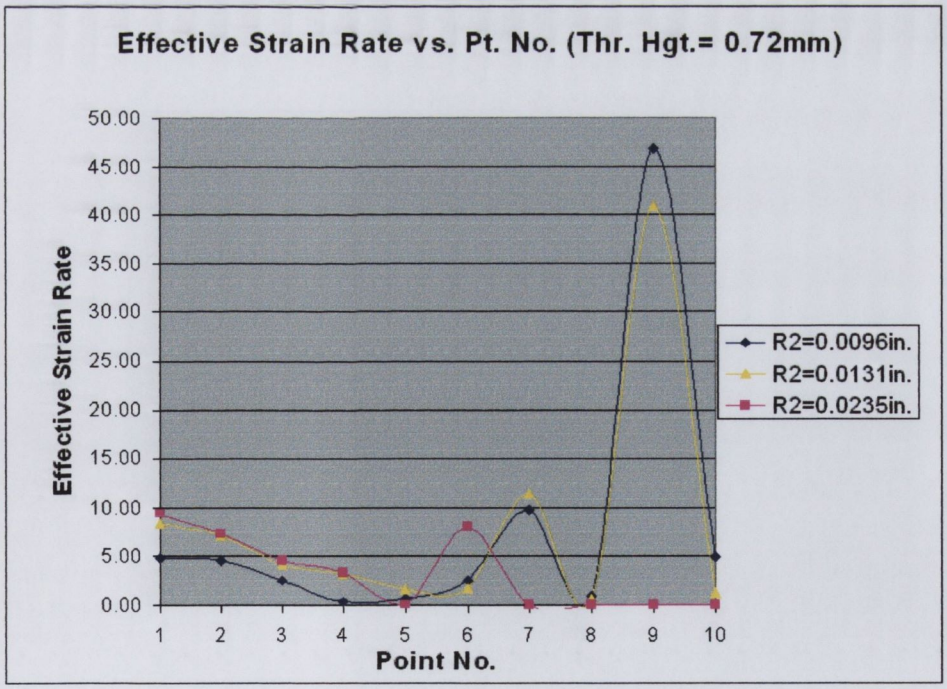

Figure 5.89: Effective Strain Rate vs. Pt. No., Thread Height = 0.72mm

5.4.4 Summary

Figure 5.90 below shows effective strain results measured at the thread root (point 1) as thread formation proceeds.

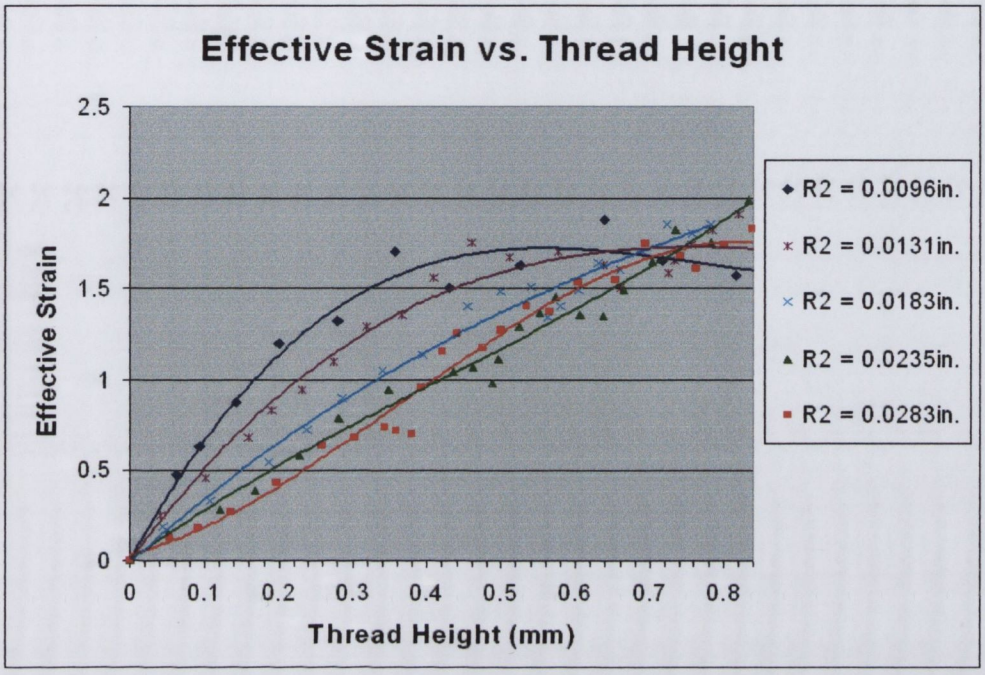

Figure 5.90: Effective Strain vs. Thread Height

The main points that can be drawn from this section may be summarised as follows.

- As in the case of the included angle design results (section 5.3.4), the standard R2, 60 Degree included angle thread form produces the highest overall strain profile over the forming process.
- The modified R2 designs produced lower strain and strain rate levels at the start of the thread formation process.
- There is a high "acceptable range" for the size of the crest radius (R2) i.e. 0.3327mm - 0.5969mm (0.0131in. - 0.0235in), that will result in lower initial strains and strain rates.
- One interesting feature of the modified crest radius designs is that all strains of the modified R2 models are higher at the end of the process which is in direct contrast to the included angle designs.

- The effective stress is not influenced significantly by modifications to the size of the crest radius. This implies that residual stresses and therefore the fatigue strength of the finished fastener will be unaffected by this design modification.

- The strain and the strain rate at the thread root decreases as R2 is increased.

- The results from the included angle designs and the modified crest radius designs raised the issue of whether a combination die design should be used? The included angle designs produced benefits at the end of the thread formation process while the modified crest radius designs produced benefits at the start of the process. If a combination of change in included angle and crest radius is used, it is possible that both benefits could be brought to bear on the effective formation of a thread.

5.5 Combination Design

The results presented in the previous two sections pointed to the possible advantage of combining the 120 degree included angle design, which reduces strains at the end of the forming process, and the R2=0.5969mm (0.0235in.) crest radius design, which reduces strain at the start of the process into one *combination* thread rolling die design. The starting form of this "combination" design thread rolling die can be seen schematically in Figure 5.91.

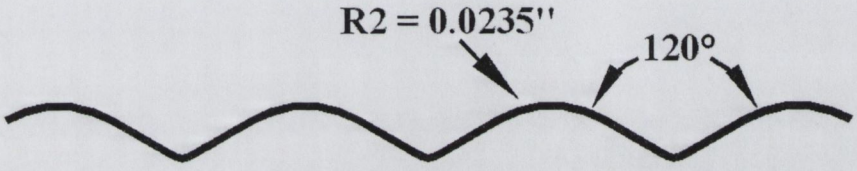

Figure 5.91: Schematic of Combination Design

5.5.1 Effective Stress Results

This section will describe the effective stress results from the combination models at three stages during the formation of the thread. These three stages correspond to the partially formed thread heights used previously of 0.09mm, 0.44mm, and 0.71mm respectively. The results for four of the designs will be presented in this and upcoming sections in the graphs of effective stress, effective strain, and effective strain rate. The purpose of these four curves will be to show a direct comparison between the included angle die designs, the modified crest radius designs, the combination die design, and the standard thread rolling die.

Thread Height = 0.09mm

The combination design in Figure 5.92 shows a very similar effective stress distribution to the R2=0.5969mm (0.0235in.) die design shown in Figure 5.93. The stress below the apex of the crest radius (point 1) is $\approx$ (1450 N/mm^2) in both designs. The depth of the effect of the effective stress is reasonably uniform beneath the thread form in both of these designs which is distinctly different from the standard 60 degree included angle with R2=0.2438mm (0.0096in.) thread form, shown in Figure 5.94. The stress directly beneath the crest radius in the standard design is equal to 1520 N/mm^2. These results again confirm that the crest radius is the dominant geometrical feature of the thread rolling die at this early stage of deformation process.

The effective stress curves shown in Figure 5.95 can be grouped into two distinct pairs, which confirm the comment above. The two thread form designs having the R2=0.2438mm (0.0096in.) crest radius, 60 degree and 120 degree included angle, follow each other in both in trend and magnitude. The magnitudes are higher by approximately 6% over points 1-6 compared to the other two curves. The second pair of curves are the two designs based on the larger crest radius (R2=0.5969mm (0.0235in.)). These latter two designs also have included angles of 60 and 120 degrees respectively but their trend and magnitudes also reflect each other almost exactly. In this case the stress does not start to drop away until point 7. As before this can be explained by the increased contact area that a larger crest radius makes during initial thread formation, and which lowers the overall stress distribution.

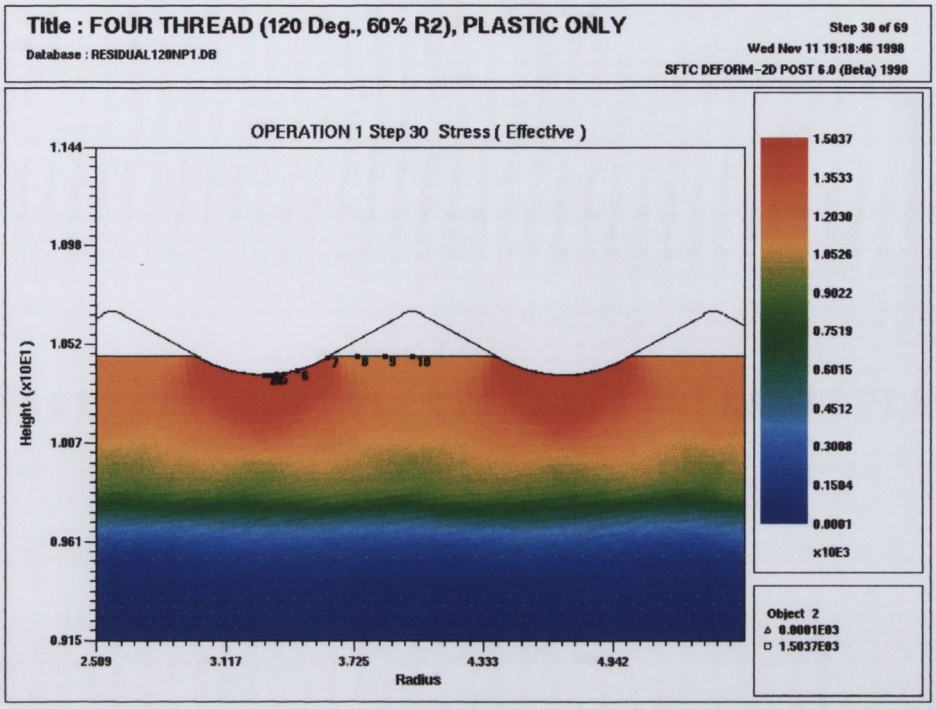

(Maximum: 1504 N/mm^2, Minimum: 0 N/mm^2)

Figure 5.92: Effec. Stress at 0.09mm, Combined 120 Deg. incl. angle & R2=0.5969mm Design

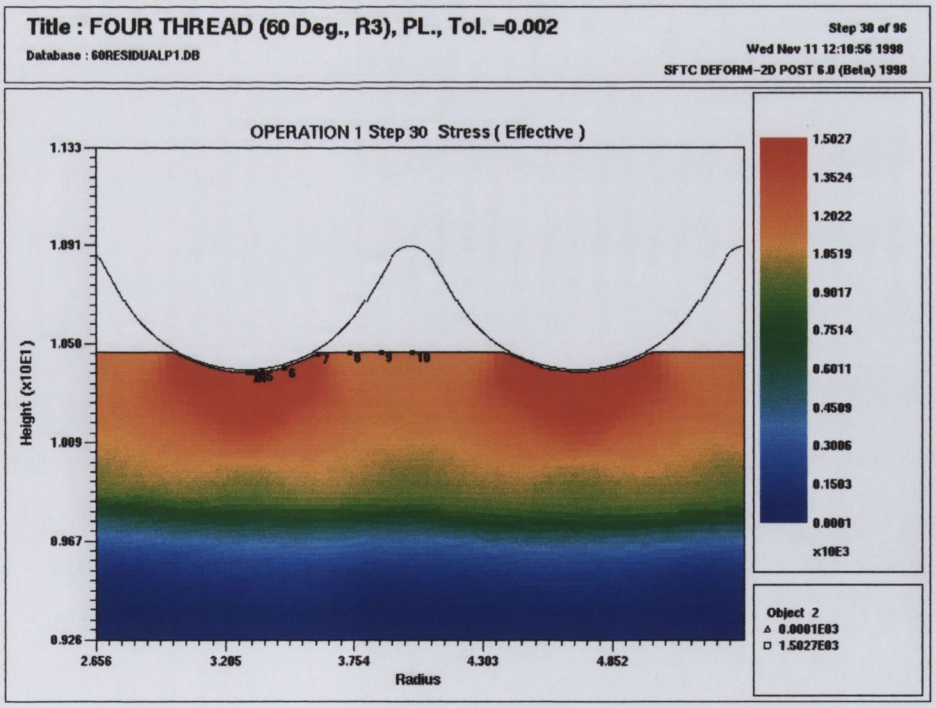

(Maximum: 1503 N/mm^2, Minimum: 0 N/mm^2)

Figure 5.93: Effec. Stress at 0.44mm, 60 Deg. incl. angle & R2=0.5969mm Design

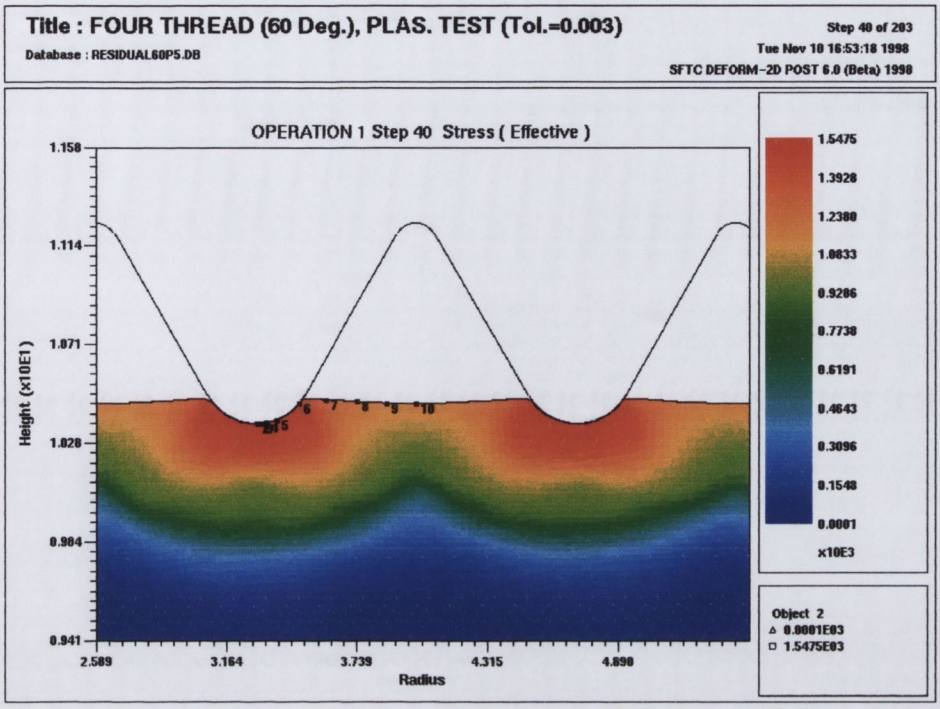

(Maximum: 1547 N/mm^2, Minimum: 0 N/mm^2)

Figure 5.94: Effec. Stress at 0.09mm, Standard 60 Deg. incl. angle & R2=0.2438mm Design

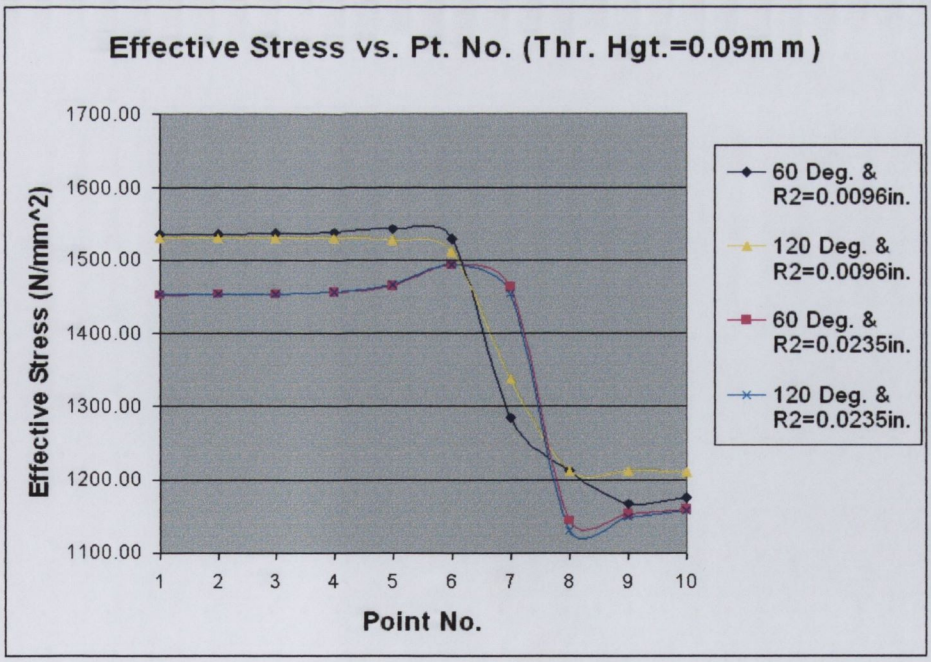

Figure 5.95: Effective Stress vs. Point No., Thread Height = 0.09mm

Thread Height = 0.44mm

By this stage of thread formation the combination design (120 degree included angle with R2=0.5969mm (0.0235in.)) has been transferred to the standard 60 degree & R2=0.2438mm (0.0096in.) die section (Figure 5.96). The distribution of the effective stress still appears to be of reasonably constant depth beneath the thread rolling die. The effect of the transition from the 120 degree included angle to the 60 degree included angle is evident on the upper portion of the partially formed thread as was also shown in some of the previous results. The 60 degree included angle with R2=0.5969mm (0.0235in.) design (Figure 5.97), presented previously in Figure 5.58 has almost reached the stage where it must be transferred to the standard thread form. At this stage an effective stress level $\approx$ 1550 N/mm^2 (red contour) is visible throughout the entire partially formed thread and has affected the fastener at an even level beneath the surface. The standard thread form (60 degree included angle with R2=0.2438mm (0.0096in.)) does not show this even stress distribution (Figure 5.98). This figure also shows regions of low stress on the flank of the thread form, which occur at point 5.

The graph in Figure 5.99 shows the effective stress levels over the tracked points for the four designs. The distinct pairings based on the two values of R2 are not very obvious by this stage of thread formation. All designs show a similar stress magnitude over points 1-4. The curve for the 60 degree included angle, R2=0.0096in. (standard) design picks up the low stress region on the flank of the thread form (point 5) and also the drop in effective stress on the free surface of the partially formed thread. The curve for the combination design (120 degree, R2=0.0235in.) also shows this low stress region on the flank of the thread form but it is smaller in size and lower in magnitude. The effective stress drops away quicker in this design as the initial use of a larger crest radius and included angle makes for a larger free surface, which is under a lower stress. The contact between the deforming material and the flank of the thread form ends earlier.

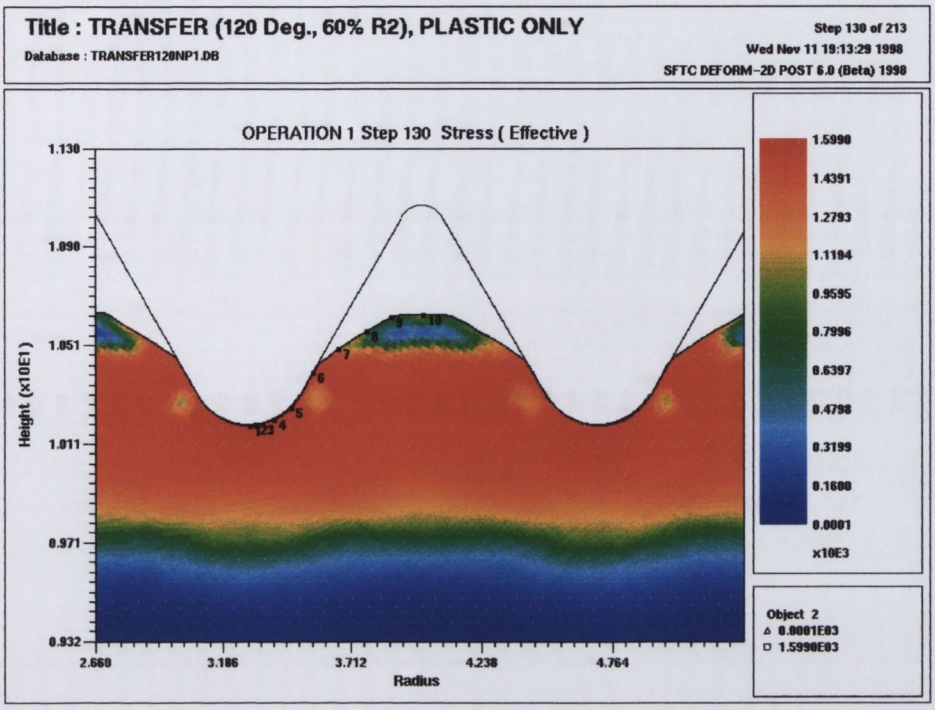

(Maximum: 1599 N/mm^2, Minimum: 0 N/mm^2)

Figure 5.96: Effec. Stress at 0.44mm, Combined 120 Deg. incl. angle & R2=0.5969mm Design

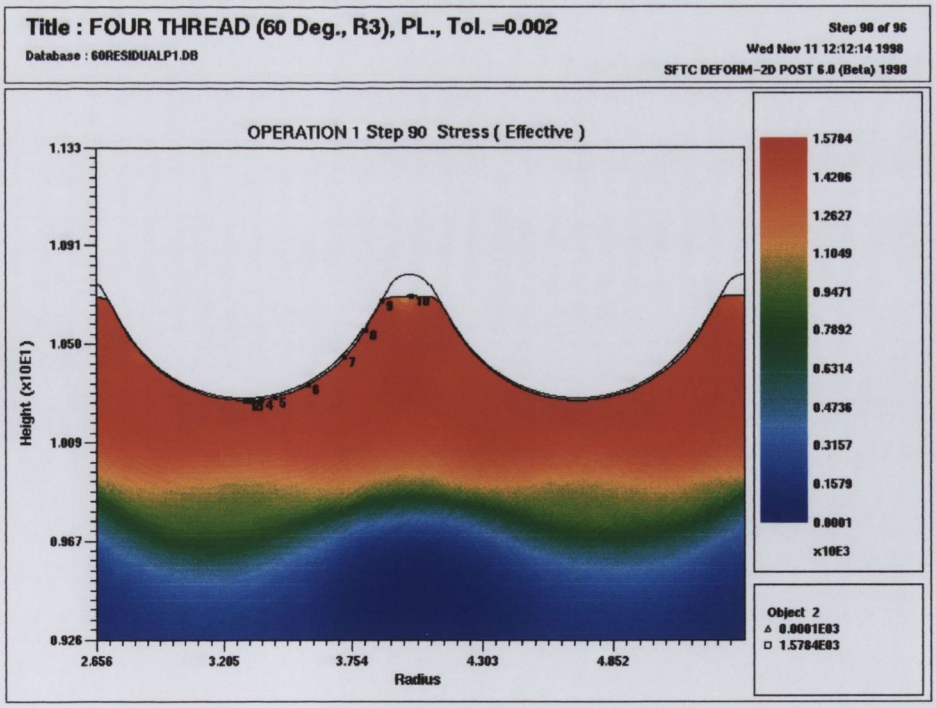

(Maximum: 1578 N/mm^2, Minimum: 0 N/mm^2)

Figure 5.97: Effec. Stress at 0.44mm, 60 Deg. incl. angle & R2=0.5969mm Design

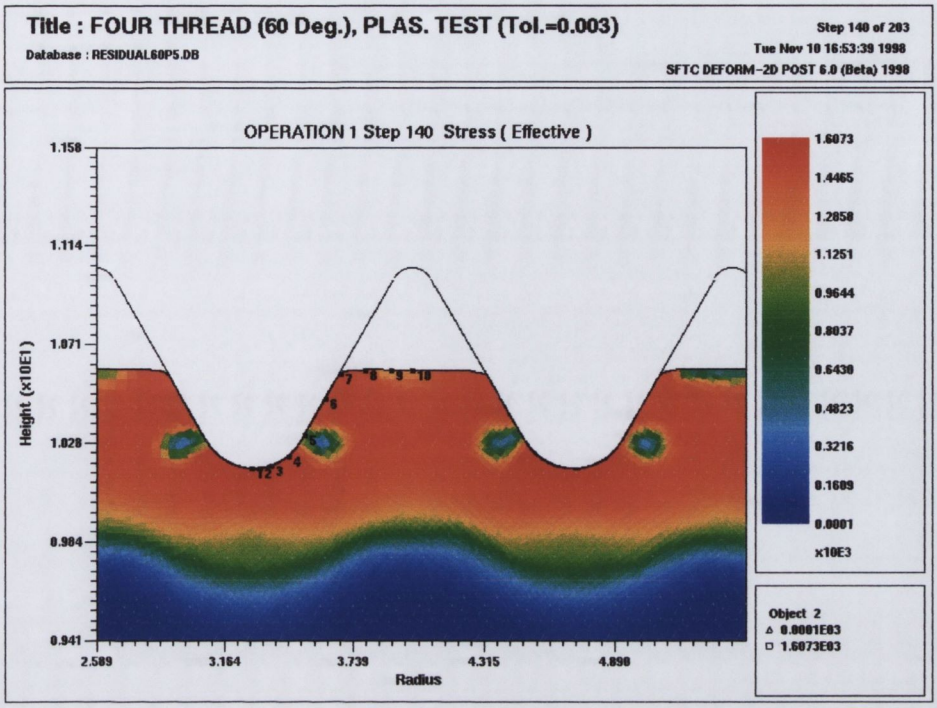

(Maximum: 1607 N/mm^2, Minimum: 0 N/mm^2)

Figure 5.98: Effec. Stress at 0.44mm, Standard 60 Deg. incl. angle & R2=0.2438mm Design

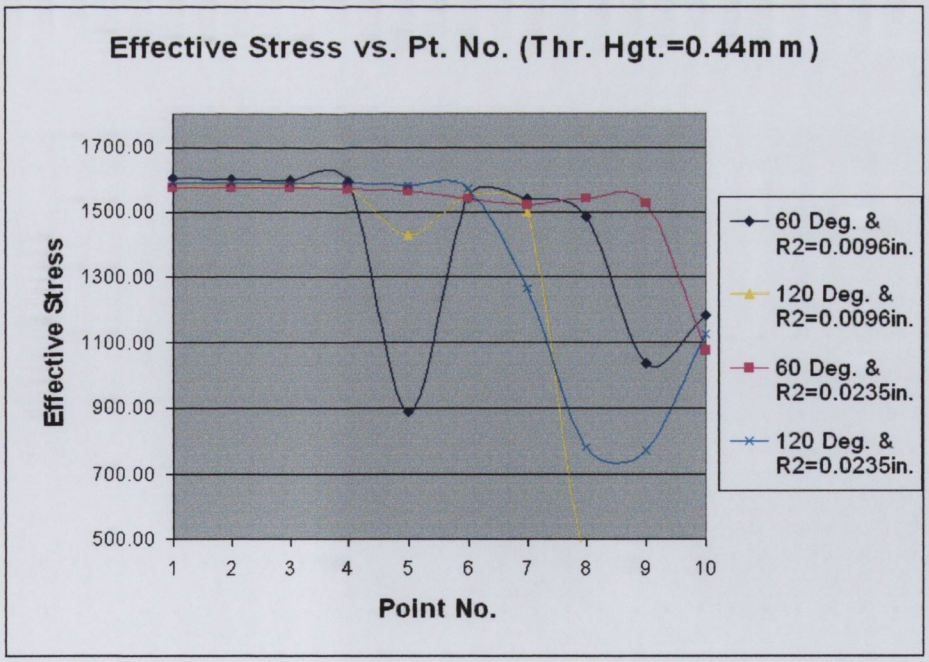

Figure 5.99: Effective Stress vs. Tracked Pt. No., Thread Height = 0.44mm

Thread Height = 0.71mm

Figure 5.100 shows the effective stress distribution for the combination die design at a partially formed thread height of 0.71mm. It can be seen that as the deforming material fills the thread form, the magnitude of the effective stress is more evenly distributed throughout the formed thread, except on the free surface (points 9-10). The depth of the stress distribution is now more pronounced beneath the two thread forms.

The 60 degree included angle with R2=0.5969mm (0.0235in.) die design, Figure 5.101, has transferred into the standard 60 degree included angle and R2=0.2348mm (0.0096in.) die design after a formed thread height of 0.53mm. It can be seen that the marks of the transition are evident on the upper part of the partially formed thread. The material slopes away from the flank of the thread form with a slight curve resulting from the large crest radius used in the initial deformation. The results for the standard 60 degree with R2=0.2348mm (0.0096in.) die design, Figure 5.102, look very similar to the combination design (120 degree included angle with R2=0.5969mm (0.0235in.)) and the material experiences the same effective stress distribution.

This would suggest that the combination die design proposed here is capable of producing the same final stress distribution as that of a fastener produced using standard dies, hence the fatigue strength should not be affected.

The graph in Figure 5.103 shows the effective stress curves for the different thread rolling die designs. All designs show similar stress magnitudes over points 1-6 ($\approx$ 1600 N/mm^2) but the different designs do give rise to very different drop-off points for the stress. The standard 60 degree included angle, R2=0.2348mm (0.0096in.) design has a high stress for all tracked points. The 60 degree with R2=0.5969mm (0.0235in.) design shows the effective stress dropping away at point 6. This is as a result of the transition from one thread rolling die form to another. The effective stress in the combination design drops off at a point which falls in between the 120 degree included angle with R2=0.2348mm (0.0096in) design and the 60 degree with R2=0.5969mm (0.0235in.) design.

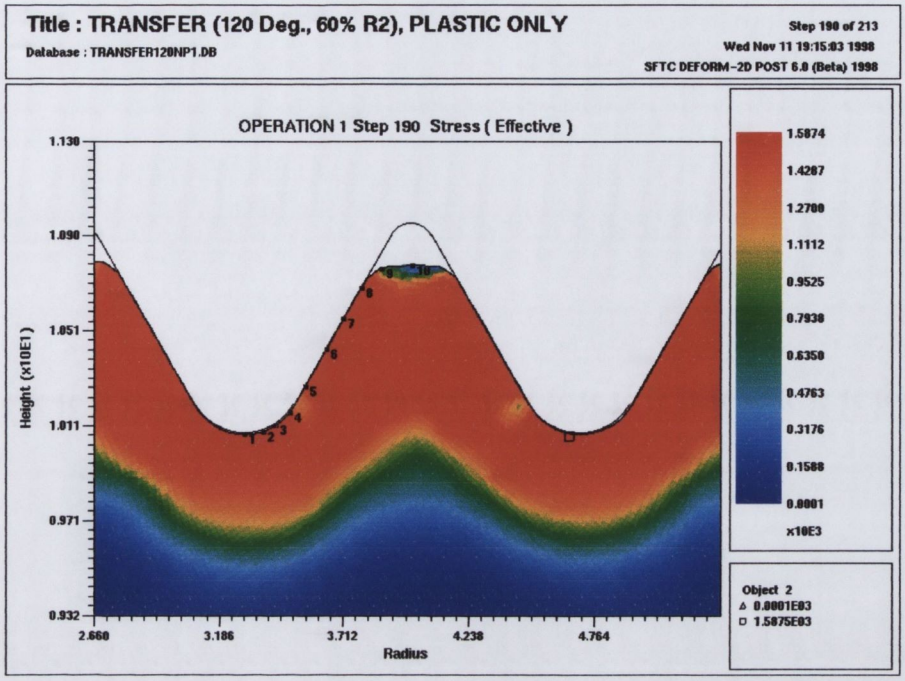

(Maximum: 1587 N/mm^2, Minimum: 0 N/mm^2)

Figure 5.100: Effective Stress at 0.71mm, Combined 120 Degree incl. Angle & R2=0.5969mm Design

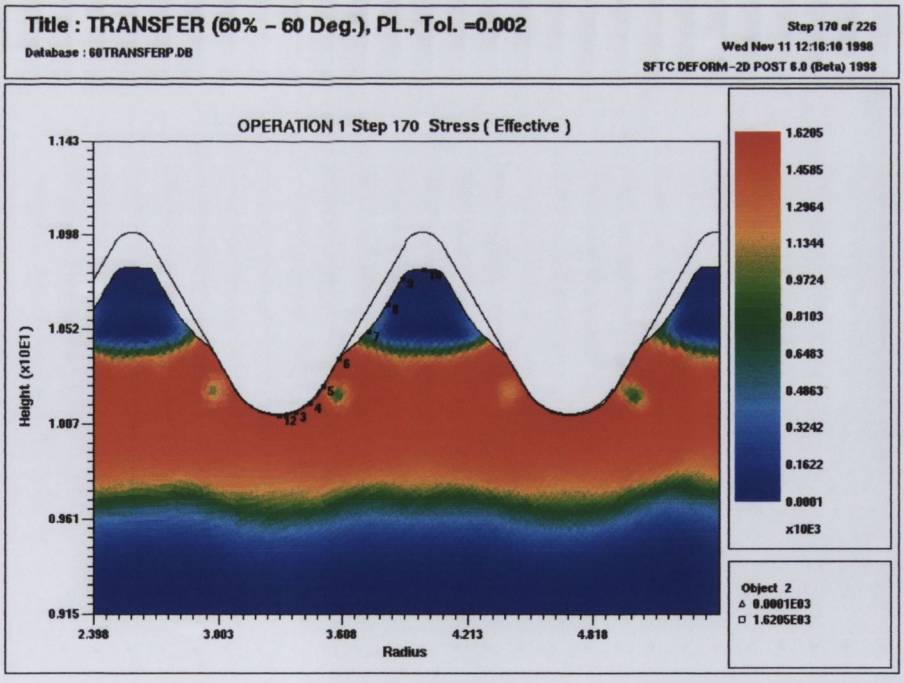

(Maximum: 1620 N/mm^2, Minimum: 0 N/mm^2)

Figure 5.101: Effec. Stress at 0.71mm, Combined 60 Deg. incl. angle & R2=0.5969mm Design

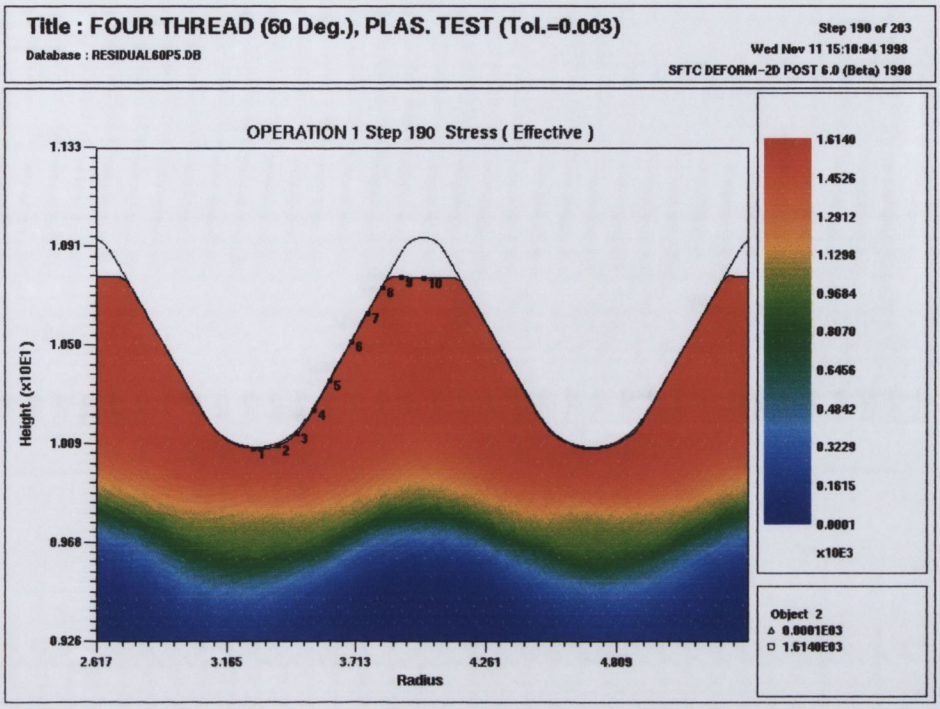

(Maximum: 1614 N/mm^2, Minimum: 0 N/mm^2)

Figure 5.102: Effec. Stress at 0.71mm, 60 Deg. incl. angle & R2=0.5969mm Design

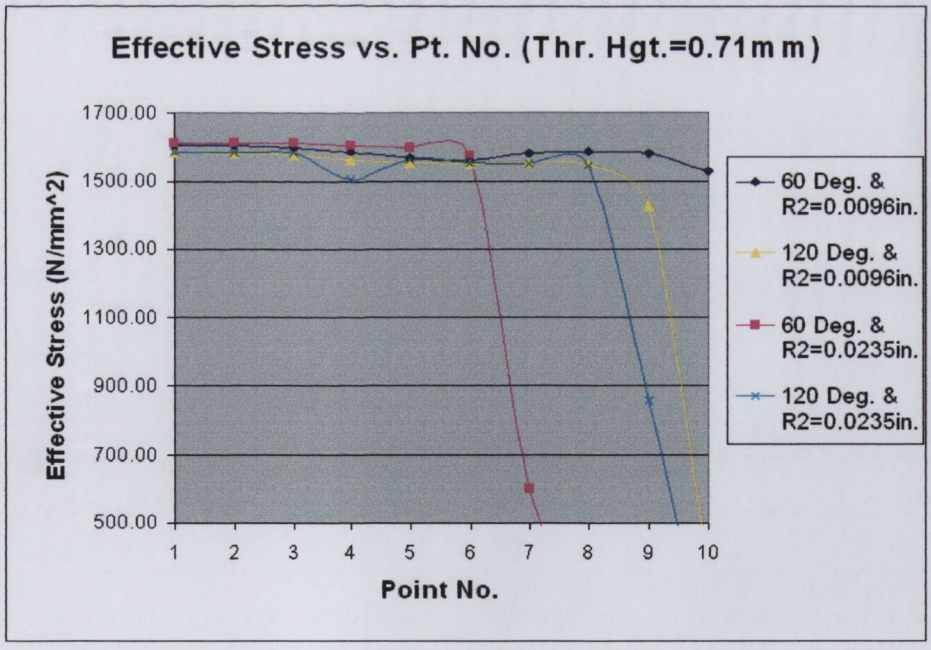

Figure 5.103: Effec. Stress at 0.71mm, Standard 60 Deg. incl. angle & R2=0.2438mm Design

5.5.2 Effective Strain Results

Thread Height = 0.09mm

The effective strain at an early stage of thread formation for the combination die design (120 degree included angle and R2=0.5969mm (0.0235in.)) is shown in Figure 5.104, and for the case of the 60 degree included angle & R2=0.5969mm (0.0235in.) design in Figure 5.105. As in case of the effective stress plots, the effective strain plots all look similar at this early stage of deformation. The maximum effective strain does not occur directly beneath the crest radius, there are also two areas of strain concentration either side of the apex of the radius, and this is where the maximum strain occurs. The magnitude of the strain for both designs is also very close (≈ 0.4). The standard 60 degree included angle with R2=0.2438mm (0.0096in.) design, in Figure 5.106, shows very distinct areas of strain concentration directly beneath the crest radius and it is of much higher magnitude than the other designs (≈ 0.7) mentioned above. The area of strain concentration is not as deep as the large R2 designs but is of a much higher magnitude.

The curves in Figure 5.107 show the same pairing aspect mentioned previously for the effective stress results (section 5.5.1). The magnitudes of the effective strain produced by the R2=0.2438mm (0.0096in.) die designs are both significantly higher over points 1-5 compared to the tooling having R2=0.5969mm (0.0235in.) This is caused by the effect of initially deforming the fastener surface with a smaller crest radius. The large R2 designs (R2=0.2438mm (0.0235in.)) confirm the definite benefit that this design change affords the deforming material. However, changing the included angle of the thread form seems to make no difference to the effective strains at this level of thread formation which also confirms the results from the previous sections. In conclusion dies having R2=0.5969mm (0.0235in.) show a dramatic reduction in strain in the thread root region compared to those having R2=0.2438mm (0.0096in).

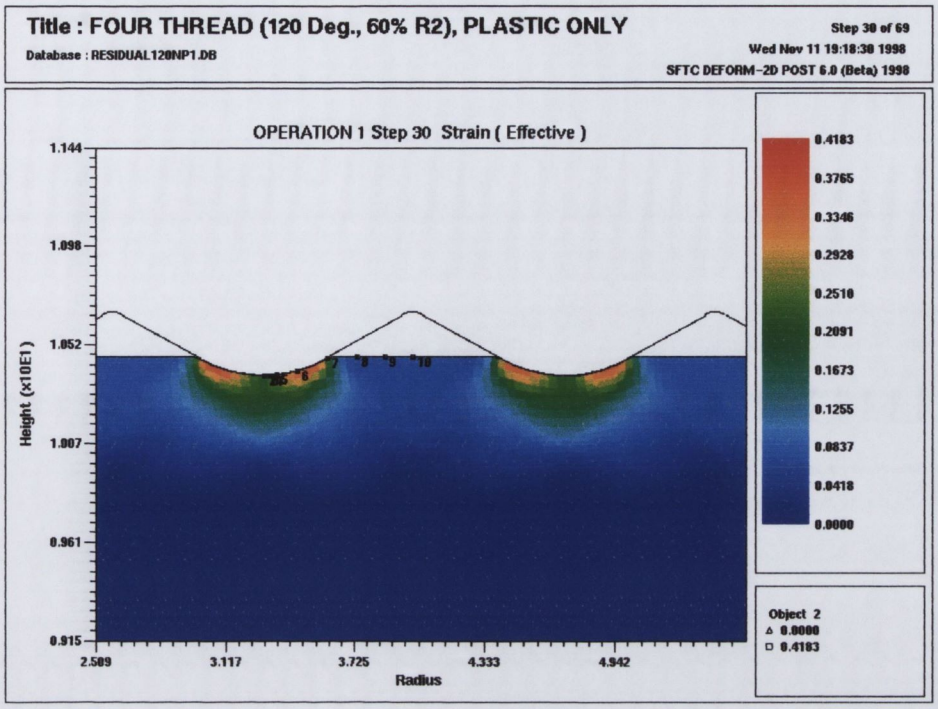

(Maximum: 0.4183, Minimum: 0)

Figure 5.104: Effec. Strain at 0.09mm, Combined 120 Deg. incl. angle & R2=0.5969mm Design

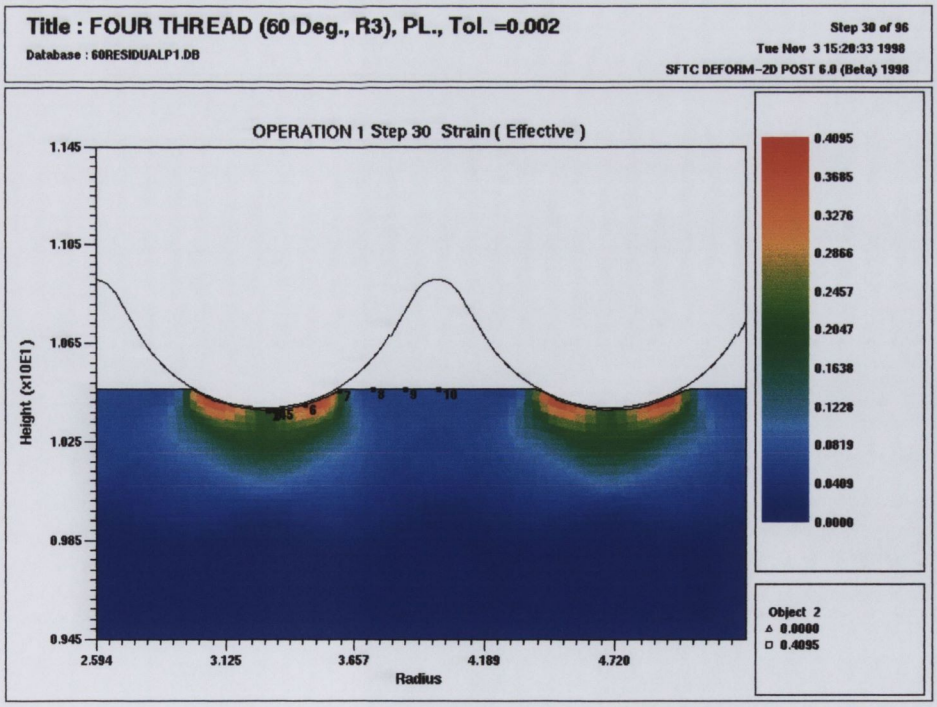

(Maximum: 0.4095, Minimum: 0)

Figure 5.105: Effec. Strain at 0.09mm, 60 Deg. incl. angle & R2=0.5969mm Design

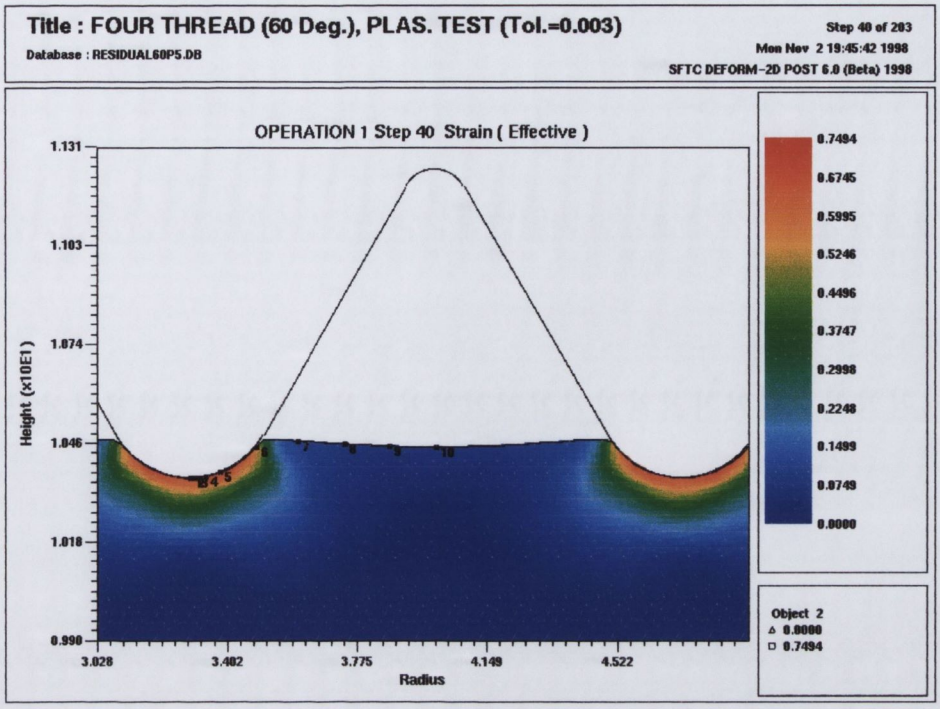

(Maximum: 0.7494, Minimum: 0)

Figure 5.106: Effec. Strain at 0.09mm, Standard 60 Deg. incl. angle & R2=0.2438mm Design

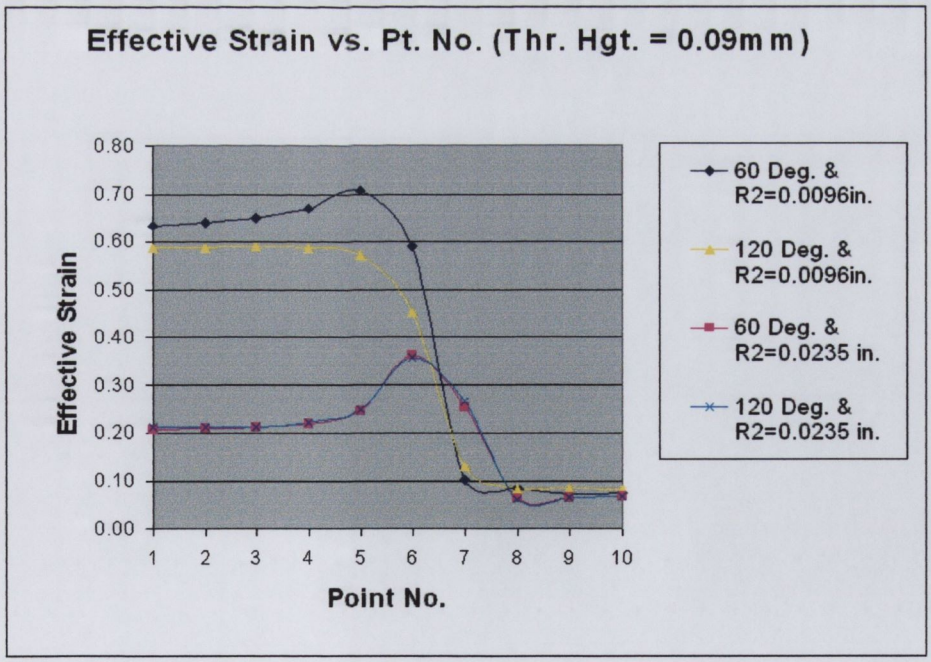

Figure 5.107: Effective Strain vs. Tracked Pt. No., Thread Height = 0.09mm

Thread Height = 0.44mm

By this level of thread formation the material in the combination design has transferred to the standard 60 degree with R2=0.2438mm (0.0096in.) thread form section of the die and deformation has proceeded as shown in Figure 5.108. Again the evidence of transition can be seen at points 7-9 on the upper portion of the thread. The material slopes away from the flank of the thread form at an angle corresponding to the earlier 120 degree included angle deformation. The maximum strain occurs beneath the apex of the crest radius at point 1 and subsequently drops away.

Figure 5.109 shows the effective strain in the 60 degree included angle, R2=0.5969mm (0.0235in.) design. This die design has almost formed the maximum thread height allowed by this geometry. Bands of high strain originating from the final contact points of the material along the flank and extending to the centre of the formed thread are evident. There are also strain concentrations beneath the crest radius. The standard 60 degree included angle, R2=0.2438mm (0.0096in.) design in Figure 5.110 clearly shows the difference between the standard and the combined design. In this case all material up to the free surface is in contact with the flank of the thread form which increases the overall strain in the material.

Figure 5.111 charts the effective strain curves over the tracking points for this level of thread formation. They all follow similar trends but the 60 degree, R2=0.5969mm (0.0235in.) design has the lowest maximum strain followed by the combination design and the 120 degree, R2=0.2438mm (0.0096in.) design. The 60 degree included angle, R2=0.2438mm (0.0096in.) (standard) design has the highest. It is evident from these curves that at this stage the 120 degree included angle is more influential than the crest radius on the thread rolling dies. This is illustrated by the fact that the effective strain distributions for both the 120 degree included angle with R2=0.2438mm (0.0096in.) and the 120 degree included angle with R2=0.5969mm (0.0235in.) are practically identical in the thread root region.

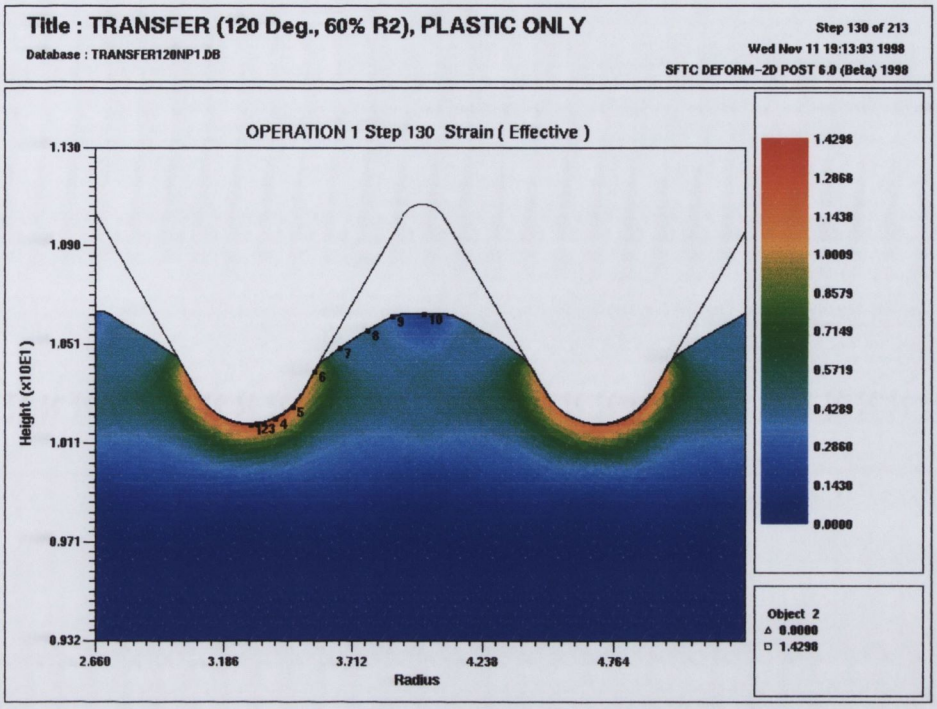

(Maximum: 1.4298, Minimum: 0)

Figure 5.108: Effec. Strain at 0.44mm, Combined 120 Deg. incl. angle & R2=0.5969mm Design

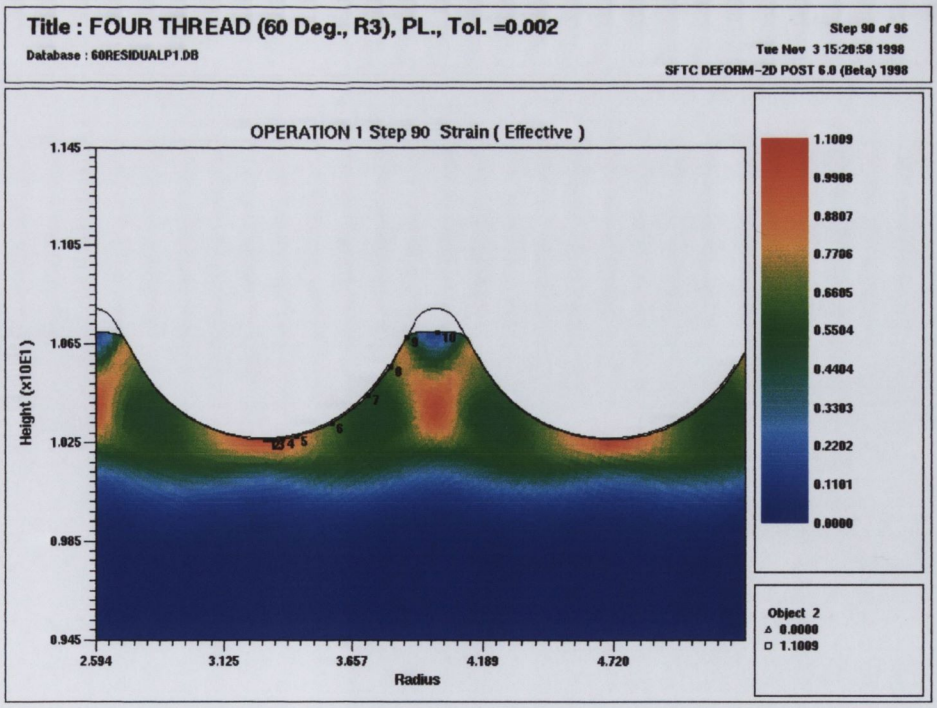

(Maximum: 1.1009, Minimum: 0)

Figure 5.109: Effec. Strain at 0.44mm, 60 Deg. incl. angle & R2=0.5969mm Design

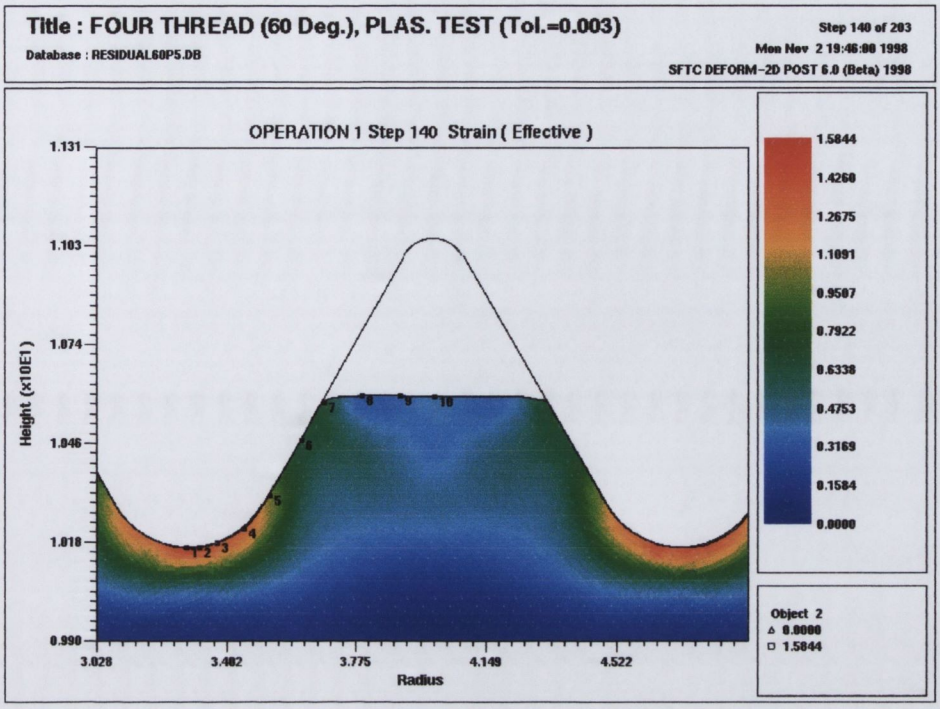

(Maximum: 1.5844, Minimum: 0)

Figure 5.110: Effec. Strain at 0.44mm, Standard 60 Deg. incl. angle & R2=0.2438mm Design

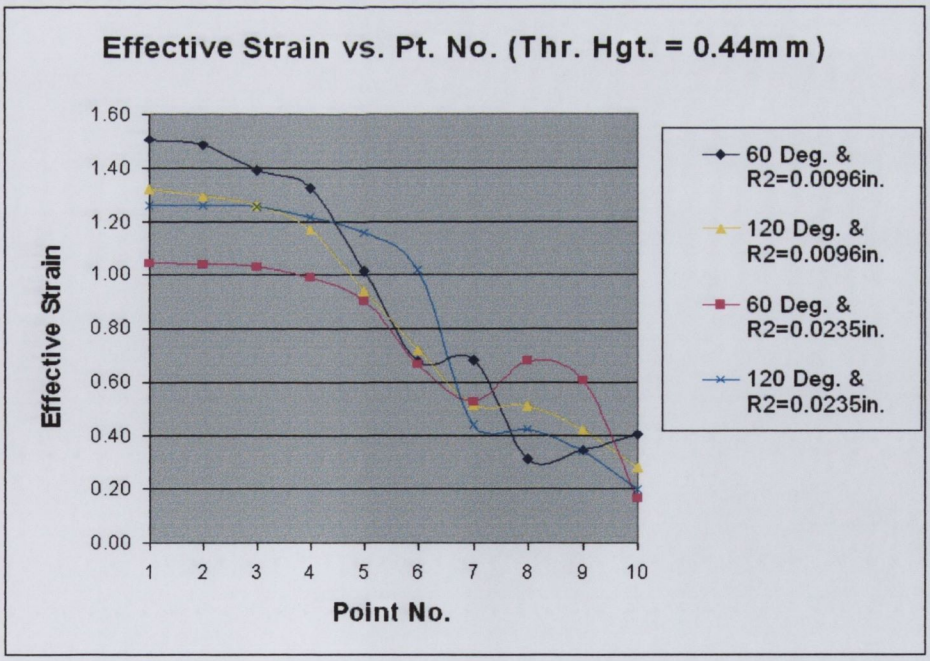

Figure 5.111: Effective Strain vs. Pt. No., Thread Height = 0.44mm

Thread Height = 0.71mm

Figure 5.112 shows the effective strain for the combination die design at an almost completely fully formed thread height of 0.71mm. The main areas of strain concentration are again beneath the apex of the crest radius and also at the centre of the forming thread where two bands of high strain extending from the flank of the thread form at approximately 45° merge (orange contours).

In Figure 5.113 the 60 degree included angle, R2=0.5969mm (0.0235in.) design the deforming material has been transferred and is being deformed by the standard (60 degree, R2=0.2438mm (0.0096in.)) die section. This transition is evident on the upper part of the partially formed thread but there are no high strain areas visible in the centre of the thread. This is because contact between the flank of the thread from and the material finishes at point 6 compared to between point 8 and 9 for the combination design.

Figure 5.114 shows the effective strain distribution for the standard thread form at this level of thread formation. It has a very similar distribution to the combination design but the magnitudes of the strains vary.

In Figure 5.115 the benefit of using the large included angle from the start of the forming process has become apparent. Both the 120 degree included angle designs indicate lower strains over points 1-6, at this level of thread formation i.e. near to completion. The advantage of using the large crest radius cannot be easily seen at this stage. However, the combination design seems to show lower strains over all the tracking points compared to all the other designs. The designs based on the 60 degree included angle starting form have higher strains over points 1-6.

In summary it has been shown that there are very distinct advantages in using the *progressive* thread rolling die design developed in this thesis. The large crest radius (R2) is beneficial at the start of the process, the large included angle towards the end. The combination die design results in lower overall strains without any significant reduction in the magnitude of the effective stress.

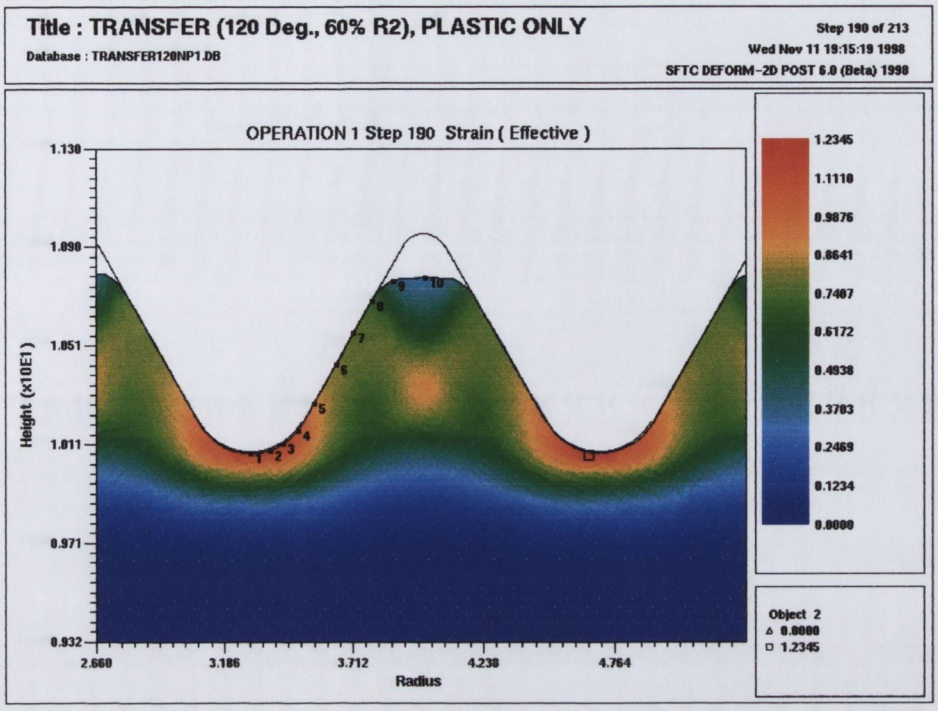

(Maximum: 1.2345, Minimum: 0)

Figure 5.112: Effec. Strain at 0.71mm, Combined 120 Deg. incl. angle & R2=0.5969mm Design

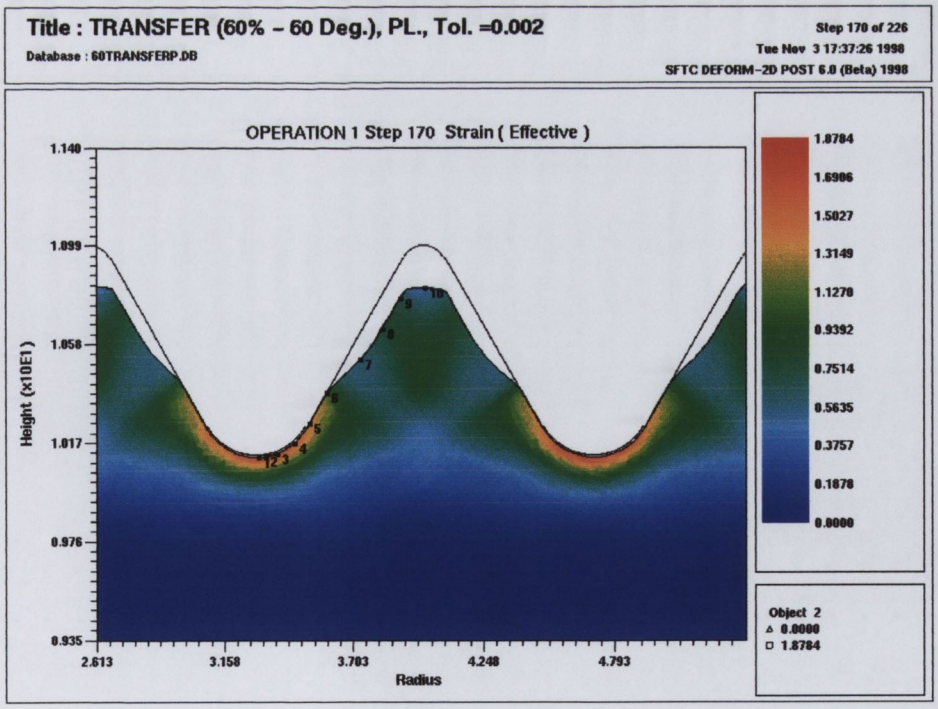

(Maximum: 1.8784, Minimum: 0)

Figure 5.113: Effec. Strain at 0.71mm, 60 Deg. incl. angle & R2=0.5969mm Design

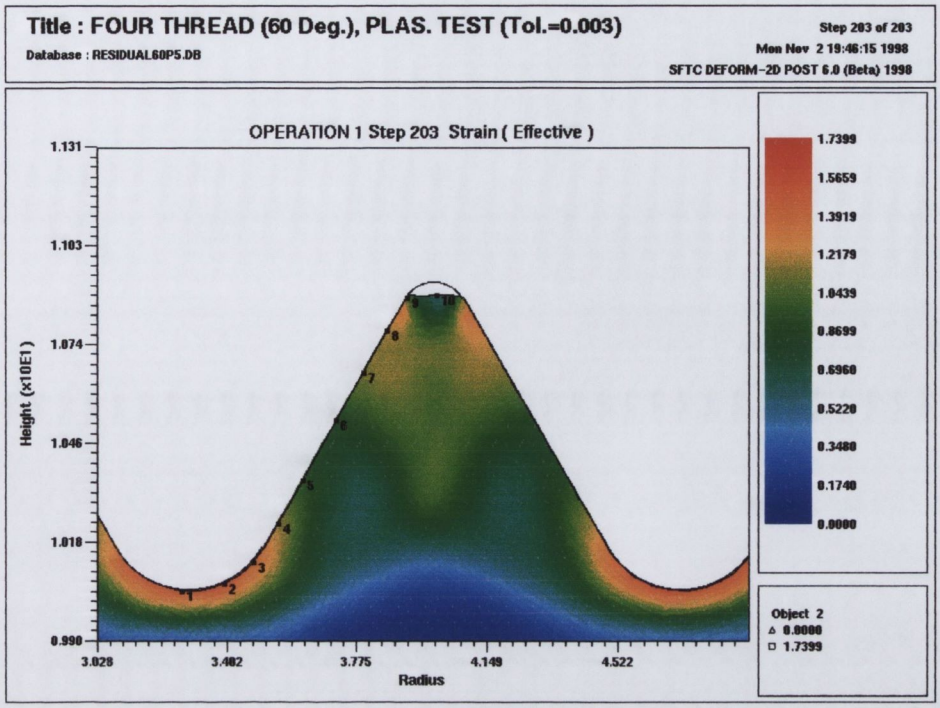

(Maximum: 1.7399, Minimum: 0)

Figure 5.114: Effec. Strain at 0.71mm, Standard 60 Deg. incl. angle & R2=0.2438mm Design

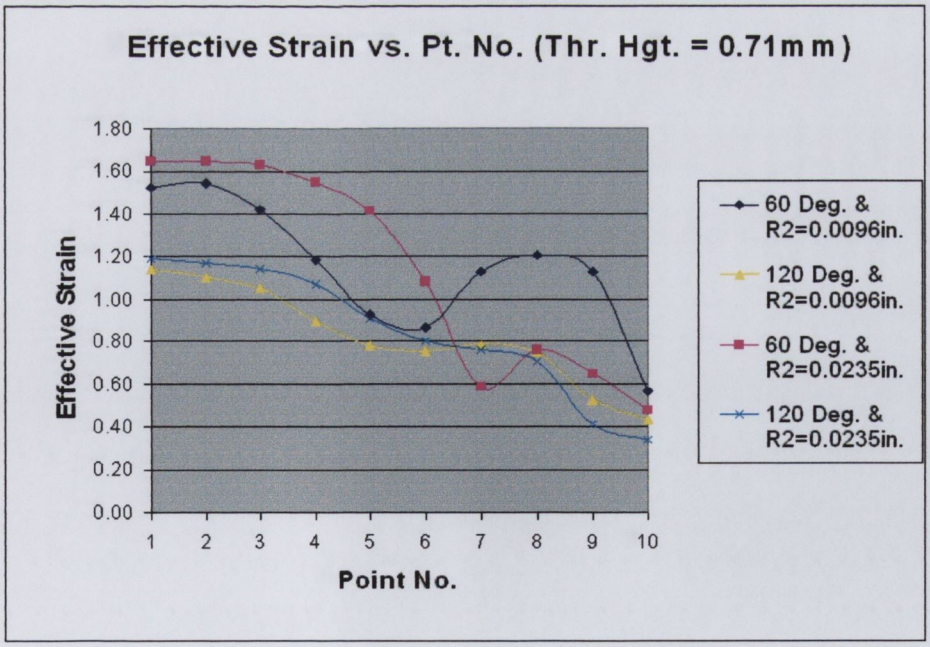

Figure 5.115: Effective Strain vs. Pt. No., Thread Height = 0.71mm

5.5.3 Effective Strain Rate Results

These results are presented for completeness, and for comparison with the results presented in section 5.3.3 and 5.4.3.

Thread Height=0.09mm

Figure 5.116 shows the effective strain rate in the combined design (120 degree & R2=0.5969mm (0.0235in.)) at a formed thread height of 0.09mm. As was seen in an earlier section the larger radius has some noticeably different effects on the strain rate pattern compared to the standard form (60 degree & R2=0.2438mm (0.0096in.), Figure 5.118. There are three distinct areas of strain rate concentration in both of the designs that initially use the larger R2 (0.5969mm) crest radius.

The maximum strain rates occur at the points where contact between the large crest radius and the fastener surface ends. The differences in the strain rate distributions between the two large R2=0.5969mm (0.0235in.) designs and the standard (60 degree included angle and R2=0.2438mm (0.0096in.)) design are very obvious from the effective strain rate plots. In the standard design the strain rate is concentrated beneath the crest radius due to the "sharper" nature of the smaller R2 (0.2438mm) crest radius.

The graph in Figure 5.119 confirms some of the comments made above. The curve for the combined die design (120 degree included angle, R2=0.5969mm (0.0235in.)) shows the lowest values for effective strain rate over points 1-5 (i.e. beneath the crest radius). A large peak in the curve occurs at point 7 where the tracking point falls in one of the adjacent strain rate concentration areas. The other large R2 design (60 degree included angle) shows the next lowest magnitudes while the 120 degree included angle with R2=0.2438mm (0.0096in.) also shows lower magnitudes than the standard (60 degree, R2=0.2438mm (0.0096in.)) design. These results again confirm that a large crest radius (R2) is of greatest benefit at the start of thread formation.

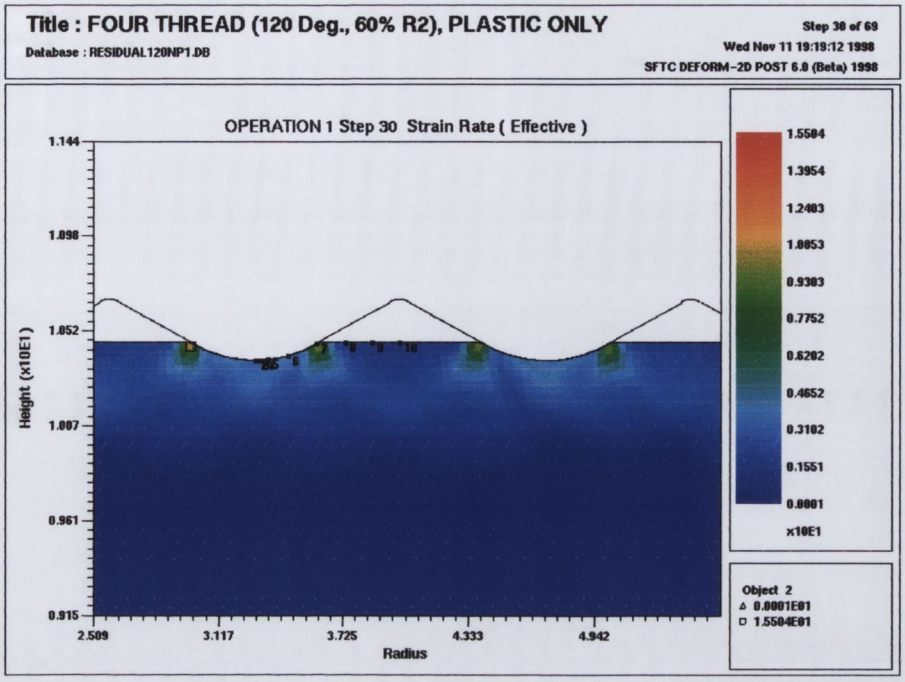

(Maximum: 15.50 s^{-1}, Minimum: 0 s^{-1})

Figure 5.116: Effec. Strain Rate at 0.09mm, Combined 120 Degree Incl. Angle & R2=0.5969mm Design

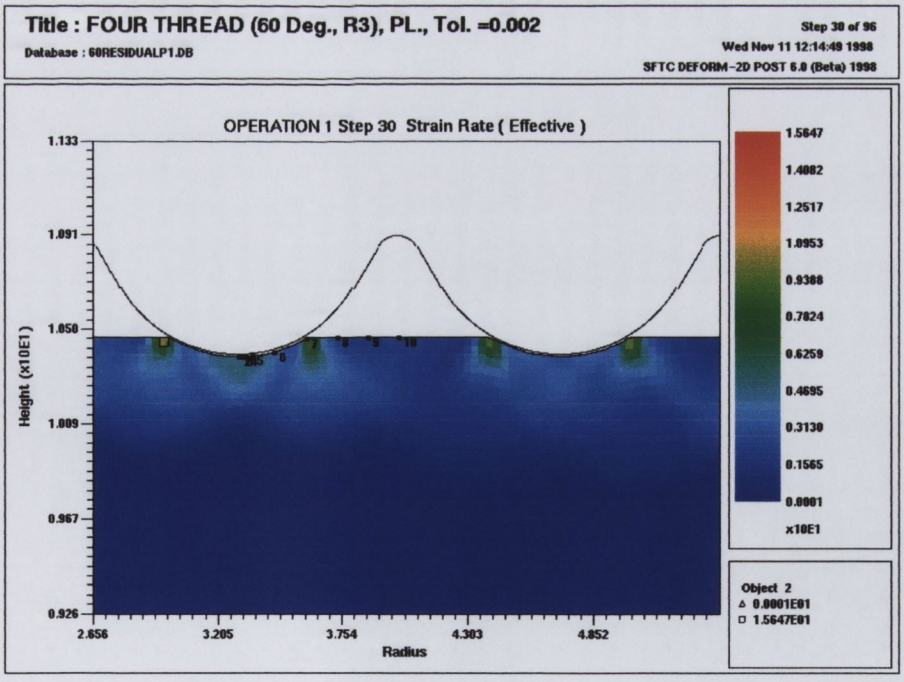

(Maximum: 15.65 s^{-1}, Minimum: 0 s^{-1})

Figure 5.117: Effec. Strain Rate at 0.09mm, 60 Deg. Incl. Angle & R2=0.5969mm Design

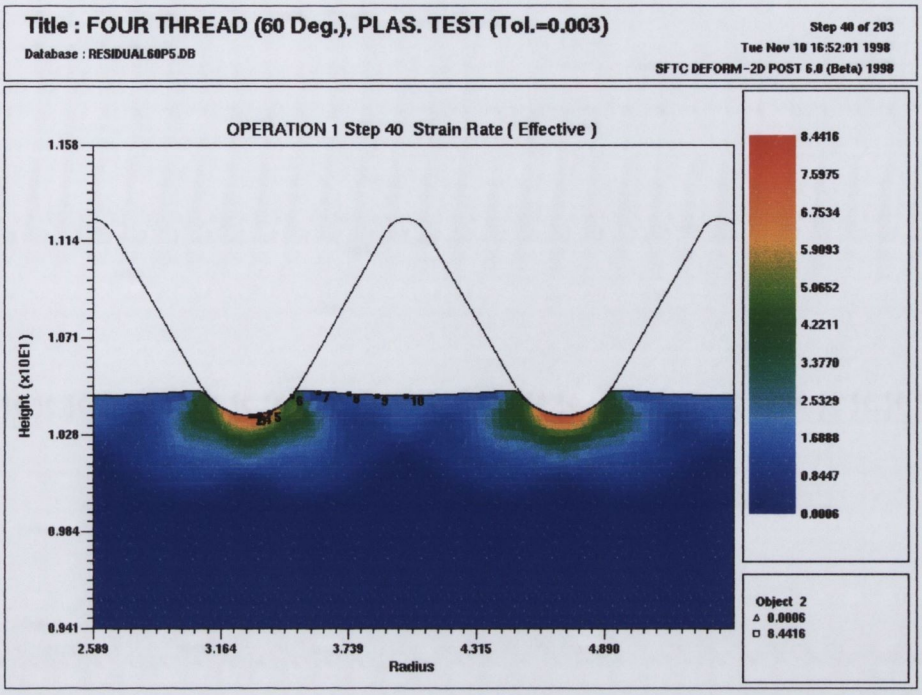

(Maximum: 8.44 s^{-1}, Minimum: 0 s^{-1})

Figure 5.118: Effec. Strain Rate at 0.44mm, Standard 60 Deg. Incl. Angle & R2=0.2438mm Design

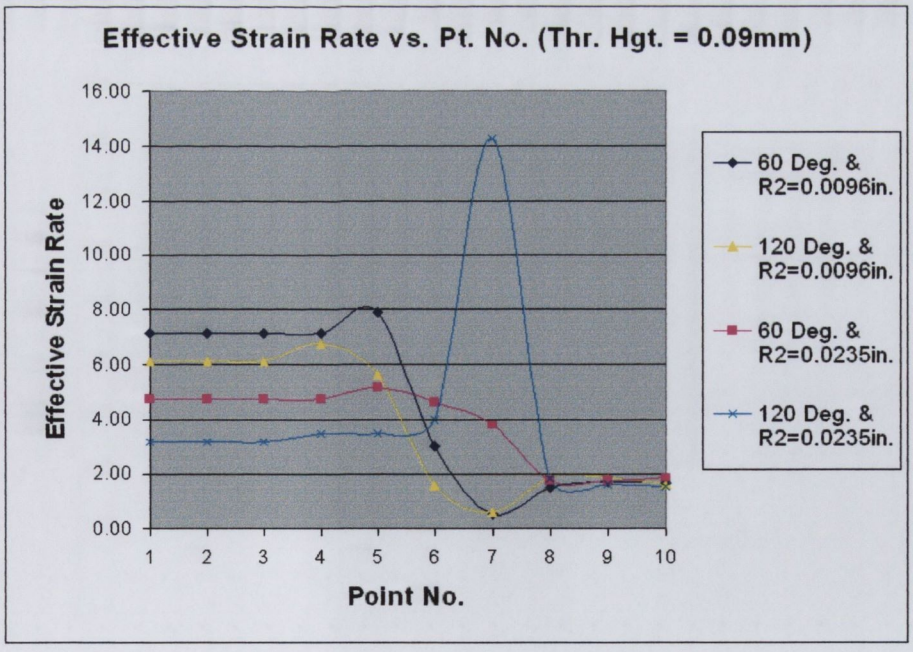

Figure 5.119: Effective Strain Rate vs. Point No., Thread Height = 0.09mm

Thread Height = 0.44mm

At a formed thread height of 0.44mm, the material in the combination die design (120 degree included angle, R2=0.5969mm (0.0235in.), Figure 5.120, has transferred to the standard thread form (60 degree included angle, R2=0.2438mm (0.0096in.) and thread formation has proceeded. The transition from the earlier thread form design can be seen on the upper half of the partially formed thread where the material slopes away from the flank of the standard thread form at an angle representing the deformation caused by the larger 120 degree included angle. As has been highlighted in previous sections, bands of high strain rate extend at approximately 45° towards the centre of the forming thread. These bands originate where contact between the material and the flank of the thread form ends and they also join with the areas of strain rate concentration beneath the crest radii.

In Figure 5.121, the 60 degree included angle, R2=0.5969mm (0.0235in.) design has almost formed the maximum allowable by this geometry of thread form design. Strain rates are concentrated in the uppermost area of the partially formed thread where material is being "packed".

In Figure 5.122, the standard 60 degree included angle and R2=0.2438mm (0.0096in.) design the strain rate distribution is similar to the combination die design results. The bands of high strain rate are again very evident as is their 45 degree nature and their merging with the sub-crest radius strain rate concentrations.

In the effective strain rate curves of Figure 5.123 some of these facets are also highlighted. The packing of material taking place in the 60 degree included angle & R2=0.5959mm (0.0235in.) design is obvious from the curve at point 9. The combination die design (120 degree included angle & R2=0.5969mm (0.0235in.)) again shows low strain rate magnitudes over points 1-4 which drop away to zero on the free surface.

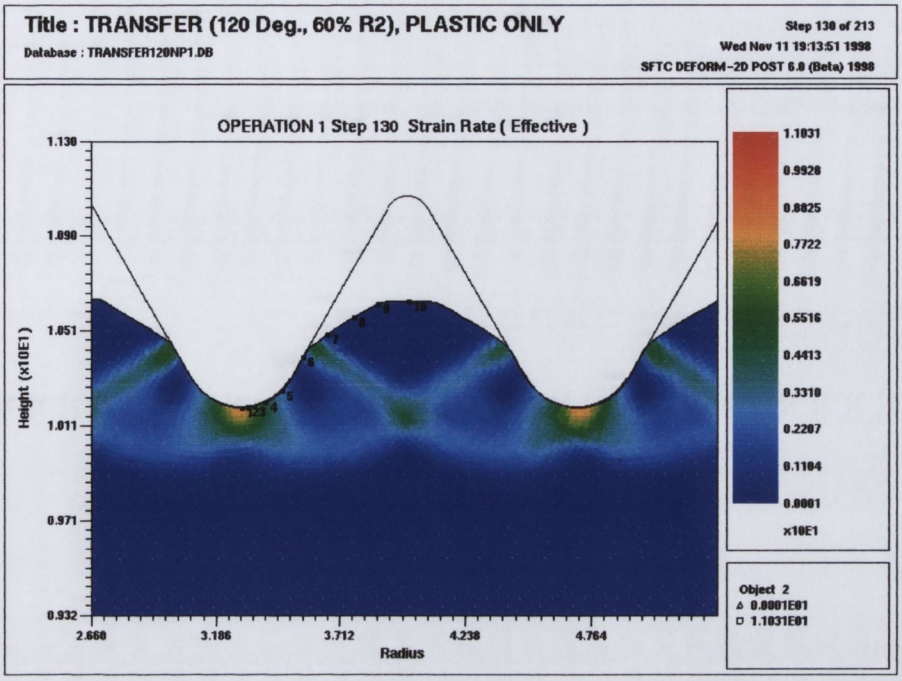

(Maximum: 11.03 s^{-1}, Minimum: 0 s^{-1})

Figure 5.120: Effec. Strain Rate at 0.44mm, Combined 120 Degree Incl. Angle & R2=0.5969mm Design

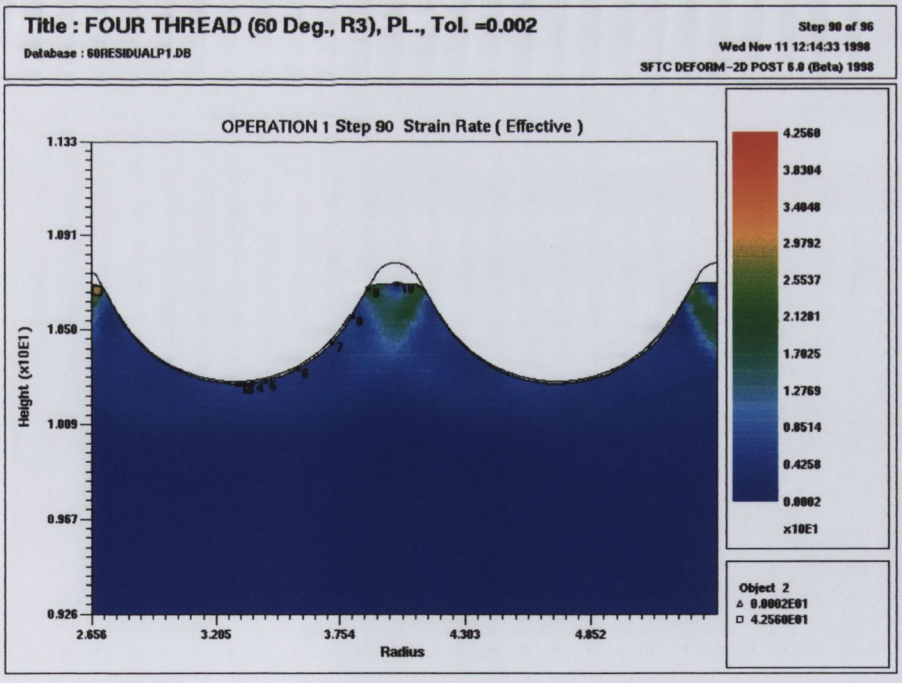

(Maximum: 42.56 s^{-1}, Minimum: 0 s^{-1})

Figure 5.121: Effec. Strain Rate at 0.44mm, 60 Deg. Incl. Angle & R2=0.5969mm Design

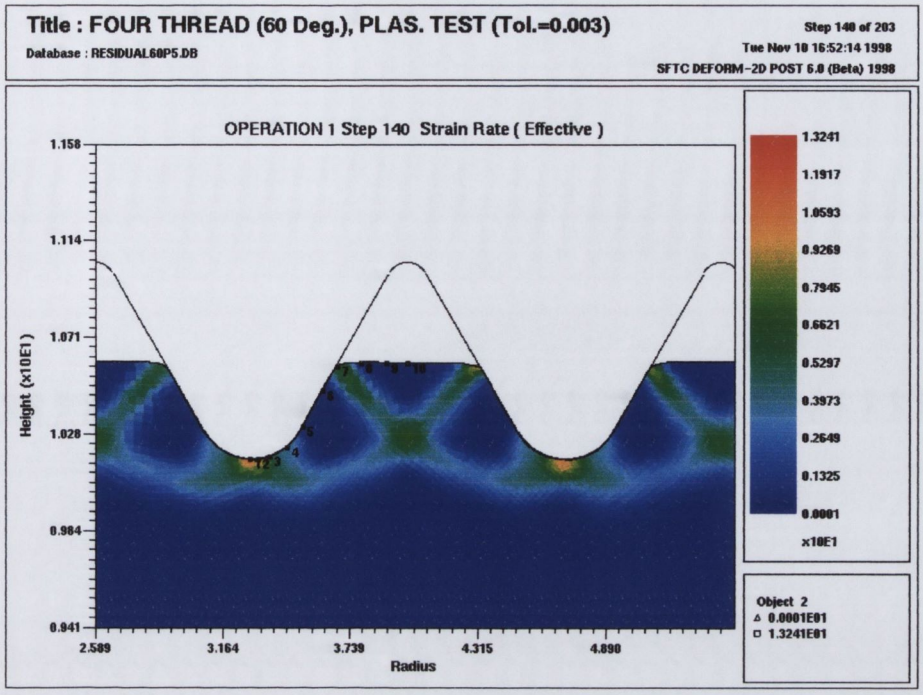

(Maximum: 13.24 s^{-1}, Minimum: 0 s^{-1})

Figure 5.122: Effec. Strain Rate at 0.44mm, Standard 60 Deg. Incl. Angle & R2=0.2438mm Design

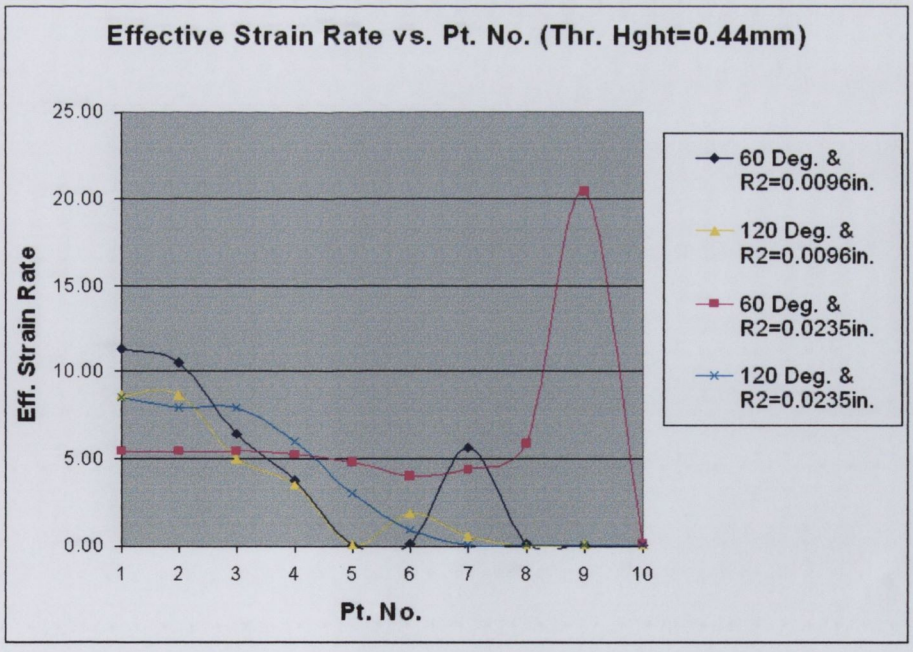

Figure 5.123: Effective Strain Rate vs. Tracking Point No., Thread Height = 0.44mm

Thread Height = 0.71mm

The packing of material is now very evident in the combination die design, Figure 5.124. The bands of high strain still originate from final contact points and extend as before to the root areas of the forming threads. The 60 degree, R2=0.5969mm (0.0235in.) die design, Figure 5.125 shows the benefit of using a larger (R2) crest radius during initial thread formation as the upper portion of the partially formed thread does not make contact with the flank of the standard thread form and thus no packing is taking place. The standard thread form (Figure 5.126) exhibits the same strain rate distributions as the combination die design but the area of strain rate concentration seems even more biased to the top of the forming thread.

In the graph of Figure 5.127 this assumption is confirmed where very high strain rates at point 9 on the curve is visible for the standard thread from design. The other three designs do not exhibit this peak but relatively high values of effective strain rate are picked up on the curves at the positions where the strain bands originate, i.e. point 6 in the 60 degree included angle, R2=0.5969mm (0.0235in.) die design.

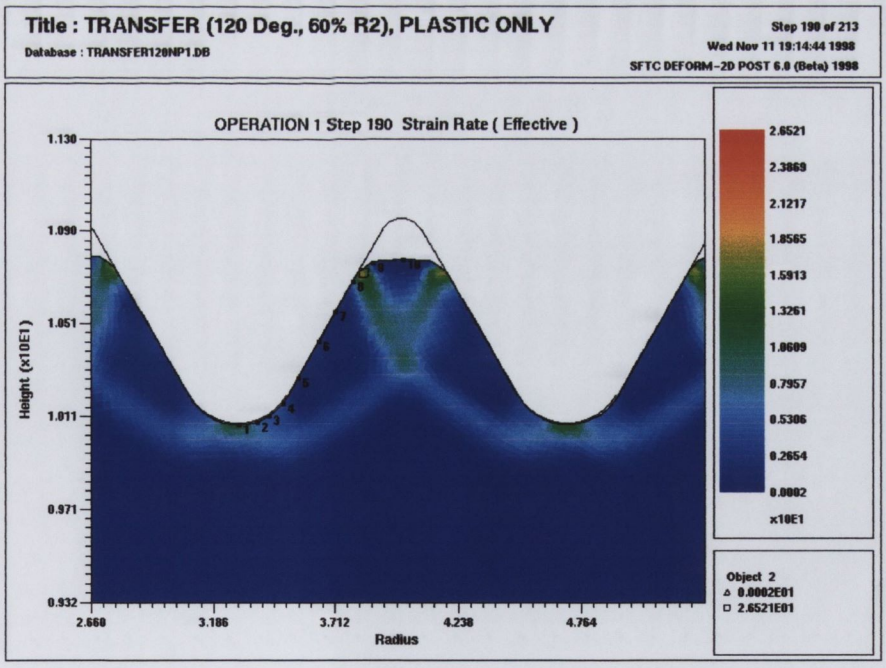

(Maximum: 26.52 s^{-1}, Minimum: 0 s^{-1})

Figure 5.124: Effec. Strain Rate at 0.71mm, Combined 120 Deg. Incl. Angle & R2=0.5969mm Design

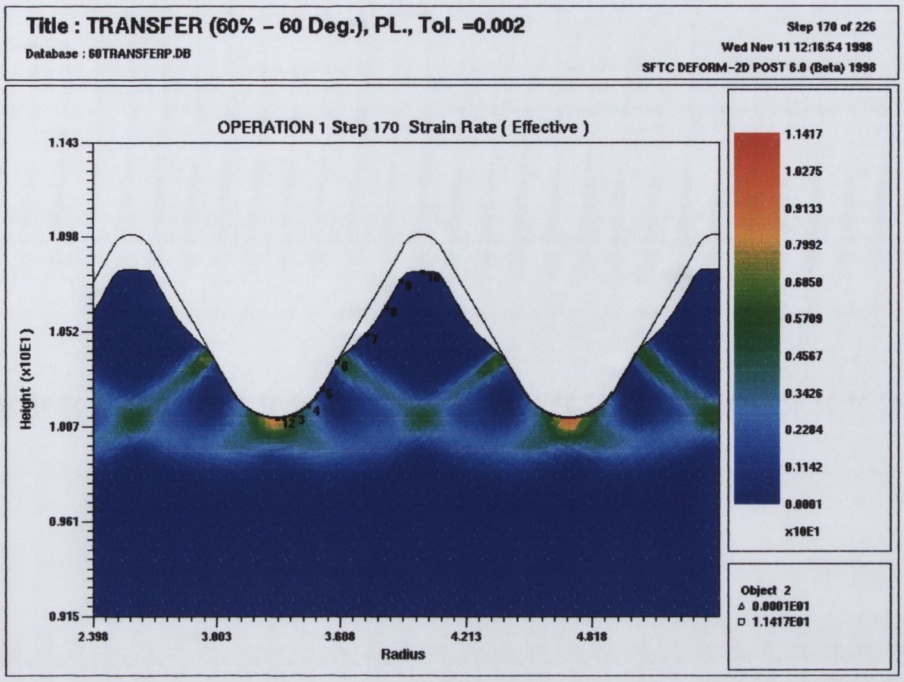

(Maximum: 11.42 s^{-1}, Minimum: 0 s^{-1})

Figure 5.125: Effec. Strain Rate at 0.71mm, 60 Deg. Incl. Angle & R2=0.5969mm Design

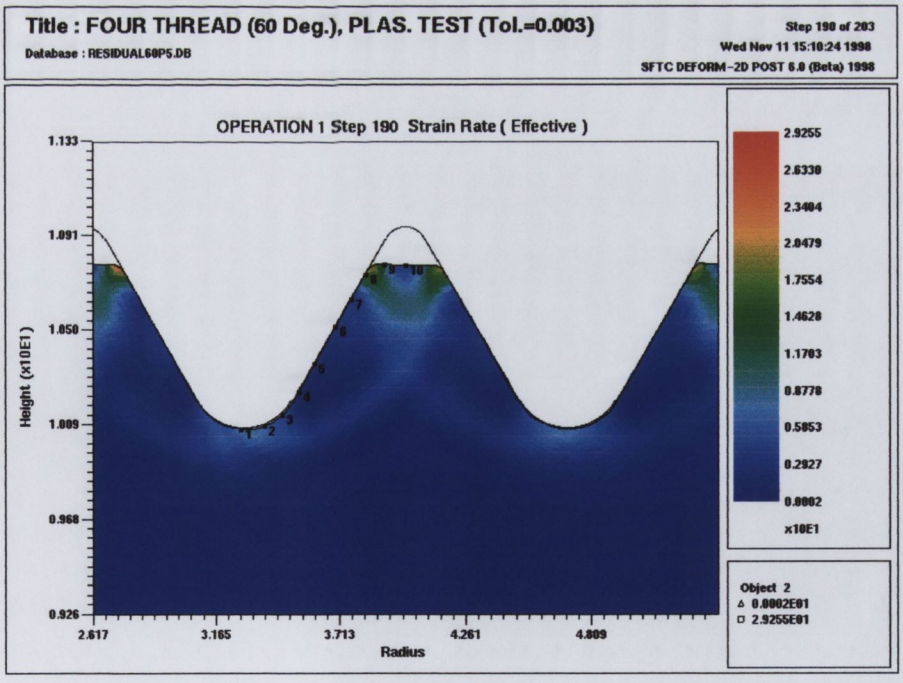

(Maximum: 29.26 s^{-1}, Minimum: 0 s^{-1})

Figure 5.126: Effec. Strain Rate at 0.71mm, Standard 60 Deg. Incl. Angle & R2=0.2438mm Design

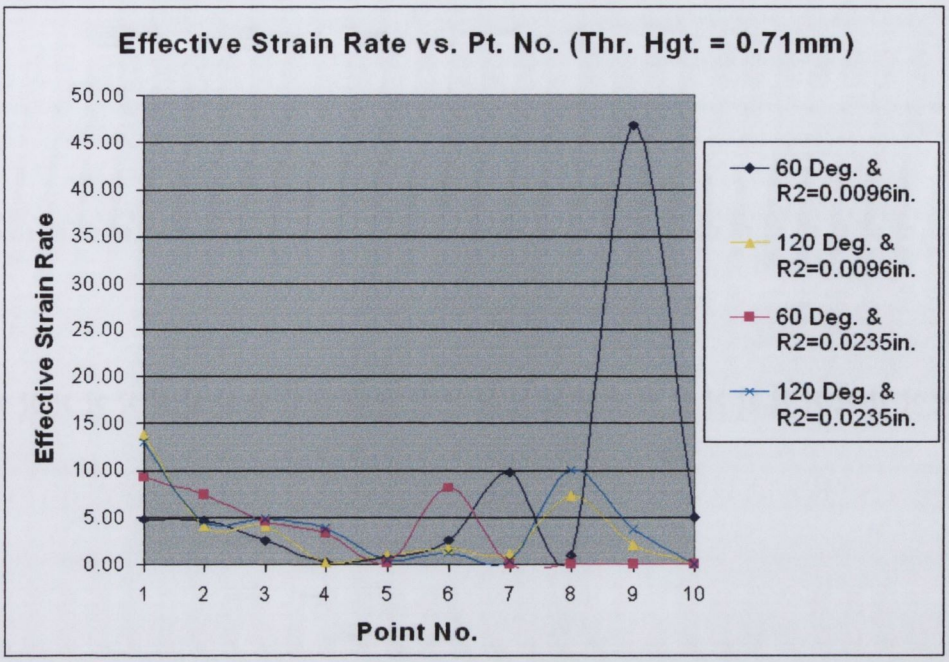

Figure 5.127: Effective Strain Rate vs. Point No., Thread Height = 0.71mm

5.6 Conclusions

Figure 5.128 below shows the effective strain results measured at the thread root (point 1) as thread formation proceeds.

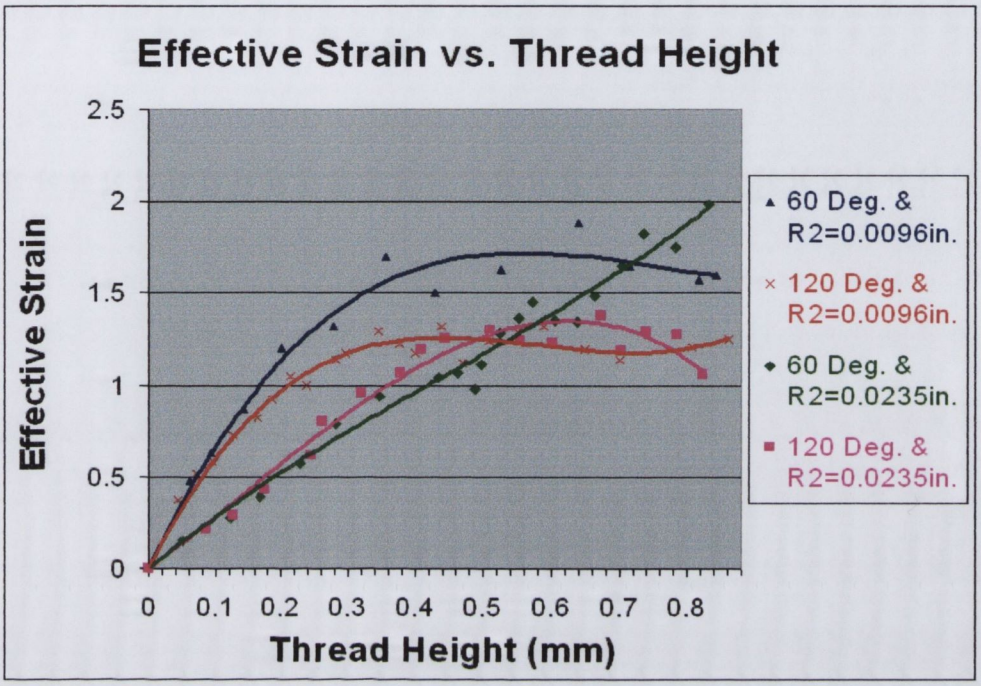

Figure 5.128: Effective Strain vs. Thread Height

The main points that can be drawn from this section may be summarised as follows.

- The magnitude of the Effective Stress is not significantly affected by the Included angle or the value of R2.
- Increasing the value of R2 has the greatest effect at the start of the process, the greater the value of R2 the lower the strains.
- The large included angle has the greatest influence towards the middle/end of the process, i.e. 120 Degrees better than 60 Degrees.
- The optimum design is the combined 120 Degree included angle and Crest Radius (R2)=0.5969mm (0.0235in.). This design seems to benefit at the start of the process from the large crest radius and at the end of the process from the large included angle.

Chapter 6

Experimental Results

6.1 Introduction

In December 1998, Hi-Life Tools, Shannon manufactured a series of *progressive* flat thread rolling dies based on the finite element results presented in the last chapter. This was in order to allow experimental trials to verify the finite element analysis predictions of low defect occurrence without any fastener strength reduction. These new progressive thread rolling dies were designated as described in Table 6.1. These die designs represent the optimum designs from the included angle, modified crest radius (R2), and combination designs respectively.

Die Design	Included Angle	Crest Radius (R2)
Die S	60 Degrees	0.2438mm (0.0096in.)
Die 1	120 Degrees	0.2438mm (0.0096in.)
Die 2	60 Degrees	0.5969mm (0.0235in.)
Die 3	120 Degrees	0.5969mm (0.0235in.)

Table 6.1: New Flat Thread Rolling Dies

Dies 1, 2, and **3** all transfer/progress to the standard 60 degree included angle with R2=0.2438mm (0.0096in.) thread form after they have formed the maximum thread height permitted by their initial die geometry, see Table 4.2, section 4.1.5 and Table

4.3, section 4.1.6.

In February 1999, the experimental tests using the new progressive thread rolling dies were undertaken at SPS Technologies, Jenkintown, Philadelphia, U.S.A. During the initial rolling trials Titanium 6Al-4V test studs were rolled from a batch of material known to be prone to defects and from which, only defect counts could be made.

In the second series of tests, threaded fasteners were rolled using a **Die S**, 60 degree included angle with R2=0.2438mm (0.0096in.), **Die 1** the 120 degree included angle & R2=0.2438mm (0.0096in.) die design, and **Die 3**, the 120 degree & R2=0.5969mm (0.0235in.) design.

These specimens were then subjected to tensile and fatigue testing to ensure that the new thread rolling die designs did not effect the mechanical properties of the fasteners detrimentally compared to fasteners manufactured using standard tooling. Some of the fasteners not used for mechanical testing were reserved for sectioning and microscopic analysis in order to determine if internal defects were present.

6.2 Test Stud Trials

When an aerospace fastener is being thread rolled, the thread rolling machine must be set-up to ensure that the very strict geometrical specifications of the product are met, i.e. pitch diameter, major diameter etc. This set-up procedure is conducted by performing pre-production runs using test studs, see Figure 6.1. For conformity the test studs are manufactured from the same material as the actual fastener product. The test studs are first rolled through the thread rolling machine and the relevant dimensions measured. When inspection of the rolled studs indicate that the machine set-up is able to produce the required dimensions within tolerance the actual product rolling can then commence.

Figure 6.1: Titanium 6Al-4V Test Studs

As mentioned in the introduction, for the initial experimental trials the test studs were chosen from a batch of material known to have a high susceptibility to the formation of internal defects. This had been established during earlier thread rolling set-up trials at Jenkintown. The studs were rolled using the thread rolling dies described in Table 6.1, the bold characters are used throughout the following sections to identify the specimens rolled using the different progressive thread rolling die designs. Care was taken to assure that the same amount of thread fill-out (thread height) was obtained for each die design tested.

6.2.1 Defect Analysis

After 2 test studs were rolled, using each of the thread rolling dies described in Table 6.1, they were sectioned into quarters. The sectioned specimens were then mounted and prepared as described in section 4.2.3 in Chapter 4. The thread length was about 15 threads, and therefore approximately 120 thread sections in total were examined for each die type.

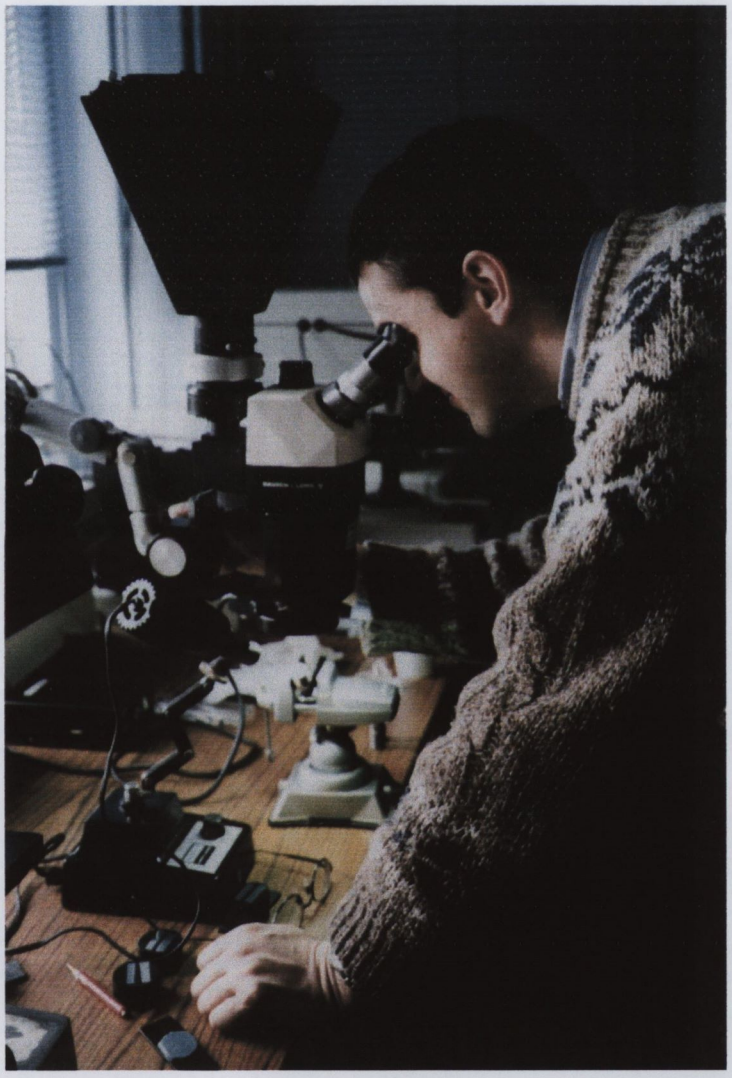

Figure 6.2: Analysing the samples with a Microscope

The total Defect Counts are presented in the following table, Table 6.2. This table lists the number of threads having either 1, 2 to 3, or more than 3 defects and confirming whether they are above or below the fastener pitch diameter. For example studs rolled using the 60 degree included angle and R2=0.5969mm (0.0235in.) design (**Die 2**) had

4 threads with 1 defect, 1 thread with 2 to 3 defects, and 1 thread with more than 3 defects below the pitch diameter. It can be seen that a considerable number of defects were found above the pitch diameter for each die tested. Figure 6.3 is a graphical representation of the tabular data.

	Below P.D.			Above P.D.		
DIE TYPE	1 Defect	2-3 Defects	>3 Defects	1 Defect	2-3 Defects	>3 Defects
Die S	11	1	1	13	14	77
Die 1	3	6	12	14	16	35
Die 2	4	1	1	11	8	24
Die 3	0	0	0	14	9	11

Table 6.2: Summary of Defect Counts for Test Studs

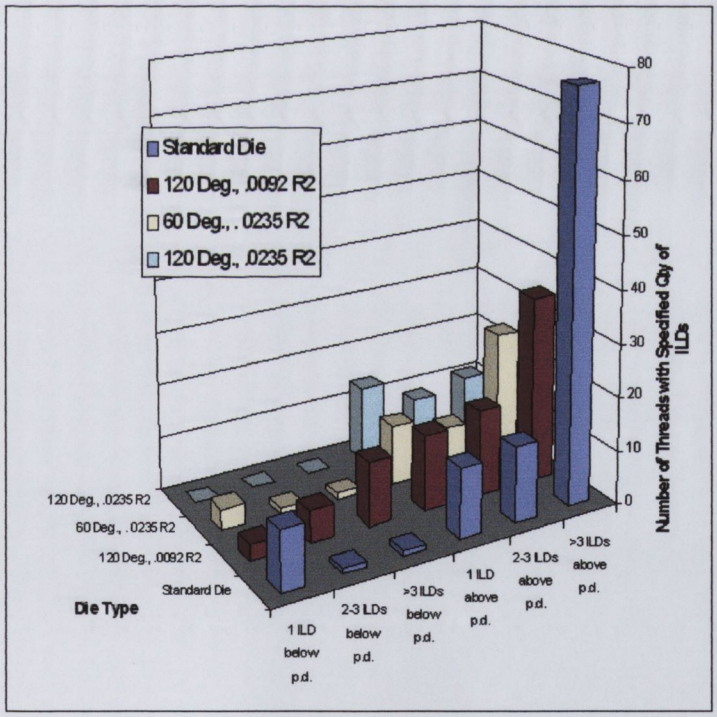

Figure 6.3: Graph of Defect Counts for Test Studs

It can be seen from Table 6.2 and Figure 6.3 that as predicted by the finite element analysis the 120 degree included angle & R2=0.5969mm (0.0235in.) progressive die design (**Die 3**) produced the best results, with zero defects below the pitch line. It was

observed that the standard form die (**Die S**) and the 120 degree with R2=0.2438mm (0.0096in.) die design (**Die 1**), had in addition to a high number of internal defects, extensive thread laps at the roots of the threads. It is significant that the threads rolled using **Die 3** based on the analysis undertaken for this thesis would have passed both Boeing and Jenkintown inspection. These results represented a substantial improvement over threads rolled currently using a standard 60 degree included angle & R2 die (**Die S**). In addition these results confirm the feasibility of using rigid plastic finite element analysis to aid in the design of metal-forming tooling.

6.3 Fastener Trials

After the promising results achieved in the test stud trials, actual Titanium 6Al-4V fasteners were rolled using the progressive thread rolling die designs derived from this thesis, see Figure 6.4. Figure 6.5 shows a rolled and unrolled titanium aerospace fastener worked on by the author. There was a dual purpose to these tests, firstly, to confirm that thread rolling with progressive dies had no effect on the mechanical properties of the rolled fasteners and secondly to confirm the trends, for reduced defects, indicated by the stud trials. SPS Technologies could only release a limited number of actual fasteners for testing, this implied that only two of the progressive dies used in the test stud trials could be used to roll actual fasteners, namely, **Die 1** (120 degrees & R2=0.2438mm (0.0096in.)) and **Die 3** (120 degrees included angle & R2=0.5969mm (0.0235in.)). This allowed determination of the influence of the modified crest radius (R2) on the rolled fasteners. The results from both of these dies were compared against those for fasteners rolled using the standard form thread rolling die, **Die S** (60 degree included angle & R2=0.2438mm (0.0096in.)).

Figure 6.4: Thread Rolling of the fasteners

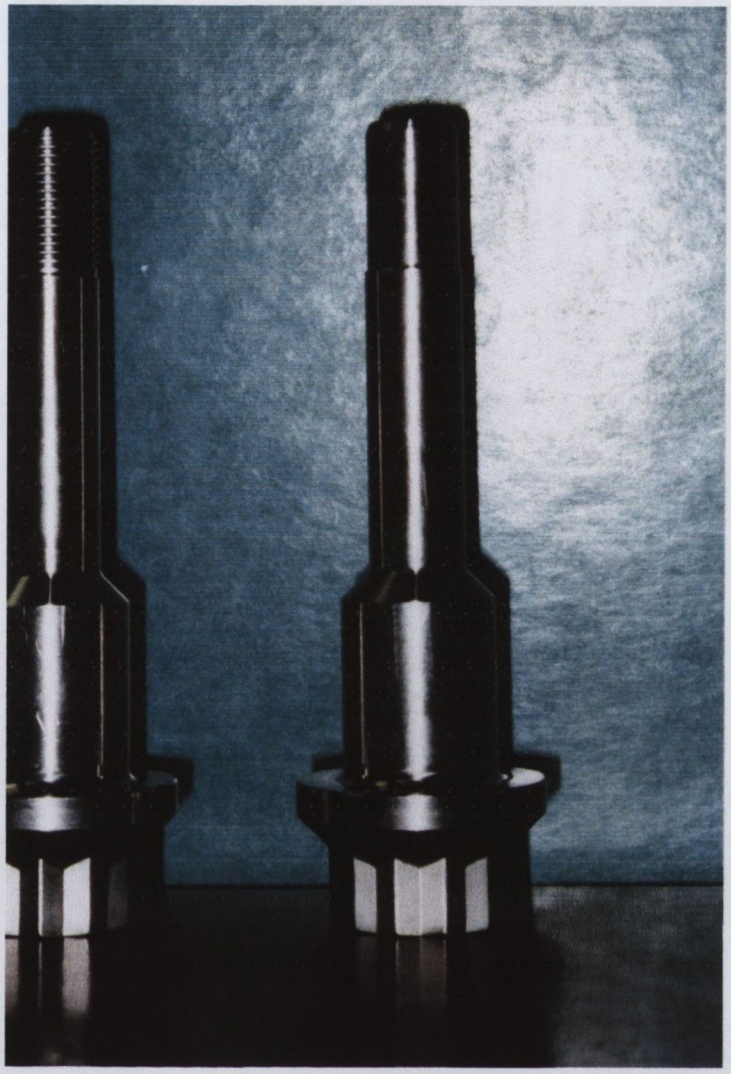

Figure 6.5: Rolled & Un-Rolled Titanium 6Al-4V fasteners

6.3.1 Tensile Tests

The rolled fasteners were divided arbitrarily into three groups of fasteners, one group for tensile testing, one group for fatigue testing, and one group for microscopic analysis and defect counts. Figure 6.6 shows a tensile test of a rolled fastener.

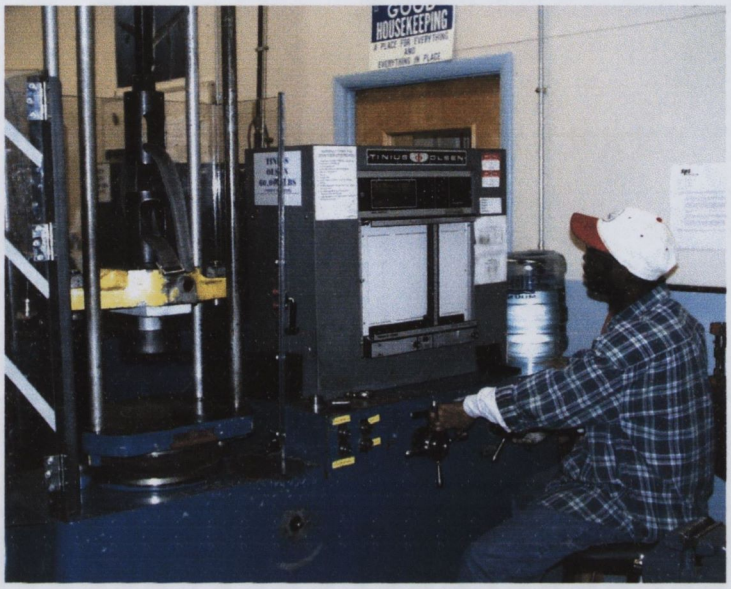

Figure 6.6: Tensile Testing of the fasteners

Table 3.1 shows the results obtained from the tensile tests on the rolled fasteners. Two fasteners from each progressive die design were tested for tensile strength. In the first column the specimen is described as follows, the first letter/number denotes the die design used to roll the piece, see Table 6.1, and the second number was an arbitrary number to differentiate between the specimens.

Specimen No.	Breaking Force (kN)	% Diff. from **S**
S.2	202.47	
S.3	200.78	
1.10	199.94	-0.85%
1.4	201.09	-0.3%
3.9	197.27	-2.2%
3.10	196.38	-2.6%

Table 6.3: Tensile Test Results of Rolled Fasteners

From these results, it is obvious that using a progressive thread rolling die design does not significantly reduce the tensile strength properties of the rolled fasteners, i.e. they are just as strong as fasteners currently manufactured using the standard (**S**) die. Figure 6.7 shows one of the titanium fasteners after a tensile test. It can be seen that it failed on the threads, which is the standard failure mode of this type of threaded fasteners under a high tensile load.

Figure 6.7: Fastener after Tensile Testing

6.3.2 Fatigue Tests

The second group of rolled fasteners were subjected to fatigue tests. These tests were performed according to the MIL-STD-1312-11 standard. Eight fasteners rolled on each thread rolling die design were fatigue tested. Figure 6.8 shows one of these tests being set up on the testing machine at Jenkintown, U.S.A.

Figure 6.8: Fatigue Testing of Rolled Fasteners

The test requires a maximum load (F_{max}) of 15,600 lbs ($\approx$ 70 kN) with R=0.1. This value of 0.1 represents the load ratio, in this case the low load is one tenth the maximum load. At this maximum load level, the fasteners rolled using the thread rolling die types **Die S**, **Die 1**, and **Die 3** ran to 200,000 cycles without failure. This

exceeds the tension fatigue requirement for such aerospace fasteners. These tests used four of the fasteners from the group of eight that were rolled on each thread rolling die design. To determine the effect of the thread rolling die designs on fatigue behaviour, the maximum load was increased to F_{max}=23,400 lbs ($\approx$ 105 kN). This load produced failures after a satisfactory number of cycles. All pieces failed in the threads which, as mentioned previously, is the standard failure mode. Table 6.4 shows the results of these fatigue tests.

Specimen No.	Cycles to Failure	Specimen No.	Cycles to Failure
S.6	33400	**3**.1	14300
S.7	76400	**3**.2	60800
S.8	30900	**3**.3	34200
S.9	54600	**3**.5	34500
1.1	16200		
1.2	28300		
1.3	25500		
1.6	34500		

Table 6.4: Fatigue Test Results of Rolled Fasteners

The graph in Figure 6.9 shows the tabulated cycles to failure graphically.

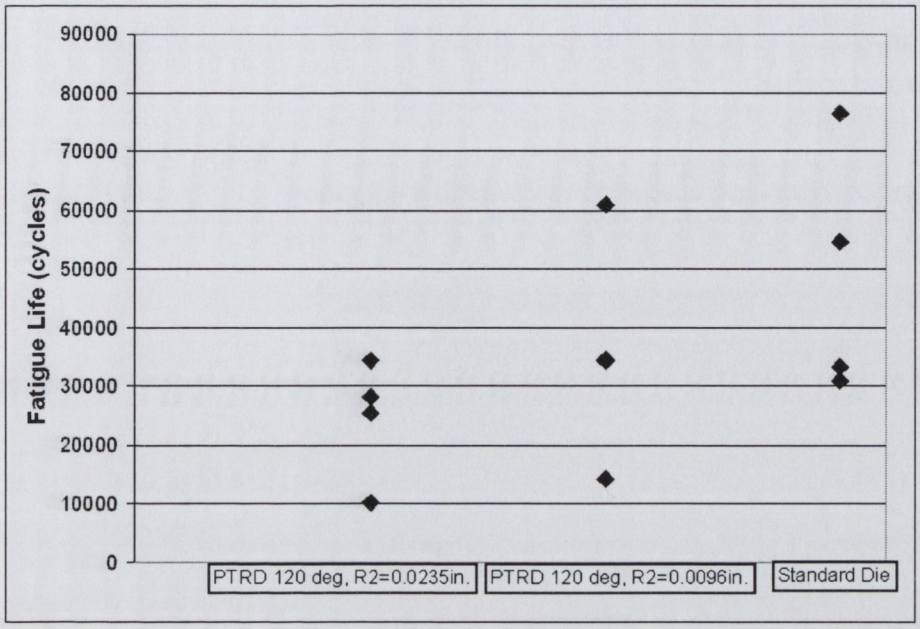

Figure 6.9: Fatigue Test Results of Rolled Fasteners

The sample population is very small and more fatigue tests at this higher F_{max} would be required to have greater confidence in these results.

6.3.3 Defect Analysis

As in the previous section, the last group of rolled fasteners were sectioned, mounted, and prepared for defect counts. The counts observed are detailed in the table below.

	Below P.D.			Above P.D.		
Die Type	1 Defect	2-3 Defects	>3 Defects	1 Defect	2-3 Defects	>3 Defects
Die S	0	0	0	2	16	35
Die 1	0	0	0	3	24	5
Die 3	0	0	0	4	12	0

Table 6.5: Summary of Defect Counts on Rolled Fasteners

As in the test stud trials, the 120 Degree included angle and R2=0.5969mm (0.0235in.) design thread rolling dies (**Die 3**) produced the lowest overall number of defects in the rolled fasteners. In none of the cases were any internal defects observed in the material below the pitch line, these results confirm the comments made in Chapter 2 that

in some cases Ti-6Al-4V thread rolls without major difficulties and the occurrence of defects can vary from one batch to another.

Chapter 7

Conclusions

The main conclusions of this report are as follows

- The research confirms that two dimensional (2D) finite element analysis can be used to model the thread rolling process.
- In addition these results confirm the feasibility of using finite element analysis to aid in the design of metal-forming tooling.
- It has been proven that finite element analysis can be used to successfully predict the likely location of internal defects in a thread rolling process.

Standard Thread Rolling Die Design

- The 60 Degree included angle with crest radius (R2)=0.2438mm (0.0096in.) thread form produces the highest overall strain profile over the thread forming process compared to a larger included angle or larger crest radius progressive thread rolling die design, see Figure 7.2

Included Angle Designs

- In thread rolling die design the results indicate that using a larger included angle at the start of a thread rolling process has a definite beneficial effect on reducing

the magnitude of the effective strain values within the fastener material at the end of the thread formation process.

Crest Radius (R2) Designs

- In thread rolling die design the benefit of using a larger crest radius (R2) at the start of thread formation can be clearly seen from Figure 7.1. The magnitude for the effective strain of the R2=0.5969mm (0.0235in.) design is lower by over 60% compared to the standard crest radius (R2) design.

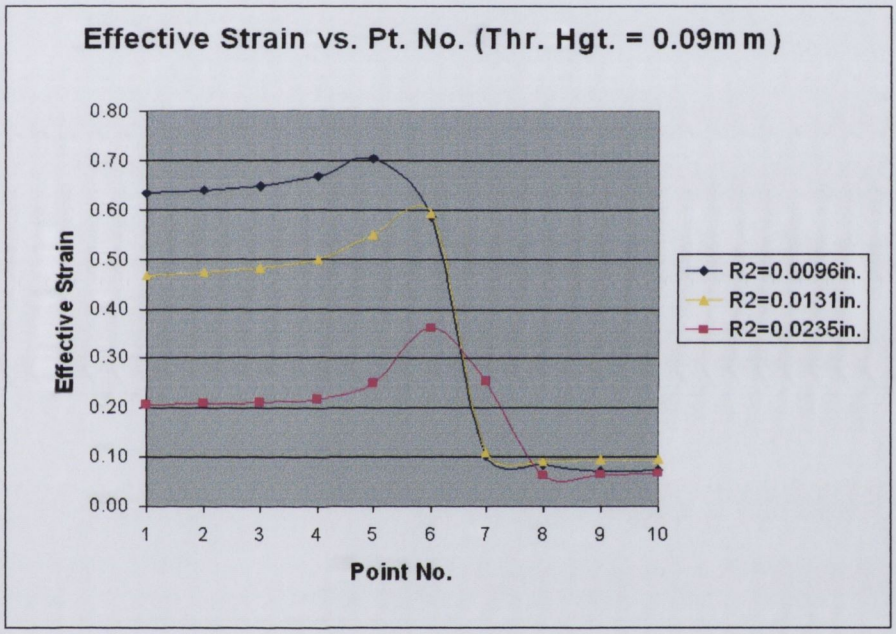

Figure 7.1: Effective Strain vs. Tracking Pt. No., Thread Height = 0.09mm

- The strain and the strain rate at the thread root decreases as the crest radius R2 is increased.

Combined Die Design

- The optimum design is the combined 120 Degree included angle and Crest Radius (R2)=0.5969mm (0.0235in.). This design seems to benefit at the start of the process from the large crest radius and at the end of the process from the large included angle, see Figure 7.2.

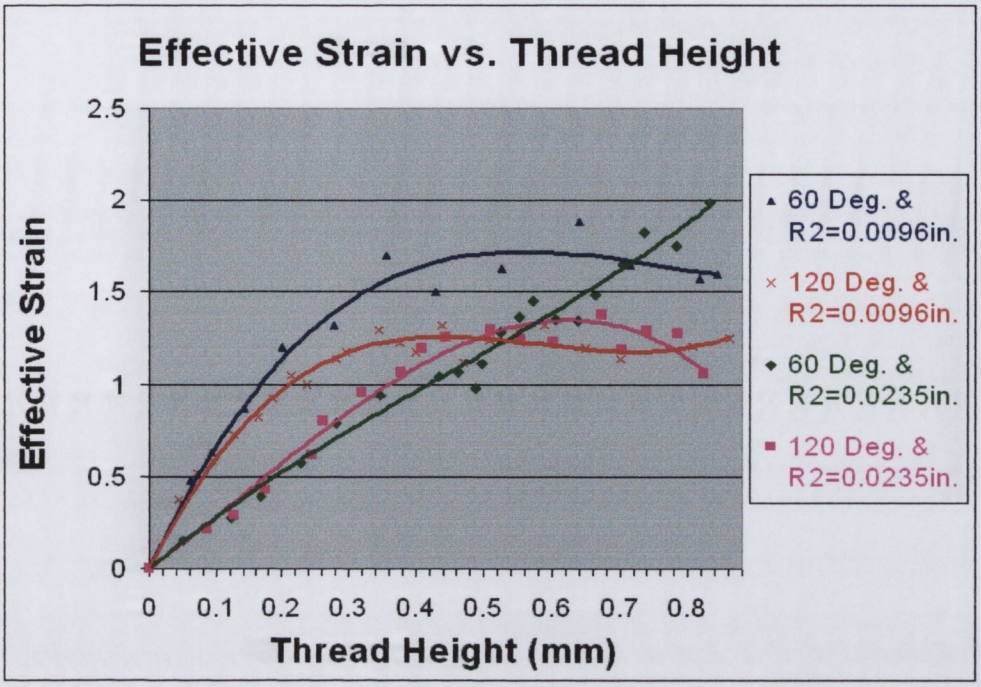

Figure 7.2: Effective Strain vs. Thread Height

Tensile & Fatigue Strength

- The effective stress in a thread rolled fastener was not influenced significantly by modifications to the size of the included angle or crest radius. This implies that residual stresses and therefore the fatigue strength of the finished fastener will be unaffected by these design modifications.

Overall Conclusion

- The occurrence of internal defects in titanium alloy aerospace fasteners was significantly reduced by the use of this optimum thread rolling die design compared to a standard thread rolling die design.

Future Work

At present only the major automotive and aerospace manufacturers use metal forming simulation on a daily basis. With the development of more powerful computer hardware and software, while the cost of implementing it drops, the modelling and simulation of metal forming processes will become easier and more accessible to industry as a whole.

The software is also becoming more user friendly and is being designed specifically for use by engineers who are involved with the metal forming industry. This will lead to more extensive use of finite element analysis on a daily basis in all industries.

The increase in computational power available to engineers will make the modelling and simulation of more complex metal forming processes feasible. This will allow the simulation and analysis of the 3D thread rolling process to become a reality outside the realms of the supercomputer.

The capability of modelling thread rolling in 3D will not only allow for better definition of the process but will also allow the 3D frictional nature of the process to be included in analyses. This is of particular importance in the case of thread rolling where the friction vector may not lie in the plane of deformation due to the entraining forces, which must be exerted on the fastener blank.

The fatigue results presented at the end of the thesis (Figure 6.9) may indicate that the new thread rolling die designs lower fatigue strength. This could be due to the effect of using a larger crest radius during the initial deformation of the fastener. This may be likened to treating the thread root as a blunt notch. Further fatigue tests should be undertaken to confirm that the new designs do not lower fatigue strength.

References

[1] Hi-Life Tools. Operator's manual, thread roll terms, set-up guide etc. Technical report, Hi-Life Tools, Shannon, Ireland, 1996.

[2] ASME. *Manufacturing Processes Vol. VII.* ASME Publications, New York, 1995.

[3] SPS Technologies. Acceptance criteria for surface discontinuities. Technical Report SPS-I-650, SPS Technologies, 1995.

[4] S.L. Semiatin and G.D. Lahoti. The occurrence of shear bands in isothermal, hot forging. *Metallurgical Transactions A*, 13A:275–288, 1982.

[5] H.C. Rogers. Adiabatic plastic deformation. *Ann. Rev. Mater. Sci.*, 9:283–311, 1979.

[6] K. Brown. Role of deformation and shear banding in the stability of the rolling textures of aluminium and al-0.8% mg alloy. *J. Inst. Metals*, 100:341–345, 1972.

[7] V. Osina. Forming of metals at high rates and energies. *Metal Treatment*, 33:193, 1966.

[8] S.V. Kailas, Y.V.R.K. Prasad, and S.K. Biswas. Microstructural features of flow instability in α-titanium cylinders under high strain rate compression at 25c to 400c. *Metallurgical Trans. A*, 24A:2513–2520, 1993.

[9] S.L. Semiatin and G.D. Lahoti. The effect of shear bands on service properties of ti-6al-2sn-4zr-2mo-0.1si forgings. *Metallurgical Transactions A*, 14A:743–750, 1983.

[10] S. Kobayashi, C.H. Lee, Y. Saida, and S.C. Jain. Analytical prediction of defects occurrence in simple and complex forgings. Technical Report AFML TR-70-90, AFML, 1970.

[11] S.L. Semiatin and G.D. Lahoti. Deformation and unstable flow in hot forging of ti-6242. *Met. Trans. A*, 12A:1705–1717, 1981.

[12] J.J. Jonas, R.A. Holt, and C.E. Coleman. Plastic stability in tension and compression. *Acta Met.*, 24:911–918, 1976.

[13] M.C. Mataya and G. Krauss. A test to evaluate flow localization during forging. *ASME J. Applied Metalworking*, 2:28–37, 1981.

[14] W.F. Hosford and R.M. Caddell. *Metal Forming: Mechanics and Metallurgy.* Prentice Hall International, London, 1983.

[15] SPS Technologies. Internal communication. Technical report, SPS Technologies, Jenkintown, USA, 1986.

[16] SFTC Technologies. *DEFORM 2D v6.0 User Manual.* SFTC Technologies, 1999.

[17] S.I. Oh, W.T. Wu, J.P. Tang, and A. Vedhanayagam. Capabilities and applications of fem code deform: the perspective of the developer. *Journal of Materials Processing Technology*, 27:25–42, 1991.

[18] O.C. Zienkiewicz, P.C. Jain, and Onate E. Flow of solids during forming and extrusion: Some aspects of numerical solutions. *Int. J. Solids & Structures*, 14:15–38, 1978.

[19] O.C. Zienkiewicz. Flow formulations for numerical solutions of forming processes. In J.F.T. Pittman et al., editor, *Numerical Analysis of Forming Processes*, page 1. Wiley, 1984.

[20] F.E. Veldpaus J.C. Nagtegaal. On the implementation of finite strain plasticity equations in a numerical model. In J.F.T. Pittman et al., editor, *Numerical Analysis of Forming Processes*, page 351. Wiley, 1984.

[21] S. Kobayashi and C.H. Lee. Deformation mechanics and workability in upsetting solid circular cylinders. In *Proc. 1st Nth. American Metalworking Research Conf.*, pages 185–204, 1973.

[22] M. Takahashi and S. Kobayashi. Some aspects of finite element analysis of plastic compression. In *Proc. 5th Nth. American Metalworking Research Conf.*, pages 87–94, 1977.

[23] H. Matsumoto, S. I. Oh, and S. Kobayashi. A note on the matrix method for rigid plastic analysis of ring compression. In *Proc. 18th Int. Machine Tool Design Research Conf.*, pages 3–9, 1977.

[24] S.I. Oh. Finite element analysis of metal forming processes with arbitrarily shaped dies. *Int. Journal of Mech. Sci.*, 24:479–493, 1982.

[25] S. Kobayashi. A review of the finite element method and metal forming process modelling. *J. Appl. Metal Working*, 2:163, 1982.

[26] S. Kobayashi. Metal forming and the finite element method - past and future. In *Proc. of the 25th Int. Conf. Mach. Tool Des. Res.*, pages 17–32, 1985.

[27] K. Osokada and K. Mori. The use of micro- and supercomputers for simulation of metal forming processes. *Annals of Cirp*, 34:241–244, 1985.

[28] A.A.M Hussin, P. Hartley, C.E.N. Sturgess, and G.W. Rowe. Non-linear finite element analysis on microcomputers for metal forging. *Journal of Strain Analysis*, 21:197–203, 1986.

[29] G.J. Creus and A.G. Groehs. Finite element analysis of large plastic deformation in metals. In J.L. Chenot and E. Onate, editors, *Modelling of Metal Forming Processes*, pages 27–36. Kluwer Academic, 1988.

[30] O. Mahrenholtz and N.L. Dung. Mathematical modelling of metal forming processes by numerical methods. *Adv. Tech. of Plasticity*, 1:3–10, 1990.

[31] L. Yan, S. Xu, and G. Li. Finite element analysis of metal forming processes on personal computers. *Journal of Engineering for Industry*, 113:441–445, 1991.

[32] J. Walters J.T. Tang, W.T. Wu. Recent development and applications of finite element method in metalforming. *Journal of Materials Processing Technology*, 46, 1994.

[33] T. Altan and V. Vasquez. Numerical process simulation for tool and process design in bulk metal forming. *Annals of Cirp*, 45:599–615, 1996.

[34] R. Hill. *The Mathematical Theory of Plasticity.* Clarendon Press, Cambridge, UK, 1950.

[35] J. Chakrabarty. *Theory of Plasticity.* McGraw Hill, New York, 1987.

[36] R. Courant. Variational methods for the solution of problems of equilibrium and variations. *Bull. Amer. Math. Soc.*, 49:1, 1943.

[37] R. W. Clough. The finite element method in plane stress analysis. In *Proc. 2nd Conf. on Electronic Computation*, page 345, 1960.

[38] P. Hartley, C.E.N. Sturgess, and G.W. Rowe. Friction in finite element analyses of metalforming processes. *Int. Journal Mech. Sci.*, 21:301–311, 1979.

[39] P. Hartley, I. Pillinger, and C.E.N. Sturgess. Modelling frictional effects in finite element simulation of metal forming. In I. Haque et al, editor, *Friction and Material Characterizations, Winter Annual Meeting of ASME, MD 10*, pages 91–96. ASME, 1988.

[40] I. Haque J.E. Jackson and T. Gangee. Some numerical aspects of frictional modelling in material forming processes. In I. Haque et. al, editor, *Friction and Material Characterizations, Winter Annual Meeting of ASME, MD 10*, pages 39–46. ASME, 1988.

[41] M. Raous, Y. Pinto, and P. Chabrand. Numerical modelling of friction for metal forming processes. In J.L. Chenot & E. Onate, editor, *Modelling of Metal Forming Processes*, pages 93–99. Kluwer Academic, 1988.

[42] N. Ramakrishnan, S. Ghantasala, and V.V. Kutumba Rao. An algorithm to incorporate friction in finite element analysis (fem) of metal working. *Journal of Materials Processing Technology*, 23:311–319, 1990.

[43] D. R. Durham, B.F. Von Turkovich, and A. Assempoor. Fillet design in cold forging dies. *Annals of Cirp*, 40:235–238, 1991.

[44] T. Altan, S.I. Oh, and H. Gegel. *Metal Forming: Fundamentals and Applications.* ASM International, Ohio, 1983.

[45] J.A. Schey. *Tribology in Metalworking: Friction, Lubrication and Wear.* American Society for Metals, Ohio, 1983.

[46] C. C. Chen and S. Kobayashi. Rigid plastic finite element analysis of ring compression. In H. Armen and R. F. Jones, editors, *Applications of Numerical Methods to Forming Processes, Winter Annual Meeting of ASME*, pages 163–174. ASME, 1978.

[47] J.H. Cheng and N. Kikuchi. A mesh rezoning technique for finite element simulation of metal forming processes. *Int. Journal for Numerical Methods in Eng.*, 23:219–228, 1986.

[48] M.J.M. Barata Marques and P.A.F. Martins. An algorithm for remeshing in metal forming. *Journal of Materials Processing Technology*, 24:157–167, 1990.

[49] M. Dyduch, A.M. Habraken, and S. Cescotto. Automatic adaptive remeshing for numerical simulations of metalforming. *Comp. Methods in Appl. Mechs, & Engineering*, 101:283–298, 1992.

[50] J. Walters. Simulation and analysis for forging companies - an industrial overview. In *39th H.R. Bergman Memorial Spring Seminar, ASM Milwaukee Chapter*, 1997.

[51] Aerospace Industries Association of America. National aerospace standard, fastener test methods, method 8, tensile strength. Technical Report NASM 1312-8, AIA, 1997.

[52] Aerospace Industries Association of America. National aerospace standard, fastener test methods, method 11, tension fatigue. Technical Report NASM 1312-11, AIA, 1997.

[53] W. Johnson and P.B. Mellor. *Engineering Plasticity.* Van Nostrand Reinhold, London, 1973.

[54] J.C. Gelin, J. Oudin, and Y. Ravalard. Determination of the flow stress-strain curves for metals from axisymmetric upsetting. *Journal of Mechanical Working Technology*, 5:297–308, 1981.

[55] T. Altan, S.L. Semiatin, and G.D. Lahoti. Determination of flow stress data for practical metal forming analysis. *Annals of CIRP*, 30:129–134, 1981.

[56] K. Washizu. *Variational Methods in Elasticty and Plasticity.* Pergamon Press, Oxford, 1968.

[57] C.H. Lee and S. Kobayashi. New solutions to rigid-plastic deformation problems using a matrix method. *Journal of Engineering for Industry*, 95:865–873, 1973.

[58] O.C. Zienkiewicz. *The Finite Element Method, 3rd Edition.* McGraw Hill, New York, 1977.

[59] S. Kobayashi and S.N. Shah. The matrix method for the analyses of metal forming processes. In Burke et. al., editor, *Advances in Deformation Processing*, pages 51–98. 1978.

Appendix A

Additional Work

A.1 Introduction

The design of a new thread rolling die form was not the only work undertaken in this research. A number of other areas were also investigated which were considered pertinent to the thread rolling process. These were the radius run-out area of a thread rolling die, see Figure A.1. The stresses and strains within the thread rolling die were looked at, as was the effect of the length of the ramp section of the thread rolling die which controls the penetration rate.

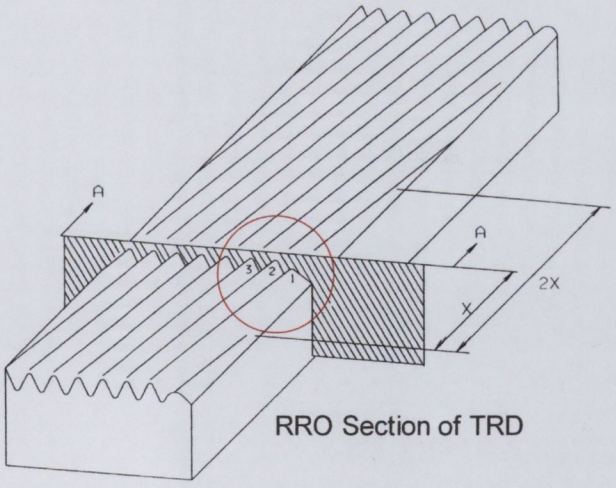

Figure A.1: Radius Run-out on a Thread Rolling Die

A.2 Radius Run-Out

The radius run-out section of a thread rolling die is the part of the die which forms the threads beneath the head of the fastener. It is only this portion of a thread rolling die that the threads on the die may have a form which does not conform with the standard 60 degree, crest radius = 0.2348mm (0.0096in.).

A.2.1 Finite Element Models

Figure A.2 shows one of the finite element models set-up for analysing the effect of altering the radius run-out geometry on the fastener material.

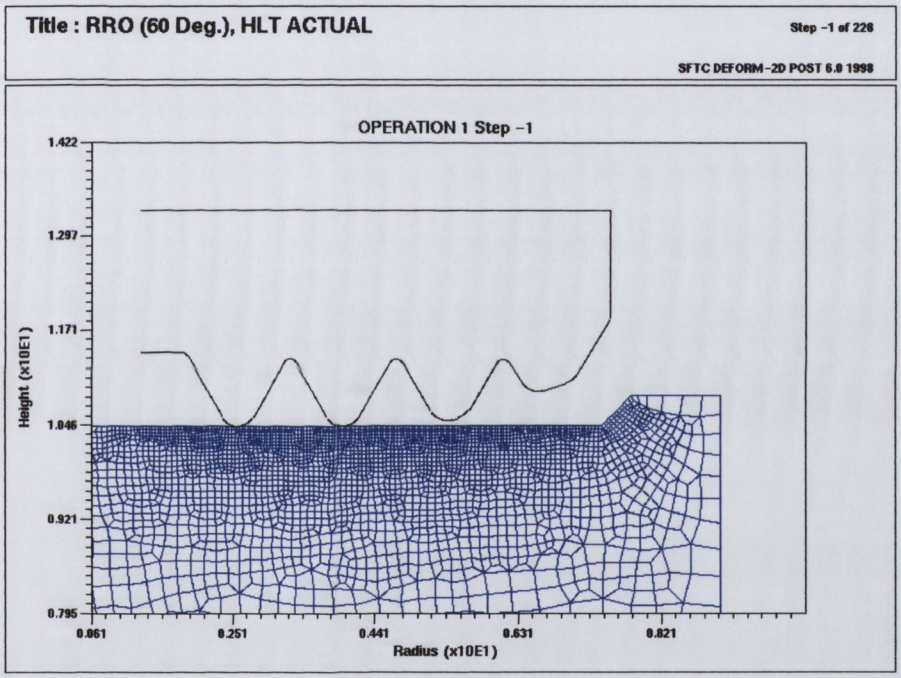

Figure A.2: Finite Element Model of Radius Run-out geometry

There were two initial geometries investigated, these were the "worst case" manufactured radius run-out section, Figure A.3, and a geometry considered the optimum geometry by Hi-Life Tools, Figure A.4. Three new radius run-out geometries were also analysed, these altered the crest radius of the second last thread (no. 2) to 0.4mm, 0.45mm, and 0.5mm compared to the radius in the "optimum" design of 0.465mm.

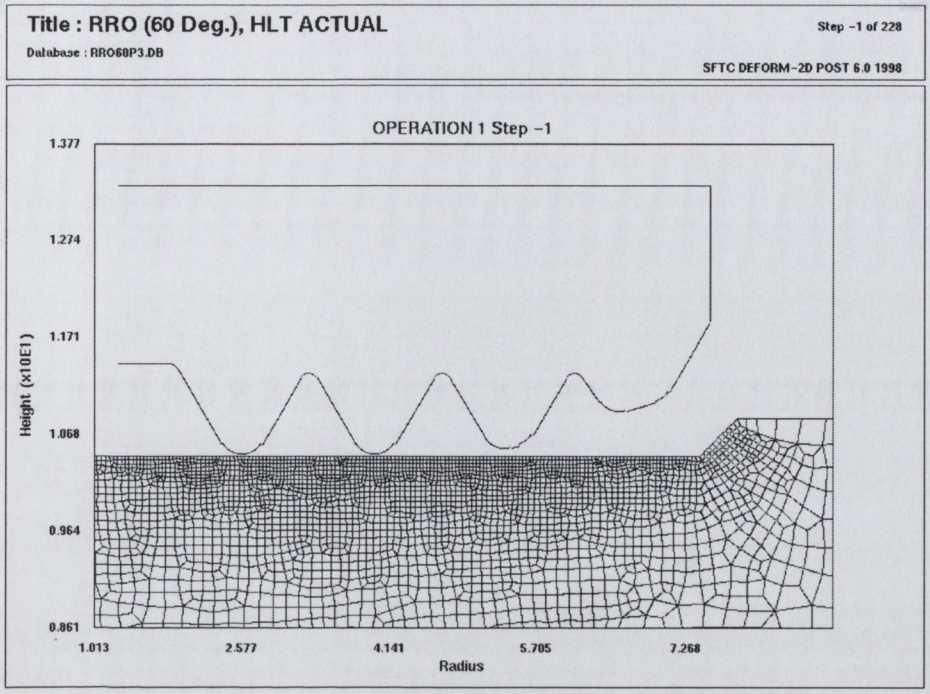

Figure A.3: Model of "Worst Case" Radius Run-out geometry

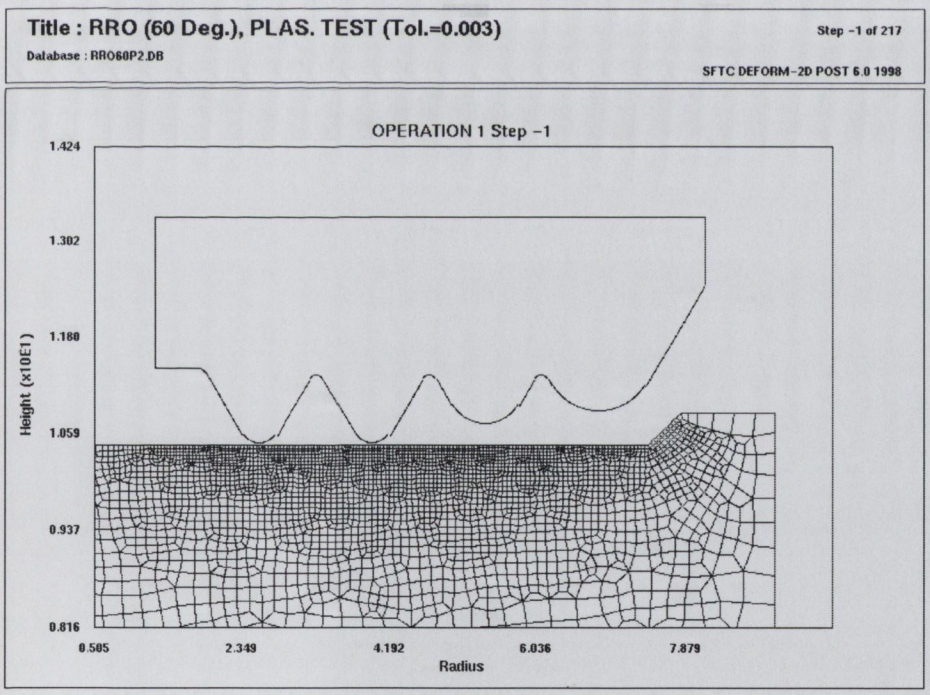

Figure A.4: Model of "Optimum" Radius Run-out geometry

A.2.2 Results

These results are shown for a Titanium 6Al-4V fastener and at a point where the leftmost thread is considered fully formed. Figure A.5 shows the effective strain for the actual radius run-out section, while Figure A.6 shows the effective strain for the "optimum" design.

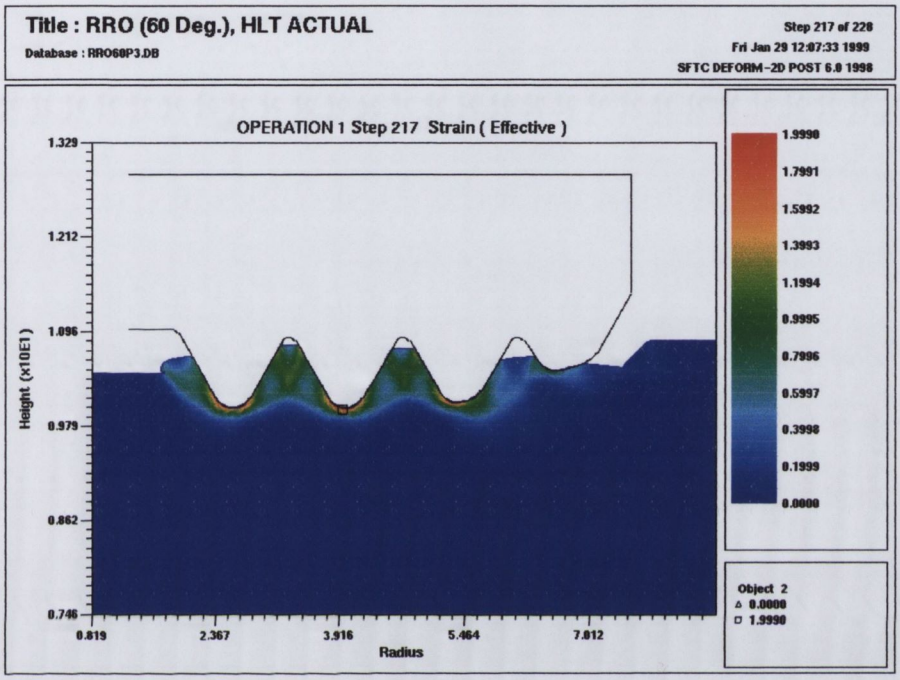

Figure A.5: Effective Strain, "Worst Case" Radius Run-out geometry

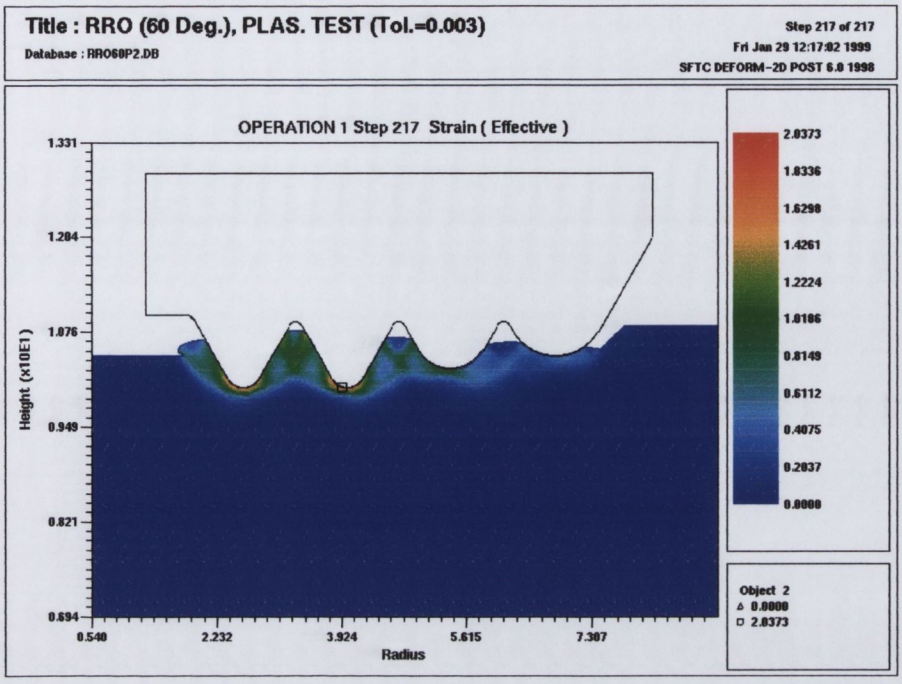

Figure A.6: Effective Strain, "Optimum" Radius Run-out geometry

Figure A.7 shows the effective strain rate for the actual radius run-out section, while Figure A.8 shows the effective strain rate for the "optimum" design.

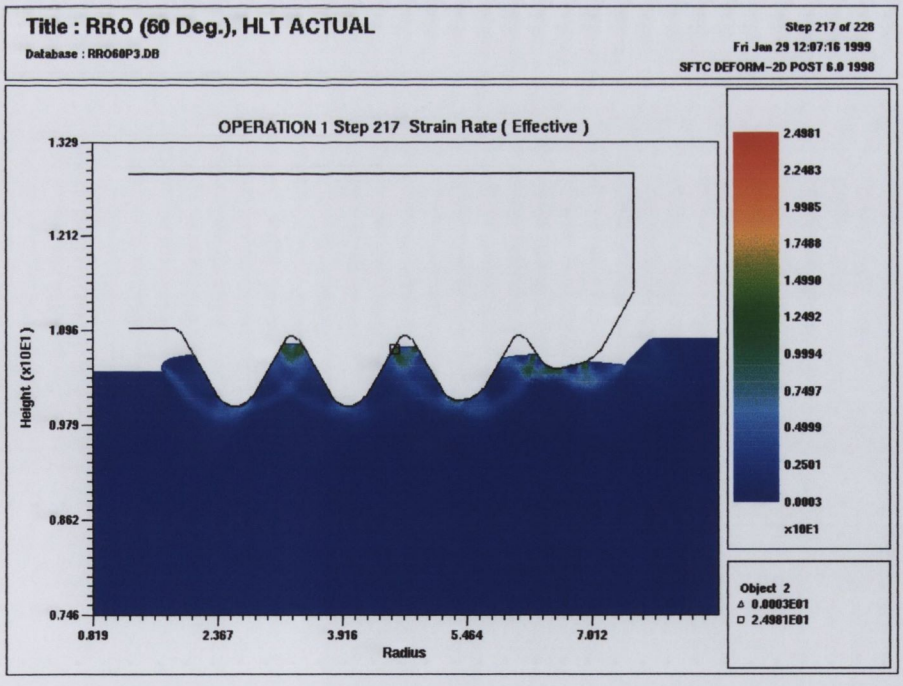

Figure A.7: Effective Strain Rate, "Worst Case" Radius Run-out geometry

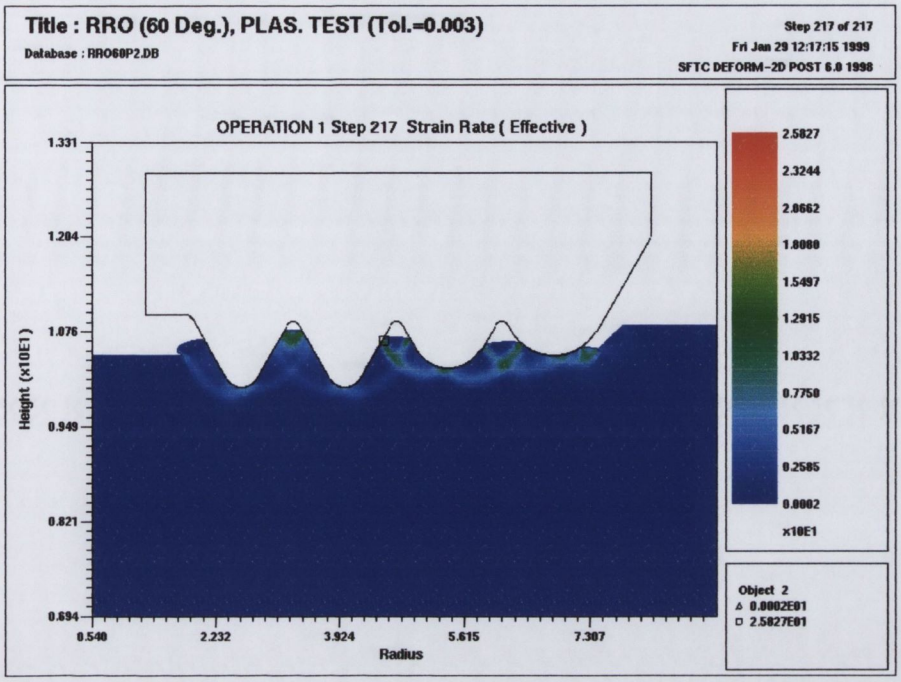

Figure A.8: Effective Strain Rate, "Optimum" Radius Run-out geometry

The graphs in Figure A.9 and A.10 show the effective strains beneath the crest radius of threads 1, 2, and 3 (which are indicated in Figure A.8.

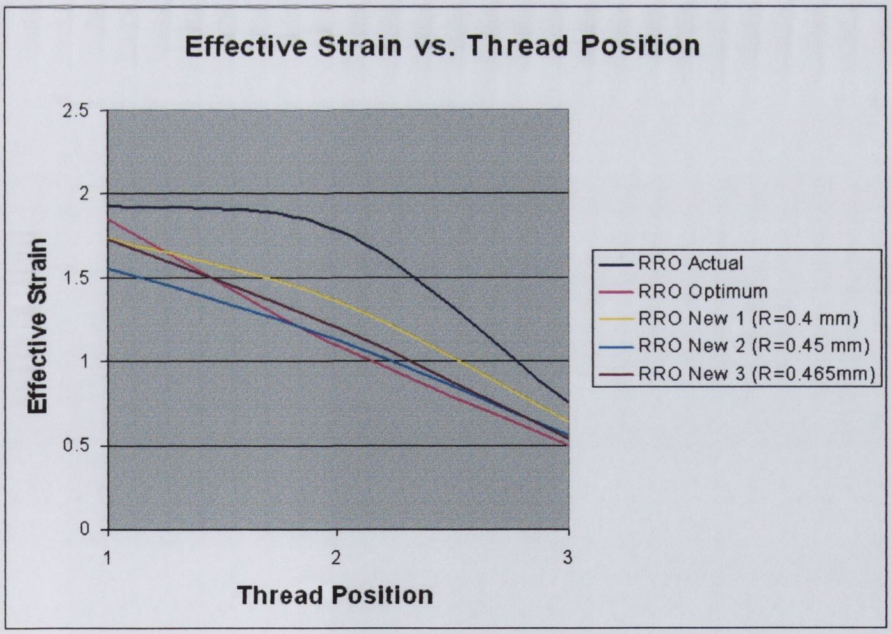

Figure A.9: Effective Strain vs. Thread Position

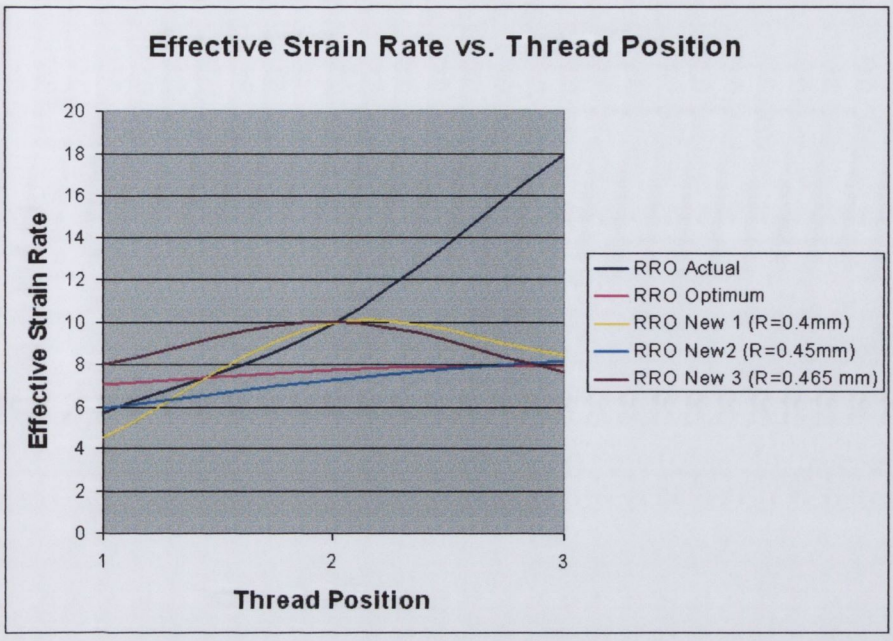

Figure A.10: Effective Strain Rate vs. Thread Position

The optimum radius run-out (RRO) design has a beneficial effect on both the strain and strain rate patterns over the last couple of threads, there is a definite decrease in maximum values. This feature is most probably due to rounded nature of the final two threads. There is a large drop in size from the second last thread to final thread on the current radius run-out design causes a strange low point in stresses along the flank of the second last thread, which is not evident in the optimum radius run-out design. The final thread on the current radius run-out (RRO) has a "pointed" aspect to it which cannot be conducive to equal deformation at the start of formation like that which would occur with the perfectly formed optimum radius run-out (RRO) design.

A.3 Thread Rolling Die Stress/Strain

A.3.1 Finite Element Models

The aim of these finite element models was to determine what effect the fastener material being rolled had on stresses in the thread rolling die. Three different fastener materials were modelled, namely Titanium-6Al-4V, SPS 0.9 Alloy, and Waspaloy. The tooling was modelled as M2 tool steel. Figure A.11 shows the finite element mesh used in all simulations. As seen previously (chapter 5) only the fastener had been modelled as a deformable object but the models now included a mesh and elasto-plastic properties for the tooling. The tool itself was meshed using over 1600 elements; the elements are concentrated in the crest part of the forming threads as this is the area where the highest stresses were expected to arise.

The run times for these simulations jumped by a factor of 4 times the previous simulations. This can be accounted for by the extra calculations, which must be undertaken by the DEFORM finite element package to analyse both elastic and plastic stresses in the tooling. Figure A.12 also contains a chart outlining the stress/strain curves used for the fastener materials and tooling in the finite element models. It should be noted that in the finite element solver once the last data point has been reached on the material curve, the solver interpolates for further data points which may give rise to erroneous material definition in later stages of a forming process.

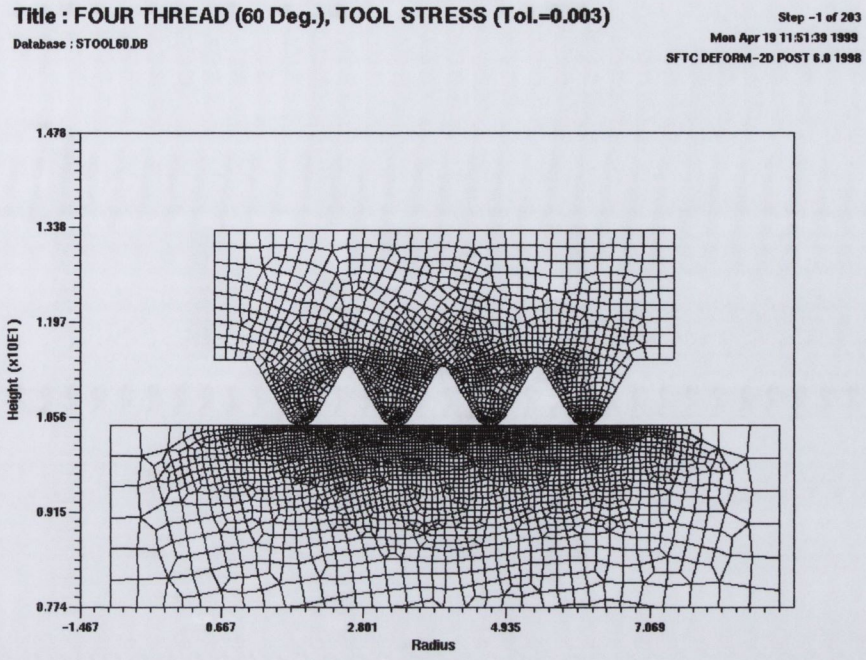

Figure A.11: Finite Element Mesh, Thread Rolling Die Model

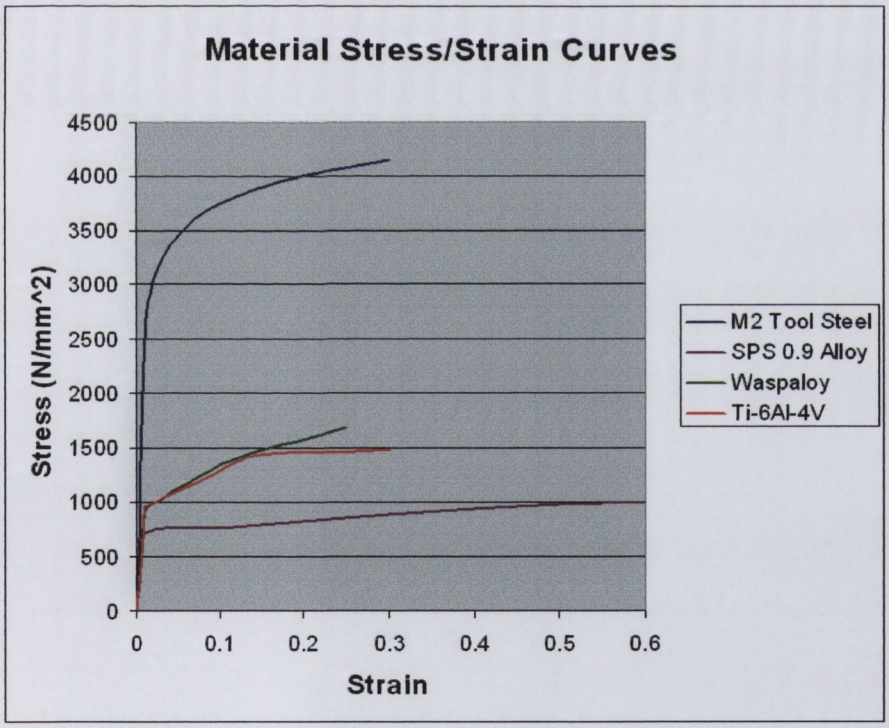

Figure A.12: Stress-Strain curves for Thread Rolling Die models

A.3.2 Results

All the plots indicate results taken at the end of the thread forming process. Only the thread rolling die has been plotted for the sake of clarity.

Effective Stress

Figures A.13 to A.15 show the effective stresses in the tooling for the three fastener materials. The highest stress (3867 N/mm^2) as expected occurs in the Waspaloy model, the harder the fastener material is to form the higher the loading and hence stress in the tooling should be. The worrying aspect is that the tooling has yielded quite a distance into the crest of the forming thread, indicated by the end of the yellow contour. This could be as a result of the material definition of the tooling or the fastener (see introduction). In both the Titanium-6Al-4V and SPS 0.9 alloy models the stress is of a somewhat lower magnitude, 2824 N/mm^2 and 2407 N/mm^2 respectively. The maximum stress in the titanium model is also above yield but this only occurs in a very localised area on the outside thread and is probably caused by the boundary conditions.

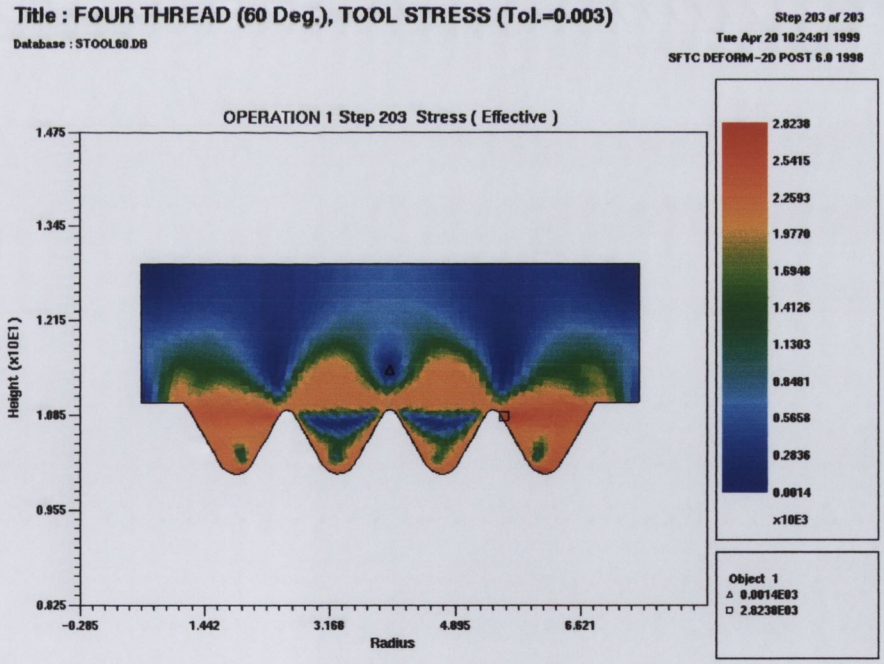

Figure A.13: Effective Strain in the Thread Rolling Die, Titanium 6Al-4V

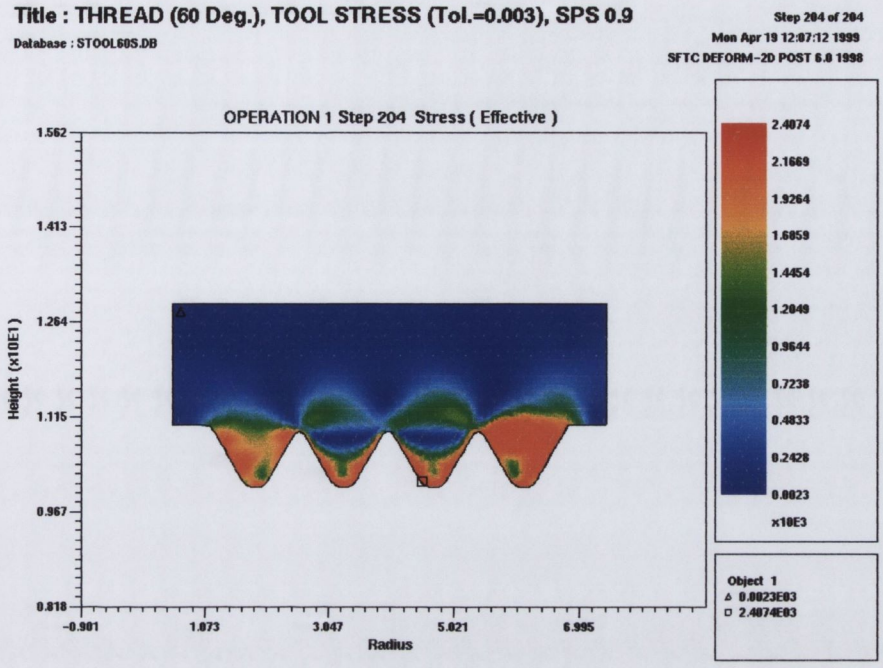

Figure A.14: Effective Stress in the Thread Rolling Die, SPS 0.9 Alloy

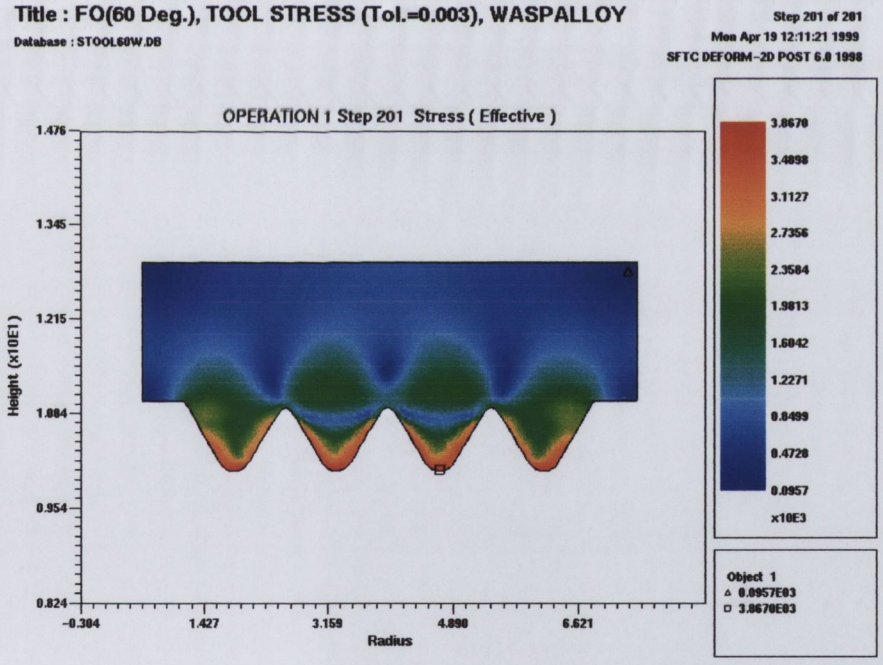

Figure A.15: Effective Stress in the Thread Rolling Die, Waspalloy

Effective Strain

Figures A.16 to A.18 indicate the effective strains in the tooling. These results follow exactly the same trend as found in the effective stress results. The area of maximum

effective strain (the small square on the plots) matches up perfectly with the area of maximum effective stress. The values mirror the stress strain curve of the materials, Titanium-6Al-4V: Tool Effective strain =0.016, SPS 0.9 Alloy: Tool Effective strain = 0.0055, Waspaloy: Tool Effective Strain = 0.14. Any effective strains above a value of 0.01 indicate an area where yielding has taken place. These results confirm the comments made in the previous section.

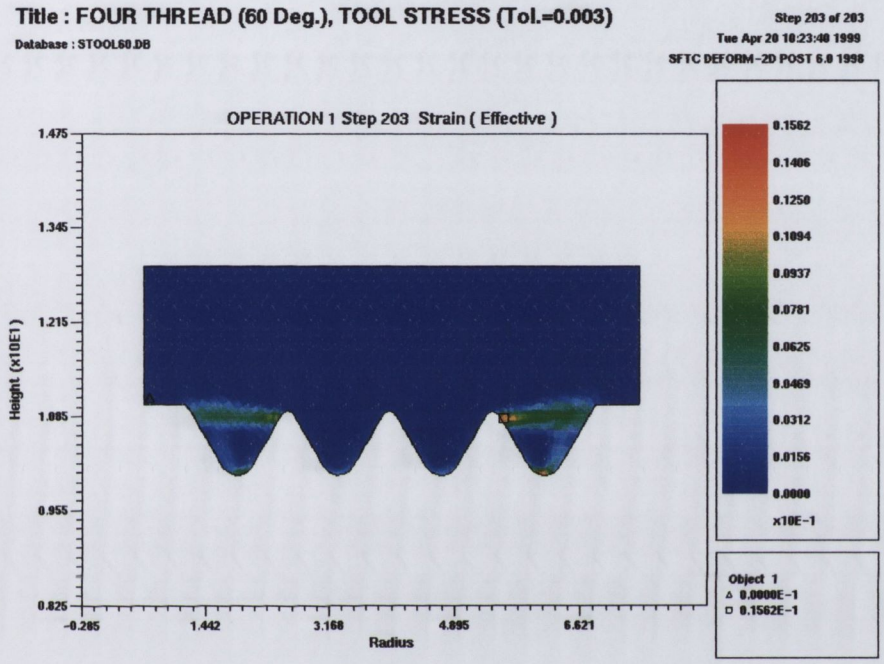

Figure A.16: Effective Strain in the Thread Rolling Die, Titanium 6Al-4V

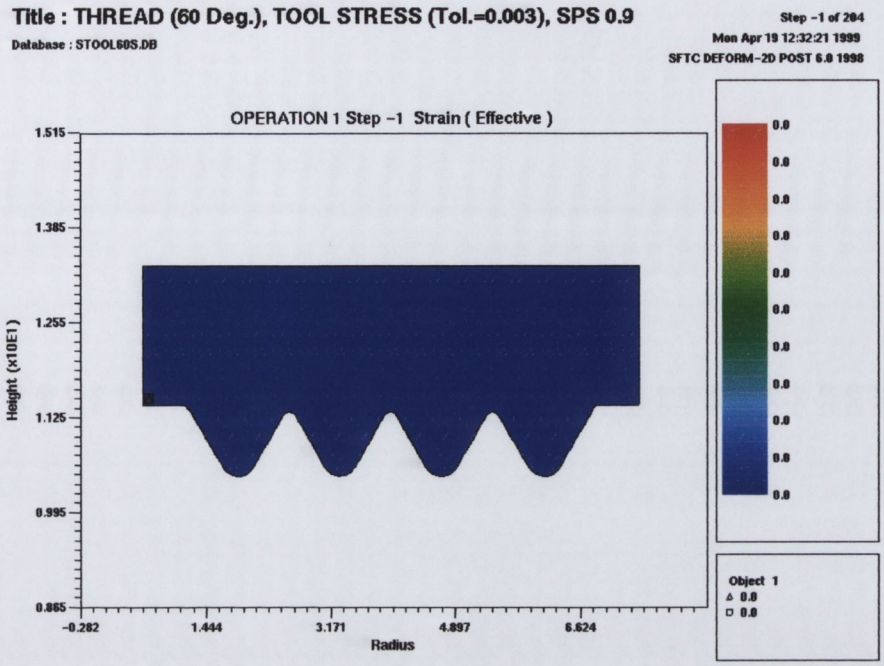

Figure A.17: Effective Strain in the Thread Rolling Die, SPS 0.9 Alloy

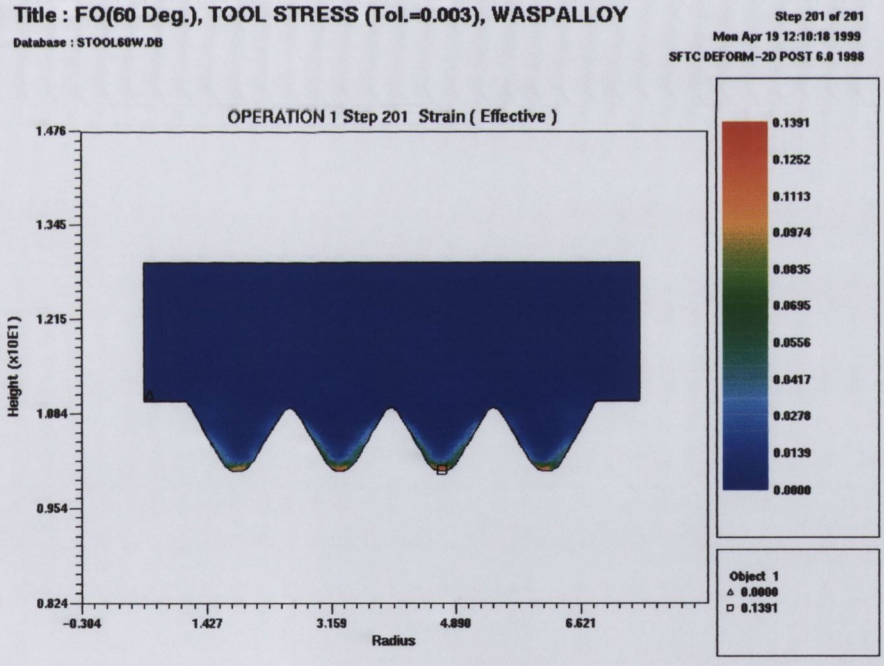

Figure A.18: Effective Strain in the Thread Rolling Die, Waspalloy

A.4 Ramp Rates

These models were created to analyse how the penetration rate of the thread rolling process affects strains and strain rates within the original finite element models. These models are the four thread standard 60 degree, crest radius (R2)=0.2438mm (0.0096in.) models (section 4.1.5). There were three ramp section designs used, namely, the standard, classic 2H, classic 3H designs. Each of these ramp section designs have progressively longer length ramp sections. This increased length will obviously decrease penetration rate. The penetration rates were calculated as follows.

All moving thread rolling dies are 16in. long with 0.5in. for match up between the thread rolling dies.

A 60 Waterbury Thread Rolling machine runs at 40 strokes per minute.

Therefore 1 stroke per 1.5 seconds

1 stroke = 16in.

16in. in 1.5 seconds :- 1in. in 0.09375 seconds

The thread is fully formed in the *ramp* section of the Thread Rolling die. We calculate the portion of the stroke in which this formation occurs.

DIE 1 (Standard Taper Design): Ramp Length = 7.5in. =0.703s

DIE 2 (Classic 2H Taper): Ramp Length = 9.45in. =0.886s

DIE 3 (Classic 3H Taper): Ramp Length = 11.187in. =1.049s

Now in the finite element model a stroke of 0.4mm on the tool (Thread rolling die) will produce a fully formed thread.

To calculate ramp rates divide this stroke by the time it takes on a real thread roll die to form the thread fully, which were calculated above

DIE 1: $0.4 \div 0.703 = 0.569$ mm/s

DIE 2: $0.4 \div 0.886 = 0.451$ mm/s (21% slower)

DIE 3: $0.4 \div 1.049 = 0.381$ mm/s (33% slower)

A.4.1 Results

The next four Figures A.19 to A.22 show graphs for effective strain and effective strain rate for tracking points 1 and 10 (section 5.3). Figure A.19 shows the effective strain at tracking point 1 for the three different ramp section designs. At point 1 there is little difference between the effective strain in the three different ramp length designs.

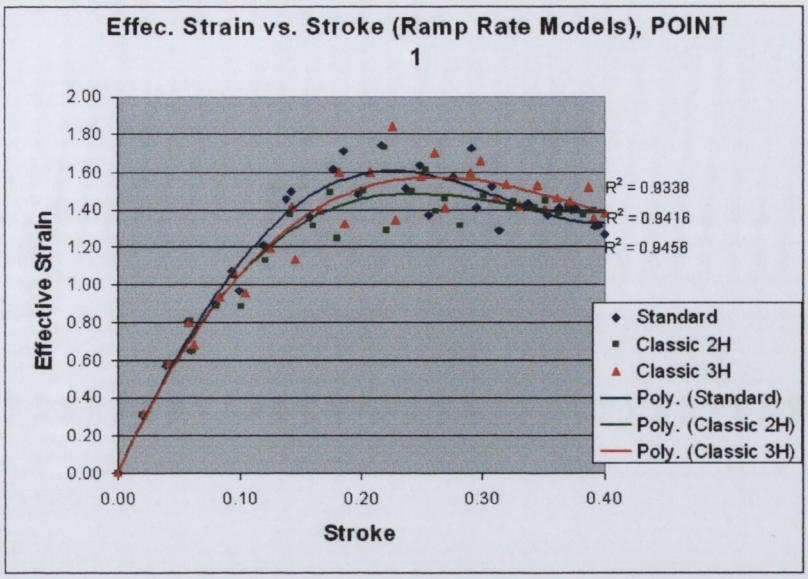

Figure A.19: Effective Strain at Point 1, Ramp section Designs

Figure A.20 shows the effective strain rate at tracking point 1 for the three different ramp section designs. At point 1 there is significant difference between the three ramp lengths. The longest ramp section shows a distinct benefit to the material as the magnitude of the strain rate is approximately 50% lower compared to the standard ramp length design.

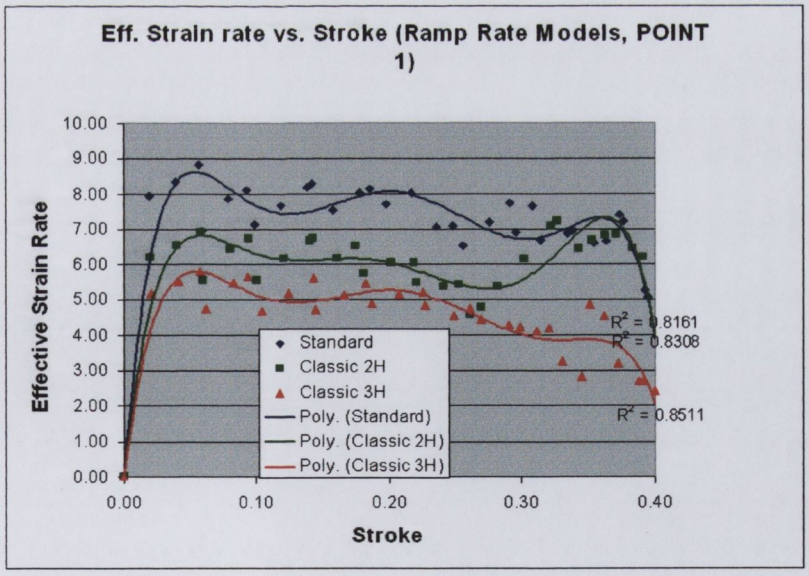

Figure A.20: Effective Strain Rate at Point 1, Ramp section Designs

Figures A.21 and A.22 indicate that changing the ramp section length has little or no effect on either the strains or strain rates at point 10.

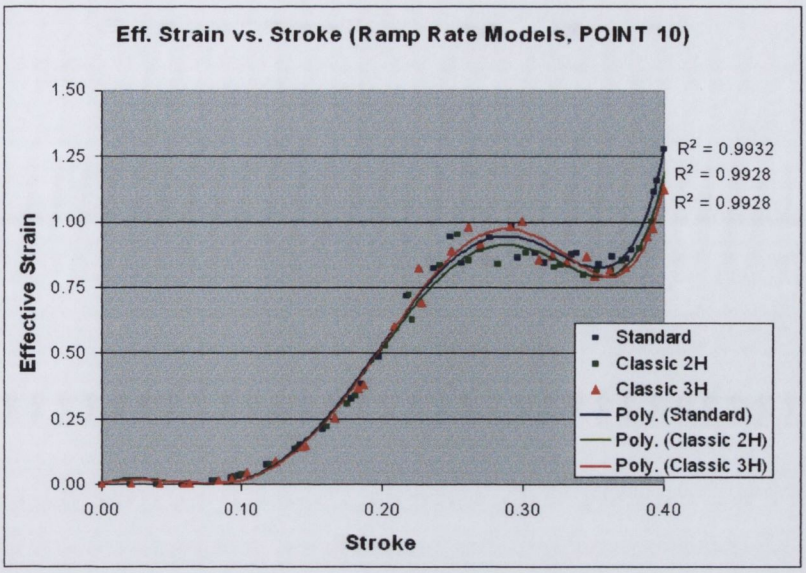

Figure A.21: Effective Strain at Point 10, Ramp section Designs

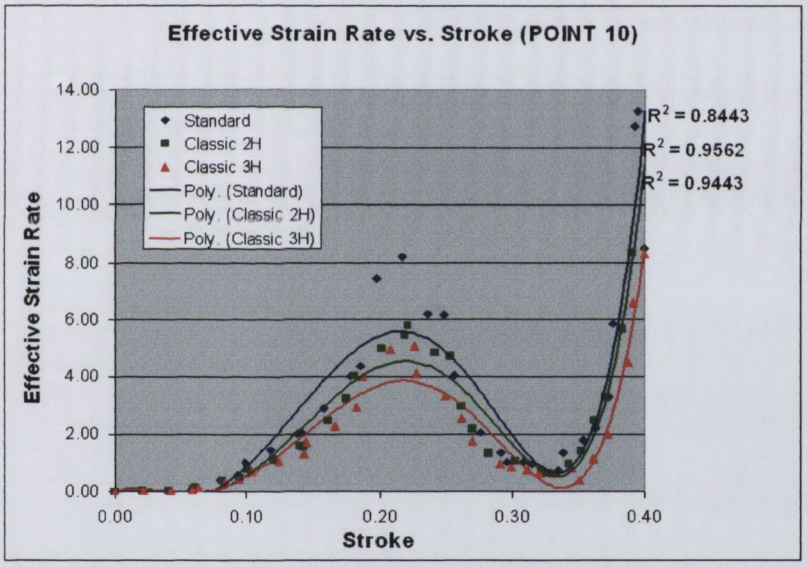

Figure A.22: Effective Strain Rate at Point 10, Ramp section Designs

Appendix B

Plasticity & Finite Element Theory

B.1 Plasticity

B.1.1 Equilibrium and Virtual Work-Rate Principle

Equilibrium Equations

In the rectangular cartesian coordinate system, the equilibrium equations, if the body force is neglected, are given by

$$\begin{aligned} \frac{\partial \sigma_x}{\partial x} + \frac{\partial \tau_{yx}}{\partial y} + \frac{\partial \tau_{xz}}{\partial z} &= 0 \\ \frac{\partial \tau_{xy}}{\partial x} + \frac{\partial \sigma_y}{\partial y} + \frac{\partial \tau_{zy}}{\partial z} &= 0 \\ \frac{\partial \tau_{xz}}{\partial x} + \frac{\partial \tau_{yz}}{\partial y} + \frac{\partial \sigma_z}{\partial z} &= 0 \end{aligned} \tag{B.1}$$

With suffix notation, eq. (B.1) are written as

$$\frac{\partial \sigma_{ij}}{\partial x_i} = 0, \quad \sigma_{ij,i} = 0 \tag{B.2}$$

In the notation used in eq. (B.2) a recurring letter suffix indicates the sum, and a comma denotes partial differentiation.

Equilibrium with Tractions

The stress along the boundary surface S is in equilibrium with an applied traction F_i (force per unit surface area). Equilibrium of the stress system is written as

$$F_i = \sigma_{ij} n_j \tag{B.3}$$

where n_j is the unit outward normal to the surface. Writing eq. (B.3) in unabridged notation in the two dimensional case (see Fig. B.1) gives,

$$\begin{aligned} F_x &= \sigma_x \left(\frac{dy}{dl}\right) + \tau_{xy} \left(\frac{dx}{dl}\right) \\ F_x &= \tau_{yx} \left(\frac{dy}{dl}\right) + \sigma_y \left(\frac{dx}{dl}\right) \end{aligned} \tag{B.4}$$

where the components of the unit outward normal n_j are given by $(dy/dl, dx/dl)$.

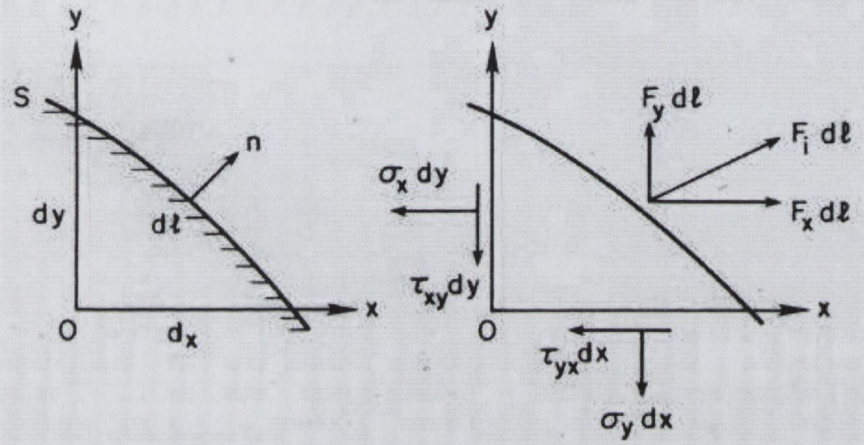

Figure B.1: Equilibrium of Surface Tractions

Virtual Work-Rate Principle

The virtual work-rate principle forms the basis of the finite element formulation which is described later in section B.2.1. The virtual work-rate principle states that for the stress field in equilibrium within the body and with the applied surface tractions, the work-rate inside the deforming body equals the work rate performed by the surface tractions for all velocity fields that are continuous and continuously differentiable (virtual velocity fields).

Let σ_{ij} be any stress field that is in equilibrium and w_j be any virtual velocity field. Then the principle of virtual work is expressed by

$$\int_V \sigma_{ij} \frac{\partial w_j}{\partial x_i} dV = \int_S F_j w_j dS \tag{B.5}$$

where V is the volume of the body and S is the surface. Since σ_{ij} is symmetric, eq. (B.5) can also be written as

$$\int_V \sigma_{ij} \dot{\epsilon}_{ij} dV = \int_S F_j w_j dS \tag{B.6}$$

where $\dot{\epsilon}_{ij}$ is the strain rate derivable from w_j according to $\dot{\epsilon}_{ij} = \frac{1}{2}(w_{i,j} + w_{j,i})$. For proof, note that

$$\sigma_{ij}\frac{\partial w_j}{\partial x_i} \equiv \frac{\partial}{\partial x_i}(\sigma_{ij}w_j) - w_j\frac{\partial \sigma_{ij}}{\partial x_i}, \qquad \text{where} \qquad \frac{\partial \sigma_{ij}}{\partial x_i} = 0$$

and

$$\int_V \frac{\partial}{\partial x_i}(\sigma_{ij}w_j)dV = \int_S w_j\sigma_{ij}n_i dS$$

For the two dimensional case, eq. (B.1.1) can be written in unabridged form as

$$\int_V \left(\sigma_x\frac{\partial w_x}{\partial x} + \sigma_y\frac{\partial w_y}{\partial y} + \tau_{xy}\frac{\partial w_y}{\partial x} + \tau_{yx}\frac{\partial w_x}{\partial y}\right)dV \tag{B.7}$$

$$= \int_V (\sigma_x\dot{\epsilon}_x + \sigma_y\dot{\epsilon}_y + \tau_{xy}\dot{\gamma}_{xy})dV$$

$$= \int_S (F_x w_x + F_y w_y)dS$$

B.1.2 Plastic Potential and Flow Rule

Hooke's Law describes the relationship between stresses and strains in the elastic deformation range. In order to derive the relationship between the stress and plastic strain, the concept of plastic potential is used. The ratios of the components of the plastic strain-rate $\dot{\epsilon}_{ij}{}^p$ (or infinitesimal plastic strain $d\epsilon_{ij}{}^p$) are defined by

$$\dot{\epsilon}_{ij}{}^p = h\frac{\partial g}{\partial \sigma_{ij}}\dot{f} \tag{B.8}$$

or

$$d\dot{\epsilon}_{ij}{}^p = h\frac{\partial g}{\partial \sigma_{ij}}df \tag{B.9}$$

where g and h are scalar functions of the invariants of deviatoric stresses and f is the yield function.

$\dot{f} < 0$ elastic unloading occurs (elastic behaviour) and the stress point returns inside the yield surface

$\dot{f} = 0$ neutral loading (plastic behaviour for a perfectly plastic material and the stress point remains on the yield surface

$\dot{f} > 0$ plastic loading (plastic behaviour for a strain hardening material) and the stress point remains on the expanding yield surface.

The function $g(\sigma_{ij})$ is called the *plastic potential.* Although eq. (B.8) is written in rate form, the relationship between stress and strain is independent of time.

Assuming a simple relation $g = f$, eqs. (B.8 and B.9) become

$$\dot{\epsilon}_{ij}{}^p = \frac{\partial f}{\partial \sigma_{ij}}\dot{\lambda} \qquad \text{or} \qquad d\epsilon_{ij}{}^p = \frac{\partial f}{\partial \sigma_{ij}}d\lambda \tag{B.10}$$

where $\dot{\lambda}$ or $d\lambda$ is a positive proportionality constant being equal to $h\dot{f}$ or hdf. Eq. (B.10) is a *flow rule* associated with the yield function $f(\sigma_{ij})$.

B.1.3 Work or Strain Hardening

After initial yielding, the stress level at which further plastic deformation takes place is dependent on the degree of plastic straining. Such a phenomenon is called work or strain hardening. For a mathematical formulation of strain hardening, it is assumed that the final yield locus is the same, no matter by what strain path a given stress state is reached. This is known as (*isotropic hardening*).

The total plastic work per unit volume during a given finite deformation is

$$W_p = \int \sigma_{ij} d\epsilon_{ij}{}^p, \tag{B.11}$$

where the integral is taken over the actual strain path.

The hypothesis that the radius of the yield locus of the Von Mises yield criterion is a function only of W_p may be written as

$$\begin{aligned} \overline{\sigma} &= \sqrt{\frac{1}{2}}\{(\sigma_1 - \sigma_2)^2 + (\sigma_2 - \sigma_3)^2 + (\sigma_3 - \sigma_1)^2\}^{\frac{1}{2}} \\ &= \sqrt{\frac{3}{2}}\{\sigma_{ij}{}'\sigma_{ij}{}'\}^{\frac{1}{2}} = F(W_p) \end{aligned} \tag{B.12}$$

where $\overline{\sigma}$ is written for Y or $\sqrt{3}k$, and is known as the *flow stress*, the *effective*, or equivalent stress.

Another hypothesis for strain hardening relates $\overline{\sigma}$ to a certain measure of the total plastic deformation. A quantity $d\overline{\epsilon}$, known as the *effective*, or *equivalent* infinitesimal plastic strain is defined according to

$$dW_p = \sigma_{ij} d\epsilon_{ij} = \overline{\sigma} d\overline{\epsilon} \tag{B.13}$$

The effective strain $\overline{\epsilon} = \int d\overline{\epsilon}$, integrated over the strain path, provides a measure of the plastic distortion. It is assumed that strain hardening characteristics can be formulated by

$$\overline{\sigma} = H\left(\int \overline{\epsilon}\right) = H(\overline{\epsilon}) \tag{B.14}$$

where H is a function depending on the metal concerned. Equation (B.14) is most frequently used for process analysis in metal forming. Methods of experimental determination of stress and strain properties were discussed earlier and are also described in [53, 54, 55, 44].

With the measures of $\overline{\sigma}$ and $d\overline{\epsilon}$ (and therefore $\dot{\overline{\epsilon}}$, effective strain rate), the proportionality factor $\dot{\lambda}$ in the Levy-Mises equations (3.20 and 3.21) can be expressed by

$$\dot{\lambda} = \frac{3}{2}\frac{\dot{\overline{\epsilon}}}{\overline{\sigma}} \tag{B.15}$$

The derivation of eq. (B.15) is as follows. The plastic work rate per unit volume using the flow rule eq. (B.10), is written as

$$\dot{W}_p = \sigma_{ij}\dot{\epsilon}_{ij} = \sigma_{ij}\frac{\partial f}{\partial \sigma_{ij}}\dot{\lambda}$$

Because the yield function $f(\sigma_{ij})$ is an homogeneous function of degree 2, namely $f(t\sigma_{ij}) = t^2 f(\sigma_{ij})$, and using Euler's theorem for homogeneous function of degree n, then $\sigma_{ij}(\partial f/\partial \sigma_{ij}) = nf(\sigma_{ij})$, the plastic work rate becomes

$$\dot{W}_p = \sigma_{ij}\frac{\partial f}{\partial \sigma_{ij}}\dot{\lambda} = 2f(\sigma_{ij})\dot{\lambda} = \overline{\sigma}\,\dot{\overline{\epsilon}}$$

From which (B.15) results for the yield function $f(\sigma_{ij})$ of (3.13) and $\overline{\sigma}$ defined by (B.12). The expression for $\dot{\overline{\epsilon}}$ in terms of strain rate components, corresponding to the effective stress $\overline{\sigma}$ of (B.12) can be obtained by inversion of the flow rule. Then

$$\dot{W}_p = \sigma_{ij}\dot{\epsilon}_{ij} = \sigma_{ij}{}'\dot{\epsilon}_{ij} = \frac{1}{\dot{\lambda}}\dot{\epsilon}_{ij}\dot{\epsilon}_{ij} = \frac{2}{3}\frac{\overline{\sigma}}{\dot{\overline{\epsilon}}}\dot{\epsilon}_{ij}\dot{\epsilon}_{ij} = \overline{\sigma}\,\dot{\overline{\epsilon}}$$

from which

$$\dot{\overline{\epsilon}} = \sqrt{\frac{2}{3}}\{\dot{\epsilon}_{ij}\dot{\epsilon}_{ij}\}^{\frac{1}{2}} \tag{B.16}$$

The numerical factors in the definition of $\overline{\sigma}$ and $\dot{\overline{\epsilon}}$ have been chosen so that the functional relationship between $\overline{\sigma}$ and $\int d\overline{\epsilon}$ is identical between true stress and logarithmic strain in a tension or compression test.

B.2 Finite Element Theory

B.2.1 Basis of the Finite Element Formulation

The variational approach mentioned earlier in section B.1.1 is based on one of two variational principles. It requires that among admissible velocities u_i that satisfy the conditions of compatibility and incompressiblity, as well as the velocity boundary conditions, the actual solution gives the following functional (function of functions) a stationary value:

$$\pi = \int_V \overline{\sigma}\,\dot{\overline{\epsilon}}\,dV - \int_{S_F} F_i u_i\,dS, \quad \text{for rigid-plastic materials} \tag{B.17}$$

where $\overline{\sigma}$ is the effective stress, $\dot{\overline{\epsilon}}$ is the effective strain rate, F_i represents surface tractions. This formulation forms the basis for solution of problems in the DEFORM finite element package used to model the thread rolling process in this thesis. The solution of the original boundary value problem is obtained from the solution of the dual variational problem, where the first order variation of the functional disappears, namely,

$$\delta\pi = \int_V \overline{\sigma}\,\delta\dot{\overline{\epsilon}}\,dV - \int_{S_F} F_i\,\delta u_i\,dS = 0 \tag{B.18}$$

where $\overline{\sigma} = \overline{\sigma}(\overline{\epsilon})$ for rigid plastic materials. The incompressibility constraint on admissible velocity fields in eq. (B.18) may be removed by introducing a Lagrange multiplier λ [56], [57] and modifying the functional (B.17) by adding the term $\int \lambda\dot{\epsilon}_v\,dV$, where $\dot{\epsilon}_v = \dot{\epsilon}_{ii}$ is the volumetric strain rate. Then,

$$\delta\pi = \int_V \overline{\sigma}\,\delta\dot{\overline{\epsilon}}\,dV + \int_V \lambda\,\delta\dot{\epsilon}_v\,dV + \int_V \dot{\epsilon}_v\,\delta\lambda\,dV - \int_{S_F} F_i\,\delta u_i\,dS = 0 \tag{B.19}$$

Another way of removing the constraint is to use the penalty form of the incompressibility [58] as

$$\delta\pi = \int_V \overline{\sigma}\,\delta\dot{\overline{\epsilon}}\,dV + K\int_V \dot{\epsilon}_v\,\delta\dot{\epsilon}_v\,dV - \int_{S_F} F_i\,\delta u_i\,dS = 0 \tag{B.20}$$

where K, a *penalty constant*, is a very large positive constant.

In eqs. (B.19 and B.20), δu_i and $\delta\lambda$ are arbitrary variations and $\delta\dot{\overline{\epsilon}}$ and $\delta\dot{\epsilon}_v$ are the variations of the strain rate derived from δu_i. Equation (B.19) or (B.20) is the basic equation for the finite element formulation [59]. Once the solution for the velocity field that satisfies the basic equation is obtained, then corresponding stresses can be calculated using the flow rule and the known mean stress distribution.

B.2.2 Finite Element Procedures

The solution satisfying equation (eq. B.17) from the previous section

$$\delta\pi = \int_V \overline{\sigma}\,\delta\dot{\overline{\epsilon}}\,dV - \int_{S_F} F_i\,\delta u_i\,dS = 0 \tag{B.21}$$

(where $\overline{\sigma}$ is the effective stress, $\dot{\overline{\epsilon}}$ is the effective strain rate, F_i represents surface tractions) is obtained from the allowable velocity fields that are constructed by introducing the shape function in such a way that a continuous velocity field can be defined uniquely in terms of the velocities of the associated nodal points. In the deformation process shown in, Figure B.2, the workpiece is divided into elements. In order to ensure continuity of the velocities over the whole workpiece, the shape function is defined such that velocities along any shared element side are expressed in terms of velocities at the same shared set of nodes (compatibility requirement). Then a continuous velocity field over the whole workpiece can be uniquely defined in terms of velocity values at nodal points specified globally.

We define a set of nodal point velocities in a vector form as

$$\mathbf{v}^T = \{v_1, v_2, \ldots, v_n\} \tag{B.22}$$

where the subscript T denotes transposition and N = (total number of nodes) $\times$ (degrees of freedom per node). An admissibility requirement for the velocity field is that the velocity boundary condition prescribed on surface S_u (essential boundary condition) must be satisfied. This condition can be imposed at nodes on S_u by assigning known values to the corresponding variables. Equation (B.21) and (B.19) or (B.20) are now expressed in terms of nodal point velocities $\mathbf{v}$ and their variations $\delta\mathbf{v}$. From arbitrariness of δv_I, a set of algebraic equations (stiffness equations) are obtained as

$$\frac{\partial\pi}{\partial v_I} = \sum_j \left(\frac{\partial\pi}{\partial v_I}\right)_{(j)} = 0 \tag{B.23}$$

where (j) indicates the quantity at the jth element. The capital letter suffix signifies that it refers to a nodal number. Equation (B.23) is obtained by evaluating the $(\partial\pi/\partial v_I)$ at the elemental level and assembling them into the global equation under appropriate constraints.

In metalforming, the stiffness equation (B.23) is nonlinear and the solution is obtained iteratively by using the *Newton Raphson* method or some other similar process. The method consists of linearisation and the application of convergence criteria to obtain the final solution. Linearization is achieved by Taylor expansion near an assumed

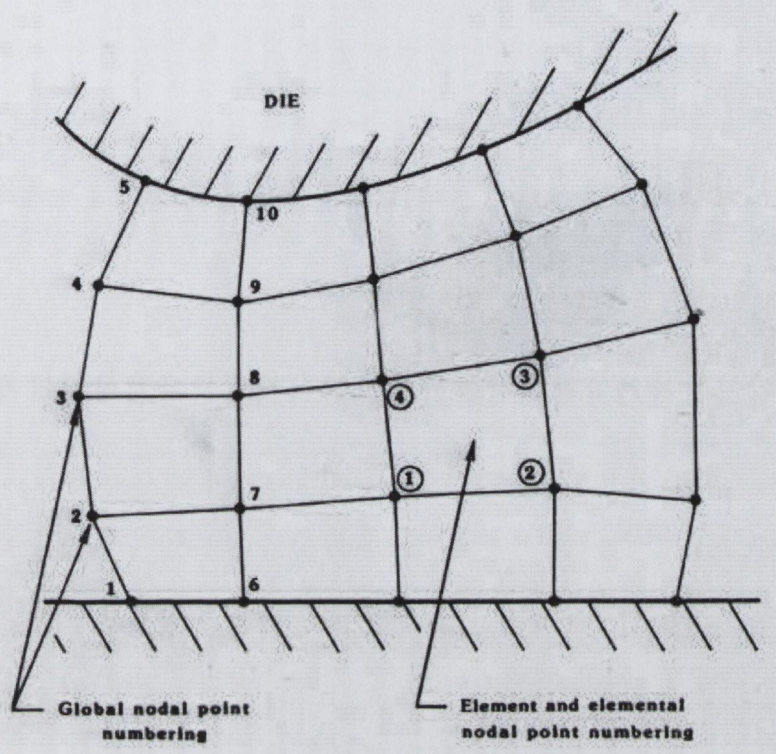

Figure B.2: Finite Element Mesh and Nodal Point Specifications

point $\mathbf{v} = \mathbf{v}_0$ (initial guess), namely,

$$\left[\frac{\partial \pi}{\partial v_I}\right]_{\mathbf{v}=\mathbf{v}_0} + \left[\frac{\partial^2 \pi}{\partial v_I \partial v_J}\right]_{\mathbf{v}=\mathbf{v}_0} \qquad \Delta v_J = 0 \tag{B.24}$$

where Δv_J is the first order correction of the velocity $\mathbf{v}_0$. Equation (B.24) can be written as follows

$$\mathbf{K}\Delta\mathbf{v} = \mathbf{f} \tag{B.25}$$

where $\mathbf{K}$ is called the stiffness matrix and $\mathbf{f}$ is the residual of the nodal point force vector. The solution of eq. (B.25) for the velocity correction term $\Delta\mathbf{v}$ is obtained using an initial guess velocity $\mathbf{v}_0$. This initial guess is then updated according to $\mathbf{v}_0 + \alpha\Delta\mathbf{v}$, where α is a constant between 0 and 1 called the *deceleration coefficient.* Iteration is continued until the velocity correction terms become negligible. This iteration process can be seen in Fig. B.3. It can be seen from this diagram that the initial guess velocity should be close to the actual solution. When the deformation process is relatively simple then this initial guess can be easy to determine but for a complex process then obtaining a good initial guess solution is difficult. This is where the direct iteration method comes into play.

Two convergence criteria may be used. One measures the error norm of the velocities, $\| \Delta\mathbf{v} \| / \| \mathbf{v} \|$, where the Euclidean vector is defined as $\| \mathbf{v} \| = (\mathbf{v}^T\mathbf{v})^{\frac{1}{2}}$, and

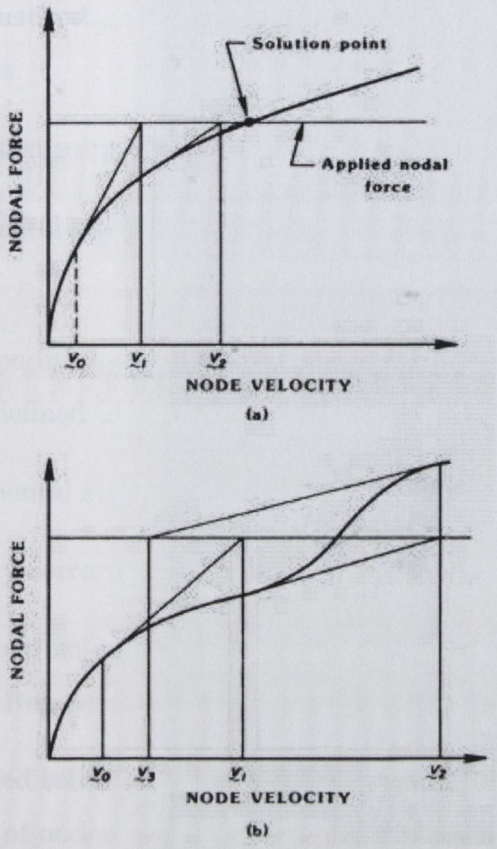

Figure B.3: Schematic representation of the Newton-Raphson method

requires such an error norm to decrease from iteration to iteration. The other criterion requires the norm of the residual equations, $\| \partial\pi/\partial\mathbf{v} \|$, to decrease. In general, the first criteria is useful when the velocity field is still far from the solution. The second test is most useful when slightly ill-conditioned systems reach the final stage of iterations. The final solution is reached when the error norm is below a certain tolerance, say 5×10^{-5}.

The finite element method procedures outlined above are implemented in a computer program as follows.

1. Generate an assumed solution velocity
2. Evaluate the elemental stiffness matrix for the velocity correction term $\Delta \mathbf{v}$ in eq. (B.25).
3. Impose velocity conditions to the elemental stiffness matrix, and repeat step 2 over all elements defined in the workpiece.
4. Assemble the elemental stiffness matrices to form a global stiffness matrix
5. Obtain the velocity correction terms by solving the global stiffness equation
6. Update the assumed solution velocity by adding the correctional term to the assumed velocity. Repeat steps 2 through 6 until the velocity solution converges
7. When the converged solution is obtained, update the geometry of the workpiece using the velocity of nodes during a specified time increment. Steps 2 through 7 are repeated until the desired degree of deformation is achieved.

B.2.3 Elements and Shape Functions

The geometry of an element, in general, is uniquely defined by a finite number of nodal points (nodes). The nodes are located on the boundary of the element or within the element, and the shape function defines an admissible velocity field locally in terms of velocities of associated nodes. Thus, elements are characterised by the shape and the order of the shape functions.

In the finite element method, interpolation of a scalar function $f(x, y)$ defined over an element is introduced in a form

$$f(x, y) = \sum_{\alpha} q_{\alpha}(x, y) \cdot f_{\alpha} \tag{B.26}$$

where f_{α} is a function value associated with the αth node, and $q_{\alpha}(x, y)$ is the shape function. It is, in general, a polynomic function of x and y defined over the element in such a way that

$$q_{\alpha}(x_{\beta}, y_{\beta}) = \delta_{\alpha\beta} \tag{B.27}$$

where (x_β, y_β) are the coordinates of the βth node and $\delta_{\alpha\beta}$ is the Kronecker delta. Owing to the property of the shape functions given by eq. (B.27), f_α in eq. (B.26) has the value of the function f at (x_α, y_α) and the f_α are independent of each other.

There are various types of elements, depending upon the shape of the element and the polynomial order of the shape functions. The only element which the DEFORM 2D finite element analysis package uses is the 4-noded quadrilateral element and this will be looked at in detail in the next section. Other elements and their shape functions can be reviewed in [58].

4 Node Rectangular Element

The shape functions of rectangular elements are, in general, defined in a parametric form over a domain $-1 \leq \xi \leq 1$, $-1 \leq \eta \leq 1$ in a local coordinate system (ξ, η). The element defined in the local coordinate system is sometimes called the *parent element*. The simplest of the rectangular elements and the element which is used in the DEFORM finite element package i.e. in all the thread rolling finite element models is the 4-node linear element shown in Fig.(B.4). The shape functions, q_α, which are bilinear in ξ and η, are defined as

$$q_\alpha(\xi, \eta) = \frac{1}{4}(1 + \xi_\alpha \xi)(1 + \eta_\alpha \eta) \tag{B.28}$$

where $(\xi_\alpha, \eta_\alpha)$ are the natural coordinates of a node at one of its corners. The value of the shape function, given by eq. (B.28), is shown schematically in Fig. B.4. Admissible velocity fields can be defined uniquely over the rectangular element by the nodal velocity components as

$$\begin{aligned} u_x(\xi, \eta) &= \sum_\alpha q_\alpha(\xi, \eta) u_x^{(\alpha)} \\ u_y(\xi, \eta) &= \sum_\alpha q_\alpha(\xi, \eta) u_y^{(\alpha)} \end{aligned} \tag{B.29}$$

where $(u_x^{(\alpha)}, u_y^{(\alpha)})$ is the velocity at the αth node and summation is over all four nodes.

Coordinates transformation from the natural coordinate (ξ, η) to the global coordinate (x, y) is defined by

$$\begin{aligned} x(\xi, \eta) &= \sum_\alpha q_\alpha(\xi, \eta) x_\alpha \\ y(\xi, \eta) &= \sum_\alpha q_\alpha(\xi, \eta) y_\alpha \end{aligned} \tag{B.30}$$

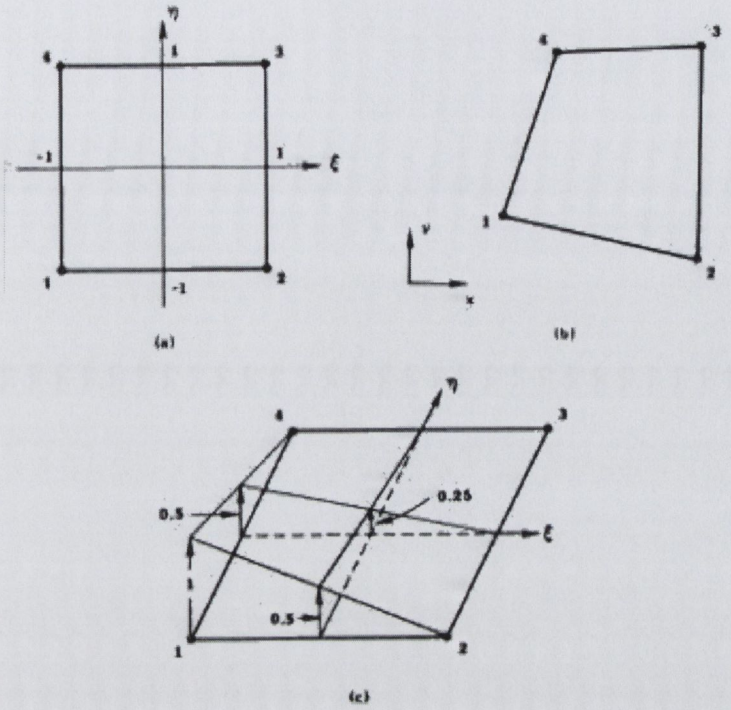

Figure B.4: (a) Local Coordinate and rectangular parent element; (b) isoparametric element (mapped on Cartesian coordinate; quadrilateral element); (c) shape function

where (x_α, y_α) are the global coordinates of the αth node. Since the coordinate transformation eq. (B.30) uses the same shape functions eq. (B.29), the linear element is isoparametric and takes quadrilateral shape in the Cartesian map, as shown in Fig. B.4b.

In expressing elemental functions, it is more convenient to express a velocity field in a vector form as

$$\mathbf{u} = \mathbf{N}^T \mathbf{v}$$

where the superscript T represents the transpose of the matrix. The vectors $\mathbf{u}$ and $\mathbf{v}$ are defined by their components according to

$$\begin{aligned} \mathbf{u}^T &= \{u_x(\xi,\eta), u_y(\xi,\eta)\} \\ \mathbf{v}^T &= \{u_x^{(1)}, u_y^{(1)}, u_x^{(2)}, u_y^{(2)}, \ldots\} = \{\upsilon_1, \upsilon_2, \upsilon_3, \ldots\} \end{aligned}$$

respectively, for the case of two dimensional deformation.

The shape functions are also arranged in the matrix form as

$$\mathbf{N}^T = \begin{bmatrix} q_1 & 0 & q_2 & 0 & q_3 & 0 & q_4 & 0 \\ 0 & q_1 & 0 & q_2 & 0 & q_3 & 0 & q_4 \end{bmatrix}$$

with

$$\begin{aligned} q_1 &= \frac{1}{4}(1-\xi)(1-\eta), \qquad q_2 = \frac{1}{4}(1+\xi)(1-\eta) \\ q_3 &= \frac{1}{4}(1+\xi)(1+\eta), \qquad q_4 = \frac{1}{4}(1-\xi)(1+\eta) \end{aligned} \tag{B.31}$$

for the two dimensional case.

B.2.4 Element Strain Rate Matrix

Previously in section 3.1.2, the strain rate components in the Cartesian coordinate system were defined by

$$\dot{\epsilon}_{ij} = \frac{1}{2}\left(\frac{\partial u_i}{\partial x_j} + \frac{\partial u_j}{\partial x_i}\right) \tag{B.32}$$

It was also shown, in the previous section, that the admissible velocity for all types of elements can be expressed by

$$u_i = \sum_\alpha q_\alpha u_i^{(\alpha)} \tag{B.33}$$

Substituting eq. (B.33) into eq. (B.32), we have

$$\dot{\epsilon}_{ij} = \frac{1}{2}\sum_\alpha \left(\frac{\partial q_\alpha}{\partial x_j} u_i^{(\alpha)} + \frac{\partial q_\alpha}{\partial x_i} u_j^{(\alpha)}\right) \tag{B.34}$$

It can be seen from eq. (B.34) that strain rate components can be evaluated if $\partial q_\alpha / \partial x_i$ is known.

For the Cartesian coordinate system, we denote the coordinate x_i by (x, y, z) for three dimensional deformation, and by (x, y) for two dimensional deformation. Since all the models used in the finite element analysis of thread rolling in chapter 4 are two dimensional, these equations will be concentrated on.

Let X_α, and Y_α be defined as

$$X_\alpha = \frac{\partial q_\alpha}{\partial x}, \qquad Y_\alpha = \frac{\partial q_\alpha}{\partial y}, \tag{B.35}$$

Then the strain rate components given by eq. (B.34) are expressed by

$$\dot{\epsilon}_x = \sum X_\alpha u_x^{(\alpha)}, \qquad \dot{\epsilon}_y = \sum Y_\alpha u_y^{(\alpha)}, \qquad \dot{\epsilon}_z = \sum Z_\alpha u_z^{(\alpha)},$$

$$\begin{aligned} \dot{\epsilon}_{xy} &= \frac{1}{2}\sum (Y_\alpha u_x^{(\alpha)} + X_\alpha u_y^{(\alpha)}) \\ \dot{\epsilon}_{yz} &= \frac{1}{2}\sum (Z_\alpha u_y^{(\alpha)} + Y_\alpha u_z^{(\alpha)}) \\ \dot{\epsilon}_{zx} &= \frac{1}{2}\sum (X_\alpha u_z^{(\alpha)} + Z_\alpha u_x^{(\alpha)}) \end{aligned} \tag{B.36}$$

It is convenient to arrange the strain rate components in a vector form. For a two dimensional element and plane strain deformation, the strain rate component can be written as

$$\dot{\boldsymbol{\epsilon}} = \begin{Bmatrix} \dot{\epsilon}_x \\ \dot{\epsilon}_y \\ \dot{\epsilon}_z \\ \dot{\gamma}_{xy} \end{Bmatrix} = \begin{Bmatrix} \frac{\partial u_x}{\partial x} \\ \frac{\partial u_y}{\partial y} \\ 0 \\ \frac{\partial u_y}{\partial x} + \frac{\partial u_x}{\partial y} \end{Bmatrix} \quad \text{for plane strain} \tag{B.37}$$

Substituting eqs. (B.35 and B.36) into eqs. B.37, the strain rate vectors are represented in unified form, as

$$\dot{\boldsymbol{\epsilon}} = \begin{Bmatrix} \dot{\epsilon}_1 \\ \dot{\epsilon}_2 \\ \dot{\epsilon}_3 \\ \dot{\epsilon}_4 \end{Bmatrix} = \begin{Bmatrix} \sum X_\alpha u_1^{(\alpha)} \\ \sum Y_\alpha u_2^{(\alpha)} \\ \sum P_\alpha u_1^{(\alpha)} \\ \sum (X_\alpha u_2^{(\alpha)} + Y_\alpha u_1^{(\alpha)}) \end{Bmatrix} \tag{B.38}$$

In eq. (B.38), u_1 and u_2 correspond to u_x and u_y, respectively, for two-dimensional deformation, and P_α is zero for plane strain deformation.

Equation (B.38) can be written in matrix form as

$$\dot{\boldsymbol{\epsilon}} = \mathbf{B}\mathbf{v} \tag{B.39}$$

where $\mathbf{B}$ is called the Strain Rate matrix and is written as

$$\mathbf{B} = \begin{bmatrix} X_1 & 0 & X_2 & 0 & X_3 & 0 & X_4 & 0 \\ 0 & Y_1 & 0 & Y_2 & 0 & Y_3 & 0 & Y_4 \\ P_1 & 0 & P_2 & 0 & P_3 & 0 & P_4 & 0 \\ Y_1 & X_1 & Y_2 & X_2 & Y_3 & X_3 & Y_4 & X_4 \end{bmatrix} \tag{B.40}$$

for a 4 noded rectangular element.

The evaluation of the strain rate matrix, or X_α, and Y_α, requires the differentiation of shape functions with respect to the global coordinate.

Since the shape functions are expressed in the natural coordinate system, it is necessary to express the global derivatives in terms of the derivatives with respect to the natural coordinates. Consider a coordinate transformation given by eq. (B.30), where shape functions are defined in the natural coordinate system. Then the derivatives of

the shape functions with respect to the natural coordinate system can be expressed, using the chain rule, as

$$\left\{ \begin{array}{c} \frac{\partial q_\alpha}{\partial \xi} \\ \\ \frac{\partial q_\alpha}{\partial \eta} \end{array} \right\} = \mathbf{J} \left\{ \begin{array}{c} \frac{\partial q_\alpha}{\partial x} \\ \\ \frac{\partial q_\alpha}{\partial y} \end{array} \right\} \tag{B.41}$$

where $\mathbf{J}$ is the *Jacobian* matrix of the coordinate transformation, given by

$$\mathbf{J} = \left[\begin{array}{cc} \frac{\partial x}{\partial \xi} & \frac{\partial y}{\partial \xi} \\ \\ \frac{\partial x}{\partial \eta} & \frac{\partial y}{\partial \eta} \end{array} \right] \tag{B.42}$$

For the rectangular element described earlier, X_α and Y_α can be evaluated from

$$\left\{ \begin{array}{c} X_\alpha \\ Y_\alpha \end{array} \right\} = \frac{1}{|\mathbf{J}|} \left[\begin{array}{cc} \frac{\partial y}{\partial \eta} & -\frac{\partial y}{\partial \xi} \\ \\ -\frac{\partial x}{\partial \eta} & \frac{\partial x}{\partial \xi} \end{array} \right] \left\{ \begin{array}{c} \frac{\partial q_\alpha}{\partial \xi} \\ \\ \frac{\partial q_\alpha}{\partial \eta} \end{array} \right\} \tag{B.43}$$

where $|\mathbf{J}|$ is the determinant of the Jacobian matrix and is expressed as

$$|\mathbf{J}| = \frac{\partial x}{\partial \xi}\frac{\partial y}{\partial \eta} - \frac{\partial x}{\partial \eta}\frac{\partial y}{\partial \eta} \tag{B.44}$$

For a quadrilateral element with the numbering of nodes shown in Fig.(B.4), X_α, Y_α, and $|\mathbf{J}|$ can be expressed in the closed form as

$$\begin{aligned} \left\{ \begin{array}{c} X_1 \\ X_2 \\ X_3 \\ X_4 \end{array} \right\} &= \frac{1}{8|\mathbf{J}|} \left\{ \begin{array}{c} y_{24} - y_{34}\xi - y_{23}\eta \\ -y_{13} + y_{34}\xi + y_{14}\eta \\ -y_{24} + y_{12}\xi - y_{14}\eta \\ y_{13} - y_{12}\xi + y_{23}\eta \end{array} \right\} \\ \left\{ \begin{array}{c} Y_1 \\ Y_2 \\ Y_3 \\ Y_4 \end{array} \right\} &= \frac{1}{8|\mathbf{J}|} \left\{ \begin{array}{c} -x_{24} + x_{34}\xi + x_{23}\eta \\ x_{13} - x_{34}\xi - x_{14}\eta \\ x_{24} - x_{12}\xi + x_{14}\eta \\ -x_{13} + x_{12}\xi - x_{23}\eta \end{array} \right\} \end{aligned} \tag{B.45}$$

Matrices of Effective Strain Rate and Volumetric Strain Rate

In the finite element formulation of metal forming, the effective strain rate $\dot{\bar{\epsilon}}$ and the volumetric strain rate $\dot{\epsilon}_v$ are frequently used. Therefore, it is necessary to express the effective strain rate and volumetric strain rate in terms of the strain rate matrix.

The effective strain rate has been defined in terms of strain rate components in section (B.1.3), eq. (B.16), as

$$\dot{\bar{\epsilon}} = \sqrt{\frac{2}{3}} \{\dot{\epsilon_{ij}}\dot{\epsilon_{ij}}\}^{\frac{1}{2}} \tag{B.46}$$

or, in the matrix form

$$(\dot{\bar{\epsilon}})^2 = \dot{\boldsymbol{\epsilon}}^T \mathbf{F} \dot{\boldsymbol{\epsilon}} \tag{B.47}$$

The diagonal matrix $\mathbf{F}$ has $\frac{2}{3}$ and $\frac{1}{3}$ as its components; corresponding to normal strain rate and engineering shear strain rate, respectively. Substituting eq. (B.39) into eq. (B.47) gives

$$(\dot{\bar{\epsilon}})^2 = \mathbf{v}^T \mathbf{B}^T \mathbf{F} \mathbf{B} \mathbf{v} = \mathbf{v}^T \mathbf{P} \mathbf{v} \tag{B.48}$$

where $\mathbf{P} = \mathbf{B}^T \mathbf{F} \mathbf{B}$.

For a plane strain problem the matrix $\mathbf{F}$ in eq.(B.47) takes the following form.

$$\mathbf{F} = \begin{bmatrix} \frac{2}{3} & & & 0 \\ & \frac{2}{3} & & \\ & & \frac{2}{3} & \\ 0 & & & \frac{1}{3} \end{bmatrix}$$

The volumetric strain rate $\dot{\epsilon}_v$ is given by

$$\dot{\epsilon}_v = \dot{\epsilon}_{kk} = \dot{\epsilon}_x + \dot{\epsilon}_y + \dot{\epsilon}_z$$

and is expressed in matrix form by

$$\dot{\epsilon}_v = \mathbf{C}^T \mathbf{v} = C_I \upsilon_I \tag{B.49}$$

with $C_I = B_{1I} + B_{2I} + B_{3I}$, where B_{IJ} is an element of the strain rate matrix $\mathbf{B}$. For the plane strain case $\mathbf{C}$ equals

$$\mathbf{C}^T = \{1, 1, 1, 0\}\mathbf{B}, \tag{B.50}$$

B.2.5 Elemental Stiffness Equation

It can be easily seen from the way in which the element stiffness formulation was introduced (section B.2.2) that the global integrals over the whole workpiece stem from the assembly of integrals over the local domain of finite elements. Therefore, it is convenient to evaluate the stiffness matrix given by eq. (B.25) at the elemental level, and to assemble into a global stiffness matrix.

Of the two variational formulations eqs. (B.19) and (B.20), DEFORM uses the penalty function method, eq. (B.20). The first, second, and third terms (including signs) of eq. (B.20) are denoted as $\delta\pi_D$, $\delta\pi_P$, and $\delta\pi_{S_F}$, respectively. In metal forming, the boundary conditions along the die-workpiece interface are mixed. Using the discrete representation of the quantities involved in $\delta\pi$ that were developed in sections B.2.3 and B.2.4, the integrals of $\delta\pi$ can be expressed in terms of nodal point velocities. Equation B.24 becomes

$$\frac{\partial\pi}{\partial v_I} = \frac{\partial\pi_D}{\partial v_I} + \frac{\partial\pi_P}{\partial v_I} + \frac{\partial\pi_{S_F}}{\partial v_I} \tag{B.51}$$

where

$$\begin{aligned} \frac{\partial\pi_D}{\partial v_I} &= \int_V \frac{\overline{\sigma}}{\dot{\overline{\epsilon}}} P_{IJ} v_J dV \\ \frac{\partial\pi_P}{\partial v_I} &= \int_V K C_J v_J C_I dV \\ \frac{\partial\pi_{S_F}}{\partial v_I} &= -\int_{S_F} F_j N_{jI} dS \end{aligned} \tag{B.52}$$

It should be noted that the term $(-\partial\pi_{S_F}/\partial v_I)$ is the applied nodal point force and that $\partial\pi_D/\partial v_I + \partial\pi_P/\partial v_I$ is the reaction nodal point force. Evaluating stiffness matrices at the elemental level from eq. (B.52), and assembling them for the whole workpiece, a set of simultaneous equations is arrived at (eq. B.25).